Next Generation Pre-polymer Coatings to Enhance In Situ Endothelialisation of Vascular Stents

A thesis submitted for the degree of
Doctor of Philosophy

by

JUN HON PANG

Division of Surgery and Interventional Science
University College London

Nov 2017

Declaration

I, Jun Hon Pang, confirm that the work presented in this thesis is my own. Where information has been derived from other sources, I confirm that this has been indicated in the thesis.

Abstract

The persistence of thrombosis and restenosis owing to inflammation and poor endothelialisation of cardiovascular stents in patients highlights the need for new biomaterials with *in situ* endothelialisation capability. This thesis describes the development of a novel chemical curing procedure using poly(carbonate)urethane pre-polymers (PCU-PP), and subsequent immobilisation of biomolecules to promote *in situ* endothelialisation.

PCU-PP coatings were chemically cured with ethylenediamine (EDA), propargylamine (PPA) and 3-mercaptopropionic acid (MPA). Anti-CD34 antibodies, which can capture endothelial progenitor cells (EPCs), were immobilised on to EDA coatings (EDA-CD34Ab). Cyclic REDV peptides (cycREDV), which are ligands selective towards endothelial cells (ECs), were immobilised on to PPA coatings (PPA-cycREDV).

EDA-curing yielded coatings with surface amine ($-NH_2$) functionality alongside micro-ridges (~8 μm) and nanofeatures (~90 nm). MPA-curing yielded carboxyl (-COOH) functionalised coatings with submicron ridges (~0.5 μm), while PPA-curing produced alkyne (-C≡C) functionalised coatings with micro-islands (~15 μm) and nanofibrous morphology (<120 nm). Human umbilical vein ECs (HUVEC) showed differential responses to these combinatorial chemistry and nanotopography platforms. Cell adhesion and proliferation were influenced primarily by surface chemistry, but were further regulated by nanotopography. Optimal cell adhesion and proliferation were impeded on EDA surfaces with 35 nm high nanofeatures, but was enhanced on 15 nm high nanofeatures. EDA-CD34Ab supported optimal adhesion and proliferation of HUVECs and endothelial colony forming cells (ECFCs), but reduced platelet adhesion and activation. ECFCs with higher CD34 expression demonstrated improved long-term survivability on EDA-CD34Ab. PPA-cycREDV enhanced HUVEC adhesion and survival compared to linear REDV chains, while also reduced platelet adhesion. Finally, combinatorial EDA-PPA curing yielded multifunctional coatings for co-immobilisation of anti-CD34Ab and cycREDV. The combined coatings did not show synergistic enhancement in HUVEC density, suggesting further optimisation in its formulation might be needed.

In conclusion, PCU-PP was developed to produce coatings with tuneable chemistry and topography. Immobilisation of biomolecules enhances EC selectivity over platelets, which is vital to promote *in situ* endothelialisation and circumvent clinical complications including thrombosis and restenosis. The tailorability of combinatorial surface properties of such coatings is important for discovery of next generation biomaterials with pro-healing capabilities.

Dedication

To the memory of my beloved mother

To the memory of my grandparents

To my father

To my family

For all their endless love and support

For their emphasis on education and personal development

Acknowledgement

I am eternally grateful to many people who have, in many different ways, contributed to the PhD journey leading to this thesis. First and foremost, my deepest gratitude goes to my supervisor, Dr Brian Cousins, for his invaluable mentorship, guidance, openness to new ideas and encouragement, which are instrumental to my PhD and personal development. I am thankful to my secondary supervisor, Ms Janice Tsui, for her kind helpfulness, support, and opportunities to be involved in other projects. I also wish to acknowledge funding from EPSRC and Action Medical Research for research funding for this project.

Furthermore, I would like to express my appreciation to the following people who contributed to my research journey:

- Mr Arnold Darbyshire for discussions and insights on polymer chemistry, and help in polymer synthesis
- Mr Jeffrey Leung, MSc student, for work on combinatorial platforms
- Prof Jane Mitchell and Ms Isra Marei (Imperial College London) who kindly provided isolated ECFCs for this project
- Dr David Scurr and Dr Long Jiang (University of Nottingham) for ToF-SIMS analysis
- Dr Remzi Becer and Mr Resat Alsakal (Queen Mary University of London) for GPC analysis
- Dr Peter Munro (UCL Institute of Opthalmology) for FE-SEM support
- Dr Junjie Zhao for assistance with AFM, and being a helpful teammate
- Dr Noora Naghavi for help with Raman spectroscopy analysis
- Dr Yasmin Farhatnia for guidance and teaching on stents and stent coating
- Mr Michael Kasimatis for his earlier work on antibody immobilisation
- Dr Bala Ramesh, Dr Gavin Jell and Dr Wenhui Song and Prof Marilena Loizidou for constructive feedbacks to my projects and presentations
- Departmental staff: Rashika Rupasinghe, Chau Chong, Stephanie Bogan, Evelin Karageorgious, Katerina McCann, Samar Hamad and Maria Menikou.

I am also very thankful to my wonderful bunch of friends and colleagues in the department for all the encouragement, advices and companionship over the last 4 years. I am blessed that the PhD has forged some wonderful relationships, particularly with Wai I Ho, Poramate Klanrit (Toke), Alex Chivu, Jerome Hunckler, Gui Zhen Teoh, Patricia Redondo, Agata Nyga, Katerina Stamati, and also Victor Lopez-Davila, Tarig Magdellin, Salfarina Saberi and Azadeh Rezaei. The great times together with the support during tough times have all made the PhD an unforgettable experience.

I also like to thank my beloved relatives, cousins and best friends for their understanding and support. Special thanks to my partner, whose constant support, patience and words of comfort have been instrumental during my PhD. Last but not least, I am indebted to the unconditional love, encouragement, acceptance and financial support from my parents, whom I dedicate this thesis to.

Table of Contents

List of Figures

List of Tables

Abbreviations

AFM	Atomic force microscopy
ANOVA	Analysis of variance
Anti-CD34Ab	Anti-CD34 antibody
APTMS	3-aminopropyltrimethoxylsilane
ATR-FTIR	Attenuated total reflectance fourier transform infrared spectroscopy
bFGF	Basic fibroblast growth factor
BMS	Bare metal stent
BSA	Bovine serum albumin
CE	Conformité Européenne
CoCr	Cobalt-chromium
CVD	Cardiovascular disease
cycREDV	Cyclic REDV peptide
DAPI	4',6-diamidino-2-phenylindole
DAPT	Dual Antiplatelet Therapy
DBU	1,8-diazabicycloundec-7-ene
DES	Drug eluting stent
dH_2O	Distilled water
DMAc	N,N-dimethylacetamide
DNA	Deoxyribonucleic acid
EC	Endothelial cell
ECFC	Endothelial colony forming cell
EDA	Ethylenediamine
EDC	1-ethyl-3-(3-dimethylaminopropyl)carbodiimide
ELISA	Enzyme-linked immunosorbent assay
EPC	Endothelial progenitor cells
ePTFE	Expanded polytetrafluoroethylene
ETOH	Ethanol
F-actin	Filamentous actin
FA	Focal adhesion
FBS	Foetal bovine serum
FDA	U.S. Food and Drug Administration
FE-SEM	Field emission scanning electron microscopy
GPC	Gel permeation chromatography
HRP	Horseradish peroxidase
HSC	Hematopoietic stem cell
HUVEC	Human umbilical vein endothelial cells
I2959	Irgacure®2959
IPA	Isopropanol
ISR	In stent restenosis
LST	Late stent thrombosis
MDI	Methylene diphenyl diisocyanate

MI	Myocardial infarction
M_n	Number average molecular weight
MPA	3-mercaptopropionic acid
MW	Molecular weight
NHS	N-Hydroxysuccinimide
NIH	Neointimal hyperplasia
NO	Nitric oxide
PBMC	Peripheral blood mononuclear cell
PBS	Phosphate buffer saline
PBST	PBS + 0.1% Tween 20
PC	Phosphorycholine
PCL	Poly(caprolactone)
PCU	Poly(carbonate)urethane
PDI	Polydispersity index
PEG	Polyethyleneglycol
PGA	Polyglycolide/poly(glycolic acid)
PLA	Polylactide/poly(lactic acid)
PO	Periodate oxidation
PP	Pre-polymer
PPA	Propargylamine
PRP	Platelet rich plasma
PtCr	Platimum-chromium
PU	Polyurethane
PUU	Poly(urea)urethane
Ra	Mean surface roughness
REDV	Arginine-glutamic acid-aspartic acid-valine
RGD	Arginine-glycine-aspartic acid
Rq	Root mean square surface roughness
RT	Room temperature
SD	Standard deviation
SEM	Standard error of mean
SMC	Smooth muscle cell
SS316L	Stainless steel 316L grade
TBO	Toluidine Blue O (assay)
TCEP	Tris(2-carboxyethyl)phosphine hydrochloride
TCP	Tissue culture polystyrene
ToF-SIMS	Time-of-flight secondary ion mass spectroscopy
TYC	Thiol-yne click reaction
UV	Ultraviolet
VE-cad	Vascular endothelial cadherin
VEGF	Vascular endothelial growth factor
vWF	Von Willebrand factor
XPS	X-ray photoelectron spectroscopy
YIGSR	Tyrosine-isoleucine-glycine-serine-arginine

Chapter 1
Introduction

1.1 Background

Cardiovascular disease (CVD) is the primary cause of death globally, claiming up to 17.5 million lives annually [1]. The most common is coronary artery disease (CAD), which is caused by formation of atherosclerotic plaques consisting of deposited lipid, calcium, inflammatory and smooth muscle cells (SMCs), hence causing narrowing of the coronary artery [2]. This life threatening disease can restrict blood supply to the heart and may consequently lead to angina and myocardial infarction (MI). Surgical intervention using the highly invasive coronary artery bypass grafting (CABG) remains the gold standard for patients with severe occlusions (>70%), but such procedure results in high cost and long recovery times. Fortunately, the advancements of interventional cardiology over the last few decades have given rise to minimally invasive treatments. For example, percutaneous transluminal coronary angioplasty (PTCA), also known as balloon angioplasty, was first introduced in 1977 and usually used in cases with vessel occlusions of 30-50% [3]. However, PTCA is also associated with relatively high rates of acute vessel recoil and restenosis (i.e. vessel renarrowing). To address these complications, in the 1980s, the revolutionary treatment of inclusion of a bare metal stent (BMS) as a permanent scaffold following PTCA was developed by several groups, most notably by Palmaz in the U.S. (Palmaz-Schatz stent) and Sigwart in Switzerland (Wallstent) [4,5]. Today, coronary stenting following PTCA is the preferred method for percutaneous coronary interventions. The advancement of stent technology has also led to a plethora of design, materials, and new paradigms including drug eluting stents (DES), bioresorbable stents and pro-healing stents, all of which aim to benefit patients by improving patency rate clinically in patients.

1.2 Evolution of coronary stents

1.2.1 Bare metal stents (BMS)

Coronary stents have evolved much since their introduction as BMS to address the high restenosis and elastic recoil rates of PTCA [6]. The advent of BMS has seen evolution in various aspects from stent design, strut thickness, mechanical behaviour to biomaterials including 316L grade stainless steel (SS316L), cobalt chromium (CoCr), nickel-titanium (NiTi) and platinum-chromium (PtCr) alloys. However, BMS suffer from up to 30% risk of in-stent restenosis (ISR), which is attributed to neointimal hyperplasia (NIH), i.e. inflammation and overproliferation of SMC leading to arterial re-narrowing, due to material hypersensitivity (Figure 1.1) [7–9].

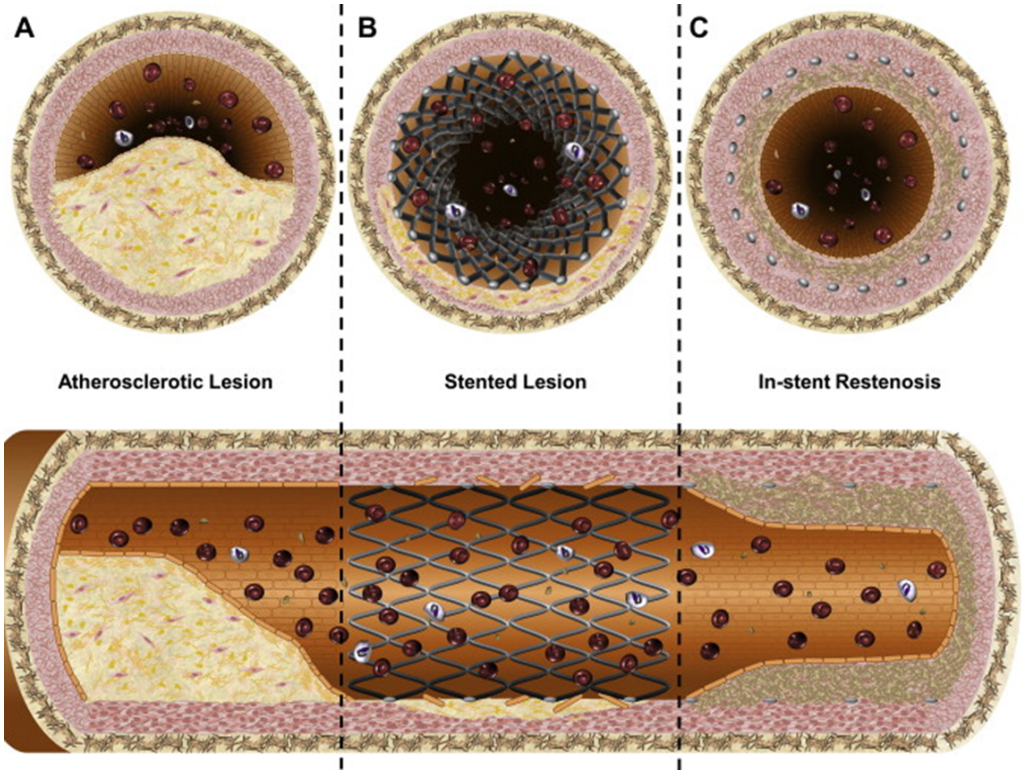

Figure 1.1. Schematic illustration showing progression of in-stent restenosis (ISR) following BMS implantation. (A) Development of atherosclerotic plaques; (B) Intervention with BMS resulting in restoration of luminal diameter but also endothelium denudation; (C) Development of ISR due to NIH. Figure was adapted from [6].

1.2.2 Drug-eluting stents (DES): durable to bioresorbable coatings

Drug eluting stents (DES) incorporating anti-proliferative drugs such as paclitaxel and sirolimus have successfully reduced ISR in BMS. Nonetheless, patients suffer from increased risks of late stent thrombosis (LST) [10]. This is attributed mainly to polymer hypersensitivity and non-specificity of the anti-proliferative drugs, which disrupts re-endothelialisation at the lesion site, resulting in a delayed vessel healing response [11]. Consequently, patients tend to be subjected to prolonged prescription of medications such as the aspirin and clopidogrel dual antiplatelet therapy (DAPT), giving rise to unwanted side effects such as risk of developing haemorrhage [12]. Table 1.1 (following page) summarises the major vascular stents in the market, which are mostly DES, and are discussed in the subsequent sections.

1.2.2.1 First generation DES: Durable coatings

In DES, polymeric coatings are favoured as localised drug delivery vehicles. First generation DES (CYPHER® and TAXUS®) focus on the initiation of the idea of controlled drug delivery using durable polymers and have shown favourable outcomes in reducing ISR. However, concerns arose with reports of potential LST, which is associated with impaired endothelialisation [10,11].

1.2.2.2 Second generation DES: Durable coatings with enhanced biocompatibility

The development of second generation DES focused on more biocompatible and haemocompatible durable polymer coatings and thinner strut design, such as phosphorycholine on Endeavor®, Biolinx® on Endeavor Resolute®, and poly(vinylidenefluoride-hexafluoropropylene) (PVDF-HFP). Phosphorycholine is a lipid component of the cell membrane, while Biolinx® is a tripolymer blend designed to prolong drug elution and retain biocompatibility compared with phosphorycholine. PVDF-HFP was described as anti-inflammatory and thromboresistant [13], and in combination with thinner strut design of Xience V® stent, this stent appears to fare best among its rivals in clinical performance, with lower occurrence of LST [14]. Indeed, *in vivo* rabbit studies have demonstrated better endothelial healing in second generation stents, particularly Xience V® stents [15].

Table 1.1. Summary of key coronary vascular stents in the market.

Stent (Manufacturer)	Coating material	Substrate material	Drug	Coating thickness (µm)	Strut thickness (µm)
(1) Durable Polymer DES (First and second generations)					
CYPHER® (Cordis)	PEVA & PBMA	SS316L	Sirolimus	12.6	140
TAXUS Express®/ TAXUS Liberté®/ TAXUS Element® (Boston Scientific)	SIBS	SS316L SS316L PtCr	Paclitaxel	16	132 97 81
Endeavor® (Medtronic)	Phosphoryl-choline	CoCr	Zotarolimus	4.3	91
Endeavor Resolute® (Medtronic)	BioLinx® tripolymer	CoCr	Zotarolimus	6	91
Xience V® (Abbott Vascular)	PVDF-HFP	CoCr	Everolimus	7.6	81
PROMUS®/ PROMUS Element® (Boston Scientific)	PVDF-HFP	CoCr PtCr	Everolimus	7.6	81
(2) Bioresorbable Polymer-coated DES					
SYNERGY® (Boston Scientific)	PLGA	PtCr	Everolimus	4	74
(3) Fully Bioresorbable DES					
Absorb GT1™ BVS (Abbottt Vascular)	PDLLA	PLLA	Everolimus	-	157*
Magmaris™ (Biotronik)	PLLA	Mg alloy	Sirolimus	7	150
(4) Non-DES Durable Coatings					
PRO-Kinetic Energy (Biotronik)	proBIO® Silicon Carbide	CoCr	-	-	60
COBRA PzF™ (CeloNova)	Polyzene-F®	CoCr	-	0.05	71
(5) EPC Capturing Stents					
Genous™ stent (Orbus Neich)	-	SS316L/ CoCr	NA	NA 80-90	- -
Combo™ stent (Orbus Neich)	NA	SS316L	Sirolimus	90-100	-

Abbreviations: PEVA, polyethylene-co-vinyl acetate; PBMA, poly(n-butyl methacrylate); SIBS, poly(styrene-*b*-isobutylene-*b*-styrene); PVDF-HFP, poly(vinylidene-fluoride-hexafluoropropylene); PLGA, poly(lactide-co-glycide); BVS, Bioresorbable vascular scaffold; PDLLA, poly(D,L-lactide); PLLA, poly(L-lactide). NA, information not available. *Including drug coating layer.

1.2.2.3 Third generation DES: Bioresorbable coatings

Despite the success and presently widespread use of DES in minimally invasive percutaneous coronary intervention, LST remains a major concern due to high risk of MI and fatality. Hence, new strategies are in demand. Bioresorbable stent coating presents a viable approach, as it aims to eliminate long-term concerns caused by polymer coatings, and has been widely pursued in both academic and industry research over the last decade [16]. Most of these stents utilise biodegradable polyester-based coatings, primarily lactic or glycolic acid polymers (PLA or PGA), which degrade into non-toxic compounds *in vivo*. The first and only FDA-approved DES with bioresorbable coating is the SYNERGY® stent, which incorporates a 4 μm thick drug-eluting PLGA coating on PtCr stents. Its clinical performance up to 12 months was reported to be non-inferior to second generation durable polymeric DES [17].

1.2.2.4 Fully bioresorbable polymeric and metallic stents

Fully bioresorbable stents or scaffold systems, whether entirely polymeric or metallic, are also developed based on the consensus that a permanent foreign body in the vessel remains a risk to further complications [18]. One such stent worth noting is the Absorb™ stent, an entirely bioresorbable drug-eluting vascular scaffold system. It is the only FDA approved (approved Jul 2016) fully bioresorbable stent so far. However, data from a 3-year randomised trial has found significantly higher late luminal loss and higher rate of target vessel MI when compared to Xience V® [19], raising questions on its capability to address long-term complications. This stent has been discontinued since Sept 2017 due to low commercial sales.

Metals overall offer higher mechanical strength and stiffness, hence providing opportunity for thinner stent strut design and reductions in elastic recoil [20]. High purity iron (Fe) and magnesium (Mg) alloys were the first two bioresorbable candidates developed. While Fe-based stents were reported to be safe *in vivo* [21,22], deposits of iron oxide were shown to accumulate near the stent region *in vivo*, which may be prone to inflammation and thrombosis [21]. Studies on Fe stents have remained within the pre-clinical stage so far. Mg stents are reported to degrade into harmless by-products and possess good haemocompatibility [23], but they are relatively brittle and degrade too rapidly than required for sufficient vessel healing duration. Alloying efforts are being developed to address these shortcomings.

Hitherto, Mg stents represents the only bioresorbable metallic stent that has proceeded to clinical trials confirming safety. Developed from an earlier bare Mg version AMS-1.0, Magmaris™ (or previously known as DREAMS 2G) is a Mg alloy stent with a sirolimus-eluting PLLA coating [24], which has obtained Conformité Européenne (CE) mark status (Jun 2016). Meanwhile, another emerging candidate for biodegradable metallic stent is zinc, which has been shown to possess reasonable degradation rates, harmless degradation product, as well as, desirable mechanical properties [20,25].

1.2.3 Stent coatings with improved biocompatibility

Apart from drug elution systems, there are also developments on coatings with improved biocompatibility. PRO-Kinetic Energy™ stent (FDA approved Feb 2017) uses a silicon carbide (SiC) coating to circumvent the release of allergenic metallic ions such as Co, Cr and Ni, while COBRA™ stents (FDA approved Mar 2017) utilises a proprietary nanocoating Polyzene-F®, likely to be a form of fluorinated polyphosphazene [26], which is reported to be anti-inflammatory, anti-thrombogenic and possess pro-endothelialisation capability [27]. The COBRA™ stent targets patients with high risk of bleeding as the stent is potentially capable of reducing DAPT duration to 30 days.

1.3 Endothelial progenitor cell (EPC) capturing stent technology to promote *in situ* endothelialisation

1.3.1 Importance of endothelialisation

The vascular endothelium consists of an intact monolayer of endothelial cells (ECs) in direct contact with the blood in a flowing environment and plays a vital role in dynamic regulation of vascular haemostasis through secretion of a range of vasoregulatory factors such as nitric oxide (NO), prostacyclin and heparan sulphate proteoglycans, hence maintaining the patency of blood vessels (Table 1.2) [28–32]. Hence, for cardiovascular implants, regeneration of a healthy and functional endothelium is extremely desirable for prevention of thrombosis and NIH, as well as for restoration of a fully functional endothelium.

Table 1.2. The role of the healthy endothelium leading to inhibition of thrombosis and NIH, as well as, continuous vessel maintenance.

Functions of Healthy Endothelium	Contributing Factors
Inhibits platelet activation	Cytokines: NO, PGI2
Inhibits blood coagulation	Cytokines: NO, TM, HSPG, TFPI
Support fibrinolysis	Cytokines: tPA, uPA
Inhibit leukocyte adhesion	Cytokine: NO
Prevents SMC over-proliferation	Cytokines: NO, TGF-β, heparin-like molecules; Physical barrier against circulating signalling molecules
Regulates macromolecule transport	Semi-permeability; Physical barrier against larger molecules
Vascular repair and remodelling	Cytokine signalling for EPC recruitment; Mechanotransduction in response to shear stress

Abbreviations: NO, nitric oxide; PGI2, prostacyclin; TM, thrombomodulin; HSPG, heparan sulphate proteoglycan; TFPI, tissue factor pathway inhibitor; tPA, tissue plasminogen activator; uPA, urokinase plasminogen activator; SMC, smooth muscle cell; TGF-β, transforming growth factor β.

1.3.2 *In situ* endothelialisation

Strategies to improve endothelialisation on vascular stents represent a viable solution to achieve desirable tissue-implant healing responses to promote arterial healing. Initial research has geared towards *in vitro* endothelialisation, i.e. pre-seeding of cells on biomaterial surfaces prior to implantation. More recently, a new paradigm, which aims to develop next generation biomaterials through surface engineering with the inherent ability to re-endothelialise after implantation *in vivo*, i.e. *in situ*

endothelialisation has emerged [33]. The field has seen tremendous progress over the last decade owing to the discovery of endothelial progenitor cells (EPCs) in peripheral blood [34], which lead to the development of EPC capturing technology. *In situ* endothelialisation aims to promote regeneration of a fully functional endothelium directly on blood-contacting surfaces of vascular devices after implantation *in vivo*. It offers a more practical approach in comparison to *in vitro* endothelialisation, where tedious and costly cell expansion and seeding process hampered its translation, hence serves as an exciting strategy for development of off-the-shelf pro-healing vascular stents. Many approaches have been explored to promote *in situ* endothelialisation, and have focused on attracting ECs from anastomotic sites, but the slow proliferation and growth rates of potentially diseased ECs remain as limitation. More recently, the idea of EPC capturing or chemoattraction has attracted a great deal of attention in the research community.

1.3.3 Endothelial progenitor cells (EPCs)

EPCs are circulating mononuclear cells in peripheral blood originally thought to be primarily derived from bone marrow, and are capable of differentiating into mature ECs, leading to generation of functional endothelium *in vivo* [35]. In fact, its application as cell therapy in regenerative medicine has recently entered clinical trials [36]. Although being widely used for research, the exact definition of EPCs remains unclear, and its nomenclature across the literature is inconsistent. Generally, the usage of the term ‘EPC’ refers to a heterogeneous population of cells, and it has been generally gathered that EPCs expresses CD34, vascular endothelial growth factor receptor 2 (VEGFR2) and CD133 (which is down-regulated over time) [37,38]. However, these markers are not specific to EPCs alone. For instance, haematopoietic stem cells (HSCs) express similar markers. A definitive way to distinguish between both cell populations remains absent, and is in need of further exploration and research. Depending on the isolation methodology, several different EPC sub-population can be identified, as summarised in Table 1.3 [37,38]. These are colony-forming unit-Hill (CFU-Hill, or Hill forming colonies), circulating angiogenic cells (CAC), and endothelial colony forming cells (ECFC).

Table 1.3. Three major isolated populations of EPCs [37–40].

	CFU-Hill	CAC	ECFC/BOEC
Morphology	Round and spindle-shaped	Round	Cobblestone
Endothelial markers*	+	+	+
Monocytic marker**	+	+	-
acLDL uptake	+	+	+
Tube formation *in vitro*	+/-	+/-	+
Form vessels *in vivo*	-	-	+
Proliferative Capability	Low	Low	High
Pro-angiogenic	+	+	+
CD34	+/-	+/-	+
Cell density in PB (cells/mL)	50-500	3	0.05-0.2

* Includes CD31, VEGFR2, von Willebrand factor (vWF), endothelial NO synthase (eNOS), VE-Cad(CD144)

** Includes CD14, CD45, CD115, and ingestion of bacteria

+/- indicates conflicting evidences from literature

Abbreviations: CFU-Hill, colony forming unit-Hill cells; CAC, circulating angiogenic cells; ECFC, endothelial colony-forming cells; BOEC, blood outgrowth endothelial cells; acLDL, acetylated low density lipoprotein; PB, peripheral blood.

The general consensus is that CFU-Hill and CAC are likely to be derivatives of haematopoietic cells committed to myeloid lineage, which are pro-angiogenic. These cells are not capable of differentiating into ECs. It is noted that the *in vitro* culture in conditioned endothelial media may have contributed to the expression of endothelial phenotypes, leading to several contradicting cell characteristics.

ECFCs are also known as blood-outgrowth endothelial cells (BOECs), and are rare circulating cells with distinct characteristics of endothelial lineage devoid of monocytic or hematopoietic characteristics [41]. These cells can contribute to vascular repair and *de novo* formation of blood vessel. ECFCs can be isolated from cord or peripheral blood via density centrifugation and subsequent plating of the blood mononuclear cells on Type I collagen-coated plates cultured under specific endothelial growth media formulations. Following media change and discard of non-adherent cells, ECFCs would appear as endothelial-like adherent colonies between 7-21 days [41,42]. Despite their low cell density in blood, ECFC are highly proliferative in culture and can be passaged at least 30-100 population doublings without obvious cell senescence [41,43]. The origin of ECFCs remains unclear, but it has been suggested that these cells are likely to be derived from bone marrow [43], or the vessel wall [44]. Altogether, ECFC possesses tremendous potential in regenerative medicine, and hence has been recognised by many as the ‘true EPC’

phenotype. It presents as a highly desirable candidate to promote *in situ* endothelialisation of vascular implants via capturing or chemoattraction of these circulating cells from circulating blood [33].

1.3.4 EPC capturing stents in clinic

The Genous™ stent and Combo™ stent (OrbusNeich Medical Technologies, Hong Kong) are by far the most prominent representation of *in situ* endothelialisation in clinical use. Both stents have achieved CE approval. Genous™ stent is the first EPC capture stent, which is a stainless steel 316L grade (SS316L) stent functionalised with anti-CD34 antibodies (anti-CD34Ab) via a biocompatible polysaccharide matrix. It is also available as CoCr stent. While its early feasibility and safety have been demonstrated [45,46], its effectiveness may have not lived up to the initial hype, with mixed clinical results across trials. Larger scale worldwide randomised trials have demonstrated that Genous™ stent was less capable of reducing NIH [47]. LST was however generally low [48], although may require longer term follow up as the durations of the trials reported so far were only up to 2 years [47]. The TRIAS studies have illustrated Genous™ stent to be non-superior to currently-used DES in patients with high risk of restenosis, leading to higher restenosis rate [49,50]. The results of anti-CD34Ab coated stents have placed EPC capture technology under scrutiny in the scientific and clinical community [48,51]. The Combo™ stent is a newer generation of the EPC capture stent, where a combination of luminal anti-CD34Ab coating and sirolimus elution via an abluminal bioresorbable matrix is utilised. First-in-man studies have reported non-inferiority to TAXUS® paclitaxel eluting stents up to 1 year with a similar degree of NIH and no ST [52]. The REMEDEE registry has reported outstanding clinical outcomes up to 1 year follow-up, with low target lesion failure, target vessel revascularisation and ST even when compared with second generation DES [53]. Prior to this, porcine model study had illustrated significantly increased endothelialisation over sirolimus-eluting stent alone both at 3 and 14 days [54]. This dual therapy approach may be promising, but longer-term studies with larger populations are awaited for more conclusive evaluation.

The clinical results of EPC capturing stents should be viewed critically. Firstly, it is worthwhile to emphasise that these are the first generations of EPC capture stents

used in patients. Research to accelerate *in situ* endothelialisation is still relatively new and complex, encompassing aspects including biomaterial surface modification, biofunctionalisation, and cell biology. Incorporation of only anti-CD34Ab may not be a complete actualisation of *in situ* endothelialisation. The orientation and *in vivo* activity of the antibodies following immobilisation, storage, sterilisation and implantation are also unclear. Furthermore, the clinical studies reporting on EPC capturing stents are by far too early to be conclusive due to their relatively smaller scale and shorter-term follow up, where LST may be more prevalent. The duration of DAPT was also different between Genous™ (30 days) and Combo™ stents (180 days) studies, although it is hypothesised that DAPT duration could be reduced for Combo™ stents [53]. As restoration of a functional endothelial layer on Genous™ stent may take time, Rossi *et al.* suggested prolonging DAPT duration up to 180 days for prevention of acute stent thrombosis [55]. In addition, the efficacy of EPC capturing technology may also be patient-specific, as age and diseases may be associated to reduction in number or functions of circulating EPCs [51].

One key lesson so far is the incidence of NIH on Genous™ stent, which may be circumvented by the combination of sirolimus elution in Combo™ stents (at least up to 1 year). The non-superiority of Genous™ stent over DES does not necessarily disapprove the concept of *in situ* endothelialisation, but emphasises the need for optimisation of biomolecular immobilisation and consideration of the complex multicellular microenvironment in the blood vessel. *In situ* endothelialisation remains a practical approach to develop the ideal blood-contacting surfaces for long-term implantation. Experiences from Genous™ stent would undoubtedly be useful for development of new EPC capture stents, as well as, any blood contacting devices.

In general, the longer-term clinical performance of latest generation of stents remains to be awaited. Bioresorbable DES and EPC capturing stents have not demonstrated superiority in overall efficacy compared to second generation DES [56], and LST and ISR remain the primary complications of concern. Nonetheless, throughout the evolution of coronary stents, the importance of a biocompatible material selection is implicated, and there is a consensus to promote long-term tissue-implant integration to reduce complications (e.g. thrombosis, restenosis and inflammation) and the need for re-stenting. This prompts the need for development of new biomaterials to promote the healing responses at the tissue-implant interface.

1.4 Biomaterial surface properties for vascular stents

A biomaterial is defined by Williams as 'a substance that has been engineered to take a form which, alone or as part of a complex system, is used to direct, by control of interactions with components of living systems, the course of any therapeutic or diagnostic procedure in human or veterinary medicine' [57]. Biomaterial surface properties (including chemistry, wettability, charge, energy and topography) are vital to guide biological responses at the tissue-implant interface to promote tissue-implant integration for enhanced long-term patency at the vascular interface. Surface modifications of biomaterials can generally be divided into physical, physicochemical and biological approaches. Physical approaches involve creating surface micro-/nanoscale textures or patterns, typically using expensive procedures such as electron beam lithography, photolithography, nanoimprint lithography, colloidal lithography and assembly or growth of nanomaterials [58–61]. Physicochemical approaches generally includes approaches such as plasma treatment [62] and chemical etching [63–65] to modify surface chemistry (functional groups, energy, wettability, charge). Biological approaches include passive or covalent mimetic coatings such as extracellular matrix (ECM) proteins or bioactive motifs [33,66–68].

For vascular stents, the ideal biomaterial should possess anti-thrombogenicity, anti-calcification, anti-inflammatory, cytocompatibility, endothelialisation capability, as well as suitable mechanical properties to match the native blood vessel. Polymeric biomaterials offer advantages such as higher potential for surface modification (physical, physicochemical or biological), controlled drug delivery, improved mechanical compliance similar to the native blood vessel, as well as, potential for improved haemocompatibility. Current polymer-coated stents offer a range of material properties such as durable and bioresorbable materials, which are optimised for drug-elution, including phosphorycholine, PVDF-HFP or PLGA. In the case of vascular bypass grafts, the use of synthetic polymers such as Dacron™ (polyethylene terephthalate - PET), and expanded polytetrafluoroethylene (ePTFE), have failed to maintain long-term vessel patency, especially for smaller diameter arteries (<6mm diameter) [69]. There is a real need for new vascular biomaterials with surface properties that can prevent thrombosis, restenosis, and inflammation, as well as, to promote endothelialisation for enhanced vessel healing.

1.5 Polyurethane as a biomaterial for vascular stent

Polyurethanes (PUs) have emerged as an important class of polymeric biomaterial due to their excellent mechanical properties that can match the viscoelasticity of native vessel, as well as, versatility and tuneability in formulation chemistry to achieve tailored properties [70,71]. The chemical versatility of PU allows it to be developed as durable or biodegradable scaffolds, surface coatings or even nanoparticles for biomedical applications, including cardiovascular implants, wound dressings, bone substitutes or nerve conduits for tissue engineering [72].

1.5.1 PU synthesis and chemical versatility

PUs were first invented by Bayer in 1937 [73], and are characterised by their typical urethane covalent bonds (NHC(O)O), which are formed via the reaction between the isocyanate groups (-NCO) of a polyisocyanate and hydroxyl groups (-OH) of a polyol (Figure 1.2A). The key components to synthesise PUs includes (i) a polyisocyanate (Figure 1.2B), (ii) a polyol and (iii) a chain extender [71,74]. Poly-ols are typically low molecular weight (MW) macro-diols, which eventually form the soft segments of PU, such as polyether, polyester and polycarbonate. Polyisocyanates are typically small aromatic or aliphatic molecules (MW < 200 $gmol^{-1}$), which are terminated by at least two reactive isocyanate groups (-NCO). NCO reactions are the essence of PU chemistry, as they react with both nucleophiles and electrophiles, including amine ($-NH_2$), hydroxyl (-OH), thiol (-SH), water (H_2O) and carboxyl (-COOH) functional groups. Chain extenders are small molecules such as diols (HO-R-OH) or diamines (H_2N-R-NH_2) which elongate the chains of the former two components, giving rise to high MW PUs, or poly(urea)urethanes (PUUs), respectively [70,75–77]. More recently, thiol-isocyanate click reactions have led to the synthesis of poly(thio)urethanes [78].

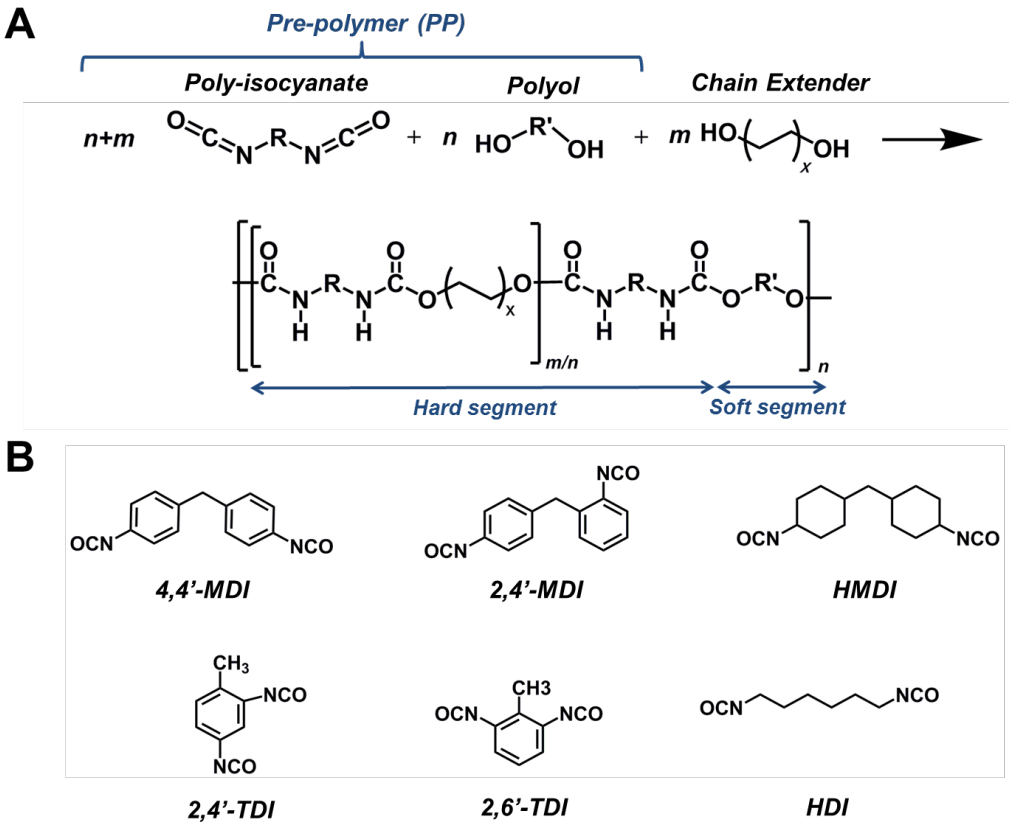

Figure 1.2. (A) General chemical reaction and structure of PU. Poly-isocyanate and polyol react to form pre-polymer (PP) in two step solution synthesis, m=0 for single phase PU and m=1,2 for segmented phase separated PU. (B) Chemical structure of commonly used poly-isocyanates. **Abbrevations:** MDI, methylene diphenyl diisocyanate; HMDI, hydrogenated MDI; TDI, toluene diisocyanate; HDI, hexamethylene diisocyanate.

Synthesis of PU can be generally classified into two reaction types: (i) a one-shot method where all reactants including polyol, polyisocyanate and chain extender are mixed altogether to form PU; and (ii) the two-step solution synthesis, also known as the 'pre-polymer (PP)' method, where the polyols are first reacted with excess poly-isocyanate to yield NCO-terminated PP, which is then reacted with the chain extender in a separate step to produce the final desired PU end product. The latter method is the preferred approach to achieve optimal control on the final structure and material properties [71]. The type of each component, formulation stoichiometry, reaction sequence and processing methodology can be used to tune the final mechanical and chemical properties of the final product, and can be fine-tuned to match the native tissue. The flexibility these parameters depicts the tremendous versatility and potential of PU chemistry to address specific requirements and desirable properties of new biomaterials.

1.5.2 Phase separation properties of PU

The soft and hard segments within the PU chain tends to undergo microphase separation, forming domains with enriched soft or hard segments, which eventually contribute to their material properties. Hard segments (typically urea or urethane domains) are more polar than molecules in the soft segments. Mechanically, hard segments could serve as physical crosslinks stabilised by hydrogen bonding, which alongside the more amorphous soft segments give rise to elastomeric properties of PU [79]. The behaviour of phase separation can be influenced by PU chemical structure, respective polarity of the hard and soft segment, chain length and processing history [74]. It may also be altered under different environments, as PU surfaces may adopt higher hard segment content under polar conditions, such as in H_2O. This effect is important in design considerations especially in relation to degradation and biological properties *in vivo* [80].

1.5.3 Diversity of PU applications

Generally, a wide range of biomedical grade PUs with varying compositions has been used over the last few decades. The major family of PUs used in cardiovascular applications are (i) poly(ester)urethanes, (ii) poly(ether)urethanes, and (iii) poly(carbonate)urethanes (PCU), or their respective forms of –(urea)urethanes. Poly(ester)urethanes such as PCL or PLA based PU, are typically biodegradable for controlled degradation and drug release applications [81]. Poly(ether)urethanes with soft segments such as polyethylene-oxide (PEO), are susceptible to oxidative degradation and environmental stress cracking [82,83]. PCUs are known to possess superior biostability with resistance to oxidative degradation and calcification [84,85], hence are useful in applications which rely on durability and long-term performance.

The versatile nature of PUs allows for a combination of different soft segments for modulation of degradability and mechanical properties, such as poly(ether-carbonate-urea)urethane [86] or poly(ester-carbonate-urea)urethane [87]. New polymers, fillers or bioactive compounds can also be incorporated into PU is possible. For example, sulfobetaine has been incorporated into the backbone of a PCL-urea-urethane to improve anti-thrombogenicity of vascular conduits [88]. Apart

from standard polyesters, Pereira *et al.* developed an elastomeric poly(glycerol-sebacate)urethane which degrades *in vivo* for cardiac drug delivery applications [89]. In a further study, a disulphide (-S-S-) bond containing chain extender was incorporated into a PCL-urethane PP in order to produce PU with triggerable degradation points along the polymer backbone, and could be degraded with the use of reducing agents [90]. Chemical incorporation of POSS nanoparticles into PCUU to form nanocomposites has also been reported to enhance the biostability, mechanical properties and haemocompatibility of vascular stents and bypass graft [91,92].

1.5.4 PU surface modification strategies

In order to promote specific cell responses or to chemically immobilise biomolecules on to PU, surface modification may be required to present reactable chemical groups (e.g. $–NH_2$, COOH). This could be achieved via simple wet chemical treatment using high concentrations of diamine solutions, such as ethylenediamine (EDA) or hexamethylenediamine, to create surface $–NH_2$ functional groups via aminolysis [64,93], although this may lead to uncontrolled surface and bulk degradation. Another common approach is plasma treatment, which could generate desired functional groups at nanoscale depths (1-5 nm) via a selection of plasma gases (e.g. O_2, N_2) [93,94], but this approach is associated to costly procedure, requirement of specialist equipment and inability to modify complex geometries [62]. Plasma immersion ion implantation (PIII), which uses higher energy ions to penetrate deeper depth, was described to be able to retain the modified functionality better over time [62,95]. Furthermore, a one-step polydopamine coating can be employed on the PU for further functionalisation [96], although specific coating conditions (e.g. pH) are required and further investigations are needed to understand its molecular and degradative mechanisms [97]. Incorporation of functionalisable nanoparticles, such as gold nanoparticles [98] or NH_2-functionalised fumed silica [99], into the polymer also represent another method for surface modification, but such approaches may be associated with aggregation and leaching, as well as, changes in surface and mechanical properties of the final material. Finally, the chemical versatility of PU could be utilised by incorporation of the functional groups during synthesis, such as by using *2,2*-bis(hydroxymethyl)propionic acid (bis-MPA) as chain extender to yield

free –COOH within the PU network [100]. This approach however is polymer-specific, and may affect the final structure and properties, hence requiring considerations during early phase of synthesis.

1.5.5 Polyurethane pre-polymers (PU-PPs)

As described previously, PU-PPs are prominent class of compounds synthesised by reacting poly-ols and poly-isocyanates in two-step solution polymerisation process to form PU. They possess an intermediate MW and at least two reactive –NCO functional groups for subsequent chain extension reactions. PU-PPs are used commercially as adhesives and surface coatings, which cure in air to form high MW PUUs via a process known as moisture curing [71,101]. Moisture curing utilises H_2O in air as the chain extenders [102], as shown in Figure 1.3. H_2O readily reacts with –NCO functional groups to yield carbamic acid, which is then decomposed to $–NH_2$ and gaseous CO_2. The $–NH_2$ terminated PU-PP chains then react with the remaining –NCO-terminated chains to yield urea linkages.

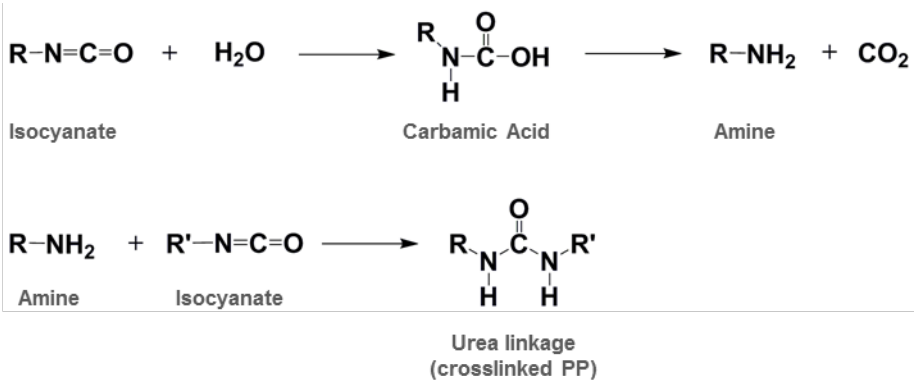

Figure 1.3. Reaction scheme on moisture curing of NCO-terminated PP.

The application of PU-PPs in the biomedical field has remained largely unexplored. Sheikh *et al.* developed a moisture-cured NCO-terminated PU-PP based on polyethylene glycol (PEG) and castor oil as a tissue bioadhesive, and reported growth of L929 fibroblast growth on the material [103,104]. Moisture-cured PU-PP was also applied as an adhesive layer between polymeric coatings and metallic stents to promote bonding [92]. In this thesis, it is postulated that the chemical reactivity of NCO-terminated PU-PPs would allow propensity for a range of chemical modifications. The synthesis, manufacture, chemical and surface modification of PU-PPs for use as a vascular stent coating are explored.

1.6 Biomaterial strategies to augment *in situ* endothelialisation

A vast amount of biomaterial-based strategies has been investigated to enhance *in situ* endothelialisation for vascular applications, including bypass grafts, stents or heart valves.

1.6.1 Immobilisation of general bioactive or biomimetic coatings

Earlier strategies utilise non-selective cell adhesive proteins or peptide motifs similar to those used for *in vitro* endothelialisation. Collagen [105], fibronectin [106], gelatin [107], and Arg-Gly-Asp (RGD) peptides [108] were the primary candidates, which are well-established candidates to favour cell adhesion and growth. Commercial products such as the FDA approved gelatin-impregnated graft Gelsoft (Vascutek, Scotland), and CE-marked collagen coated graft PolyMaille® (Perouse Medical, France) are readily available. However, as these coatings are non-specific to ECs, other circulating cells in the blood including platelets, leukocytes and SMCs may adhere and contribute to thrombosis and NIH. A study comparing patients implanted with gelatin-coated and uncoated vascular grafts reported an elevated inflammatory response and higher hospitalisation cost in patients with coated grafts [107]. Furthermore, for the case of collagen, it is pro-thrombogenic. Hence, these non-cell specific surface coatings may not be suited towards *in situ* endothelialisation and applications where cell growth needs to be controlled.

1.6.2 Biochemical approaches to enhance endothelialisation

Growth factors or small biomolecules are capable of stimulating EC (or EPC) growth and behaviour. While the *in vivo* mechanism of such biological molecules affect a number of target tissues through a variety of biochemical pathways, *in vitro* and *in vivo* studies have illustrated their ability to stimulate endothelialisation. Some of the key biomolecules are discussed in the following sections:

1.6.2.1 Vascular endothelial growth factors (VEGF)

Vascular endothelial growth factor (VEGF) is known for its role in the development of the vasculature, and is an important regulatory molecule for ECs [109–111]. Surface immobilised VEGF was discovered to be capable of promoting endothelialisation by increasing EC adhesion, proliferation and migration *in vitro*

[112]. Sustained release of VEGF is also possible [113], but uncontrolled release of VEGF may lead to tumour development [114]. In addition, gene delivery has also been utilised for delivery of VEGF genes using a baculovirus based stent. Data from *in vivo* dog study has shown improved re-endothelialisation (55% at week 2 and 94% at week 16), as well as reduction in NIH compared to VEGF-negative and BMS controls [115]. Further investigations are required to access the long-term effects *in vivo* particularly regarding the safety of gene delivery vectors.

VEGF is also a key candidate in facilitating EPC differentiation to the endothelial lineage [111]. It can also act as a chemotactic biomolecule to promote EPC homing by targeting the VEGFR1 and VEGFR2 receptors [116,117]. Upon capturing, VEGF can induce differentiation and support cell function of the endothelium [116,117]. Mononuclear cells cultured on VEGF coated surfaces were reported to have longer survival and higher expression of endothelial markers for 2 weeks compared to anti-VEGFR1 and anti-VEGFR2 antibodies (Ab) coated surfaces [118]. Under arterial flow, VEGF was shown to be more efficient than anti-VEGFR2 Ab in capturing and retaining EPCs [119]. Based on these studies, Takabatake *et al.* developed a VEGF coated EPC capture stent and illustrated that it is more specific and effective in reducing NIH compared with anti-CD34Ab coated stents [120]. However, it is vital to note that VEGF is also expressed by a small fraction of monocytes [110], and is also known to be involved in tumour development [121], hence its overall safety should be critically evaluated.

1.6.2.2 Other growth factors: SDF-1α, BDNF, NGF

Intriguingly, stromal cell-derived factor-1α (SDF-1α) is also capable of stimulating early attraction of stem cells including EPCs, hence improving endothelialisation and reduce NIH and thrombosis [106]. Brain derived neurotrophic factors (BDNF) and nerve growth factor (NGF) were separately attributed to enhancement of EPC chemoattraction and differentiation, promoting endothelialisation via paracrine effects. For instance, BDNF was reported to induce VEGF secretion from early EPCs. In both studies, incorporation of growth factors into vascular grafts have successfully improved graft patency rates in a rat model [122,123].

1.6.2.3 Nitric oxide (NO)

Elution of NO has attracted a great deal of attention in cardiovascular implants. NO is capable of modulating thrombosis, supporting EC proliferation and viability, as well as playing a protective role in the vascular system [124]. It is suggested that this may involve EPC chemoattraction and differentiation [125]. Due to its short half-life in the body, much research have focused on investigating NO donors, such as *S*-nitrosothiols and diazeniumdiolates to develop NO-eluting implants [126–129]. For instance, de Mel *et al.* have reported improved anti-thrombogenicity, EPC attachment, and decreased platelet adhesion by incorporating *S*-Nitroso-*N*-acetyl-penicillamine (SNAP) into a patented polymer nanocomposite, i.e. polyhedral oligomeric silsesquioxane-poly(carbonate-urea)urethane (POSS-PCUU), demonstrating controlled release of NO [126].

1.6.2.4 Heparin

Heparin, known for its anti-coagulatory effect, is one of the most common drugs used for vascular stents and grafts to prevent thrombosis. There is also supporting evidence for its role in promoting EC while inhibiting SMC adhesion and proliferation, and improving re-endothelialisation of vascular grafts *in vivo* [93,130]. Conversely, Wang *et al.* reported no enhancement of endothelialisation from heparin [131]. Nonetheless, based on a large scale clinical trial, the performance of heparin-bonded expanded-polytetrafluoroethylene (ePTFE) grafts are comparable to native autologous vein grafts when used for femoropopliteal and femorocrural bypass procedures [132].

1.6.2.5 Gallic acid

Gallic acid (*3,4,5*-trihydroxyl-benzoic acid) is a naturally occurring compound found in food and beverages such as red wine, berries, herbs and tea. Surface immobilisation of gallic acid was reported to enhance HUVEC adhesion, proliferation, migration and NO release while inhibiting SMC adhesion and proliferation [133]. Consistent results was also achieved via controlled elution of gallic acid, which also additionally reports decreased platelet activation [134].

1.6.3 Selective cell capturing biomolecules

Biomolecules capable of targeting specific surface receptors of EPCs (or ECs) could be immobilised on biomaterial surfaces to promote capturing and chemoattraction of these cells to achieve *in situ* endothelialisation. A successful wound healing response using EPCs would require chemoattraction, adhesion, migration, proliferation, growth and differentiation of EPCs into fully functional and mature EC phenotypes capable of restoring the damaged endothelium (Figure 1.4). Table 1.4 summarises the biomolecules that have been used in literature, which are primarily composed of antibodies (Ab), growth factors, peptides and aptamers.

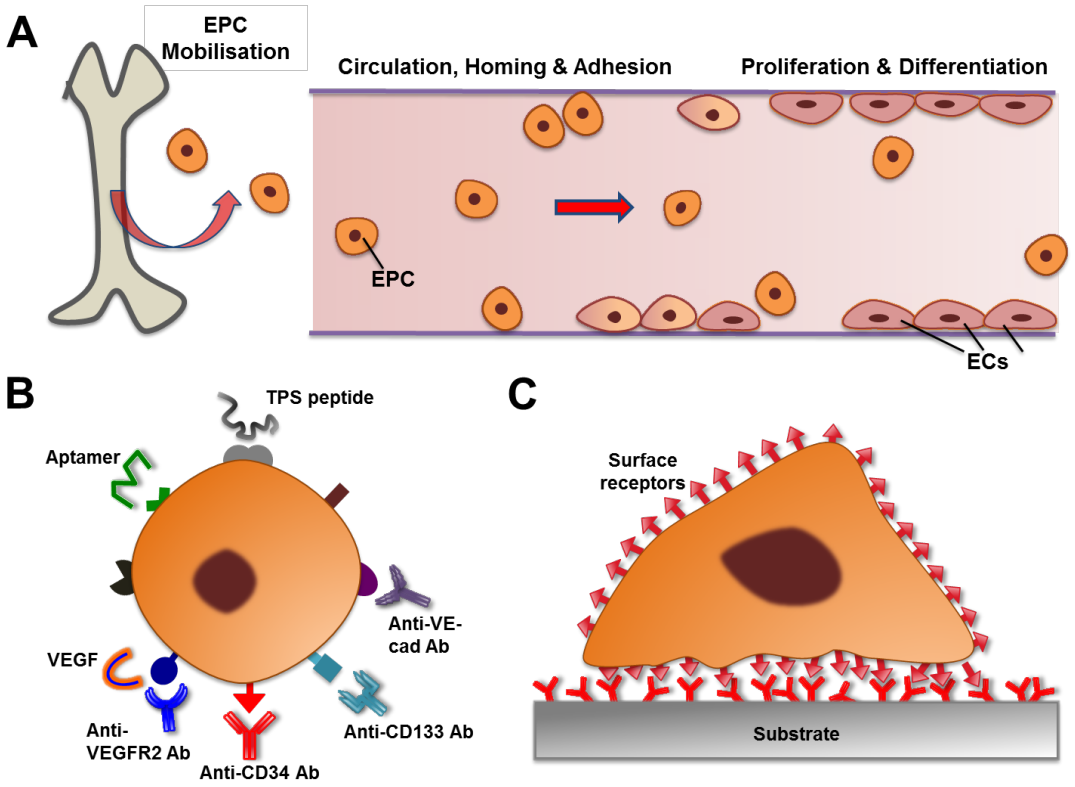

Figure 1.4. Schematic diagram outlining the concept of *in situ* endothelialisation. (A) EPCs are mobilised from bone marrow to circulation and migrate to site of endothelial injury and differentiate into functional mature ECs. (B) Surface receptors on EPCs can be targeted using a range of antibodies, cell-specific peptides or aptamers. It is noted that surface receptors on EPCs have yet to be fully elucidated. (C) Antibodies or other EPC-specific ligands can be immobilised on biomaterial surface to target their respective cell surface receptor counterparts to achieve EPC capturing. **Abbreviations:** Ab, antibodies; VEGF, vascular endothelial growth factor; VEGFR2, vascular endothelial growth factor receptor-2; VE-cad, vascular endothelial cadherin**.**

Table 1.4. List of EPC or EC capturing biomolecules.

Capture Biomolecules		Promises	Concerns	Latest Stage	Ref
Antibodies	Anti-CD34Ab	• Targets EPCs • Widely investigated • Success in commercialisation for human use	• Very limited specificity to EPCs; may capture platelets, HSCs • Differentiation into undesirable cell type • Inability of Genous stent to inhibit NIH	Commer-cialised (Genous™, Combo™ stent)	[48]
	Anti-VEGFR2 Ab	• Targets EPCs • Role in vascular repair • Higher specificity than anti-CD34Ab	• Limited specificity to EPCs; may capture inflammatory cells • Lack of *in vivo* studies	*In vitro*	[135, 136]
	Anti-VE-cad Ab	• Targets late EPC and ECs • Higher capture efficiency and specificity than anti-CD34Ab • Promising *in vivo* results	• Performance in human not known	*In vivo* (rabbit)	[137, 138]
	Anti-CD133Ab	• Targets early EPCs	• EPC loses CD133 over time	*In vivo* (porcine)	[139]
Growth Factor	VEGF	• Targets EPCs • Reportedly more effective than anti-CD34Ab and anti-VEGFR2 Ab • Promising *in vivo* results	• Performance in human not known • Role in tumour development	*In vivo* (porcine)	[120]
Peptides	REDV	• Specific to ECs • Also targets EPCs	• *In vivo* stability	*In vivo* (rabbit)	[140]
	YIGSR	• Targets ECs and EPCs over platelets	• Also supports SMC adhesion and proliferation • Limited specificity • *In vivo* stability	*In vitro*	[141, 142]
	TPS	• Targets EPCs • Very high specificity	• *In vivo* stability	*In vitro*	[143, 144]
	CRRETAW AC	• Targets ECs • Very high specificity	• *In vivo* stability • Limited proliferation capability of ECs	*In vitro*	[145]
Aptamers	Cell-specific aptamers	• Targets EPCs or ECs • Requires no knowledge of targeted cell surface molecules • Very high specificity • Strong binding affinity • Easy to synthesise reproducibly	• *In vivo* results showed similar NIH compared to uncoated CoCr stent • *In vivo* stability • Long term *in vivo* safety in question	*In vivo* (porcine)	[146, 147]

Abbreviations: Ab, antibodies; HSC, haematopoetic stem cells.

1.6.3.1 Antibodies (Ab)

There are several common Ab and target epitopes to identify EPCs. Anti-CD34Ab is by far the most popular EPC targeting candidate used in the manufacture of stent coatings, such as the Genous™ and Combo™ stents (as described in section 1.3.4). It is also widely studied in different polymer matrices and conjugation chemistries [99,148,149]. Microfluidic devices developed using anti-CD34Ab have shown success in isolating outgrowth ECFCs [150]. Anti-CD34Ab immobilisation has also been reported to improve haemocompatibility of biomaterials via reduced platelet adhesion, activation and delayed clot formation [151]. Despite its relatively established use for EPC capturing, the use of anti-CD34Ab is not without concerns. CD34 is not entirely specific to EPCs: it is also expressed by other cell types, which includes HSCs and platelets [36,38,152], and could lead to differentiation to undesired cell phenotypes or induce thrombosis. It has been reported that captured $CD34^+$ cells may differentiate into SMCs and even cardiomyocytes [153]. This may be further supported by observations of multicellular aggregates around anti-CD34Ab coated stents and increased NIH on anti-CD34Ab coated grafts in porcine models [120,154], which is consistent with the clinical results of Genous™ stent relating to NIH [48].

Anti-VEGFR2 Ab is another candidate used for EPC capturing. Its usage is based on the rationale that a sub-population of circulating $CD34^+$ cells co-express VEGFR2 and CD133, which could differentiate to the endothelial lineage [155]. This suggests that targeting VEGFR2 may be more specific than CD34. Studies have shown ECs and EPCs can be selectively captured using anti-VEGFR2 Ab under flowing conditions [119,136]. Nevertheless, to our knowledge, there is still no convincing experimental evidence comparing anti-VEGFR2 Ab to other antibodies. It should also be noted that VEGFR2 may be expressed by some macrophages and monocytic cells and may stimulate an unwanted immune response [38,156].

Vascular endothelial cadherin (VE-cad) is exclusively expressed on late EPCs and ECs. Kim's group has developed an anti-VE-cad Ab coated stent, based on the rationale that late EPCs would be more committed towards the endothelial lineage [137,138]. Using *in vitro* assays and rabbit models, the stent was shown to result in increased endothelialisation and reduced NIH compared to BMS [137] and an anti-CD34Ab coated stent [138]. An improved capturing specificity and reduction in

neointimal area of anti-VE-Cad Ab over anti-CD34Ab coated stent was reported. It is further noted that the antibodies in these studies are polyclonal and randomly oriented, which may allow further optimisation.

While CD133 (or AC133) is down-regulated in EPCs as they become more committed, anti-CD133Ab has also been investigated to capture early EPCs. However, an *in vivo* study of anti-CD133Ab coated stent has shown similar re-endothelialisation and neointimal formation compared to BMS [139].

1.6.3.2 Cell-specific binding peptides

The fibronectin-derived Arg-Glu-Asp-Val (REDV) peptides have emerged as a popular candidate due to its EC-binding specificity over SMC and platelets [157]. REDV binds to the $\alpha_4\beta_1$ integrins, which are abundant on ECs. Several studies immobilising REDV on substrates including polycaprolactone (PCL), PCU, elastin-like recombinamers and peptide amphiphiles have supported such selectively towards EC with enhanced EC adhesion (including under flow), proliferation and migration [140,141,158–160]. Enhanced EC adhesion on REDV coated surfaces was also demonstrated under microfluidic flow conditions [161]. In contrast, Noel *et al.* contradictorily reported that REDV failed to support HUVEC adhesion compared to Tyr-Ile-Gly-Ser-Arg (YIGSR) and RGD peptides.

YIGSR peptides which are derived from laminin, presents specificity towards ECs over platelets [162,163]. Its presentation increases EC adhesion and proliferation. However, it also promotes SMC adhesion and proliferation [163], although it has been shown to be able to enhance ECs but not SMC migration [164,165].

REDV and YIGSR remain the most widely used EC-specific peptide sequences. The ability for both peptides to support dynamic adhesion of ECFCs have been reported [166], and warrants further investigation pertaining to cell fate. Another peptide Cys-Ala-Gly (CAG), a collagen IV enriched peptide, was immobilised on to PCU surfaces by Khan et al and were reported to selectively enhance EC adhesion and proliferation over SMC and platelets [67].

More cell-specific peptides can be identified by phage display technology, which allows identification of specific ligands to a particular cell surface protein even without prior knowledge of the molecules. The technology utilises bacteriophages due to the direct linkage between their phenotype and genotype [167]. Veleva *et al.*

identified TPSLEQRTVYAK (TPS), a peptide ligand specific to ECFC [168]. Subsequently, several studies attempted to incorporate TPS into biomaterials have demonstrated highly specific capturing of EPCs over ECs, platelets or MSCs, as well as enhancing its proliferation [143,144,169,170]. The peptide is also capable of supporting EC function. However, one major challenge is to prevent non-specific protein adsorption, which could mask the effects of TPS and hence requiring strategies such as passivation using PEG [144,169]. Another phage display derived peptide motif that may be useful is CRRETAWAC. This sequence is specific to ECs, and has a low affinity to platelets [145]. It was further shown that this sequence can also bind to porcine ECs [171], hence facilitating future animal studies.

1.6.3.3 Cell-specific aptamers

Aptamers are short single stranded oligonucleotides capable of specifically bind to a certain target molecule with high affinity. The nucleotide sequences are selected *in vitro* using a combinatorial chemistry process known as SELEX (systematic evolution of ligands by exponential enrichment), in which a target-specific aptamer is isolated from a library consisting of different oligonucleotide sequences. Aptamers are capable of binding to cell surface proteins and can be identified using the whole cell (cell-SELEX technology) even without the knowledge of the target cell surface molecules (Figure 1.5) [172]. An EPC-aptamer (sequence: 5'-CTT TAA TGC GGG GTA ATT TCT TTT CCA TAA TCG C-3') was electrostatically immobilised on a plasma-polymerised allylamine layer and was shown to promote selective capturing of EPCs without inhibiting proliferation of ECs and SMCs [173]. Furthermore, an aptamer against porcine $CD31^+$ EPCs was shown to be able to selectively capture EPCs from porcine whole blood under flow and subsequently differentiated into endothelial-like cells [146]. Aptamers against ECs have also been applied on coronary stents *in vivo* using swine model but results have shown no superiority over uncoated and polymer-coated stents in terms of NIH [147].

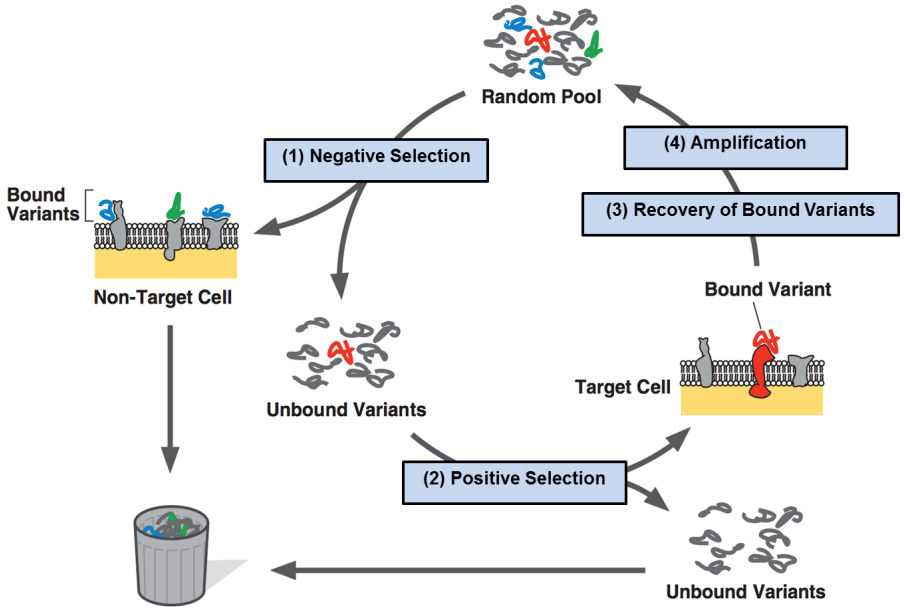

Figure 1.5. Schematic illustration of cell-SELEX technology process. Briefly, iterative steps of negative selection, positive selection and amplification allow acquisition of a target cell-specific aptamer from a library pool of random nucleotide sequences. The negative selection eliminates non-target cell-specific sequences from the pool, while the positive selection identifies the desired cell-specific aptamer. Figure was adapted from [172].

It is worthwhile to note that aptamers for EPC capturing have not been extensively studied. Many aspects especially their *in vivo* stability and performance are poorly understood and certainly require thorough investigations. Aptamers are prone to enzymatic and nuclease digestion in biological environment. Some aptamer sequences may cause undesirable immune responses, and hence newly derived aptamer sequences require more evaluation [174]. Furthermore, extracted EPCs, which are cultivated *in vitro* may have slightly different phenotype as circulating EPCs *in vivo*, hence may decrease the efficacy of the designed apatamers to target EPCs *in vivo* and will need to be further investigated.

1.6.4 Other strategies: Nanotechnology

Magnetic forces have been used to enhance *in situ* endothelialisation at specific sites. This is typically done by labelling isolated EPCs with magnetic particles, such as superparamagnetic iron oxide nanoparticles (SPIONs) or microspheres, followed by localisation to the site of injury using external magnetic field [175,176]. However, such approach requires additional EPC isolation step, which contradicts the purpose of *in situ* endothelialisation to address the impracticalities of *in vitro*

endothelialisation. The long-term effects of micro/nanoparticle labelled cells *in vivo* are uncertain, especially in relation to long-term cell fate, aggregation and accumulation in organs such as liver or spleen. Astanina *et al.* reported an increased intercellular gap between ECs and reduced NO secretion under influence of non-cytotoxic doses of SPIONs [177].

Furthermore, physical surface patterning on biomaterials using established micro- and nanoscale fabrication technologies (e.g. electron beam lithography, photolithography) had been utilised to stimulate *in situ* endothelialisation. Conceptually, this involves creation of physical microenvironments that favour endothelialisation over other competing cell types including SMCs and platelets. While micro-patterned ridges appear to influence EC alignment and subsequently cell fate [178], it is interesting to note that nanotubular structures may appear to be selective towards ECs. Two separate studies have shown that PCL substrates with nanopillars and NiTi substrates of nanotubular structures both demonstrate preferential EC proliferation over fibroblasts or SMCs respectively, although the exact mechanism has yet to be elucidated [59,179].

1.6.5 Combinatorial immobilisation strategies

While the immobilisation of individual bioactive molecules have shown promise alongside their shortcomings, it is postulated that a combination of biomolecules could give rise to synergistic effects for improved outcomes of *in situ* endothelialisation. Different ligands may activate different receptor subtypes giving rise to varying degrees of endothelial protein/gene expression to influence cell fate.

EPC-capturing antibodies have been combined with heparin, growth factors and drugs in a number of studies. The most prominent example is the Combo^{TM} stent, where EPC-capturing anti-CD34Ab is combined with everolimus elution to reduce SMC proliferation leading to reduced NIH. Anti-CD34Ab and anti-CD133Ab were also individually combined with heparin-collagen layer for further improvement in endothelialisation and EPC capturing [180,181]. By combining anti-CD133Ab with a heparin/collagen layer on a ePTFE grafts, Lu *et al.* showed improved endothelialisation in a porcine model [182]. Melchiorri *et al.* illustrated improvement in lumen diameter and up-regulation of eNOS on anti-CD34Ab-heparin-functionalised polyester graft compared to VEGF-heparin in mice [183]. Yang *et al.*

co-immobilised anti-CD34Ab and VEGF via gallic acid linkage on to a plasma-polymerised allyamine layer and demonstrated that this combination further improve EPC capturing and HUVEC proliferation [184]. Incorporation of VEGF+heparin or VEGF+basic fibroblast growth factor (bFGF) microparticles with anti-CD34Ab were also separately shown to further augment EPC adhesion and proliferation [113,185]. Anti-CD34Ab remains the primary candidate in studies investigating combinatorial strategies, possibly due to its established use in the commercialised Genous^{TM} and Combo^{TM} stents, as well as lack of an ideal EPC marker. Apart from antibodies, EPC-specific TPS peptide was also co-immobilised with serum albumin to reduce fibrinogen and platelet adhesion, possibly addressing the tendency of peptides to be prone to masking by non-specific protein adsorption [186]. SDF-1α and VEGF dual-releasing PU graft has also illustrated enhanced EPC mobilisation and differentiation, as well as enhanced endothelialisation *in vivo*.

1.7 Bioengineering considerations

EPCs appear to be promising targets to attain *in situ* endothelialisation. Similar cell-targeting approaches have been used in other research fields including cancer targeting [187,188] and biosensors development [189]. The present primary challenge of EPC-capturing technology lies in the search for more specific and effective EPC surface receptors for targeting. The biology and identity of EPCs, are yet fully understood [36,37], and needs to be further studied in the search of better target epitopes. While anti-CD34Ab seem to be the current 'gold standard' despite its limitations, aptamers, peptides and anti-VE-cad Ab described previously may appear as promising candidates.

Apart from EPC-capturing, the immediate nano-/microenvironment, which is described by the surface properties of biomaterial (chemistry, energy, charge, wettability and topography), should be capable of supporting differentiation and subsequently function of the differentiated mature ECs in the complex *in vivo* environment. Translation of such idea requires substantial technical considerations, including surface modification, bioconjugation, processing and manufacturing of biomaterial substrates.

1.7.1 Substrate biomaterial selection and surface modification

For blood-contacting materials, it is important that the biomaterial substrates are of low thrombogenicity, non-cytotoxic, and are capable of supporting endothelialisation alongside with the interfacing immobilised biomolecules. High throughput biomaterial screening may be useful for discovery for new materials with innate cell-selective properties, for instance a polyacrylate biopolymer (termed '8g7' by the authors) was reported to be favourable towards EC and EPC adhesion, as well as, low platelet adhesion [190].

Surface activation of biomaterial is required in order to present suitable surface chemical groups (e.g. $–NH_2$, -COOH) for subsequent immobilisation of biomolecules. The challenges often lie with the stability, distribution and density of the functional groups generated, all of which could influence subsequent bioconjugation and hence efficacy of the whole device. Surface rearrangements of polymer chains causing loss of functional groups over time may occur, and this can

be influenced by storage conditions. Goddard *et al.* reported storing surface modified polyethylene films in water to prevent migration of functional groups into the bulk [191]. It is also important to reassess the properties of the modified polymer as they may be altered by the treatment conditions, which may include stability, mechanical properties, monomer leeching, haemocompatibility and cytotoxicity.

Moreover, there are also research suggesting surface chemistry of biomaterial surface influences conformation and functionality of immobilised biomolecules [192]. More hydrophilic surfaces tend to induce lesser conformational changes hence retaining their functionality, but also have lower binding capability to proteins [192,193]. It was reported that anti-CD34Ab exhibited better functionality when immobilised on more hydrophilic plasma immersion ion implantation (PIII) treated polycarbonate surfaces compared with untreated surfaces [194]. Whittle *et al.* also demonstrated differential binding behaviour of antibodies, collagen II and vitronectin on to differently plasma polymerised polystyrene surfaces, with antibodies showing preferential adsorption towards aminated surfaces (-NH_2) [195]. Altogether, the discussion illustrates the importance of biomaterial selection and surface modification to yield optimal bioconjugation and immobilisation approaches to achieve *in situ* endothelialisation.

1.7.2 Bioconjugation strategies

Chemical immobilisation of biomolecules (including antibodies, peptides or growth factors) presents greater long-term stability and safety in comparison to non-covalent approaches (i.e. physical adsorption) by providing an anchorage to biomaterial substrates, as well as, yielding greater control of biomolecule orientation [196,197]. The crosslinking chemistry selected should possess high reaction efficiency, relatively simple procedure for ease of scaling-up, and present maximal functionality of the biomolecule. The orientation of the immobilised biomolecule should be directed to readily expose bioactive sites to cells at the cell-material interface. Generally, -NH_2, -COOH or occasionally –SH moieties on these biomolecules are utilised as sites for crosslinking using a wide range of chemical methods. One popular method utilises *N*-hydroxysuccinimide (NHS) and 1-ethyl-3-(3-dimethylaminopropyl)carbodiimide (EDC) crosslinking reaction, which activates and reacts the -COOH and -NH_2 groups on the biomolecules to allow conjugation to

biomaterials [99,198]. However, the prevalence of such chemical groups on biomolecules reduces the control over correct orientation to present specific binding sites to their target epitopes.

Therefore, further site-directed chemistries need to be considered to overcome problems relating to presentation of active binding sites upon conjugation. In the case of Ab, due to their unique 'Y' shape configuration, the antigen binding domains are prone to being masked from antigens due to problems in their orientation, which ultimately influence the reactivity of immobilised Ab (Figure 1.6) [193]. Several studies have shown enhanced antigen or EC capturing using oriented anti-CD34Ab compared to randomly oriented Ab [136,148,197]. -NH_2 groups are distributed throughout an Ab, hence the EDC/NHS or other crosslinking chemistries targeting these sites tend to result in a random orientation. Importantly, there are a number of possible site-selective bioconjugation chemistries, which have been reported, such as employing sodium periodate oxidation on antibodies to oxidise the carbohydrate moiety at the Fc region of antibodies to aldehyde groups, which can subsequently react to an surfaces with –NH_2 or hydrazides [148,197]. Another possible approach is by reduction of the disulphide bridges at hinge regions of antibodies to form thiolated (-SH) half-antibody fragments, which can then immobilise to surfaces with gold or maleimide groups [199]. Alternatively, a coating of protein-G, which specifically binds to the fragment crystallisable region (Fc) of antibodies can also be used for this purpose [136].

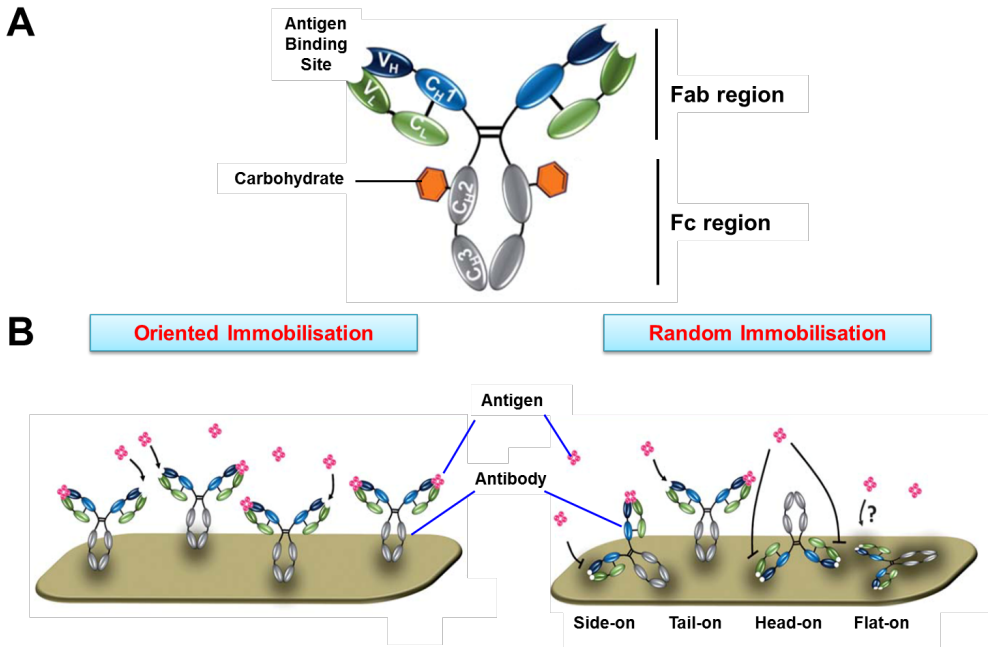

Figure 1.6. (A) General structure of antibodies (e.g. Immunoglobulin G). Antigens bind to variable regions V_H and V_L; (B) Schematic illustration of oriented and random immobilisation of antibodies. Oriented antibodies are more effective in antigen or cell binding. Randomly immobilised antibodies could be oriented side-on, tail-on, head-on and flat-on. Figure was adapted from [200].

On the other hand, synthetic peptides tend to have distinct N-terminus or C-terminus, which could be used for site-directed chemical immobilisation on to biomaterials. It was reported that immobilisation of a 22-residue peptide via the N-terminus and C-terminus have led to a 'stand up' and 'lie down' conformations respectively, with the former illustrating higher functionality [201]. Peptide functionality can also be improved by cyclisation, which is very common for RGD sequences [202]. Cyclisation improves cell affinity, specificity, as well as, stability of the peptides [202–204], and is believed to better mimic conformation of native ligands. Improving spacer arm length or longer repetitive active sequences [205] may also be subject of interest to improve biomolecule functionality. Lee *et al.* revealed optimal spacer arm length of at least four glycine units required to minimise cellular stress [206].

1.8 Summary

It is clear that current stent technologies demand new biomaterials and pro-healing technologies to promote endothelialisation for long-term patency. *In situ* endothelialisation represents a next generation bioactive platform to promote desired selective cellular responses at the tissue-implant interface, i.e. pro-endothelialisation, anti-platelet and anti-SMC overproliferation. Many strategies have been explored, and future platforms may present a combination of such developments, mimicking the native endothelium. A combination of capturing biomolecules and growth factors may synergistically promote *in situ* endothelialisation. New biomaterial platforms are in great demand to expand the toolkit for scientists and engineers to develop optimal approaches towards biofunctionalisation for use in the complex *in vivo* environment. While designing the ideal platform, it is essential for researchers to consider the balance between design complexity and practicality. *In situ* endothelialisation has the potential to revolutionise the field of cardiovascular medicine, seeing its applications in vascular stents, bypass grafts, heart valves and potentially other devices such as left ventricular assist devices and cardiac patches to repair and regenerate the tissues in the treatment of CVD.

1.9 Aims and objectives

The aim of this thesis is to develop a new bio-interfacial stent coating platform technology with pro-healing *in situ* endothelialisation capabilities using PU-PP for surface modifications. A non-degradable poly(carbonate)urethane pre-polymer (PCU-PP), whose building blocks were already used in biomaterials, was selected for development. The main hypothesis of this study was that PCU-PP can be applied as coatings on to metallic surfaces or stents, which can be chemically cured to present desirable surface chemistry for control of cell fate, as well as, subsequent immobilisation of biomolecules to enhance *in situ* endothelialisation.

The main objectives of this thesis are as follows:

(i) To optimise PCU-PP coatings on metallic substrates such as SS316L used for vascular stents

(ii) To develop new chemical curing approaches for PCU-PP coating to tailor surface chemistry

(iii) To assess EC fate on a range of chemical cured PCU-PP coatings

(iv) To immobilise EPC-capturing anti-CD34Ab and EC-selective REDV peptides on to chemical cured PCU-PP coatings, and assess their effect to enhance *in situ* endothelialisation

(v) To demonstrate the potential of chemical curing procedure to produce tailorable multifunctional coating chemistries for co-immobilisation of anti-CD34Ab and REDV peptides on the surface of the stent coating to provide a synergistic outcome in promoting *in situ* endothelialisation.

Chapter 2

Coating Optimisation of Moisture Cured Pre-polymer on Stainless Steel Substrates and Stents

2.1 Introduction

Urethane pre-polymers (PU-PPs) play an important role as adhesive coatings in a wide range of industrial applications, such as in flexible food packaging, wood adhesives, moisture repellent floor coatings, sealants in construction, and automotive interior applications [71]. For biomedical applications, it has also been developed as moisture cured tissue bioadhesive [103], injectable and polymerisable orthopaedic scaffold [207], self-healing material [208], and bonding agent for use between metals and polymers in vascular stents [92]. In most cases, PU-PPs are NCO-terminated and are cured in air via crosslinking reaction with moisture in air to form poly(urea)urethanes (PUU). Among PUs, poly(carbonate)urethane (PCU) possesses high degradative resistance and good mechanical properties, as well as an established use as a polymeric biomaterial [84,85].

This chapter describes the synthesis and optimisation of poly(carbonate)urethane pre-polymer (PCU-PP) coatings on to medical grade SS316L substrates. Circular SS316L coupons were selected as a model substrate material used in a range of vascular stents. Spin-coating was selected as a coating methodology due to its simplicity to yield uniform and thin film coatings, as well as, rapid solvent evaporation during the process leading to a dry PCU-PP film post-coating, which is similar to ultrasonic atomisation spray coating, an important technique used to coat vascular stents in industry with high coating precision and uniformity at the micron scale [209].

2.2 Materials and methods

2.2.1 Synthesis of PCU-PP

All reagents were purchased from Sigma-Aldrich UK unless otherwise specified. Poly(hexamethylenecarbonate)-diol was purchased from Bayer Material Science, UK with number average molecular weight (M_n) ~2000 $gmol^{-1}$. 36 g of the diol was heated to liquid state and stirred in a nitrogen-filled reaction flask equipped with a mechanical stirrer and gas inlet, as illustrated in Figure 2.1. Subsequently, 10 g *4,4'*-methylene-diphenyl-diisocyanate (MDI) was added in to the reaction vessel and stirred for 3 h at 60-70 ºC forming PCU-PP (NCO/OH ratio= 2.22). The PCU-PP was then gradually diluted by drop-wise addition of 184 g anhydrous tetrahydrofuran (THF). The concentration was determined by weighing the end product after dilution to account for THF evaporation, and concentrations were in the range of 25-28 wt%.

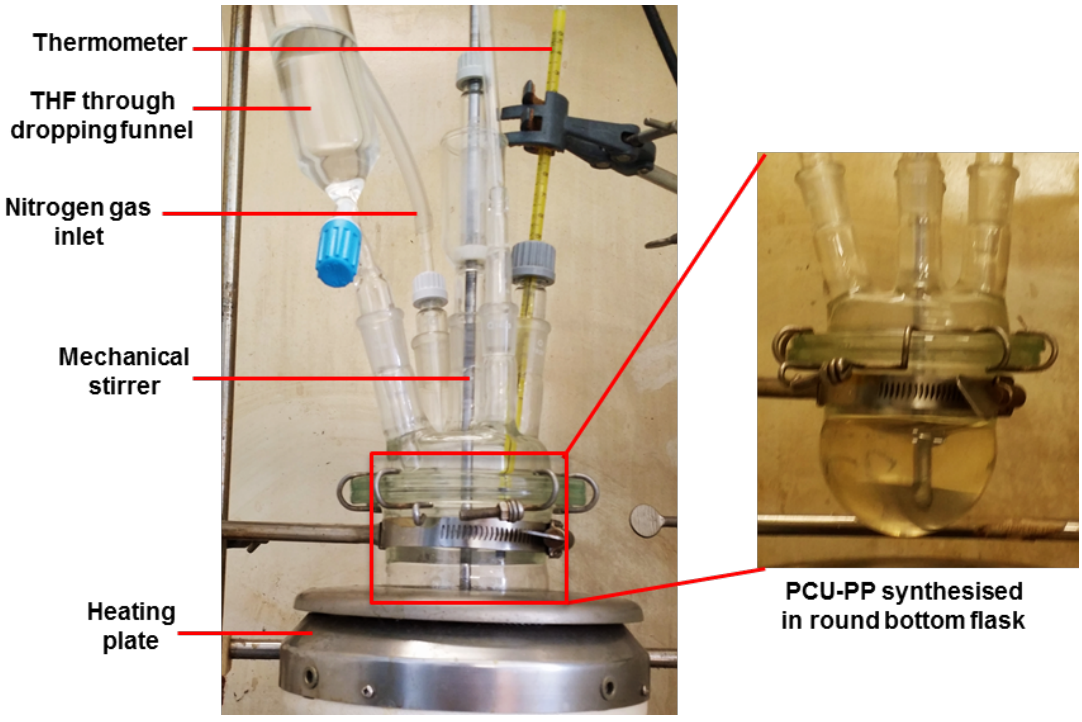

Figure 2.1. Digital image of experital equipment used for PCU-PP synthesis.

PCU-PP was synthesised using a NCO/OH ratio of 2.22 in order to provide an excess of NCO to allow termination instead of crosslinking of MDI on each poly(hexamethylenecarbonate)-diol chain. The expected chemical structure of the synthesised PCU-PP is depicted in Figure 2.2.

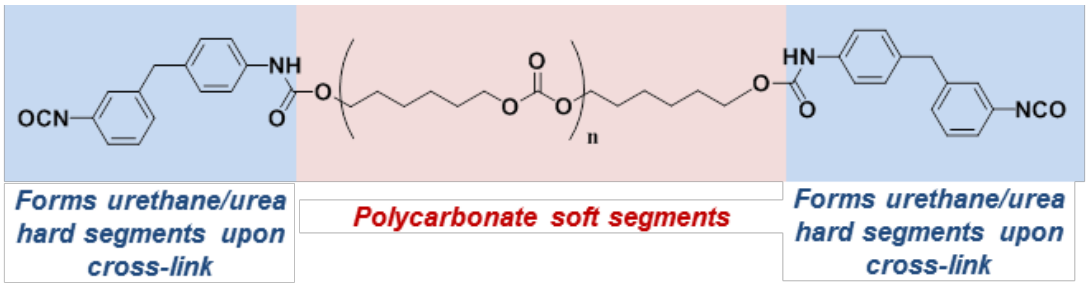

Figure 2.2. Chemical structure of PCU-PP.

PCU-PP solution was characterised by fourier-transform infrared spectroscopy (FTIR), gel permeation chromatography (GPC), and quantification of NCO-content using a back titration procedure in accordance to ASTM D 2572-97 [210]. The data are shown in Appendix A. Briefly, the expected chemical moieties of the PCU-PP were observed in the FTIR spectrum. The –NCO content determined was consistent with theoretical calculations at ~4 wt%, and remained stable throughout storage at -20ºC up to 5 months. As PCU-PP are sensitive to moisture, freshly synthesised PCU-PP was stored in nitrogen (N_2) purged single-use aliquots in -20ºC for a maximum period of 5 months before being used for experimentation. Care was taken to minimise exposure to environmental moisture prior to coating on SS316L substrates.

2.2.2 Cleaning and silanisation of stainless steel

Circular SS316L coupons (Bibby Precision Engineering Ltd, UK) with diameter of 13 mm and thickness of 1 mm, were cleaned via ultrasonication with 100% *N,N*-dimethylacetamide (DMAc) and acetone prior to use. SS316L coupons were silanised with 1 vol% *3*-aminopropyltrimethoxysilane (APTMS) diluted in isopropanol (IPA) heated to reflux at 70 ºC on a heating plate for 20 min. SS316L coupons were rinsed with IPA and cured at 65 ºC for at least 30 min. Coupons were rinsed with acetone and dried in 65 ºC oven prior to use.

2.2.3 Spin-coating of pre-polymer and moisture curing

Spin coating is a common procedure to apply thin film coatings of nm to µm scale thicknesses on to flat substrates. The solution of the intended material is deposited on to the substrate surface, and subjected to rotation. Centrifugal forces spread out the polymer towards the edge of the substrate to form a thin film coating. The final thickness of the coating can be determined by parameters such as the solution

viscosity or concentration, spin speed or duration and acceleration rate. For instance, a higher spin speed or lower solution concentration would give rise to a thinner coating. In this study, a bench-top spin coater (SCK200, Instras Scientific, USA) depicted in Figure 2.3 was used.

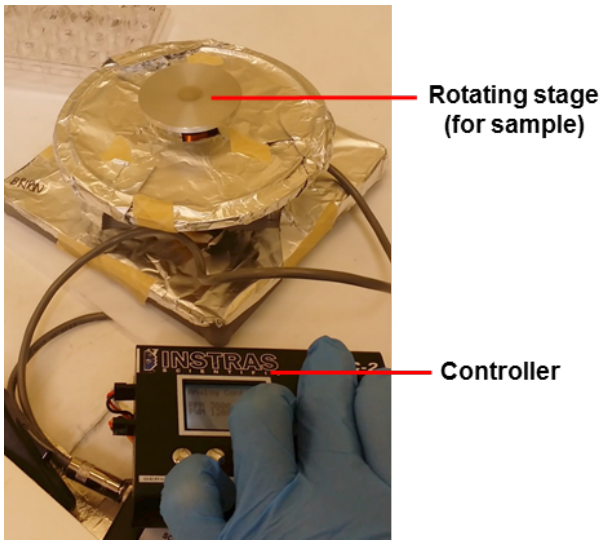

Figure 2.3. Bench-top SCK200 spin coater configuration

To spin coat PCU-PP on to silanised SS316L coupons, the synthesised PCU-PP solution (25-28 wt%) described previously was diluted with anhydrous THF to 15 wt% PCU-PP before use. 100 µL 15 wt% PCU-PP in THF was evenly spread on each SS316L coupons and spin-coated at 3000 rpm for 30 s using a bench-top spin coater. PCU-PP coated coupons were then moisture cured in air (ambient conditions), or in 1 mL distilled water (dH_2O) overnight (18 h) to form PCU-PP-AIR and PCU-PP-H_2O coatings respectively. A schematic diagram summarising these steps is shown in Figure 2.4. Both coatings were then stored in a desiccator prior to characterisation.

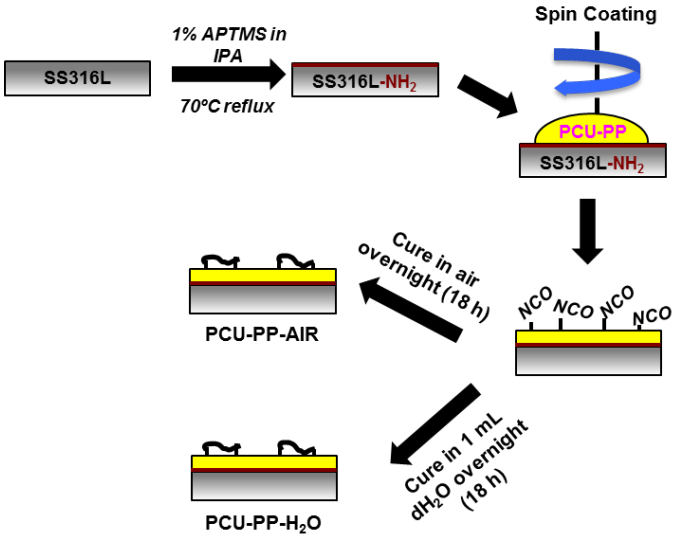

Figure 2.4. Schematic diagram showing the silanisation of SS316L coupons, spin coating of PCU-PP and subsequent moisture curing in air and dH_2O.

2.2.4 Coating of stents via ultrasonic atomisation spray coating

Bare metal stents (BMS) was coated with PCU-PP using ultrasonic atomisation spray coating technique (Medicoat DES 1000, SonoTek Corporation, USA). The ultrasonic atomisation setup is illustrated in Figure 2.5.

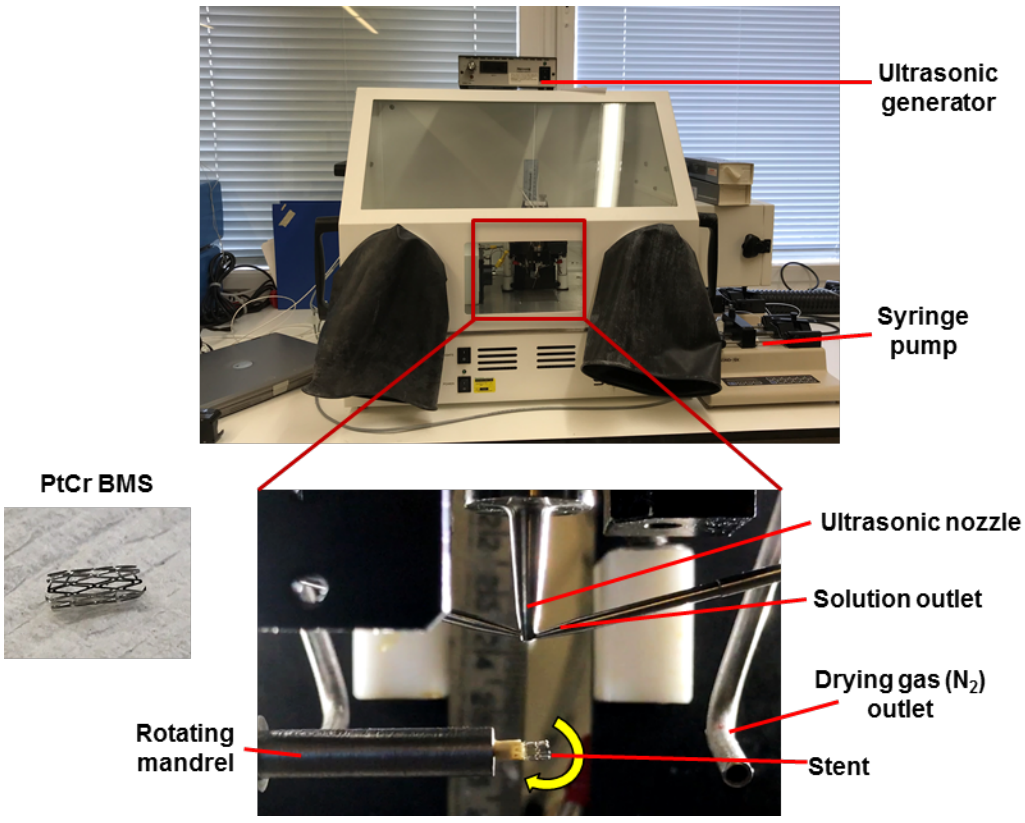

Figure 2.5. Coating procedure for BMS using ultrasonic atomisation spray coating.

In ultrasonic atomisation spray coating, dilute polymer solutions are fed through a syringe pump to the ultrasonic nozzle tip, which vibrates ultrasonically and is controlled by an ultrasonic generator. At this point, the polymer solution is atomised into fine droplets and a focusing N_2 gas focused through the centre of nozzle shapes and targets the atomised droplet stream on to the stent. Stents are mounted on to a mandrel which moves forward while rotating at a pre-determined speed, allowing polymer droplets to deposit, flow and evaporate [209,211]. Ultrasonic atomisation allows for efficient and precise fine coating of polymer droplets on to the intricate design of the stents. Such technique can be applied with automation to support industrial-scale manufacturing, and is commonly applied for coating of drugs, as well as, a range of durable and bioresorbable polymers on to medical devices such as DES, drug eluting balloons, catheters and blood collection tubes. However, there are several coating parameters that require optimisation each stent design and drug/polymer, including polymer concentration, flow rate, and ultrasonic power. For this study, Rebel^{TM} PtCr BMS (Boston Scientific, UK) were first silanised with the same protocol described previously (section 2.2.2), and were mounted on to a mandrel for spray coating. The coating parameters used for PCU-PP solution are summarised in Table 2.1, and was comprised of two sets of four back-and-forth cycles, with one N_2 drying cycle in between.

Table 2.1: Summary of ultrasonic atomisation spray coating parameters for BMS.

Parameters	Values
PCU-PP concentration	1 wt% in THF
Ultrasonic power	0.65 W
Polymer flow rate	0.03 ml/min
Distance from stent to nozzle	15 mm
Focusing gas	1.5 psi
Drying gas	3.0 psi
Translational speed	0.2 cm/s
Rotational speed	120 rev/min

2.2.5 Characterisation of coatings

2.2.5.1 Water contact angle (θ°) measurements

Water contact angle (θ°) is defined as the angle between the solid and the liquid-vapour interface. It measures the surface wettability or hydrophilicity of surfaces of materials. θ° of metals and coatings were measured using sessile drop method with

KRÜSS DSA 100. Samples were ensured to be dry under ambient conditions. Droplet volume was 5 µl and θ° were measured after 10 sec of dispensing using Drop Shape Analysis software. For each condition, a total of 3 measurements were taken at different areas on at least 3 samples (n=3).

2.2.5.2 Attenuated total reflectance fourier transform infrared spectroscopy (ATR-FTIR)

ATR-FTIR was used to detect specific chemical bonds of a material. Infrared (IR) irradiation is applied on the sample to excite molecular vibrations of molecules or chemical bonds that undergo a change in dipole moment upon absorption of IR. This absorption profile across the IR range provides a chemical fingerprint of the sample. With an ATR crystal attachment, ATR-FTIR allows surface sensitive detection at a depth of 0.5-3 µm [212]. In this study, spectra of PCU-PP coatings were obtained using a Jasco FTIR 4200 Spectrometer with an ATR attachment. Samples were placed in intimate contact with the ATR crystal. Spectra were taken at 50 scans per run at a resolution of 4 cm^{-1}, and were plotted using OriginPro 2016 software (OriginLab Corp., USA).

2.2.5.3 Field emission scanning electron microscopy (FE-SEM)

FE-SEM employs a field-emission source to liberate electrons, as opposed to thermionic sources in conventional SEM. A field emission source typically employs a sharp tungsten tip, and electrons are extracted by a strong electric field, hence resulting in a more focused and finer electron beam, which leads to better spatial resolution and improved signal-to-noise ratio. The electron beam bombards the sample surface, leading to a range of electron-specimen interactions. Two types of electrons are generally utilised in FE-SEM: (i) secondary electrons and (ii) backscattered electrons. Secondary electrons emitted from the material surface are detected by a secondary electron detector and give rise to the surface structure or topography of the sample. An immersion-lens (Inlens) detector is a newer type of detector that measures lower energy secondary electrons (SE1) emitted by initial interaction with the sample, thus providing better spatial resolution. On the other hand, backscattered electron imaging yields contrast correlated to atomic number of elements on the sample, hence providing detailed composition information. In this study, a Zeiss SIGMA FE-SEM equipped with an Inlens detector was used for high

resolution imaging of surface morphology of air and H_2O cured coatings. Samples were coated with 1 nm platinum using a Cressington Sputter Coater prior to imaging to minimise sample charging. An accelerating voltage of 3-5 kV and aperture size of 30 μm were used. To determine thickness of the coatings, a thin film from a PCU-PP-AIR coating was sliced with a sharp surgical scalpel blade, and the cross section of the dissected thin film was imaged with the sample stage being tilted. Cross-sectional thickness (n=1) was measured using ImageJ v1.49 software (NIH, USA).

2.3 Results

2.3.1 Coating optimisation of PCU-PP on SS316L coupons

SS316L coupons were firstly silanised with APTMS in order to yield $–NH_2$ groups to react with -NCO on PCU-PP to promote metal-polymer bonding [92]. PCU-PP was then spin coated on to the coupons and allowed to moisture cure in air or dH_2O overnight (18 h). 15 wt% PCU-PP in THF was evenly distributed on to the surface of SS316L coupons, as depicted in Figure 2.6.

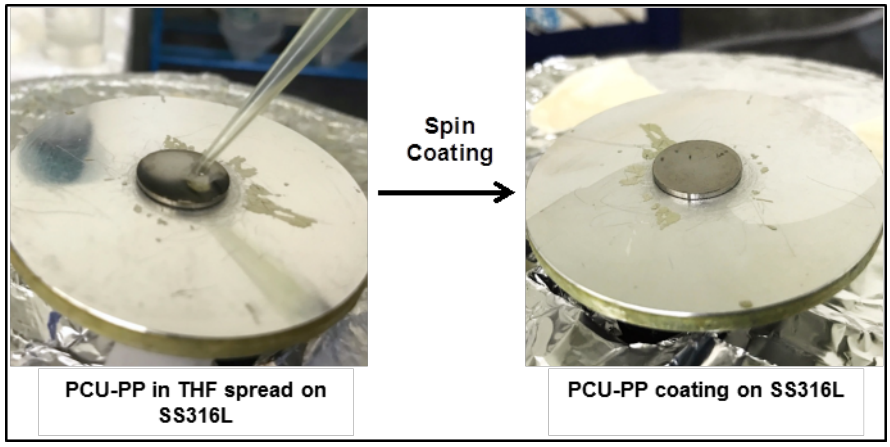

Figure 2.6. Digital images showing spin-coating procedures of PCU-PP on to SS316L coupons.

The spin coating parameters including spin speeds (1500-3000 rpm) and coating durations (30-60 s) were optimised based on macroscopic morphology of PCU-PP coatings as shown in Figure 2.7. At a lower speed of 1500 rpm, a defective surface morphology along with deposition of a thicker layer of PP around the circumference of the SS316L coupons was observed. This is likely due to the evaporation of THF evaporation before the fluid thins till the edges, as THF is a volatile solvent that evaporates readily in room temperature. Spin-coating at 3000 rpm was able to forming a macroscopically uniform surface coating devoid of the defects. Prolonging the duration of coating did not result in any observable changes in macroscopic coating uniformity, as THF has mostly evaporated by 30 s of spin coating. Hence, subsequent spin-coatings were performed at 3000 rpm for 30 s for reproducibility and coating uniformity.

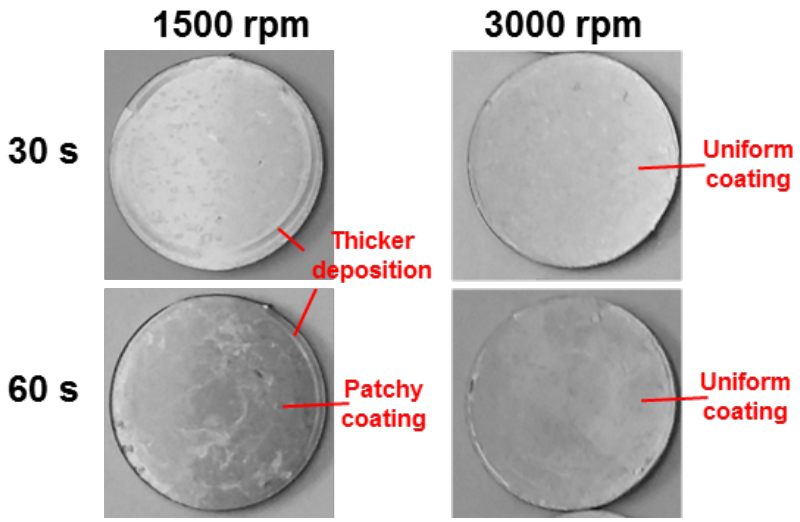

Figure 2.7. Macroscopic gross morphology of PCU-PP spin coated with varying speed and duration.

Spin-coated PCU-PP was tacky upon coating. Upon moisture curing in air overnight (18 h), tackiness was absent and a uniform stable coating had adhered to the SS316L coupons. The dry weight of PCU-PP deposited on to SS316L coupons after spin coating was measured to be 1.13±0.15 mg (n=3). The coatings were allowed to moisture cure in air overnight, and no measureable changes were detected after moisture curing in air. In addition, the coating thickness of PCU-PP after air curing measured with a micrometre provides a value of 1.89±0.69 μm (n=3).

2.3.2 Water contact angle (θº) of moisture cured coatings

Upon spin coating with PCU-PP on silanised SS316L coupons, PCU-PP was allowed to moisture cure in air (PCU-PP-AIR) or dH_2O (PCU-PP-H_2O) to investigate the effect of curing environment on coating surface properties. θº can be employed as a screening tool to access changes in surface chemistry from SS316L organosilane treatment to the application of surface coatings (Figure 2.8). Clean SS316L were found to be hydrophilic in nature (θ°= 42.6º±5.5). Silanisation with APTMS increased θ° to 65.2º±0.3 consistent to previous studies [92], hence suggesting successful modification. PCU-PP freshly coated on to the coupons revealed an increase of θ° to 91.4º±1.3, indicative of hydrophobic surface properties. Curing in air (PCU-PP-AIR) did not show much changes in θº (88.7º±0.8) compared to freshly coated PCU-PP, which also indicates a hydrophobic surface coating. However, coatings cured in dH_2O (PCU-PP-H_2O) had a lower θº of 77.3º±0.5, implying a more hydrophilic coating compared to PCU-PP-AIR.

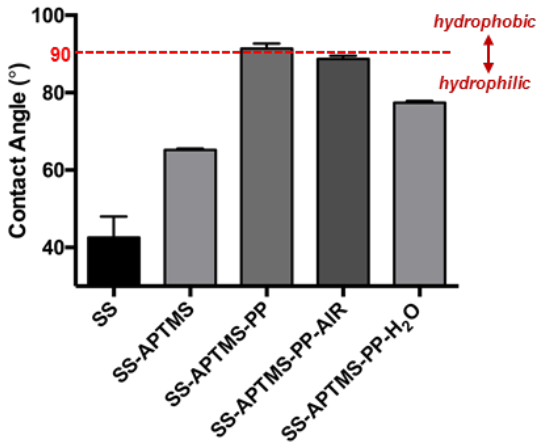

Figure 2.8. θº measurements of SS316L before and after silanisation, PCU-PP coating and moisture curing in air or dH_2O (n=3). Data reported as mean ± standard deviation (SD).

2.3.3 ATR-FTIR of moisture cured coatings

Moisture cured coatings were tested via ATR-FTIR to detect changes in chemistry. The spectra of PCU-PP and PCU-PP-AIR and PCU-PP-H_2O are shown in Figure 2.9.

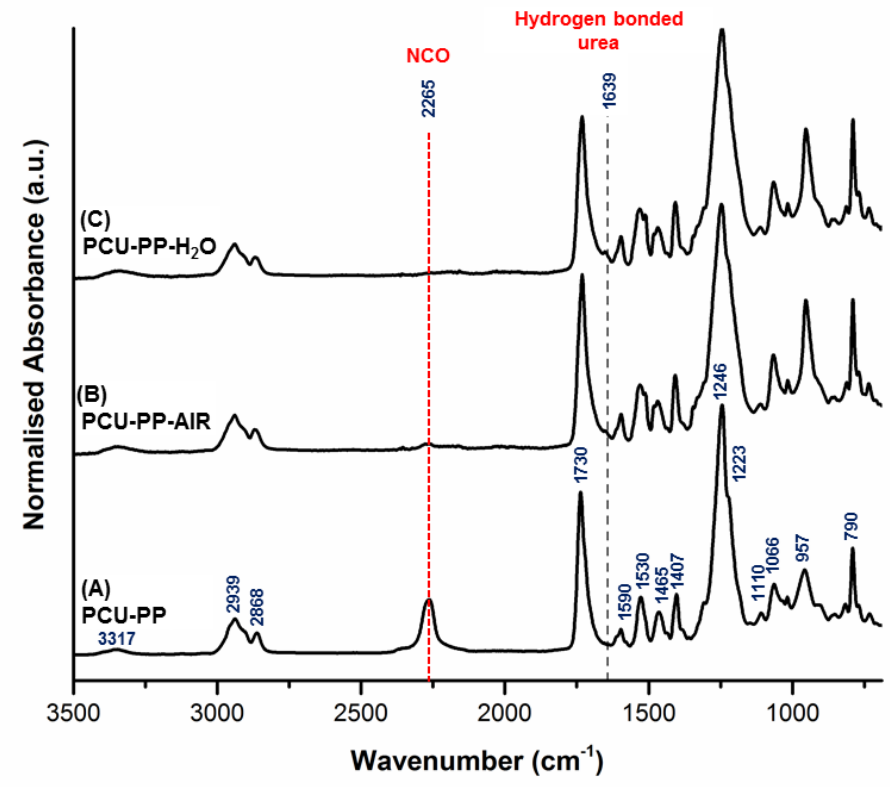

Figure 2.9. ATR-FTIR spectra of PCU-PP coating before and after moisture curing (in air and dH_2O).

The assignments of the detected ATR-FTIR peaks are summarised in Table 2.2. Freshly spin-coated PCU-PP revealed expected chemical groups on PCU-PP, particularly a notable –NCO peak (2265 cm^{-1}). Spectra of both PCU-PP-AIR and PCU-PP-H_2O appear identical, with absence of -NCO peak and appearance of a hydrogen-bonded urea peak (1639 cm^{-1}) in comparison to PCU-PP. It is noted that as the penetration depth of ATR-FTIR (~3 μm) is in the same range as the coating thickness, thus the spectra can be attributed to the bulk chemistry of the coatings. Hence, the results suggest that –NCO groups within the coatings have reacted with H_2O to form urea groups in both PCU-PP-AIR and PCU-PP-H_2O, which is consistent to moisture cure reactions (as described in section 1.5.5).

Table 2.2. Assignment of ATR-FTIR peaks for PCU-PP, PCU-PP-AIR and PCU-PP-H_2O.

Wavenumber (cm^{-1})	Assignment
3317	NH stretching
2939	CH stretching
2868	CH stretching
2265	NCO stretching
1730	C=O stretching
1590	Aromatic C=C stretching
1530	C-N bending
1465	Aromatic C=C stretching
1407	C-H bending
1246	C-O-C stretching
1223	C-N stretching
1110	Aromatic C=C bending
1066	C-O stretching
957	Aromatic C=C bending
790	Aromatic C=C bending

2.3.4 FE-SEM for imaging of surface morphology and cross-section of moisture cured coatings

FE-SEM was employed for imaging of surface morphology of PCU-PP-AIR and PCU-PP-H_2O coatings, as shown in Figure 2.10. Both coatings appeared as uniform layers on the SS316L coupons, with appearance of some surface pores. The coatings appeared to be characterised by plate-like structures (~10-20 μm in size), which were separated by boundaries. Such structures were more apparent on PCU-PP-H_2O coatings. Higher magnification images revealed observable differences between PCU-PP-AIR and PCU-PP-H_2O, where PCU-PP-AIR presented appearance of fine micro-wrinkled structures, which was not found in PCU-PP-H_2O. PCU-PP-H_2O appeared relatively flat compared to PCU-PP-AIR.

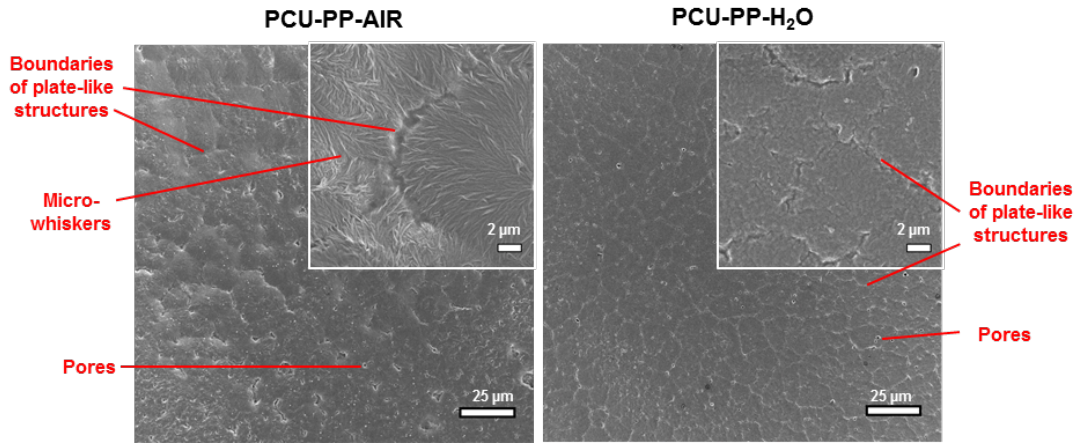

Figure 2.10. FE-SEM images of PCU-PP-AIR and PCU-PP-H_2O coatings. Magnification = 1000× (scale bar = 25 µm). Inset magnification = 10000× (scale bar = 2 µm).

To further support the coating thickness measured by micrometre reported previously, cross-section of PCU-PP-AIR sliced by a scalpel blade was imaged by FE-SEM, as shown in Figure 2.11. It can be observed that the surface of the SS316L coupon was comprised of grain boundaries of ~10 µm in size. An intact PCU-PP-AIR coating could be observed adhering to the SS316L substrate. The plate-like structures as described previously could be observed, and its formation may seem to be due to conformation of the PCU-PP-AIR coating with the grain boundaries of the SS316L coupons. The cross-sectional thickness was measured using the high magnification image, and were estimated at ~3.3 µm (n=1), which is in similar range as the measurements with micrometre (1.89±0.69 µm) reported earlier.

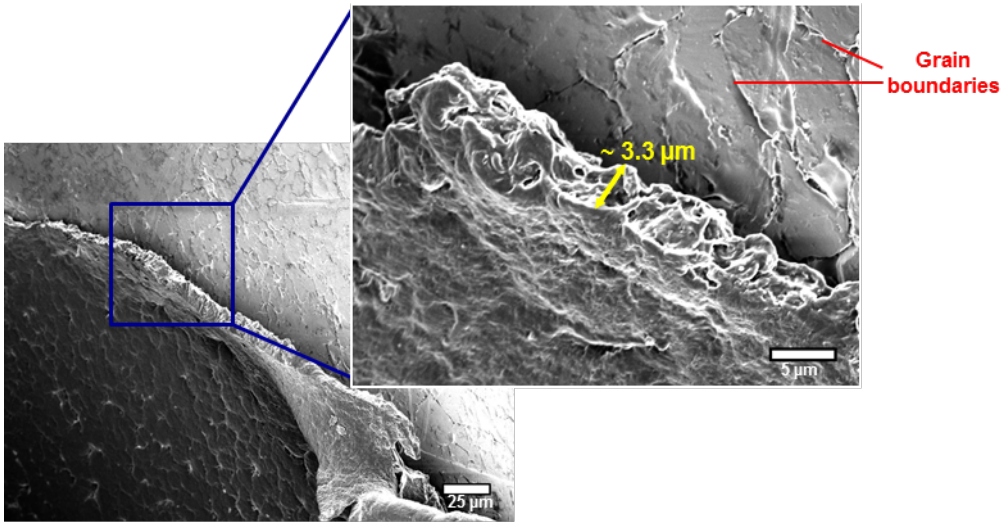

Figure 2.11. Cross sectional FE-SEM images of air-cured PCU-PP on SS316L coupon.

2.3.5 Optimisation of PCU-PP coating on coronary BMS

To demonstrate applicability of PCU-PP as a coating on coronary artery stents, PCU-PP was coated on to a PtCr BMS and allowed to moisture cure in air. FE-SEM imaging was employed to assess the coating uniformity, surface coverage and gross morphology, as shown in Figure 2.12.

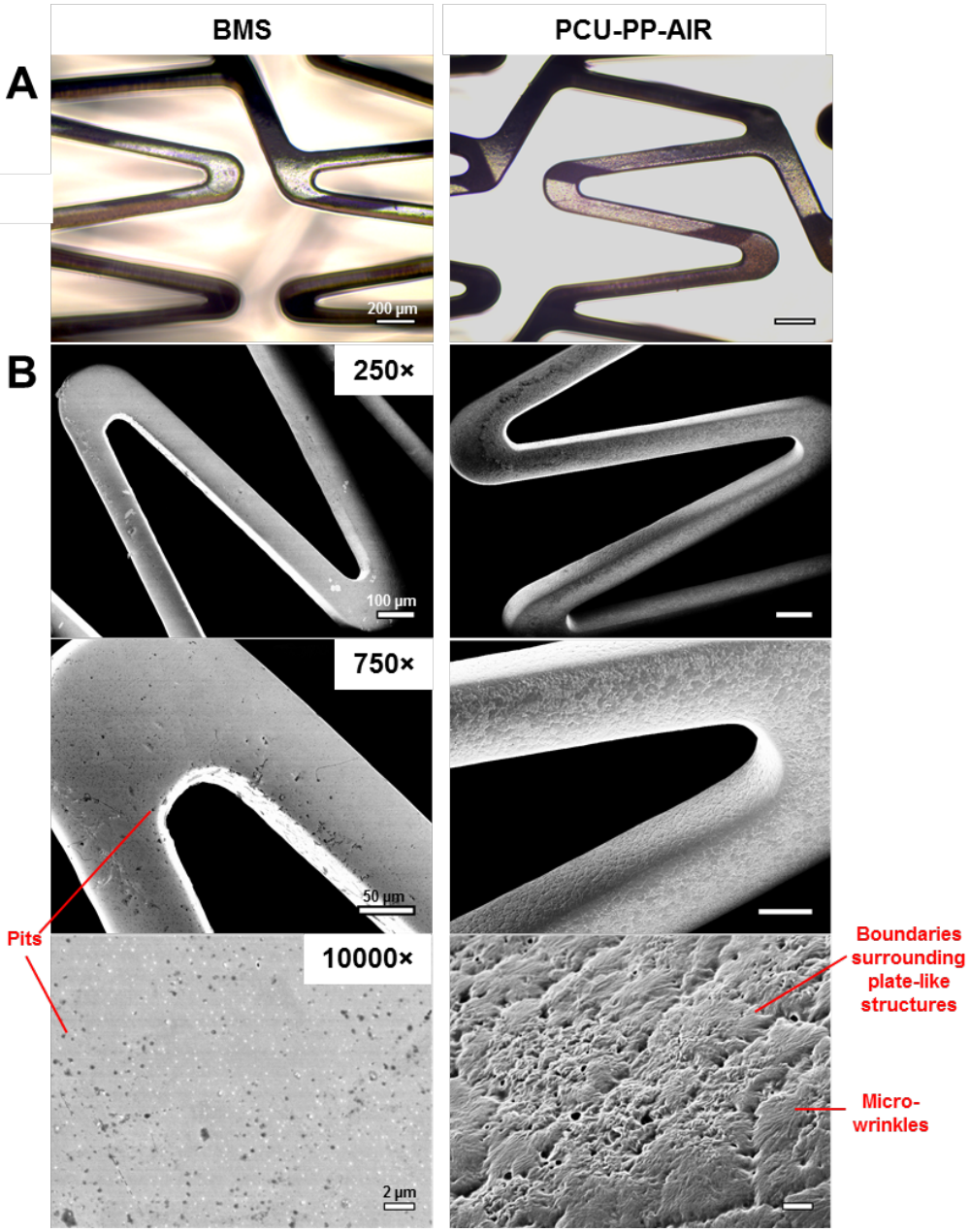

Figure 2.12. (A) Phase contrast optical microscopy images (Objective magnification = 10× , scale bar = 200 µm) and (B) FE-SEM images of BMS and PCU-PP coated BMS after air-curing at different magnification. Scale bar for 250×, 750× and 10000× images are 100, 50 and 2 µm respectively.

A relatively smooth morphology devoid of grain boundaries was observed on BMS, plausibly due to employment of laser cutting and polishing during the manufacturing process, although defects of irregular sized pits were apparent. Coating stents with PCU-PP and subsequent moisture curing in air resulted in a uniform and intact PCU-PP coating layer covering the metallic stent struts. Webbing, which is a common spray coating defect formed by bridging of polymer between the edges of the stent struts, was not apparent throughout the stent. However, plate-like boundaries were visible on the coating. Higher magnification images (10000×) showed evidence of surface micro-wrinkles as reported previously for PCU-PP-AIR coatings on SS316L coupons.

2.4 Discussion

Spin coating was capable of achieving uniform thin film coatings of PCU-PP on the surface of SS316L coupons. During the process, thinning of the PCU-PP film is achieved by combination of outward fluid flow and solvent evaporation [213,214]. The choice of a volatile organic solvent (THF) allows for rapid evaporation leading to a fast production of uniform thin films on the surface of SS316L for subsequent characterisation and further modifications. At the optimised spin coating parameters (3000 rpm, 30 s), the coating thickness was determined to be ~3 μm, as corroborated by micrometre measurements and FE-SEM cross-sectional image analysis. The range of coating thickness generated here are comparable to polymer coatings used in second generation DES, which are presently the preferred DESs in clinic [16]. The spin coating parameters such as polymer concentration and spin speed could be used to further fine-tune the thicknesses of the coatings, as a lower concentration and higher spin speed could result in thinner coatings. It is noted that the thickness measurement techniques employed here (micrometre and FE-SEM) are relatively crude. The measured thickness values were within the lower range of sensitivity of the micrometre, and FE-SEM analysis is merely semi-quantitative. More accurate thickness measurements could be achieved by techniques such as ellipsometry.

θº demonstrated successful organosilane treatment of SS316L coupons with APTMS consistent to a previous study [92]. As reported in the same study, the APTMS treatment generates surface $–NH_2$ that could react with –NCO groups of the PCU-PP to form covalent urea linkages in order to promote bonding between the SS316L and the coating. Furthermore, the APTMS treatment could potentially yield more controlled surface chemistry of different metallic substrates, increasing reproducibility of subsequent coating on other types of metals, including CoCr, PtCr and Nitinol commonly used for vascular stents.

Moisture curing of PCU-PP coating in air (PCU-PP-AIR) and dH_2O (PCU-PP-H_2O) revealed similar ATR-FTIR spectra, which showed successful moisture curing reactions for both coatings to form PCUU coatings, and that there was no major difference in bulk chemistry between both coatings. PCU-PP-AIR was similarly hydrophobic as freshly coated PCU-PP, suggesting minimal increase in hydrophilic urea groups at the coating surface. However, PCU-PP-H_2O coatings were more hydrophilic. It can be postulated that the immersion in H_2O may concentrate newly

formed polar hard segments on the surface due to hydrogen bonding with surrounding H_2O [215], thus leading to the increased hydrophilicity compared to PCU-PP-AIR. In addition, surface morphology of both coatings similarly revealed formation of plate-like structures separated by boundaries, whose dimensions largely match the surface grain boundaries of the SS316L coupons, hence suggesting that such plate-like structures were formed due to conformation of the coatings with the grain boundaries. By using a smooth electropolished SS316L surface, it is likely that a smoother coating without such plate-like structures could be obtained. Furthermore, the surface pores observed could be attributed to release of gaseous CO_2 during the moisture curing reaction. One key difference between both coatings was that PCU-PP-AIR revealed micro-wrinkled structures, which were not apparent in PCU-PP-H_2O. Such difference may be attributed to differential phase separation effect at the surface, which is a phenomenon observed commonly in segmented PU [80,216,217]. In PCU-PP-AIR coatings, the PCU soft segments and newly formed hard segments (urea linkages) undergo phase separation to form enriched domains [218], which can be associated with the formation of the micro-wrinkled morphology. In PCU-PP-H_2O, the relatively flat morphology devoid of micro-wrinkles may be explained by the plasticising effects of H_2O, which was described in several studies [219,220]. The presence of excess H_2O in the curing environment may lead to increased H_2O absorption to the coating to form hydrogen bonds with the newly formed hard urea segments, hence increasing mobility of polymer chains due to disrupted hydrogen bonding between the urea hard segments and the polycarbonate soft segments of individual polymer chains. The increased chain flexibility may contribute to the flatter surface morphology and surface enrichment of urea hard segments as described previously. The resultant surface properties of the chain-extended PCU-PP-H_2O coatings were retained upon drying in air.

The moisture curing duration of 18 h was in agreement with other moisture-cure studies. It was shown that PEG-based pre-polymers of similar thickness with 4% or 10% -NCO content was able to moisture cure completely within 14 h [221]. Addition of catalyst such as triethylamine or dibutyltin dilaurate can further accelerate the curing process. The potentially different moisture-cure reaction kinetics between PCU-PP-AIR and PCU-PP-H_2O, which leads to the different surface hydrophilicity and morphology, warrants further investigations. Further confirmation of the

proposed mechanisms requires surface sensitive characterisation techniques such as X-ray photoelectron spectroscopy (XPS) to analyse the surface compositions. The effect of different levels of moisture content on mechanical properties of polyether-urethane pre-polymer have been previously studied, and have consistently shown decreased mechanical stiffness and strength for pre-polymer cured at higher moisture levels, although these effects were reversible after re-drying of the coatings [102,220]. The results reported here is potentially the first study on surface properties of PU-PPs moisture cured at varying moisture content. One limitation of this study is that the moisture content in terms of relative humidity for PCU-PP-AIR was not well defined, as the coatings were cured in ambient conditions, whose moisture content may differ slightly across different batches of samples. Future work could cure the PCU-PP coatings in chambers with defined relative humidity.

Finally, the ability to coat PCU-PP on to surfaces of PtCr stents was also successfully demonstrated using ultrasonic atomisation spray coating technique. PCU-PP-AIR coating on the PtCr stents revealed similar surface morphology compared to those observed on SS316L coupons, including formation of micro-wrinkles. However, despite absence of distinctive surface grain boundaries on the PtCr stent, some plate-like structures separated by boundaries was still present. One possible explanation is that such structures were formed due to incomplete fusion of PCU-PP droplets deposited on to the stent surface during the spray coating process, and could be exacerbated by the multiple cycles of coatings. Ultrasonic atomisation spray coating is a highly precise and preferred technique for coating of polymers such as phosphorylcholine, PLGA, SIBS and PUs on to stents [222,223]. Further optimisation of coating parameters can provide control over coating surface morphology and thickness [209]. Importantly, the results here demonstrate the transferability of PCU-PP coatings on to PtCr stents, which may imply the possibility of coating PCU-PP on to other types of metallic stents (SS316L, CoCr and Nitinol). For translation on to stents, it is important to study the stability and integrity of the coatings during stent deployment, as well as, under physiological simulations of a pulsatile flow circuit, which mimics shear stress caused by blood flow in a blood vessel.

2.5 Conclusion

In this chapter, moisture cured PCU-PP coatings have been optimised on to SS316L substrates and PtCr BMS. PCU-PP coatings demonstrated different surface morphology and wettability when cured in air and H_2O. This sets the foundation for subsequent chapter to study chemically modified substrates based on PCU-PP platforms for generation of surface functional groups for subsequent immobilisation of biomolecules. The differential surface morphology and wettability observed at varying curing conditions illustrates the tailorability of PCU-PP coatings to yield combinatorial surface chemistry and topographical features.

Chapter 3

Development of Chemical Cured Pre-polymer Coatings

3.1 Introduction

The surface properties of biomaterials including chemistry (wettability, charge, energy) and micro- or nanoscale (1-100 nm) topography are of great importance to guide cell-material interactions *in vitro*, as well as, short- and long-term *in vivo* responses [58,66,224]. Reactive surface chemistry such as amines (-NH_2), carboxyl (-COOH) or alkyne (-C≡C) serve as reactive sites for subsequent chemical immobilisation of biological molecules including peptides or antibodies to guide cellular fate, including adhesion, proliferation, growth and differentiation.

Much effort has focused on surface modification of biomaterials to guide cell-material interactions at the tissue-implant interface to improve the performance of medical devices. These strategies can be generally divided into physical, physicochemical and biological approaches, as described in section 1.4. However, a combination of these approaches to controllably engineer both surface chemistry and topography often involve expensive and time-consuming multi-step procedures, and are restricted to relatively small surface area and simple planar geometries [225,226]. For instance, Bachhuka *et al.* utilised electrostatic binding of gold nanoparticles of varying sizes to surfaces of plasma polymerised allylamine to create controlled nanotopography, followed by an overcoat of plasma polymer of varying chemistry (-NH_2, -COOH and –CH_3) to control the surface chemistry [226].

Polyurethane pre-polymers (PU-PPs) are terminated with isocyanate (–NCO) functional groups, and are more amenable for chemical modification. -NCO groups are highly reactive, and their chemistry is central to the synthesis of the vast range of synthetic polymers, especially PUs [70]. The hydroxyl-NCO and amine-NCO reactions, which give rise to urethane and urea linkages respectively, are the most well-known and widely exploited reactions in PU synthesis. More recently,

Hensarling *et al.* demonstrated base-catalysed click reactions between thiol (-SH) and -NCO on polymer brush surfaces to form thiourethane covalent linkages [227]. The versatility of -NCO provides the possibility to tailor PU-PP chemistry leading to a range of surface chemical properties.

As described previously in Chapter 2 PCU-PP coatings were optimised on to SS316L substrate and PtCr bare metal stents and allowed to moisture cure. This chapter reports on the development of a chemical modification procedure, termed as chemical curing, to modify the chemistry of PCU-PP coatings. PCU-PP coatings were subjected to curing using small molecular precursors including ethylenediamine (EDA), propargylamine (PPA) and *3*-mercaptopropionic acid (MPA) to yield different chemical functional groups. Such small molecular precursors can react with the PCU-PP via autocatalytic amine-isocyanate (NH_2-NCO) reactions or base-catalysed thiol-isocyanate (SH-NCO) click reactions. The original hypothesis was that EDA curing would generate highly crosslinked -NH_2 functional surfaces similar to that observed in biological systems, while MPA and PPA curing would lead to -COOH and -C≡C functional surfaces respectively. The curing procedure would correlate with each precursor and reaction types to generate surfaces with a range of distinct chemical properties. The expected reaction scheme is shown in Figure 3.1.

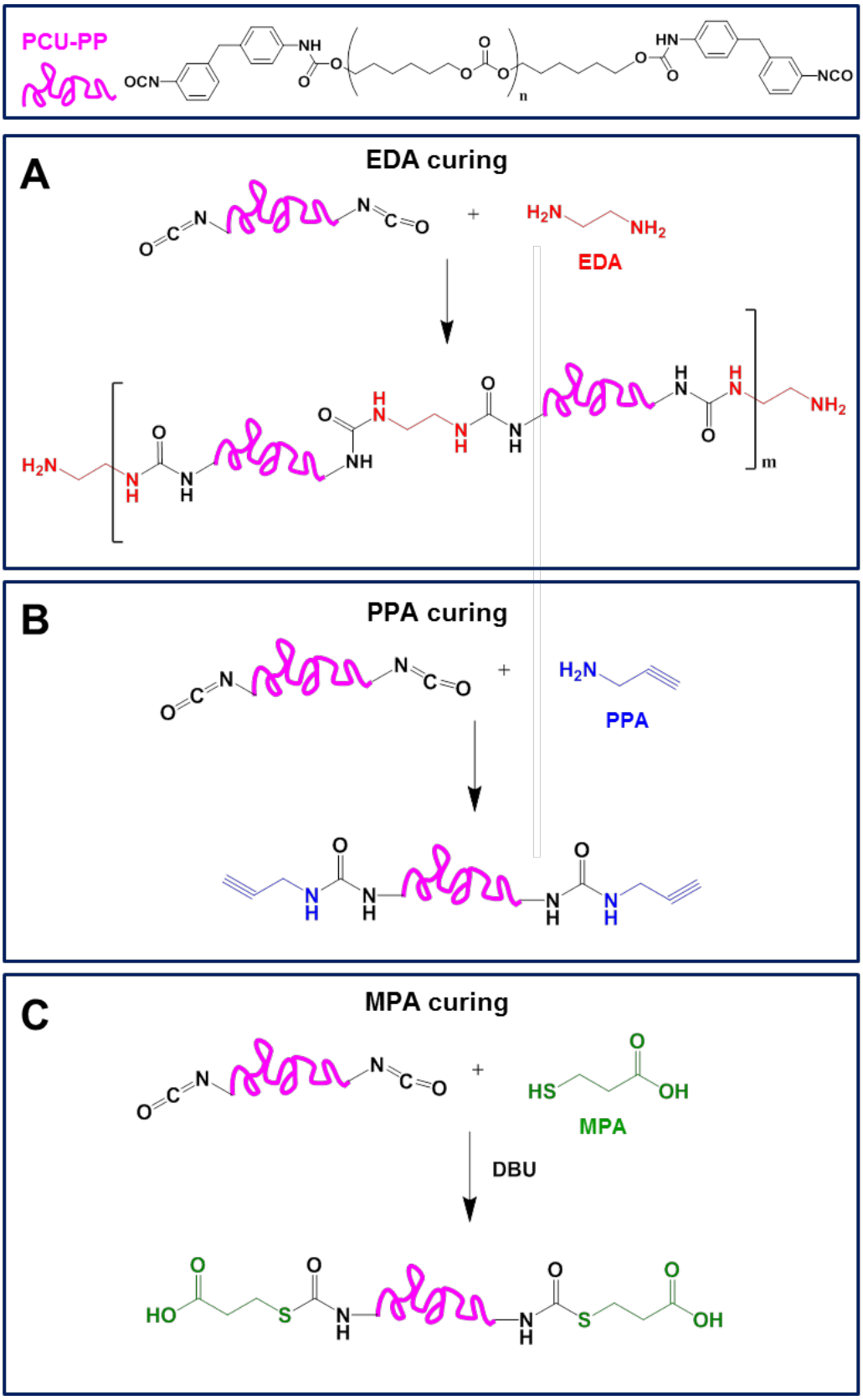

Figure 3.1. Hypothesised reaction schemes for (A) EDA, (B) PPA and (C) MPA curing reactions with PCU-PP.

3.2 Materials and methods

3.2.1 Spin coating of PCU-PP on to silanised SS316L coupons

All reagents were purchased from Sigma-Aldrich UK unless otherwise specified. PCU-PP was spin-coated on to SS316L coupons (diameter = 13 mm), which had been chemically treated with APTMS, as described in section 2.2.2 and 2.2.3.

3.2.2 Post-coating chemical-curing procedure

Upon spin-coating of PCU-PP on to SS316L substrates, chemical-curing was performed by immediate immersion of each coated coupons into 1mL ethylenediamine (EDA), *3*-mercaptopropionic acid (MPA) or propargylamine (PPA) diluted in 100% anhydrous isopropanol (IPA). The curing duration was varied from 1-15 min and was optimised at 15 min for subsequent experiments. The concentration of curing solutions was varied from 0-500 mM. For MPA solutions, *1,8*-diazabicycloundec-*7*-ene (DBU) at 0.2 mol% with respect to thiol groups was added as catalyst for the thiol-NCO click reactions, as described by Hensarling *et al.* [227]. Finally, samples were rinsed with IPA and copious amount of dH_2O prior to storage in air in 6-well plates. 0 mM (100% IPA) was employed as a control, while overnight (18 h) air-cured coatings were designated as untreated controls. Table 3.1 summarises the chemical curing conditions produced in this study.

Table 3.1. Summary of cured PCU-PP coatings used for experimentation

Samples		**Curing condition***
Control	**Untreated**	Cured in air overnight (18 h)
Experimental control	**0 mM**	100% IPA
(1) EDA	**25 mM**	25 mM EDA in IPA
	50 mM	50 mM EDA in IPA
	100 mM	100 mM EDA in IPA
	500 mM	500 mM EDA in IPA
(2) PPA	**25 mM**	25 mM PPA in IPA
	50 mM	50 mM PPA in IPA
	100 mM	100 mM PPA in IPA
	500 mM	500 mM PPA in IPA
(3) MPA	**25 mM**	25 mM MPA + DBU** in IPA
	100 mM	100 mM MPA + DBU** in IPA
	500 mM	500 mM MPA + DBU** in IPA

*Cured for 15 min unless otherwise stated
** 0.2 mol% with respect to –SH groups of MPA

The chemical curing procedure and expected coating chemistry are depicted in Figure 3.2.

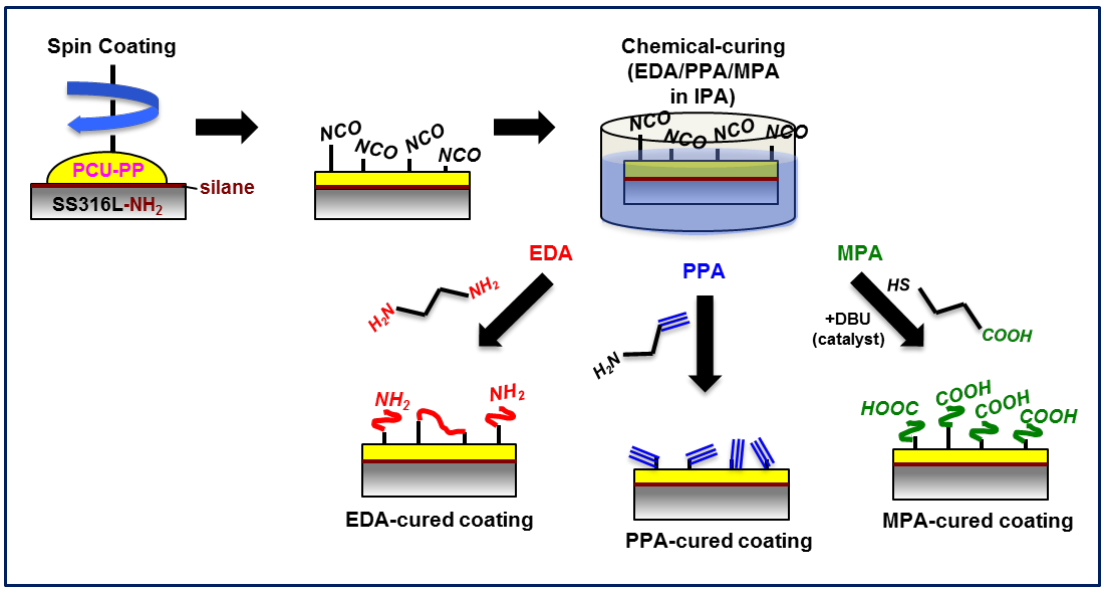

Figure 3.2. Schematic diagram depicting chemical curing procedure of PCU-PP coatings in EDA, PPA and MPA to yield surface $–NH_2$, -C≡C, and –COOH groups.

3.2.3 Demonstration of chemical-curing procedure on stent coating

Rebel^{TM} PtCr bare metal stents (Boston Scientific, UK) were coated with PCU-PP using ultrasonic atomisation spray coating as described in section 2.2.4. PCU-PP coated stents were then immediately immersed into selected curing solutions (50 mM PPA and 50 mM EDA) as described previously, followed by IPA and dH_2O rinsing prior to storage in air in Eppendorf tubes.

3.2.4 Materials characterisation of chemical cured PP coatings

3.2.4.1 Attenuated total reflectance fourier transform infrared spectroscopy (ATR-FTIR)

ATR-FTIR was used to monitor the kinetics of the curing reactions. Samples undergoing chemical curing at different time points (1–15 min) were removed and subjected to rinsing with 100% IPA. Samples were then dried under a stream of nitrogen flow followed by analysis with ATR-FTIR. ATR-FTIR was also used to characterise the cured samples after storage in air overnight (18 h) (n=3 per condition). The operating details were described in section 2.2.5.2.

3.2.4.2 Water contact angle (θ°) measurements

θ° of chemical cured coatings were measured as described in section 2.2.5.1.

3.2.4.3 Colorimetric assay quantifying surface functional groups

Colorimetric assays were employed to measure surface -NH_2, -COOH and -C≡C groups of EDA, MPA and PPA cured coatings respectively. The Orange II assay was used for detection and quantification of surface -NH_2 on EDA cured coatings. Each sample was immersed in 1 mL 1mM Orange II sodium salt in pH 3 dH_2O (adjusted with 1M HCl) for 3 h at room temperature (RT) with gentle shaking. Subsequently, samples were rinsed extensively with pH 3 dH_2O to remove unbounded dye. Samples were then immersed and agitated overnight in 500μL pH 12 dH_2O (adjusted with 1M NaOH) for dye desorption, and the absorbance was read at 492 nm using a microplate reader (Biotek, USA). A standard curve of known concentrations of Orange II sodium salt in pH 12 dH_2O was generated (Appendix B.1), and the amount of –NH_2 density on the coatings were calculated based on the assumption that each Orange II sodium salt molecule complexes with one –NH_2 group.

The Toluidine Blue O (TBO) was used for detection and quantification of surface -COOH. Samples were each immersed in 1 mL 0.5mM TBO in pH 10 dH_2O (adjusted with 1M NaOH) for 3 h at RT with gentle shaking. Samples were rinsed with copious amount of pH 10 dH_2O to remove unbounded dye. 500 μL 50 wt% acetic acid was used for elution of bounded dye for each sample, and absorbance was read at 630 nm using a microplate reader (Biotek, USA). A standard curve of known concentrations of TBO in 50 wt% acetic acid was generated (Appendix B.2), and the amount of –COOH density on the coatings were determined based on the assumption that each TBO molecule complexes with one –COOH group.

For PPA-cured coatings, surface -C≡C groups were quantified via an indirect approach. Samples were reacted via UV-induced thiol-yne click reaction (TYC) with MPA yielding surface –COOH groups, which could correlate with surface reactable -C≡C groups. The TYC reaction is an emerging radical mediated click reaction, and is highlighted in Figure 3.3. TYC reactions were performed by wetting surfaces of coatings with 100 μL 1% (v/v) MPA in ethanol, with thee addition of Irgacure® 2959 as a photoinitiator at 1 mol% (with respect to MPA) followed by UV irradiation (254

nm, 3.0 mW/cm^2) for 2.5 min. Samples were then rinsed with dH_2O and surface –COOH groups was quantified using TBO assay as reported previously.

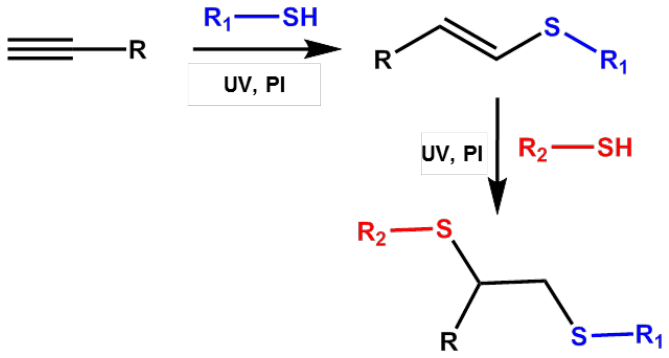

Figure 3.3. Reaction scheme of thiol-yne click reactions. UV irradiation and presence of photoinitiator (PI) generates thiyl radicals (R_1-S•) from thiol groups, which reacts with -C≡C resulting in addition of the radicals to the -C≡C and ultimately leads to formation of vinylthioether. Vinylthioether is also reactive to thiyl radicals (R_2-S•) to give a dithioether.

3.2.4.4 X-ray photoelectron spectroscopy (XPS)

XPS is a surface sensitive technique that detects the elemental composition and chemical state on the nanometre scale (~5 nm) surface of materials. Monochromatic X-rays are irradiated on to a material, leading to emission of characteristic photoelectrons of varying binding energy (B.E.) from the material surface. The B.E and its intensity can then be used to interpret the identity of elemental composition, as well as, their respective chemical states.

Untreated and chemical cured coatings were characterised using Thermo Scientific K-alpha X-ray Photoelectron spectrometer. Samples were loaded into analysis chamber and pumped down to ultra-high vacuum of $<5\times10^{-7}$ Pa. Monochromatic Al Kα X-rays (h=1486.6 eV) were focused on to samples with a spot size of 400µm. A survey spectrum was first obtained for each sample, which could provide the composition of detected elements (n=3 per condition). High-resolution spectra were obtained on each element of interest. Spectral analysis was conducted using CasaXPS software version 2.3.16 (Casa Software Ltd). Static charging was corrected by calibration of the C1s adventitious aliphatic hydrocarbon peak to binding energy of 285 eV [228]. The baseline was subtracted using a Shirley-type background. High resolution spectra of C1s, N1s and S2p peak regions acquired with pass energy of 50 eV were peak-fitted with Gaussian-Lorentzian function, with full widths at half maximum (FWHM) of all component peaks, and were constrained to be equal.

3.2.4.5 Raman spectroscopy

Raman spectroscopy provides a chemical fingerprint of a material based on inelastic scattering of laser, which undergo energy shifts upon interaction with molecular vibrations of a material. In contrast to FTIR, which depends on change in dipole moment, the energy shift for Raman spectroscopy is dependent on the molecular polarizability. Raman spectroscopy was employed in this study to detect -C≡C groups on PPA-cured coatings, which has a weak signal in FTIR spectra.

Raman spectroscopy of untreated and PPA-cured coatings was conducted using a Renishaw InVia Raman microscope. The laser wavelength used was 514.5 nm, and laser power was set at 100%. Number of scans per sample was set to 5 and the exposure time was 30 s per spectrum.

3.2.4.6 Gel permeation chromatography (GPC)

GPC measures the MW distribution and polydispersity index (PDI) of polymers based on size separation using size-exclusion column packed with porous beads. Smaller chains tend to more readily retained in the pores and hence have a higher retention time (t_R) in the column. In this study, chemical cured coatings were dissolved in *N,N*-dimethylformamide (DMF) via ultrasonication for 10 min. Dissolved samples were filtered with a 0.2 μm Nylon-6,6 filter prior to measurements. GPC measurements were performed on an Agilent 1260 Infinity system operating in DMF eluent with 5 mM ammonium tetrafluoroborate (NH_4BF_4), and equipped with refractive index (RI) and variable wavelength (VW) detectors, two Agilent PLgel 5 μm mixed-C columns (300×7.5 mm), an Agilent PLgel 5 mm guard column (50×7.5 mm) and an auto sampler. The columns and RI detector were set to operate at 50°C. The instrument was calibrated using linear narrow poly(methylmethacrylate) (PMMA) standards with molar mass range of 1010 $gmol^{-1}$ to 617,500 $gmol^{-1}$.

3.2.4.7 Field emission scanning electron microscopy (FE-SEM)

Surface morphology of chemical cured coatings was obtained using FE-SEM, as described in section 2.2.5.3.

3.2.4.8 Atomic force microscopy (AFM)

AFM imaging uses a sharp tip mounted on to a cantilever to measure the interaction force between the tip and the sample surface with nanoscale resolution. The force is obtained by measuring the displacement of the cantilever with a laser beam deflection system. This force or displacement interactions between the tip and the sample surface allows three-dimensional (3D) topographical profiles of the sample surface to be obtained. There are three main scanning modes for AFM, which includes: (i) contact mode, where the tip is in contact with the sample surface. This mode is destructive to the sample and tip, and is also prone to interference by adhesive forces, leading to image distortion; (ii) non-contact mode, where the tip constantly oscillates at its resonance frequency, and are generally of low resolution and tend to be suffer interference from adsorbed water molecules; and (iii) tapping mode, which intermittently contacts the surface while it oscillates at its resonance frequency, hence minimally destructive and capable of providing higher resolution images. Tapping mode is the most commonly employed AFM imaging mode for the analysis of materials. In this study, topographical profiles of the coatings were mapped using a Dimension Icon AFM (Bruker, UK). Samples were imaged at room temperature using PeakForce Tapping mode with a tapping frequency of 1 Hz. A SCANASYST-AIR probe (Bruker, UK) with silicon tip radius of 12 nm. Data were analysed using Nanoscope Analysis v1.7 (Bruker, Germany). Measurement of surface micro- and nanofeatures were performed on line profiles of at least 3 individual images (n=3) per condition. Surface roughness parameters, including (i) mean surface roughness (*Ra*) and (ii) root mean square roughness (*Rq*) were quantified using the AFM images (n=3 per condition). *Ra* is defined as the arithmetic mean of the absolute values of surface height deviation from the mean plane measured over the evaluation length. *Rq* is the root mean square average of the height deviation from the mean plane measured over the evaluation length. The equations for *Ra* and *Rq* are as follows:

$$\text{(i) } Ra = \left(\frac{1}{L}\right) \int_0^L |Z(x)|\, dx$$

$$\text{(ii) } Rq = \sqrt{\left(\frac{1}{L}\right) \int_0^L Z(x)^2 dx}$$

where L: evaluation length; Z(x): profile height function in terms of height (Z) and position (x) of the sample.

3.2.5 Statistical analysis

Data were reported as mean ± standard deviation (SD) unless otherwise stated. Statistical analysis was conducted using Prism GraphPad software (version 6.0). One-way ANOVA with Tukey's post-hoc test was used for analysis of θ° and width and height profile of nanofeatures on EDA cured coating measured by AFM. *P* values of $p<0.05$ were considered to be statistically significant.

3.3 Results

Freshly spin-coated PCU-PP coupons were chemically cured in EDA, PPA and MPA in IPA at varying concentrations of 0-500 mM. Air-cured coatings (PCU-PP-AIR) served as untreated controls.

3.3.1 Monitoring reaction kinetics with ATR-FTIR

ATR-FTIR was used to monitor the reaction kinetics of chemical curing of PCU-PP coating (Figure 3.4). Curing in 0mM (100% IPA) for 15 min retained an apparent –NCO peak (2265 cm^{-1}), indicating incomplete reaction of NCO, which would be subsequently moisture cured upon storage in air. EDA and PPA coating reactions completely depleted –NCO peak even at lowest concentration employed (25 mM), illustrating the rapid nature of the NH_2-NCO reaction. In MPA cured coatings, residual NCO remained detectable after 15 min at higher concentrations of 100-500 mM. Therefore, curing time for subsequent experiments was standardised at 15 min.

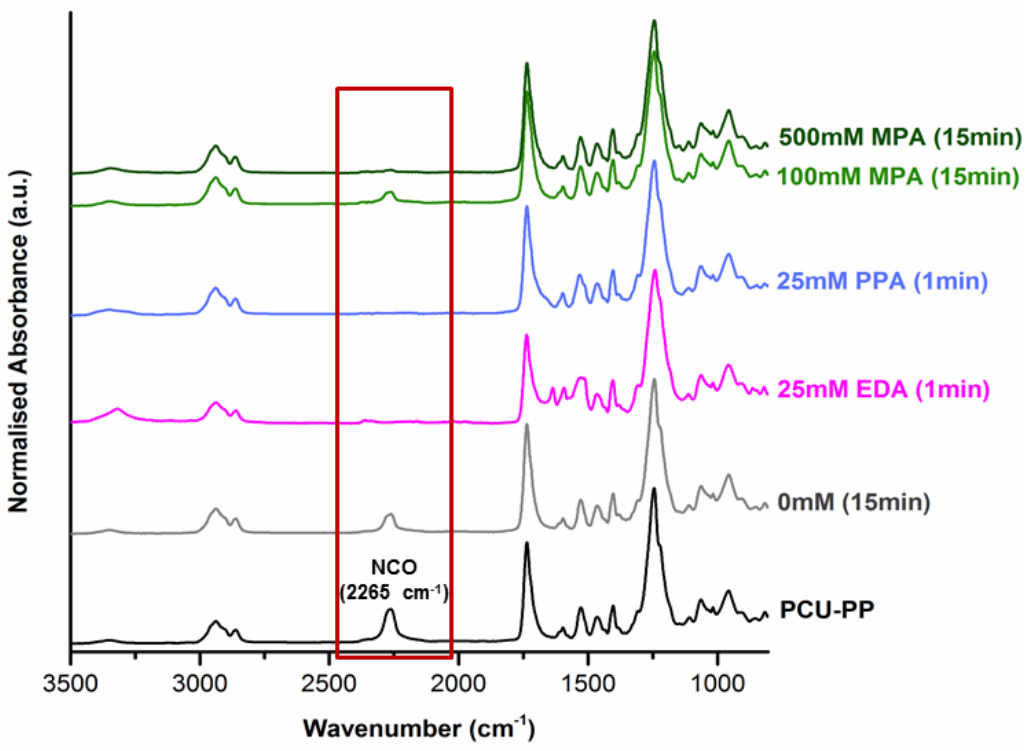

Figure 3.4. Monitoring of curing reaction kinetics of selected concentrations of EDA, PPA and MPA using ATR-FTIR.

3.3.2 Surface chemistry of chemical cured coatings

3.3.2.1 ATR-FTIR of chemical cured coatings

Figure 3.5 presents ATR-FTIR spectra of all cured-coatings at varying curing concentrations.

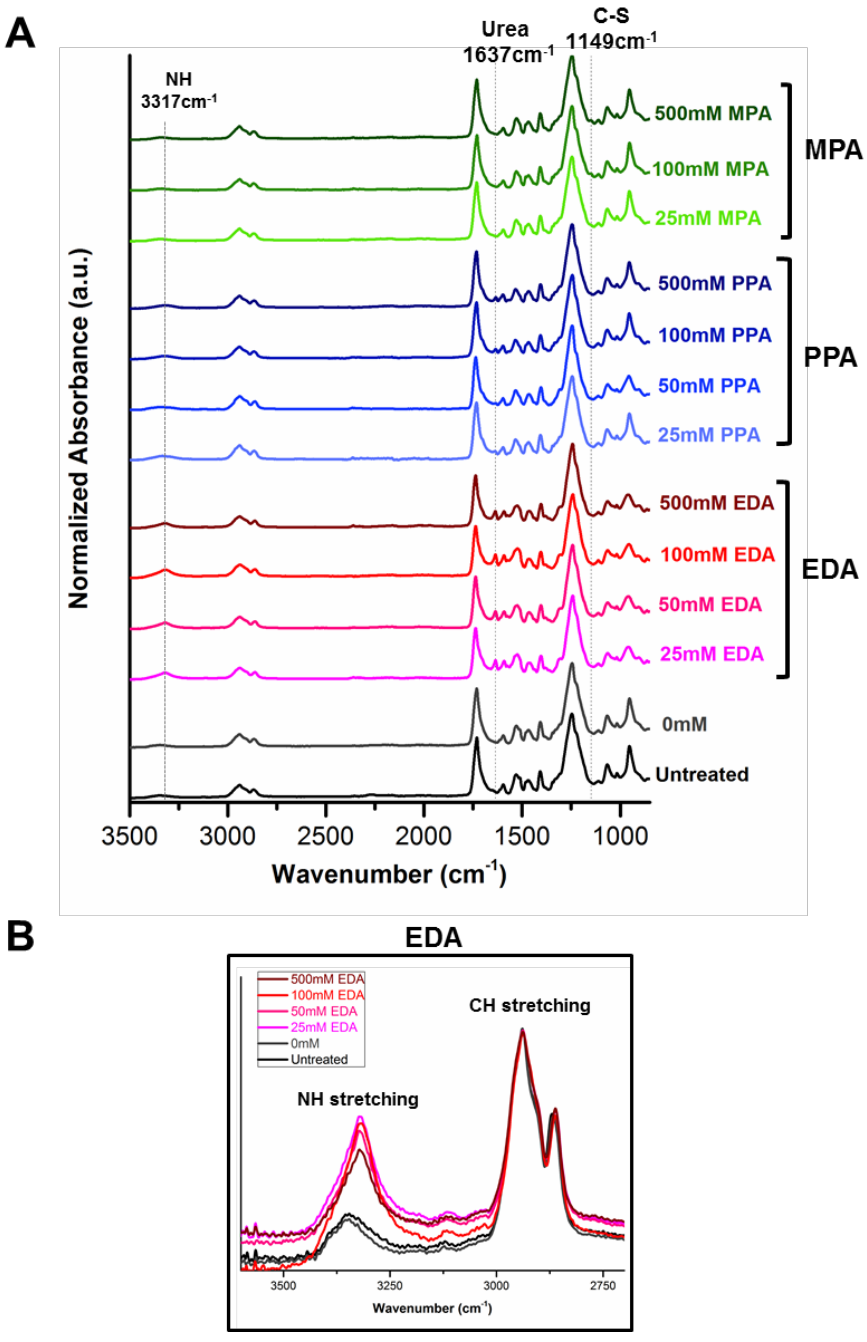

Figure 3.5. (A) ATR-FTIR spectra of EDA, PPA and MPA cured coatings of varying concentration. (B) ATR-FTIR spectra normalised with respect to absorbance at 2939 cm^{-1} (C-H asymmetric stretch) at 3600-2700 cm^{-1} region for EDA-cured coatings, which showed an increase in N-H stretch (3317 cm^{-1}) at lower EDA curing concentration.

Spectra of EDA-cured coatings revealed the generation of a notable hydrogen bonded urea peaks (1637 cm^{-1}), which was also present in untreated controls due to moisture curing reactions albeit at lower intensity. This peak is indicative of successful NH_2-NCO reactions on EDA-cured coatings. Furthermore. an increased -NH peak intensity (3317 cm^{-1}) was revealed at lower 25-100 mM EDA-curing concentrations in comparison with 500 mM EDA (Figure 3.5B), suggestive of a higher density of urea, urethane or $-NH_2$. Apart of these, all other peaks remained similar to untreated and 0mM control.

All PPA-cured coatings also displayed hydrogen bonded urea peak (1637 cm^{-1}), implying success in NH_2-NCO reactions leading to incorporation of -C≡C groups.

In MPA-cured coatings, hydrogen-bonded urea peak (1637 cm^{-1}) was undetected owing to absence of urea linkage formation. In addition, emergence of a peak at 1148 cm^{-1} was observed at higher MPA concentrations (100-500 mM), which were undetected in 25 mM MPA as well as other samples. This peak may be assigned to C-S with support from separate studies [229,230], as well as its detection in neat MPA. It is noted that such peak were not explicitly mentioned in some studies despite their existence on their spectra [78,227].

3.3.2.2 Water contact angle (θ°) of chemical cured coatings

θ° measurements of all chemical cured coatings are shown in Figure 3.6.

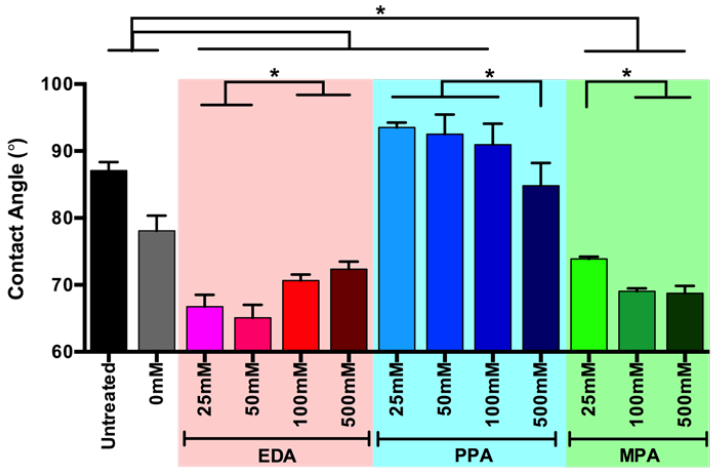

Figure 3.6. θ° measurements on EDA, PPA and MPA cured coatings of varying concentration (n=3). One-way ANOVA with Tukey's post-hoc tests were performed separately within each cured coating group (EDA, PPA and MPA) and revealed significant differences. *p<0.05.

A significantly lowered θ° was detected on all EDA-cured coatings compared to untreated and 0mM controls. This indicates hydrophilic surface properties after treatment, which can be attributed to surface -NH_2 groups. A further decreased θ° on 25-50 mM cured coatings was also detected.

On the other hand, PPA-cured coatings showed significantly higher θ° in comparison to controls with the exception of 500 mM PPA, which showed a slightly decreased θ° comparable to controls (p>0.05).

For MPA-cured coatings, θ° generally decreased following MPA treatment across all concentration, indicating increased hydrophilicity. θ° at higher concentration (100-500 mM) were significantly lower than 25 mM. Altogether, the results showed that each chemical curing step resulted in change in θ°, hence providing confidence that chemical reactions had occurred.

3.3.2.3 Colorimetric assay detecting surface functional groups

Surface -NH_2 group densities on EDA-cured coatings were measured using Orange II assay (Figure 3.7). -NH_2 groups were barely detectable on untreated and 0mM controls, but were clearly detected on all EDA-cured coatings. Surface -NH_2 groups decreased with increasing curing concentration from 25mM to 100mM, but rose back at concentration of 500 mM to a level comparable to 25 mM.

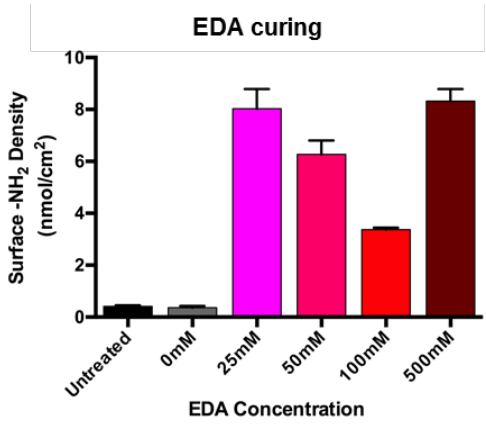

Figure 3.7. Quantified surface –NH_2 density on EDA-cured coatings via Orange II assay (n=4).

Surface -C≡C groups were measured indirectly by employing thiol-yne click (TYC) reaction with MPA and subsequently quantifying the surface –COOH groups by TBO assay. Figure 3.8 illustrates that simply incubating PPA (100mM) coating with MPA without UV-irradiation and photoinitiator did not greatly enhance –COOH

density, indicating barely any reaction had taken place. With UV-irradiation and photoinitiator, higher –COOH density was detected on all PPA-cured coatings compared to controls, suggesting presence of reactable -C≡C on the coatings. No distinctive differences were detected between the different curing concentrations of PPA. Nevertheless, although not significant, there appeared to be a trend of decreasing –COOH density as concentration increased from 25 -500 mM.

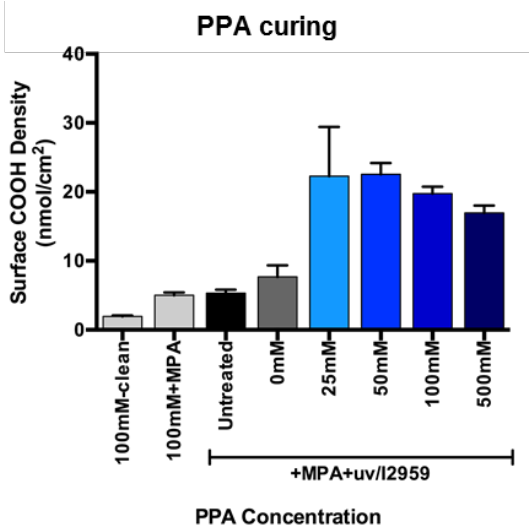

Figure 3.8. Indirect measurement of surface -C≡C density on PPA-cured coatings by measuring –COOH density using TBO assay after TYC reaction with MPA (n=3).

On MPA-cured coatings, surface -COOH groups were measured using TBO assay. The TBO assay (Figure 3.9) confirmed successful generation of -COOH groups across all of the treated samples. The density of -COOH groups increased with increasing MPA concentration from 25-500 mM. The results altogether indicated successful modification step from chemical curing for each type of precursor.

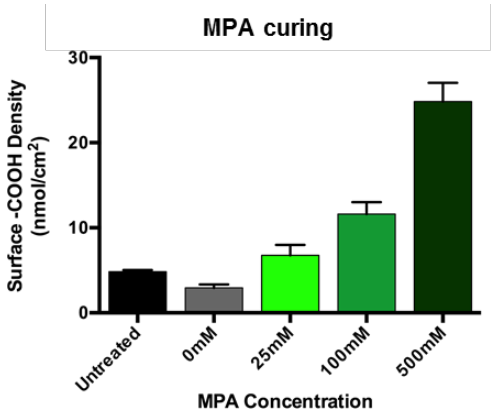

Figure 3.9. Quantified surface –COOH density on MPA-cured coatings via TBO assay (n=4).

3.3.2.4 X-ray photoelectron spectroscopy (XPS) of chemical cured coatings

XPS was performed to further elucidate the surface chemistry of the chemical cured coatings. Table 3.2 summarises the surface atomic compositions of detected elements on selected cured coatings. High resolution C1s and N1s spectra of the coatings were peak-fitted based on logical deduction of chemical environments [228].

Table 3.2. Summary of surface atomic composition of EDA, PPA and MPA-cured coatings detected by XPS (n=3).

Samples		N (%)	C (%)	O (%)	S (%)
Controls	**Untreated**	4.52 ± 0.12	82.38 ± 0.65	13.09 ± 0.77	-
	0mM	2.60 ± 0.28	78.83 ± 2.92	18.58 ± 2.63	-
(1) EDA	**25mM**	14.16 ± 0.68	74.14± 0.47	11.69 ± 0.65	-
	50mM	11.88 ± 1.33	76.89 ± 2.37	11.23 ± 1.11	-
	100mM	7.87 ± 0.16	71.62 ± 0.31	20.51 ± 0.16	-
	500mM	4.46 ± 0.58	71.86 ± 1.04	23.69 ± 0.46	-
(2) PPA	**50mM**	3.73 ± 0.69	72.42 ± 0.57	23.85 ± 1.12	-
	500mM	3.66 ± 0.55	71.99 ± 1.17	24.35 ± 0.67	-
(3) MPA	**25mM**	3.18 ± 0.35	75.82 ± 0.74	20.56 ± 1.01	0.44± 0.06
	100mM	2.41 ± 0.20	74.22 ± 0.64	22.48 ± 0.43	0.89 ± 0.17
	500mM	2.54 ± 0.72	77.68 ± 2.24	18.83 ± 2.63	0.95 ± 0.04

0mM controls exhibited a lowered %N content but higher %O in comparison to untreated control. EDA-cured coatings exhibited increasing %N composition at lower EDA concentration, which is consistent to the trends observed in $–NH_2$ density, θ° and ATR-FTIR. In particular, 25-50 mM EDA displayed almost three-fold increase in %N compared with untreated controls. High resolution C1s spectra of both controls and EDA cured coatings (Figure 3.10) demonstrated chemical environments including carbonate (O-C(O)-O), urethane (O-C=O), urea (N-C=O), carbonyl (C-O), C-N bond and alkyl (C-C), which is in agreement with the earlier hypothesised reaction scheme in Figure 3.1. Interestingly, 25-50 mM EDA revealed lower proportion of surface carbonate (O-C(O)-O) intensity, as well as, a higher urea (-N-C=O) and C-N intensity compared with 500 mM EDA. Surface urea was barely detectable on untreated controls. This suggests a urea (i.e. hard segment) enriched surface on 25-50 mM EDA. In addition, high resolution N1s spectras of all EDA cured coatings illustrated additional -N chemical environments (B.E.=402.0 eV) apart from the N-C peak (B.E.=400.0 eV), which is not observed in controls. This peak could be assigned to $-NH_2$ (or NH_3^+) functional groups [94,231].

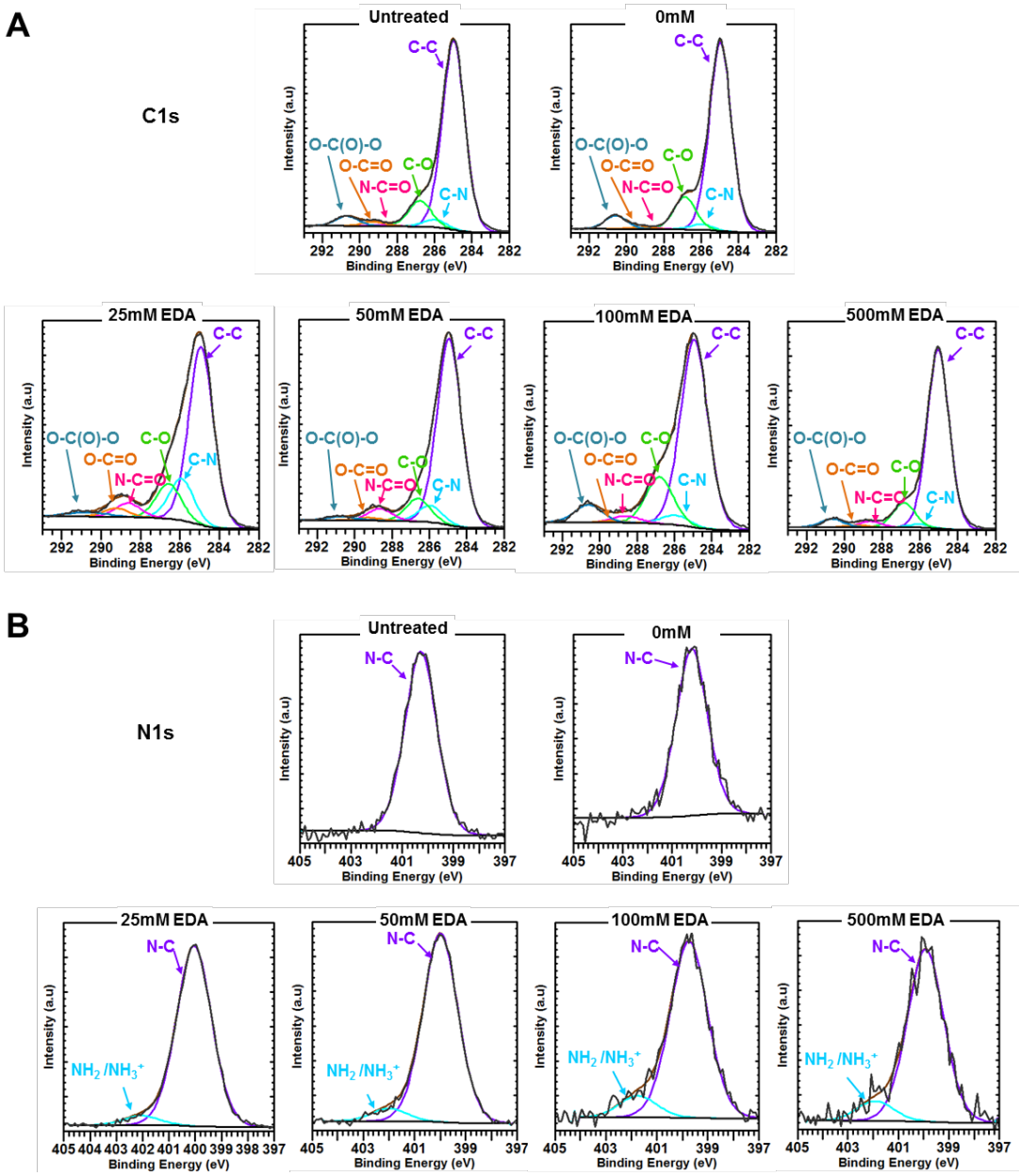

Figure 3.10. High resolution XPS (A) C1s and (B) N1s spectra of EDA cured coatings, along with untreated and 0mM (100% IPA) controls. C1s spectra was peak fitted with C-C at binding energy of 285.0 eV, C-N/C-S at 286.0 eV, C-O-C at 286.9 eV, N-C=O (urea) at 288.7 eV, O-C=O (urethane) or S-C=O (thiourethane) at 289.3 eV and O-C(O)-O (carbonate) at 290.7 eV. N1s spectra was fitted with N-C(O) peak at 400.0 eV and NH_2 or NH_3^+ at 402.0 eV.

PPA-cured coatings (50 and 500mM) showed higher %N compared with 0mM controls, but slightly lower than untreated coating. The surface elemental compositions between both concentrations were similar. High resolution C1s spectras (Figure 3.11A) showed presence of similar peaks to controls, with a higher intensity of carbonate (O-C(O)-O). Surface urea appeared to be of lower intensity compared to EDA-cured coatings, and more similar to that of untreated and 0mM

controls. High resolution N1s spectras (Figure 3.11B) did not reveal $-NH_2$ peak observed in EDA-cured coatings. Similar to other studies, -C≡C was not easily detected using XPS [232].

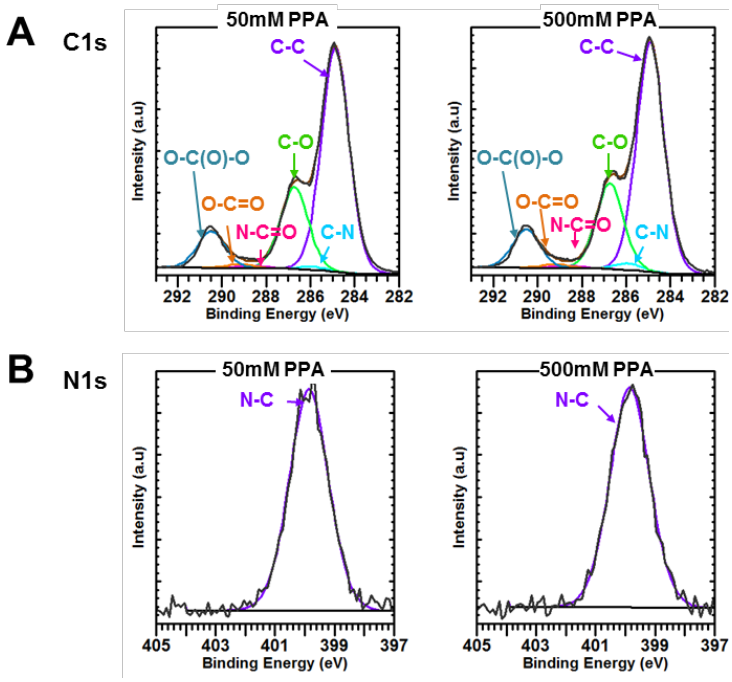

Figure 3.11. High resolution XPS (A) C1s and (B) N1s spectra of PPA cured coatings. C1s spectra was peak fitted with C-C at binding energy of 285.0 eV, C-N at 286.0 eV, C-O-C at 286.9 eV, N-C=O (urea) at 288.7 eV, O-C=O (urethane) at 289.3 eV and O-C(O)-O (carbonate) at 290.7 eV. N1s spectra was fitted with N-C(O) peak at 400.0 eV.

On MPA-cured coatings, surface %S was detected on all concentrations (25-500 mM), with a trend of increasing %S composition with increasing concentration observed. High resolution C1s spectrum depicted in showed possible presence of C-S and thiourethane (S-C=O) chemical environments (Figure 3.12A), which coincides with C-O and urethane (O-C=O) spectra respectively. N1s spectrum only illustrated a single C-N (Figure 3.12B). High resolution S2p spectrum revealed a typical S2p spin-doublet shape on 100 mM MPA (Figure 3.12C), which can be assigned to C-S from the thiourethane linkage [230], thus confirming successful SH-NCO reactions between PCU-PP and MPA.

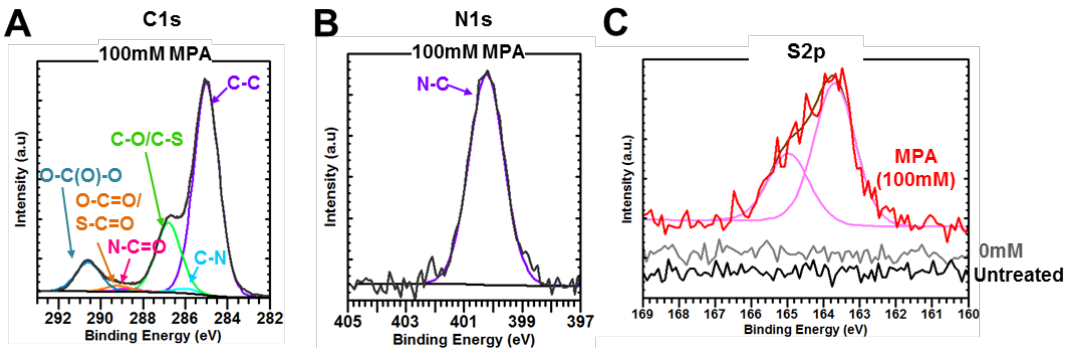

Figure 3.12. High resolution XPS (A) C1s; (B) N1s and (C) S2p spectra of MPA cured coating. C1s spectrum was peak fitted with C-C at binding energy of 285.0 eV, C-N at 286.0 eV, C-O/C-S at 286.9 eV, N-C=O (urea) at 288.7 eV, O-C=O (urethane) or S-C=O (thiourethane) at 289.3 eV and O-C(O)-O (carbonate) at 290.7 eV. N1s spectrum was fitted with N-C(O) peak at 400.0 eV. S2p spectrum was compared with untreated controls, and was fitted with spin-doublet C-S peaks at binding energies of 163.7 and 165.0 eV.

3.3.2.5 Raman Spectroscopy (for PPA-cured coating)

For direct confirmation of surface -C≡C on PPA-cured coatings, Raman spectroscopy was used due to its ability to detect -C≡C band. The Raman spectra of selected 50 mM PPA coating and untreated control are shown in Figure 3.13. The assignment of bands are summarised in Table 3.3 [233,234].

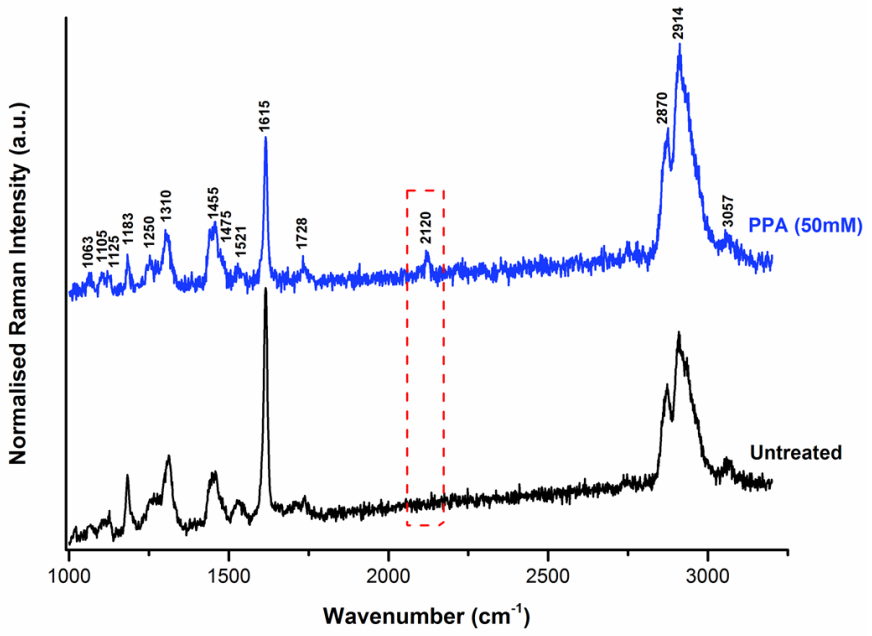

Figure 3.13. Raman spectra of PPA-cured coating (50 mM) in comparison to untreated control, illustrating appearance of a peak at 2120 cm^{-1} following PPA curing. (Analysis conducted by Dr Noora Naghavi)

Table 3.3. Assignment of Raman signals for 50 mM PPA and untreated control.

Wavenumber (cm^{-1})	Assignment
3057	Aromatic CH stretching
2914	Assymetric CH stretching
2870	CH stretching
2120	C≡C stretching
1728	C=O stretching
1615	Aromatic C=C stretching
1521	NH bending, CN stretching
1475	OCH_2 bending
1455	CH_2 bending
1310	C-N stretching, C-O stretching
1250	Aromatic C-N stretching
1183	C-O-C stretching, aromatic CH bending
1125-1105	C-C stretching
1066	C-O-C bending

Comparing to untreated coatings, PPA-cured coatings revealed an additional band at 2120 cm^{-1}, which can be assigned to -C≡C [235]. Other bands are quanlitatively no different between the 2 samples, and are in agreement with the expected chemical structure consisting of urethane, urea and carbonate moieties.

3.3.3 Molecular weight changes by gel permeation chromatography (GPC)

As chemical curing of PCU-PPs relies on chain extension, GPC is employed to determine the molecular weight (MW) changes before and after chemical curing. Figure 3.14 shows retention time (t_R) distribution of selected cured coatings.

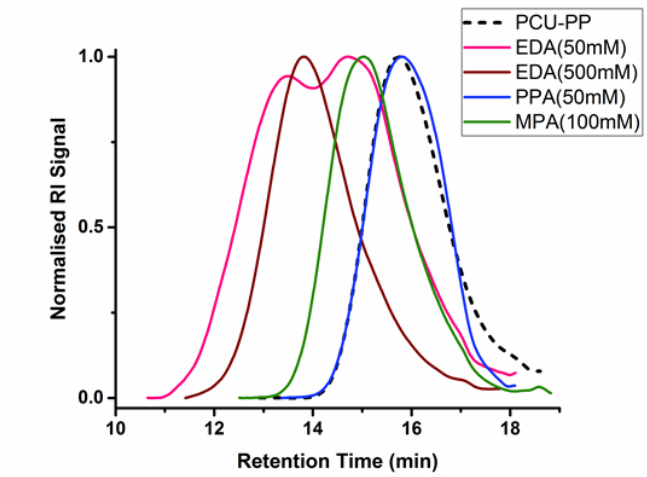

Figure 3.14. GPC measurements on selected cured PCU-PP coatings. (Analysis conducted by Mr Resat Aksakal and Dr Remzi Becer at Queen Mary University of London, UK).

The number average MW (M_n) and polydispersity index (PDI of the coatings are summarised in Table 3.4.

Table 3.4. Summary of GPC data obtained with PCU-PP, EDA and MPA-cured coatings. (Analysis conducted by Mr Resat Aksakal and Dr Remzi Becer at Queen Mary University of London, UK)

Samples	$M_{n,theo}$ ($g.mol^{-1}$)	$M_{n,GPC}$[a] ($g.mol^{-1}$)	PDI[a]
PCU-PP	2501	8297	1.87
EDA (50mM)	-	28158[b]	5.58
EDA (500mM)	-	61976	2.99
PPA (50mM)		10609	1.53
MPA (100mM)	-	16120	2.13

[a] DMF eluent, PMMA standards
[b] Bimodal peak distribution

Neat PCU-PP had a prolonged t_R (16 min) in the column due to its short M_n. While PPA-cured coating illustrated a lower M_n in the range similar to uncured PCU-PP, both EDA and MPA-cured coatings displayed chain lengthening with a higher M_n. PDI was increased for both coatings. M_n for EDA-cured coatings (50 and 500 mM) appeared to be higher than that of MPA-cured coatings (100 mM). Between 50 and 500 mM EDA, 500 mM EDA was presented as a single Gaussian distribution, while interestingly 50mM EDA revealed a relatively broad bimodal peak MW distribution with much higher PDI, suggesting two distinct populations.

3.3.4 Surface morphology and topography of chemical cured coatings

Apart from characterisation of the coating chemistry, the surface morphology and topography of the chemical cured coatings were also characterised by FE-SEM and AFM.

3.3.4.1 FE-SEM of chemical cured coatings

Figure 3.15 shows surface morphology of EDA cured coating at varying concentration. Control samples (0 mM) appeared to be microscopically flat with irregular surface imperfections in higher magnification FE-SEM images. Interestingly, EDA-curing revealed concentration dependent formation of distinct surface topography. Curing under lower EDA concentrations (25-100 mM) produced a combination of micro-scale corrugated ridges and nanoscale features (~100 nm), whereas a higher concentration of 500 mM EDA yielded only flat surfaces devoid of any micro- or nanofeatures. It is observable that the nanofeatures diminished as EDA curing concentration increases from 25 to 500 mM.

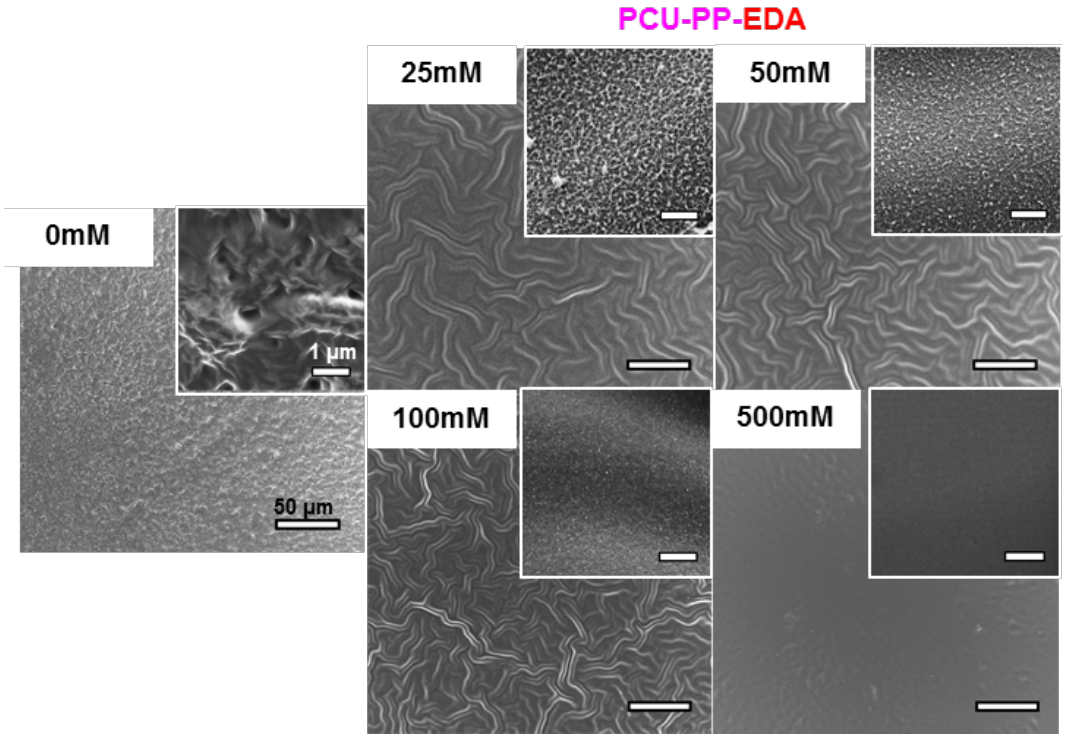

Figure 3.15. Representative FE-SEM images of EDA cured coatings at varying concentrations. Magnification = 500× (scale bar = 50 µm), inset magnification = 25000× (scale bar = 1 µm).

As shown in Figure 3.16, PPA-cured coatings showed distinct changes in surface morphology in comparison to controls. Microscopically, morphology of lower curing concentrations (25-100 mM) appeared with rounded-islands, which diminished to relatively flat morphology as concentration increases to 500 mM. The micro-islands were measured to be ~15 µm at 25-50 mM PPA. Higher magnification images depict appearance of nanofibrous-like structures across all samples, along with irregular imperfections and pores.

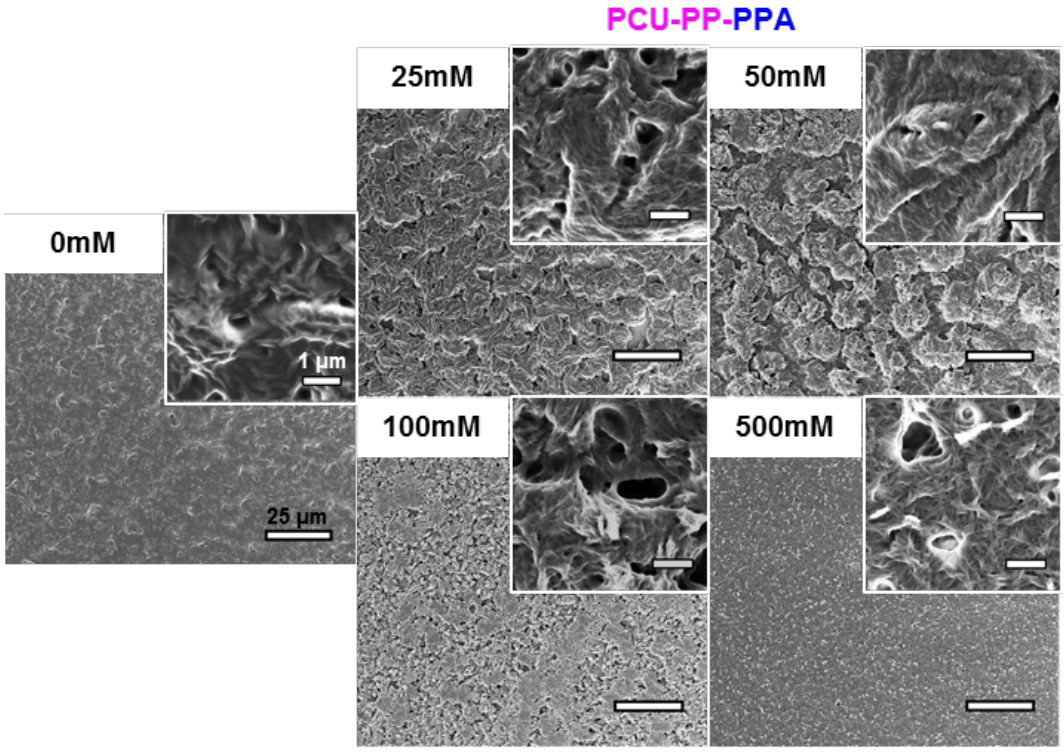

Figure 3.16. Representative FE-SEM images of PPA cured coatings at varying concentrations. Magnification = 1000× (scale bar = 25 µm), inset magnification = 25000× (scale bar = 1 µm).

MPA-curing revealed a differential concentration-dependent morphological trend compared to EDA and PPA (Figure 3.17). At lower concentration (25 mM), the coating revealed similar morphology to controls (0 mM). Increasing MPA concentrations from 100-500 mM revealed the appearance of submicron ridges. It is noted that micro-ridges on MPA-cured coatings are less distinctive compared to EDA, likely due to their lower height (~15-20 nm) alongside observable surface imperfections.

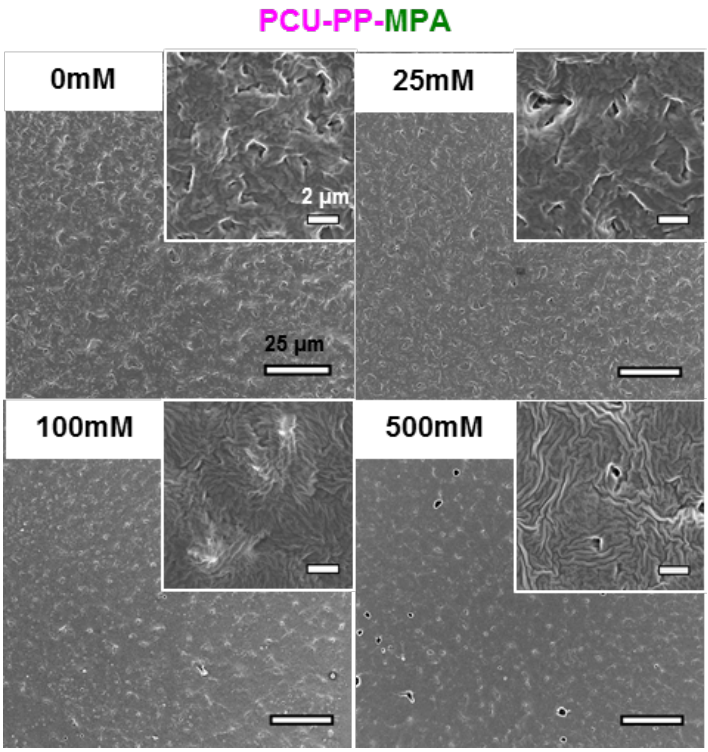

Figure 3.17. Representative FE-SEM images of MPA cured coatings at varying concentrations. Magnification = 1000× (scale bar = 25 µm), inset magnification = 10000× (scale bar = 2 µm).

3.3.4.2 AFM and roughness analysis of chemical cured coatings

The height profiles of EDA-cured coatings are presented in Figure 3.18, in two different scales (25×25 and 1×1 µm) illustrating both micro- and nanofeatures observed in FE-SEM. The images are in agreement with observations in FE-SEM described above, but permit more precise visualisation and quantification of topographical features. Table 3.5 summarises the dimensions of the micro-ridges and nanofeatures measured from line profiles on AFM images. Generally, the micro-ridges on 25-100 mM EDA were measured to be ~7-10 µm wide, and ~0.5 µm high on 25-50 mM EDA but more elevated (~1 µm) on 100 mM EDA. The nanofeature dimensions (both width and height) were larger at lower EDA concentrations (Figure 3.18B), and diminished as concentration increases. At 500 mM EDA, such nanofeatures were not noticeable, but formation of some nano-pits could be observed. Surface roughness *Ra* and *Rq* was also quantified based on 1×1 µm images, and showed increased surface roughness as EDA concentration decreased (Figure 3.18C).

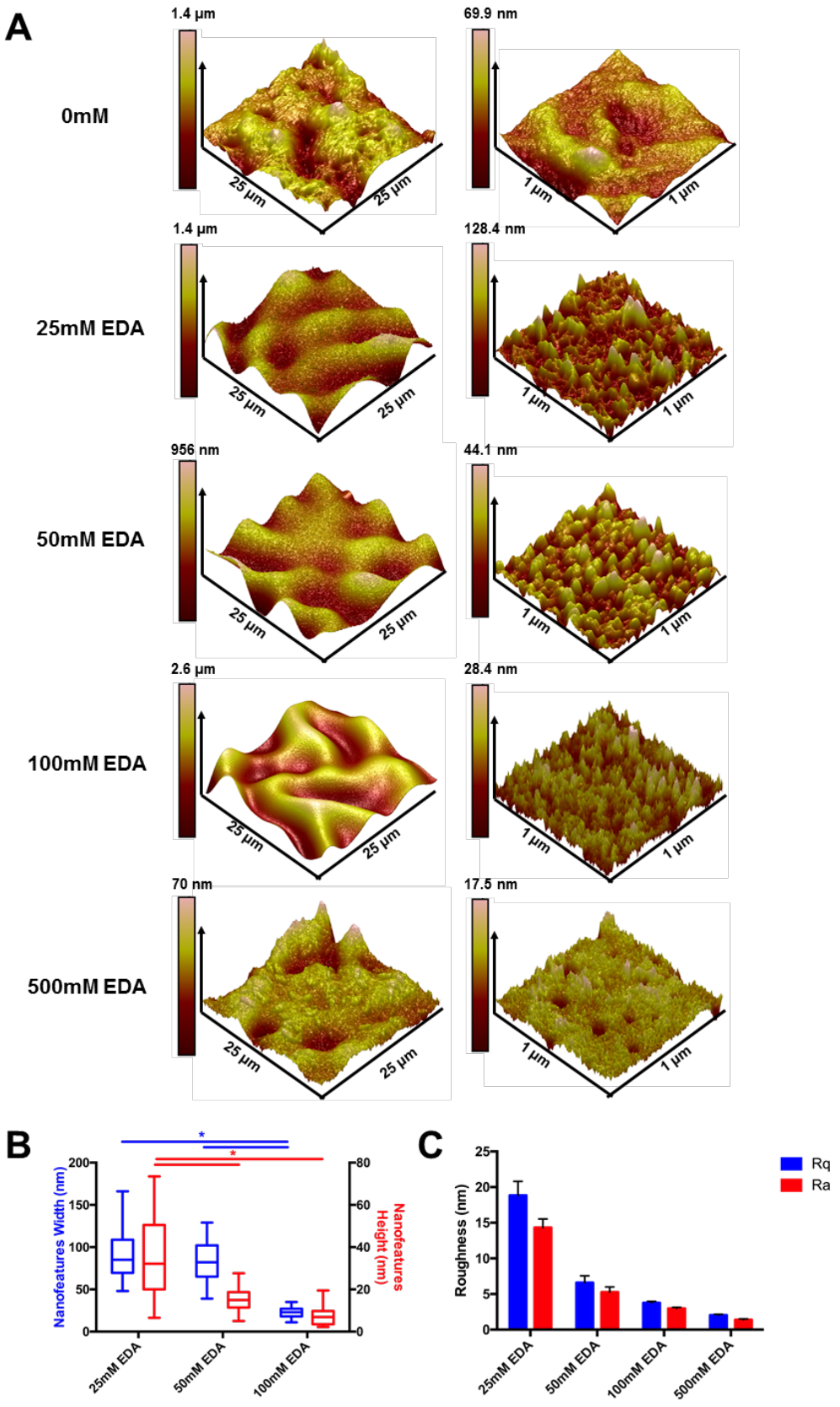

Figure 3.18. (A) AFM 3D height images of EDA-cured coatings at 25×25 and 1×1 µm; (B) Width and height distribution of nanofeatures measured on 25-100 mM EDA-cured coatings (n=30). Statistical analysis between groups were performed using one-way ANOVA with Tukey's post-hoc test. *p<0.05 (C) Roughness *Ra* and *Rq* values of EDA-cured coatings (n=3). (Imaging performed by Dr Junjie Zhao)

Table 3.5. Measurement of width and height of micro-ridges (n=15 from at least 3 samples per condition) and nanofeatures (n=30 from at least 3 samples per condition) on EDA-cured coatings (25-100 mM).

Samples	Micro-ridges		Nanofeatures	
	Width (µm)	Height (µm)	Width (nm)	Height (nm)
25mM EDA	9.0±2.0	0.7±0.3	90±31	35±18
50mM EDA	8.0±0.7	0.4±0.2	84±25	15±6
100mM EDA	7.6±0.9	1.0±0.2	23±7	7±4

On PPA-cured coatings, 5×5 µm images of 50 and 500 mM PPA revealed an irregular surface topography with nanofibres observable, similar to that observed in FE-SEM (Figure 3.19). The dimensions of nanofeatures were measured and summarised in Table 3.6, and showed no detectable differences between 50 and 500 mM PPA. It is noted that many thinner nanofibres were difficult to measure at this scale. The image *Ra* and *Rq* values also appeared lower on 500 mM in comparison to 50 mM PPA (Figure 3.19B).

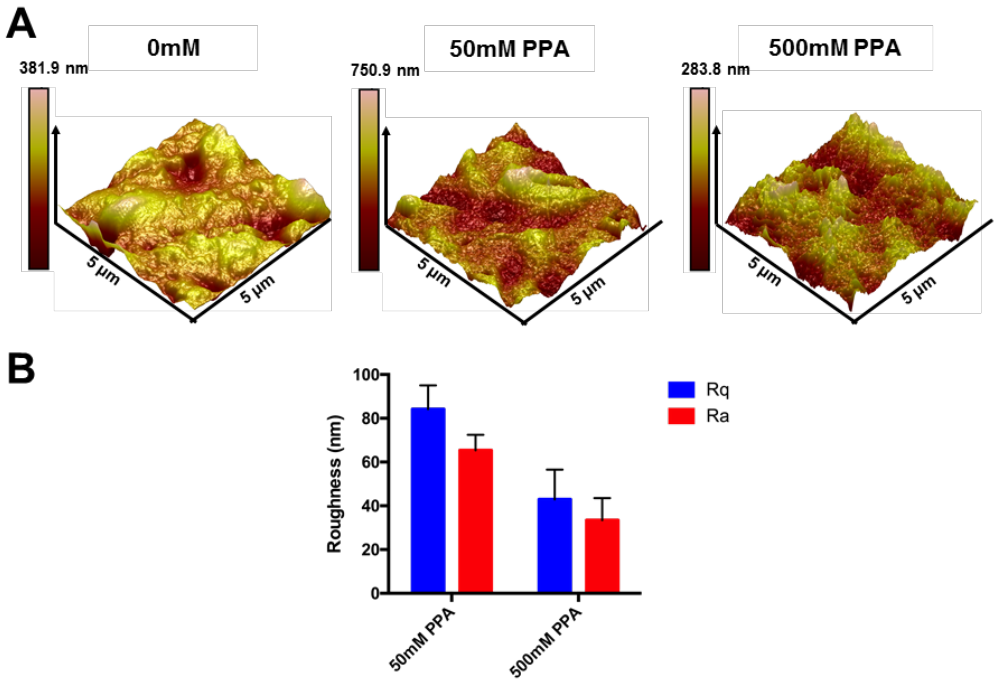

Figure 3.19. (A) AFM 3D height 5×5 µm images and (B) Image roughness *Ra* and *Rq* values (n=3) of PPA cured coatings. (Imaging performed by Dr Junjie Zhao)

Table 3.6. Width and height of nanofibres measured on 50 and 500 mM PPA (n=13 from 3 samples per condition).

Samples	Nanofibre	
	Width (nm)	Height (nm)
50mM PPA	131±24	24±10
500mM PPA	129±33	33±8

Regarding MPA-cured coatings, sub-micron ridges were visible on 5×5 µm images on 100-500 mM MPA (Figure 3.20), and were measured to be ~0.5 µm in both cases (Table 3.7). The roughness parameters *Ra* and *Rq* between both 100 and 500 mM MPA were not distinctly different (Figure 3.20).

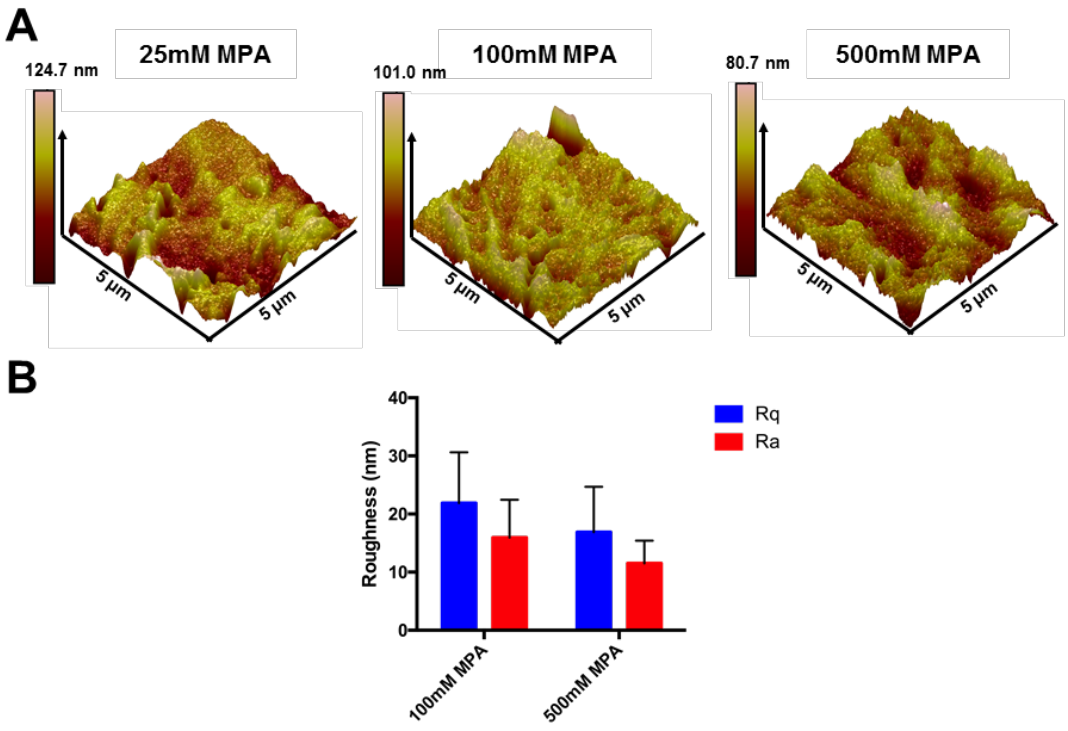

Figure 3.20. (A) AFM 3D height 5×5 µm images and (B) image roughness *Ra* and *Rq* values (n=3) of MPA cured coatings. 0 mM control presented in Figure 3.19. (Imaging performed by Dr Junjie Zhao)

Table 3.7. Width and height of micro-ridges measured on 100-500 mM MPA (n=10 from 3 samples per condition).

Samples	Micro-ridges	
	Width (µm)	Height (nm)
100mM MPA	0.50±0.15	21±6
500mM MPA	0.56±0.15	15±3

3.3.5 Chemical curing of PCU-PP on coated bare metal stents

50 mM EDA and PPA chemical curing of PCU-PP were selected to demonstrate the versatility of the chemical curing procedure to be transferred on to a vascular stent with complex geometry. The FE-SEM images are shown in Figure 3.21.

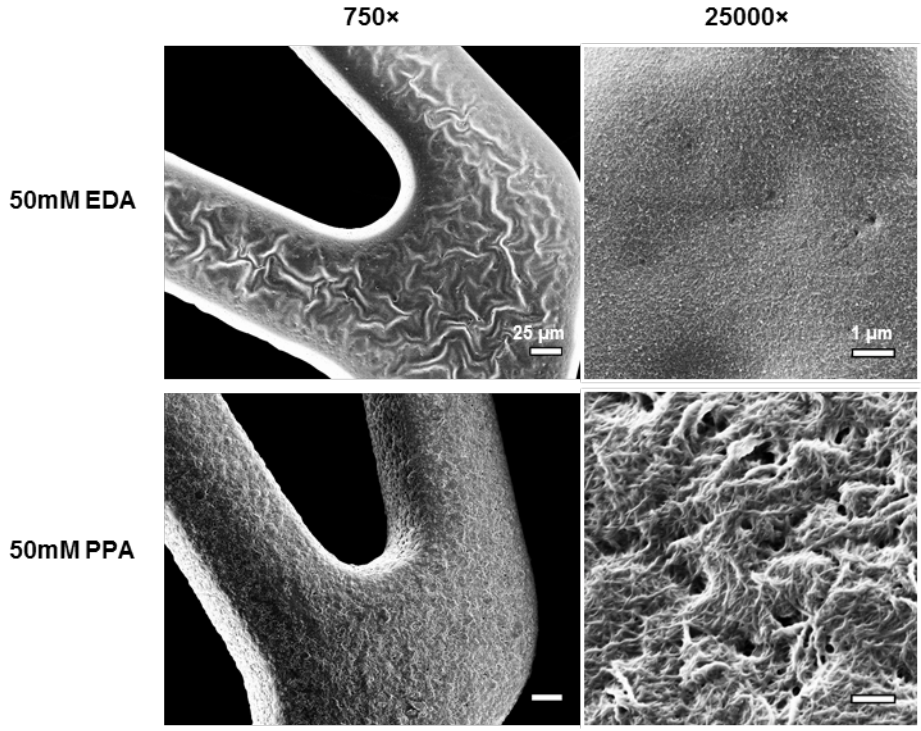

Figure 3.21. FE-SEM images of 50 mM EDA and PPA cured PCU-PP coating on BMS.

EDA-cured stent coating displayed surface micro-ridges and nanofeatures, while PPA-cured coating showed appearance of some microscale rounded-islands and nanoscale fibrous-like morphology. The results appear similar to those observed on cured SS316L coupons reported earlier (Figure 3.15).

3.4 Discussion

Results thus far demonstrate that curing reactions between PCU-PP and small molecular precursors (EDA, PPA and MPA) can produce coatings with unique surface coating chemistries in combination with distinctive surface micro- and nanofeatures. Each of these curing systems exhibited differential concentration-dependent behaviour, which influences the final properties and subsequent surface chemistry profile of the coatings.

3.4.1 EDA curing

EDA curing reactions can be efficiently achieved without catalyst due to the rapid reactions between $–NH_2$ and –NCO. NH_2-NCO is a well known autocatalytic reaction commonly employed for synthesis of poly(urea)urethane (PUU) or polyurea. It is noted that –OH groups from IPA could also react with –NCO, but proceeds at a slower rate than $–NH_2$ especially being a secondary –OH [70]. The choice of IPA as a diluent is due to its being a non-solvent for PCU-PP and minimising interference to –NCO reactions.

EDA curing yields a highly crosslinked, $–NH_2$ functionalised coating with surface micro-ridges and nanofeatures at a lower concentration range (25-100 mM), and a flat surface at 500 mM. The formation of the unique topography may be associated with phase separation, which is a known phenomenon in segmented PUs [80,216,217]. The distinct formation of micro-ridges resembles that of observed in block copolymers and waterborne polydimethylsiloxane polyurethane (PDMS-PU) and styrene-butadiene block copolymers induced by phase separation [217,236].

Similar to the topographical trend, all chemistry data reported seem to suggest a differential surface chemistry composition at lower curing concentrations (25-50 mM) compared to high concentration (500 mM). One could argue that the higher $–NH_2$ density and increased hydrophilicity at 25-50 mM compared with 100 EDA may be due to the presentation of nanofeatures at 25-50 mM, leading to increased surface roughness and presumably surface area [237]. However, the three-fold increase in %N content, surface urea enrichment and a broad bimodal MW distribution remains unknown at present.

It can be postulated that during the curing process, IPA acted to swell the PCU-PP by interactions via its polar –OH moiety and hydrophobic alkyl moiety, potentially increasing chain mobility [238,239]. The small-molecule nature of EDA allowed it to diffuse within the coating to initiate chemical reactions, hence the complete depletion of –NCO groups occurred within 1 min. Due to the bifunctional nature of the EDA molecule, the chemical reactions between EDA and NCO-terminated PCU-PPs may include three possible scenarios depicted in Figure 3.22: (i) chain termination, where one end of $–NH_2$ reacts with PCU-PP leaving the other part as a free primary $–NH_2$, which were detected by Orange II assay and XPS; (ii) crosslinking, or chain extension, where both ends of $–NH_2$ reactions with two chains of PCU-PP, which in turn contributes to the increase in M_n and possibly urea-enriched surface; and (iii) aminolysis, where one $–NH_2$ end of the EDA molecule reacts with the main chain of the polymer via nucleophilic cleavage reactions. Aminolysis has been commonly employed to generate surface $-NH_2$ groups on synthetic polymers [64,240,241], and it is typically employed with a high concentrations up to 40 vol% (~6 M).

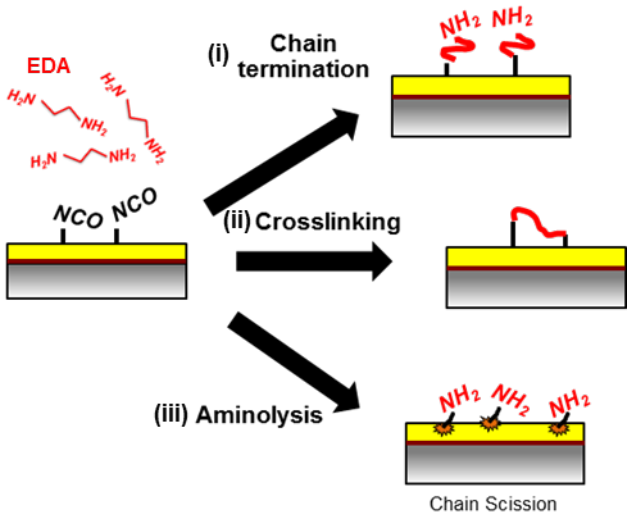

Figure 3.22. Schematic diagram showing possible EDA reaction scenarios with PCU-PP.

The concentration-dependent chemical and topographical properties may be attributed to different level of dominance of these chemical reactions at varying concentrations. It is likely that the chain termination and crosslinking reactions are more dominant at lower EDA concentration range (25-50 mM), leading to enrichment of urea linkages on the coating. Upon curing, urea groups could form hydrogen bonds with moieties such as carbonate or urethane groups, or even between themselves, leading to some extent of supramolecular phase separation yielding

surface enrichment of –NH moieties and the distinct micro-corrugated and nanoscale features [242]. These features remained stable upon rinsing and storage in air, which may be attributed to the strong hydrogen bonds and existence of long chains formed by crosslinking. At high curing concentrations (500 mM), it is likely that aminolysis became dominant over crosslinking, which could explain the higher $–NH_2$ density measured by Orange II assay despite a lower NH or nitrogen content in comparison to 25-100 mM EDA. The higher extent of aminolysis in 500 mM may also be related to the loss of smaller and larger chains leading to a lower PDI when compared with 50 mM EDA. The high concentration of the EDA molecules may have disrupted the hydrogen bonding between polymeric chains, which may explain the flat surface morphology.

The actual mechanism of formation of such unique combination of surface chemistry and topography warrants further investigation. The selection of IPA as a diluent may have contributed to the distinct properties in this EDA curing system. It is hypothesised that curing in a different solvent system may result in a varied surface morphology and possibly chemistry, although this warrants further study.

EDA curing reported here presents a useful processing method to simultaneously tailor the surface chemistry and topography, particularly at the lower concentration range (25-100 mM), which exhibits increasing surface nanofeatures as the concentration decrease. Furthermore, the urea enriched EDA cured coatings could potentially be more superior in biostability owing to its higher MW, as well as hydrogen bond interactions between urea [218]. In addition, such surface urea groups could also be utilised for further immobilisation or delivery of biomolecules or drugs via hydrogen bond interactions with urea moieties [242].

3.4.2 PPA curing

PPA curing relies on the rapid NH_2-NCO to allow presentation of surface -C≡C. Unlike EDA curing, chain extension reactions are not expected to occur due to the specific reaction between $–NH_2$ on PPA with –NCO. Chain termination reactions are expected, leading to a low MW as confirmed by GPC.

PPA cured coatings demonstrated an increased hydrophobicity, -C≡C functionalised coating with surface micro-scale rounded-island structures and

nanofibrous-like morphology. The morphology can also be an effect of phase-separation, which appears different from that of EDA, plausibly due to the more hydrophobic nature of -C≡C groups as opposed to the hydrophilic $–NH_2$ groups. The low MW nature of PPA cured coatings may also lead to increased chain mobility and increase the degree of phase separation. The defective porous morphology of the coating could be attributed potential leaching of shorter chains during the curing and rinsing steps. The diminishing appearance of micro-rounded-islands and decreased surface roughness at higher PPA concentration (500 mM) remains to be investigated, but may be attributed to high extent of aminolysis effects or differential chain arrangements under increased presence of PPA molecules.

The expected -C≡C surface chemistry was successfully generated on PPA cured coatings, and no major differences were detected between varying treatment concentration (25-500 mM). The only discrepancy is a lower θ° at 500 mM PPA compared to other PPA coatings, which may be attributed to the varied surface topography or higher extent of aminolysis, although XPS did not detect significant difference between 50 and 500 mM PPA. Although direct quantification -C≡C is not possible due to the lack of direct assays, the thiol-yne click reaction (TYC) quantified surface reactable -C≡C groups. Furthermore, there is evidence from Raman spectroscopy to support the presence of such groups.

The presence of -C≡C terminals can be employed for efficient thiol-yne or azide-alkyne click reactions., which have been increasingly prevalent for immobilisation of biomolecules on biomaterials [235,243–246]. In comparison to thiol-ene click chemistry, TYC reaction could allow two SH-terminated molecules to react to each -C≡C terminal [246,247], potentially enhancing the efficiency and density of biomolecules. Moreover, the morphologically defective surface coating could also be applied in other applications such as a degradable porous coating, although the toxicity would have to be studied further.

3.4.3 MPA curing

Another curing system was developed using MPA, which requires DBU as catalyst to initiate SH-NCO click reactions. Monitoring of the reaction kinetics showed slower curing rates of MPA compared to the other $–NH_2$ based curing precursors (i.e.

EDA and PPA). This is in contrast to what was described by Hersarling *et al.*, where SH-NCO click reactions are highly efficient and comparable to $–NH_2$-NCO reactions [227]. However, it is also possible that the untreated –NCO may be attributed to steric hindrance due to the larger nature of MPA (106.14 $gmol^{-1}$) and DBU (152.24 $gmol^{-1}$) molecules compared with EDA (60.22 $gmol^{-1}$) and PPA (55.08 $gmol^{-1}$).

MPA cured coatings showed a relatively proportional trend of increasing surface sub-micron features, hydrophilicity and –COOH density with increasing MPA concentrations, indicating increasing modifications with increased curing concentrations. The surface sub-micron features likely due to phase separation upon functionalisation with thiourethane and –COOH groups. The presence of detectable C-S linkages by ATR-FTIR and XPS further confirms the successful chemical curing reactions. GPC data for 100 mM MPA revealed a slightly higher M_n compared to PPA, which could be due to chain extension of residual -NCO with moisture or -COOH after curing.

3.4.4 Potential of the chemical-curing procedure

The presentation of varying degrees of surface micro- and nanoscale topography along with surface functional groups using the PCU-PP chemical curing approach represents an ideal candidate towards new biomaterial platforms. The combination of varying degrees of surface chemistry and topography will allow interesting studies for probing cell-material interactions. The chemical functionality generated via this curing procedure also permit further modification with peptides, antibodies and growth factors) to augment bioactive properties that could lead to enhanced wound healing or tissue repair for a range of medical devices [66]. Furthermore, this highly versatile chemical-curing approach can be employed with other small molecular precursors or combinations other than EDA, PPA and MPA on other types of PU-PPs, such as PCL-PP, to offer tailorable multifunctional platforms for a range of biomedical applications.

In addition, the chemical curing procedure can be performed simply in ambient laboratory conditions without the need for specialised equipment. With care taken to minimise influence of ambient moisture by using anhydrous and freshly prepared solutions (up to 4-6 hours), the coatings properties are highly reproducible in this study. The procedure also permits consistent modification of the coatings with

complex geometry. Its transferability on to BMS stent was successfully demonstrated using PPA and EDA systems based on FE-SEM morphological images. Stents possess complex 3D geometry, and are typically a challenge to achieve uniformity for many surface modification technologies such as plasma treatment or lithography based patterning approaches.

However, it is acknowledged that one limitation of the chemical curing approach is the lack of control on the types of topographical features produced. Further understanding the mechanism of formation of the features may provide insights to tailor such properties. The mechanism of the phase separation during curing reactions at the molecular level remains unknown at present. Further investigations in to the phase separation effects can be studied by differential scanning calorimetry (DSC) or in-depth phase imaging using AFM. Moreover, while chemical and topographical properties were extensively characterised as reported, the mechanical properties of the coatings remain to be fully elucidated. It is likely that the mechanical properties of the coatings would be enhanced as a result of chain extension or crosslinking as shown in their increase in MW, particularly for EDA and MPA coatings. In addition, it will be interesting to characterise the surface mechanical properties through techniques such as nanoidentation, as substrate stiffness are known to influence cell behaviour. It can be hypothesised that the varied phase separation behaviour on each chemical curing systems can lead to different stiffness properties. For example, the hard segment enrichment on 25-50 mM EDA cured coatings may lead to variation in strength and stiffness.

3.5 Conclusion

In this study, a facile *in situ* chemical-curing approach of PCU-PP, which allows simultaneous modification of the surface chemistry and micro-/nanotopography have been developed. Three different small molecular precursors was explored as curing agent: (i) rapid, catalyst-free EDA-curing, which leads to highly crosslinked coatings with surface enrichment of $-NH_2$ and urea groups, as well as, micro-corrugated and nano-features at lower concentrations; (ii) rapid, catalyst-free PPA curing, which leads to low MW, -C≡C functionalised coatings with micro-rounded islands and porous nanofibrous structures; and (iii) base-catalysed MPA 'click' curing, which leads to intermediate MW coatings with surface -COOH groups alongside sub-micron ridges. It is envisaged that such highly versatile and low-cost platform technology can steer promising avenues in biomaterials and regenerative medicine to modulate cell-material interactions.

Chapter 4

Endothelial Cell Response to Moisture and Chemical Cured Pre-polymer Coatings

4.1 Introduction

In a healthy native blood vessel, a layer of endothelial cells (ECs) lines the inner lumen interfacing with blood, and is vital in maintaining vessel patency via a range of vasoactive function (as described in section 1.3.1). Blood–contacting biomaterials suffer from impaired endothelialisation, hence leading to a range of complications including thrombosis and neointimal hyperplasia (NIH). A material surface with pro-endothelialisation capability is an important attribute to biologically control events at the vascular interface. Hence it is important to evaluate EC responses on blood-contacting biomaterials. Cell sense and respond to the surface of biomaterials based on recognition of adsorbed proteins, which rapidly adsorbs on the material surface within seconds of contacting the blood. The physicochemical properties of the material, such as chemistry (charge, wettability and energy) and topography influence protein adsorption, hence leading to differential cell response [248–250] . For adherent cells such as ECs, adhesion to the substrate surface is the initial step which influences cell fate such as proliferation and differentiation. Cell adhesion is mediated by recognition of cellular trans-membrane receptors known as integrin towards specific ligands (e.g. fibronectin, laminin and vitronectin), leading to the formation of focal adhesions (FAs) [248,249]. FA leads to integrin-mediated signal transduction of physical and chemical cues of the extracellular environment to intracellular biochemical signals. This regulates cellular processes, such as cytoskeletal reorganisation, cell spreading and migration, and determines cell behaviour including function, proliferation and differentiation [251].

Surface chemistry and topography have been widely exploited to promote tissue-implant integration by manipulation of surface cues to influence the cellular

responses [59,225,226,252,253]. For example, De *et al.* showed improved EC adhesion and density on helium plasma treated polyurethane (PU), which displayed increased roughness and hydrophilicity [254]. ECs also respond to nanotopographical features including nanoislands and nanotubes. Dalby *et al.* demonstrated on EC spreading behaviour on polymer surfaces with nanoislands of 13 nm in size [255]. Nanotubular Nitinol coatings was also reported to enhance EC spreading and migration but reduce smooth muscle cell (SMC) migration, extracellular matrix (ECM) production and proliferation [59]. Nanotopography alone, decoupled from chemistry effects via multiple casting and recasting steps, was reported to be able to enhance EC densities [253]. While it is clear that suitable chemistry and topographies can influence cell fate, the precise mechanism on how cell respond to the interplay between chemistry and topography remain poorly understood at present.

The previous chapters (Chapter 2-3) have described the production of moisture cured (PCU-PP-AIR and PCU-PP-H_2O) and chemical cured (EDA, PPA and MPA) PCU-PP coatings with a range of surface chemistry, as well as, simultaneous formation of distinctive micro- and nanoscale topography. The aim of this chapter is to study the interaction of human umbilical vein endothelial cells (HUVEC) on these moisture and chemical cured PCU-PP coatings.

4.2 Materials and methods

4.2.1 Preparation of moisture and chemical cured coatings

Moisture cured PCU-PP coatings on SS316L coupons in air and water (PCU-PP-AIR and PCU-PP-H_2O) were prepared as described in section 2.2.3. Chemical cured PCU-PP coatings on SS316L coupons with EDA, PPA and MPA were fabricated as described in section 3.2.2. Table 4.1 summarises the samples prepared for evaluation of cell response.

Table 4.1. Summary of samples for *in vitro* evaluation

Experiment	Samples		Description
Moisture cured (Section 4.3.1)	**PCU-PP-AIR**		Cured in air
	PCU-PP-H_2O		Cured in dH_2O
Chemical cured (Section 4.3.2)	**Controls**	**Untreated**	Cured in air (PCU-PP-AIR)
		0 mM	100% IPA (15 min)
	EDA	**25 mM**	-NH_2 functionalised, micro-ridges and nanofeatures (25-100 mM) which diminished to flat morphology at 500 mM
		50 mM	
		100 mM	
		500 mM	
	PPA	**25 mM**	Hydrophobic, -C≡C functionalised, irregular morphology with some nanofibrous features
		50 mM	
		100 mM	
		500 mM	
	MPA	**25 mM**	Increasingly -COOH functionalised, submicron ridges at higher concentration
		100 mM	
		500 mM	

4.2.2 Cell culture and maintenance

Human umbilical vein endothelial cells (HUVECs, pooled from multiple donors) were purchased from Thermofisher Scientific, UK, and were cultured in humidified 37 ºC and 5% CO_2 incubator using M200 media supplemented with low-serum growth factor kit (Thermofisher Scientific, UK) and 1% penicillin-streptomycin. The final concentrations of additional supplements in the growth media were 2% (v/v) foetal bovine serum (FBS), 1 μg/mL hydrocortisone, 10 μg/mL heparin, 10 ng/mL human epidermal growth factor, and 3 ng/mL basic fibroblast growth factor (bFGF). Growth medium was changed completely every other day. Cells were sub-cultured upon attaining 70-90% confluency. Trypsinisation was performed with 0.125% Trypsin/EDTA following rinsing with warm phosphate-buffered saline (PBS). Growth medium with 10% (v/v) FBS was added to neutralise trypsin. Trypsinised cell suspension were centrifuged at 1200 rpm for 5 min to obtain a cell pellet, which

was then resuspended in growth media for use, or freezing media for cryopreservation.

Cryopreservation of cells was performed at earlier passages (P1-4) at $>1\times10^6$ cells/mL in freezing media suggested by the manufacturer, which consists of 70% conditioned growth media, 20% FBS, and 10% dimethylsulfoxide (DMSO). Cells in cryovials were quickly transferred to Mr Frosty™ Freezing Container (Thermofisher Scientific, UK) to be cooled at -1ºC/min overnight. Cryovials were then stored in liquid nitrogen at -196ºC for longer-term (>1 month) storage. Thawing of cells was performed by immersion of cryovial in 37 ºC water bath, followed by quick transfer into new T25 or T75 flasks containing fresh growth media and placed in cell incubator. Media was changed 18 h later to remove residual DMSO.

4.2.3 Preparation of samples and cell seeding

In order to minimise chances of infection, samples were immersed in 70% (v/v) ethanol in sterile 6-well plates for 20 min, followed by copious rinsing of at least 4 times with PBS. Samples were then transferred to 24 well plates for cell experiments. For experiments, HUVECs were trypsinised and seeded on to each sample at a density of 1.5×10^4 cells/cm^2 in 1 mL media, and were maintained over 7 days. Tissue culture polystyrene (TCP) served as positive control for each experiment. Samples were transferred into new wells using autoclaved tweezers on day 1 and also before quantitative cell-based assays. HUVEC of passages between P4-7 were used.

4.2.4 Quantitative cell-based assays

Quantitative cell culture experiments were repeated independently at least 3 times (n=3), each with triplicated technical repeats for each condition.

4.2.4.1 Cell metabolic activity using AlamarBlue® assay

HUVEC metabolic activity was quantified using AlamarBlue® assay (AbD Serotec, UK) at Day 1, 4 and 7, following manufacturer's instructions. Each samples was incubated in 1 mL of 10% AlamarBlue® reagent in growth media for 4 h. 100 µL of the supernatant of each sample were transferred to a black 96 well plate, in duplicates. The fluorescence of the supernatant was measured at excitation and emission wavelengths of 530 nm and 620 nm respectively using Fluoroskan Ascent

FL (Thermo Labsystems, UK) fluorescent plate reader. The final results were obtained by subtraction of background of each set of experiment, and normalisation to sample area of 1 cm^2.

4.2.4.2 Cell proliferation using total DNA quantification

HUVEC proliferation was measured using via total DNA quantification at Day 1, 4 and 7 following AlamarBlue® assay. Each individual samples were gently rinsed with 37 ºC PBS and trypsinised, followed by transferring to 1.5 mL Eppendorf tubes for centrifugation at 350 r.c.f. for 8 min. To lyse the cells, each tube were resuspended and vortexed in 100 µL molecular grade water, followed by 4 × freeze-thaw cycles at -70 ºC and 37 ºC. Total DNA content in the cell lysate were measured using Fluorescence Hoechst DNA Quantitation Kit, according to manufacturer's instructions. The fluorescent dye Hoechst 33258 was diluted with assay buffer to a concentration of 1 µg/mL. 100 µL of cell lysate were mixed with equal volume of the fluorescent dye, and transferred to a new black 96 well plate. Fluorescence of the DNA content was measured at excitation and emission wavelengths of 360 and 460 nm respectively using a TECAN Infinite 200 Pro microplate reader. A standard curve was created using known concentrations of calf thymus DNA (Appendix B.3).

4.2.5 Qualitative cell imaging

4.2.5.1 Fixation of HUVECs

For immunofluorescence imaging, cells on samples were gently rinsed with 37 ºC PBS, and fixed with 10% Formalin (CellPath, UK) at room temperature (RT) for 30 min, and storage in 4 ºC in PBS. For FE-SEM imaging, cells were rinsed with 37 ºC PBS, followed by fixation with 2.5% (v/v) glutaraldehyde grade I (EM grade) diluted in PBS at RT for 15 min. Samples were then stored 4 ºC in PBS prior to dehydration.

4.2.5.2 Fluorescence staining of HUVECs: F-actin, DAPI, Vinculin

Cell adhesion, morphology and cytoskeletal arrangement were assessed via cytoskeletal filamentous actin (F-actin) staining and nuclear staining. Fixed samples were blocked with 1 w/v% bovine serum albumin (BSA) in 0.1% Tween 20-PBS (PBST) for 30 min at RT, followed by incubation for 30 min at RT with AlexaFluor-488®-Phalloidin (Thermofisher Scientific, UK) diluted at 1:200 in PBS. Nuclear staining was performed by incubation of samples in 300 nM *4',6*-Diamidino-2-

Phenylindole (DAPI) (Thermofisher Scientific, UK) for 10 min at RT. Samples were rinsed thrice with PBST after each incubation step and stored in PBS before imaging.

Vinculin is a component of the focal adhesion complex, which are directly connected to the cytoskeleton [251,256]. Immunofluorescence staining of vinculin was also performed on selected samples to probe the distribution of cellular focal adhesions on the coatings. Samples were permeabilised with 0.1% Triton X-100 for 10 min at RT prior to blocking with 1 w/v% BSA in PBST. Rabbit anti-vinculin antibody (ab129002, Abcam, UK) at dilution factor of 1:150 in 1%BSA/PBST were incubated on each sample for 1 h at RT, following by 3× rinses with PBST. Goat anti-rabbit Alexa Fluor® 594 (ab150080, Abcam, UK) was used as secondary antibody at 1:400 dilution in 1%BSA/PBST and incubated for 1 h at RT. Subsequently, samples were extensively rinsed with PBST for up to 5×10-min rinses. To aid visualisation of vinculin localisation with respect F-actin, samples were also stained with AlexaFluor-488®-Phalloidin and DAPI as described above.

Stained samples were imaged using EVOS Fluorescent Microscope (Life Technologies, UK) with GFP (Ex/Em: 470/510 nm), Invitrogen Texas Red (Ex/Em: 585/624 nm) and DAPI (Ex/Em: 357/447 nm) light cubes, which consists of LED light and filter.

4.2.5.3 FE-SEM of HUVECs

Glutaraldehyde-fixed samples were dehydrated in a series of increasing concentration of molecular grade ethanol (ETOH) in distilled water. Each sample was immersed in 1 mL of the following ETOH concentrations for at least 15 min each: 0%, 30%, 50%, 70%, 90%, 100% and 100%. Samples were then air-dried in the fume hood overnight and mounted on to SEM stubs for FE-SEM imaging. Samples were coated with 1 nm platinum using a Cressington Sputter Coater and imaged using Zeiss SIGMA FE-SEM at an accelerating voltage of 3-5 kV.

4.2.6 Statistical analysis

Data were reported as mean ± standard error of mean (SEM), n=3, unless otherwise stated. Statistical analysis was conducted using Prism GraphPad software (version 6.0). *In vitro* assays were statistically tested using two-way ANOVA with Tukey's post-hoc test. *P* values of $p<0.05$ were considered to be statistically significant.

4.3 Results

4.3.1 HUVEC response to moisture-cured coatings

PCU-PP-AIR and PCU-PP-H_2O as described in Chapter 2 were prepared and seeded with HUVECs. Total DNA content, which correlates to cell number, as well as metabolic activity measured by AlamarBlue® assay, were quantified at day 1, 4 and 7 and is presented in Figure 4.1A-B. TCP was used as the positive control, which demonstrated enhancement at each time point on both total DNA content and metabolic activity data. However, both DNA amount and metabolic activity of PCU-PP-AIR and PCU-PP-H_2O remained notably low from day 1 to 7, indicating low level of cell density and proliferation in culture.

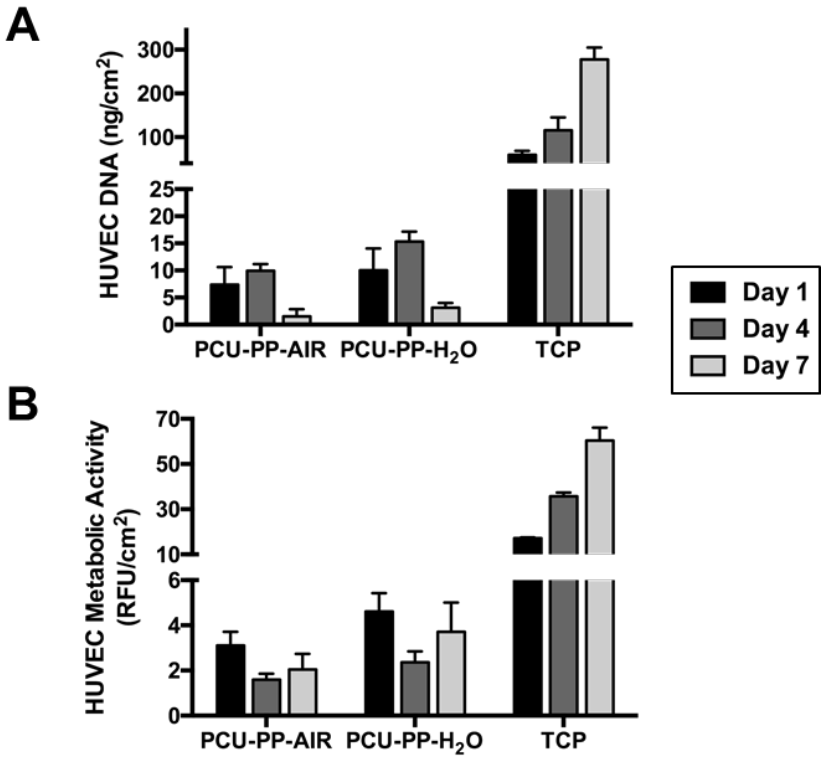

Figure 4.1. (A) HUVEC proliferation using total DNA quantification and (B) metabolic activity data of HUVECs on moisture cured coatings (PCU-PP-AIR and PCU-PP-H_2O) and TCP (n=3).

Cells were stained with cytoskeletal F-actin stain to permit visualisation of cell morphology, and the images are displayed in Figure 4.2. While cells displayed spread cobblestone morphology typical of HUVECs on TCP on day 1, cells exhibited rounded morphology on both PCU-PP-AIR and PCU-PP-H_2O. On day 7, there were barely any cells remaining on both coatings, although there were more

spreaded cells detected on PCU-PP-H_2O. On the other hand, TCP displayed a confluent monolayer of HUVECs.

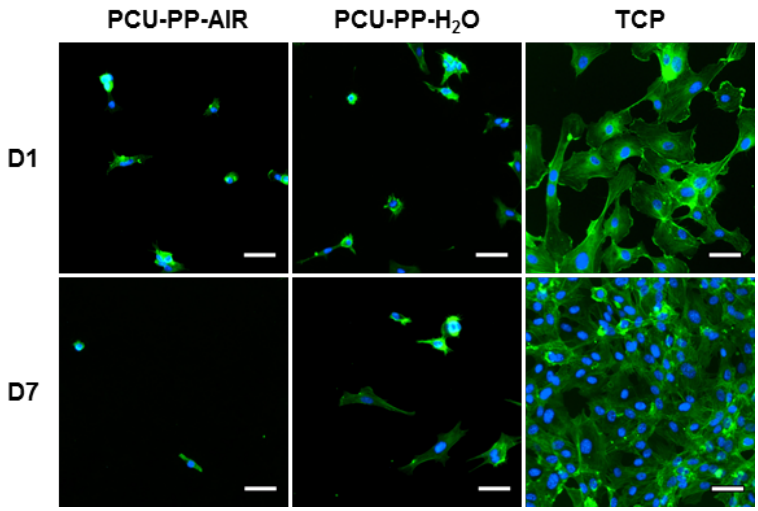

Figure 4.2. Fluorescent images of HUVECs on moisture cured coatings (PCU-PP-AIR and PCU-PP-H_2O) and TCP. Scale bar = 50 µm. Green: F-actin, blue: nuclei.

The results altogether consistently indicate that moisture cured coatings (PCU-PP-AIR and PCU-PP-H_2O) were unable to support HUVEC adhesion and proliferation. For evaluation of chemical curing coatings in the following sections, PCU-PP-AIR was used as an untreated control substrate for cell culture.

4.3.2 HUVEC response to chemical-cured coatings

As described in Chapter 3, chemical cured coatings including (i) EDA; (ii) PPA and (iii) MPA possess distinct micro- and nanoscale surface topography, as well as, surface (i) –NH_2, (ii) -C≡C and (iii) –COOH respectively. This section aims to report HUVEC responses on these coatings.

4.3.2.1 Cell proliferation and metabolic activity on chemical cured coatings

The results of total DNA quantification and metabolic activity are presented in Figure 4.3. Both datasets appeared to corroborate with each other and showed similar trends. 0mM (100% IPA) revealed similarly low total DNA content and metabolic activity compared to untreated controls. Total DNA content and metabolic activity were significantly enhanced on 50-500mM compared to untreated controls on day 4 and 7. In particular, 50-100 mM EDA with nanofeatures resulted in higher total DNA content and activity comparable to TCP up to day 7 (p>0.05), indicating

optimal cell proliferation and growth. However, 25mM EDA showed minimal increase in DNA content and metabolic activity over 7 days.

On the other hand, PPA cured coatings of all concentrations (25-500 mM) showed low levels of DNA content and metabolic activity comparable to the untreated and 0 mM controls (p>0.05) on all experimental time points.

As for MPA cured coatings, both total DNA content and metabolic activity increased over 7 days on higher MPA curing concentration (100-500 mM). Total DNA content showed significant enhancement compared to untreated control at day 7, while metabolic activity showed significance from day 4-7 (p<0.05). In fact, metabolic activity of 100-500 mM MPA was comparable to that of TCP. In contrast, low concentration 25 mM MPA showed minimal increase in DNA content and metabolic activity, and are similar to untreated controls.

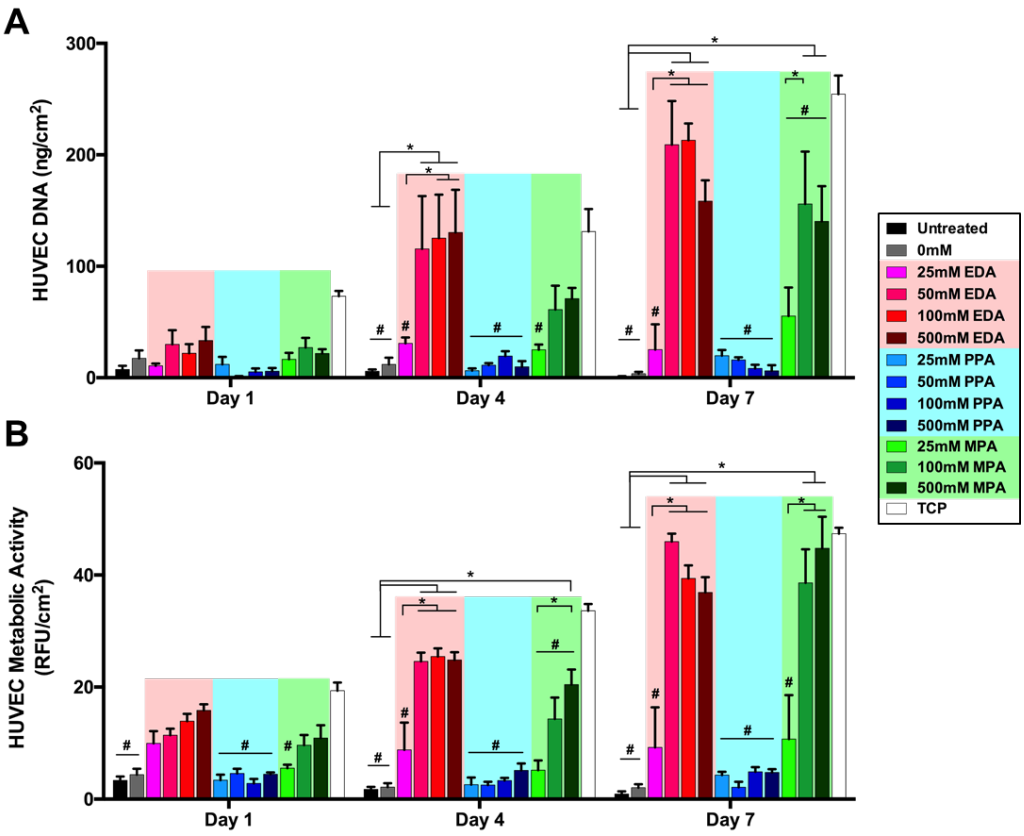

Figure 4.3. (A) Total DNA content and (B) metabolic activity of HUVECs measured on EDA, PPA and MPA cured coatings at varying curing concentrations, along with untreated and positive TCP controls (n=3 independent experiments). EDA cured coatings were highlighted in red, PPA in blue and MPA in green. Two-way ANOVA were performed for each coating group (EDA, PPA and MPA), and Tukey's post-hoc tests revealed significant differences between conditions at each time point. *=p<0.05. #=p<0.05 compared to TCP.

4.3.2.2 HUVEC morphology on chemical cured coatings

Figure 4.4 demonstrates F-actin stained cells seeded on the different cured coatings on day 1 and 7. On day 1, cells displayed a rounded cell morphology, and non-spread phenotype on untreated and 0mM controls. On 25 mM EDA, cells appear slightly more spreaded but also elongated with irregular membrane protrusions. Above 50 mM EDA, cells showed typical spread morphology with clear presence of F-actin stress fibres similar to TCP, indicative of optimal cell adhesion. After 7 days, cell coverage reached confluence on the coatings where cells displayed preferential adhesion, whereas cell distribution appeared patchy on 25 mM EDA.

On all PPA-cured coatings (25-500 mM), HUVECs exhibited a rounded and non-spread morphology similar to untreated controls on day 1. Cells did not show signs of proliferation up to day 7, where only few poorly adhered cells were detected.

As for MPA-cured coatings, HUVECs preferentially adhered with spread morphology with well-defined actin fibres on 100-500 mM MPA on day 1, but only partially spread on 25 mM MPA. After 7 days, cell coverage increased at higher MPA concentration. Cells remained on 25 mM MPA appeared relatively spreaded compared to untreated control. Altogether, the findings here for all chemical cured coatings were consistent with DNA content and metabolic activity data reported previously.

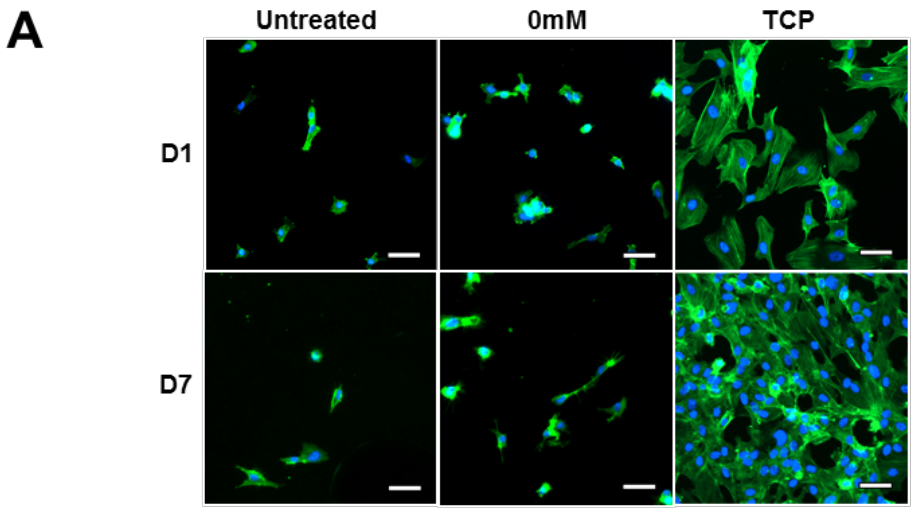

Figure 4.4. (Continued on next page) Fluorescent micrographs of HUVECs on (A) controls, (B) EDA, (C) PPA and (D) MPA cured coatings of varying curing concentrations at day 1 and 7. Scale bar = 50 µm. Green: F-actin, blue: nuclei.

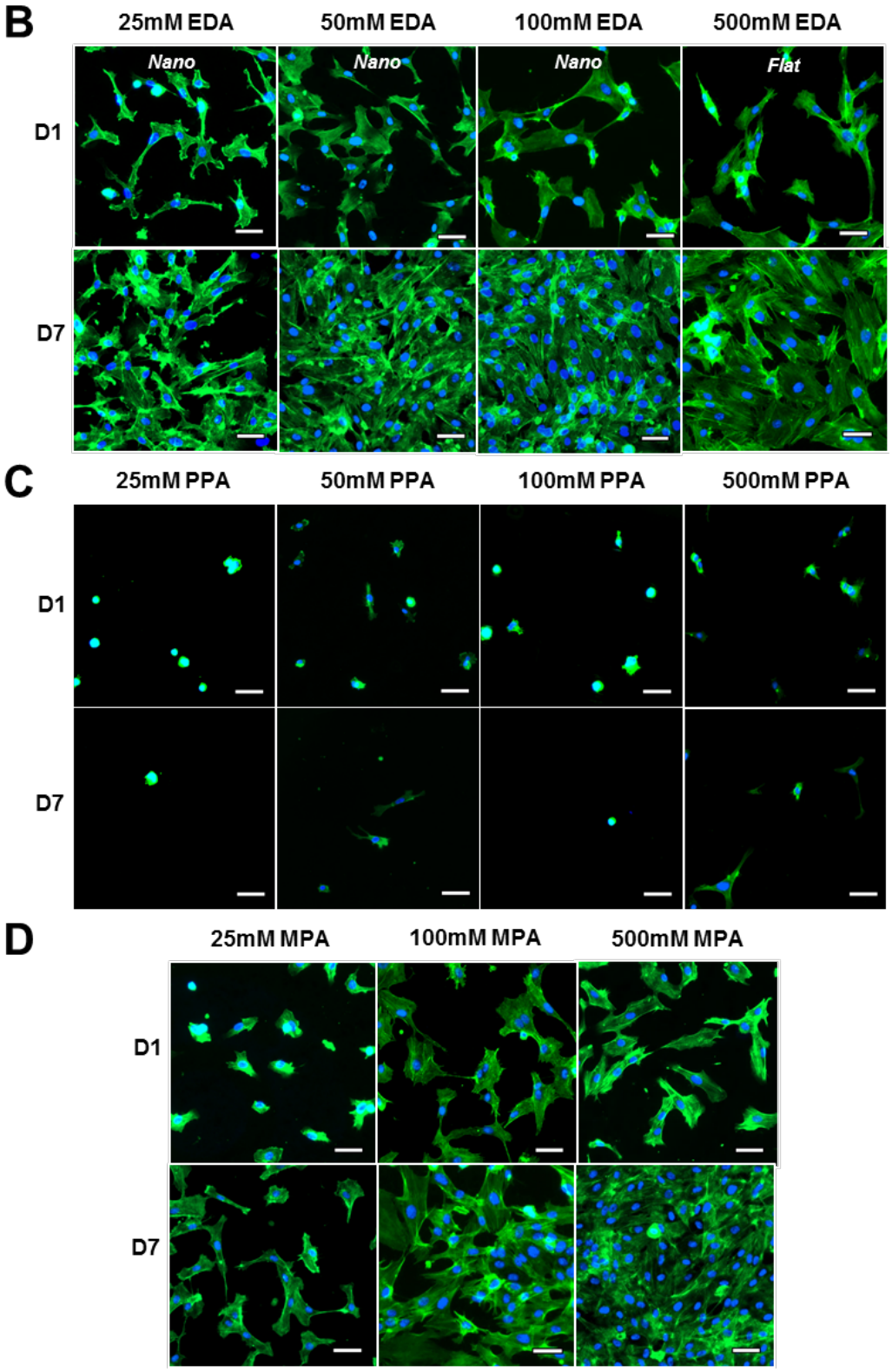

Figure 4.4. (Continued)

4.3.2.3 HUVEC focal adhesion on chemical cured coatings

Immunostaining with anti-vinculin antibodies alongside F-actin cytoskeletal staining was employed to probe distribution of focal adhesions (FA). The images for the controls and EDA cured coatings are shown in Figure 4.5. On all coatings, a background staining of vinculin is apparent in the cytoplasmic area around the nucleus, which is indicative of s soluble pool of inactive vinculin [257,258]. On untreated control, non-spreaded cells with highly condensed vinculin stain and F-actin without distinguishable localisation were apparent. On Thermanox^{TM} cover slips (positive control), clear, elongated dash-like FA sites of vinculin could be observed concentrated around the cell periphery, and appeared highly localised with well-defined F-actin fibres.

On EDA-cured coatings, 25 mM EDA displayed sparse, small dot vinculin-containing FA seemingly concentrated more towards the ends of membrane protrusions, alongside F-actin stress fibres. On the other hand, 50 and 100 mM EDA demonstrated densely distributed vinculin FA plagues all over the cells, with plagues at the peripheral edges of cells adopting elongated dash-like conformation. Localisations of vinculin with F-actin stress fibres were strong. On 500 mM EDA, while dash-like vinculin FA plagues were apparent, the distribution within the cell periphery appears to be patchy.

Cells on 50 mM PPA coatings appear non-spread with condensed vinculin distribution, similar to untreated control.

For MPA-cured coatings, cell spreading was slightly improved on 25 mM MPA compared to untreated controls, with minimal dot-like vinculin-containing FA sites and defined F-actin fibres. More defined F-actin fibres and densely distributed, longer dash-like vinculin plagues were apparent on 100 – 500 mM MPA, with a strong localisation between both.

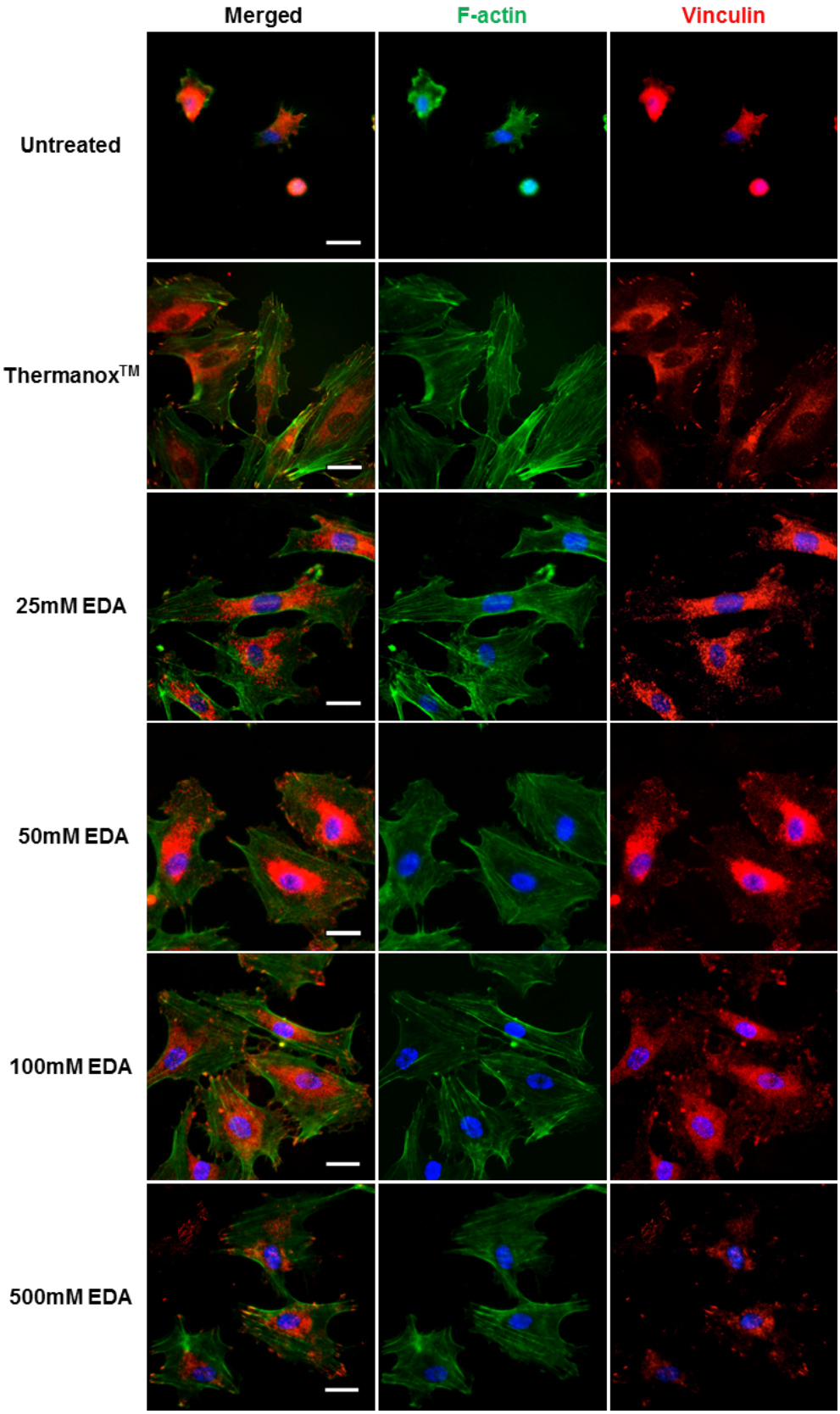

Figure 4.5. (Continued on next page) Representative fluorescent images of HUVECs stained for focal adhesion complexes and cytoskeletal organisation on day 1 on untreated control, Thermanox™ cover slips (positive control) and EDA, PPA and MPA cured coatings. Scale bar = 20 µm. Green: F-actin, red: vinculin, blue: nuclei.

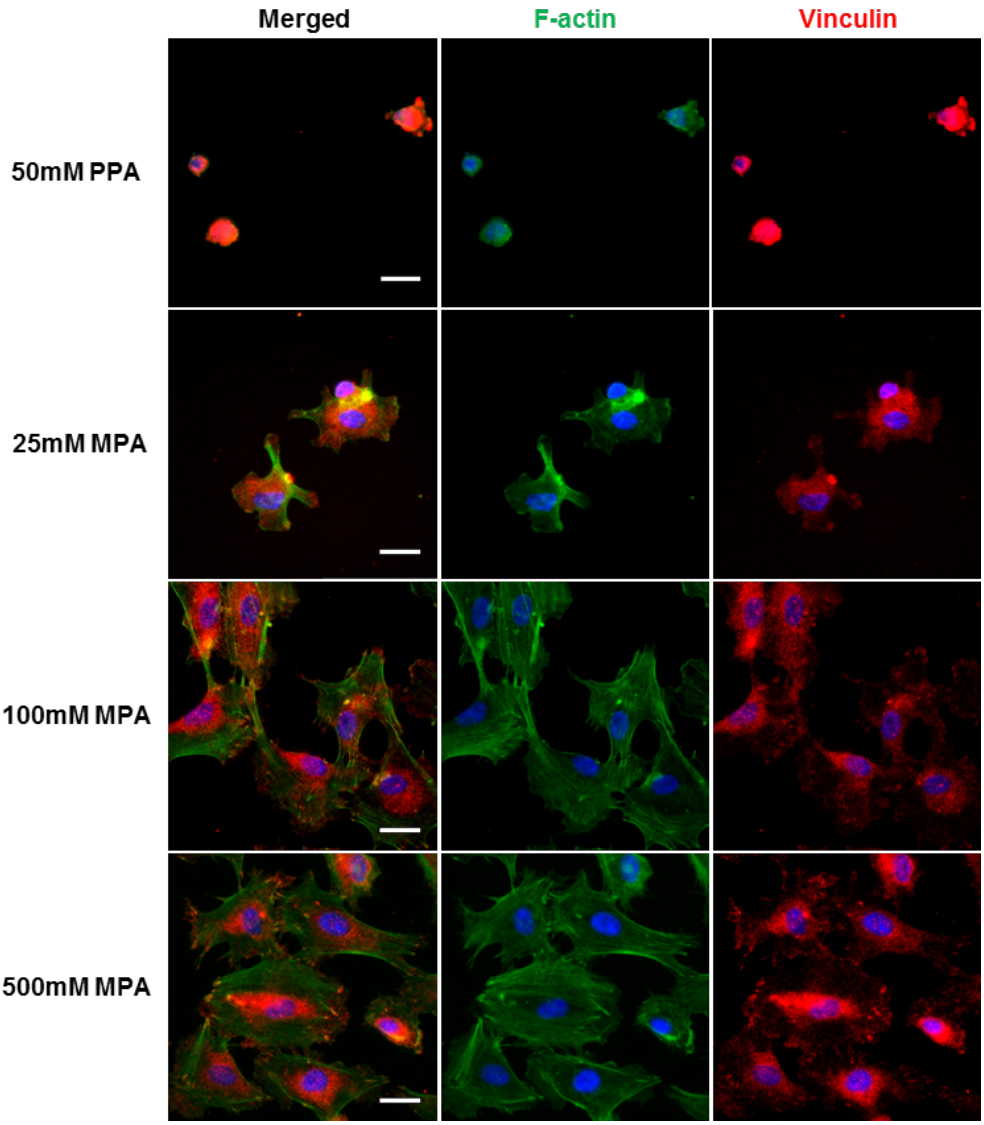

Figure 4.5. (Continued)

4.3.2.4 FE-SEM of HUVECs on chemical cured coatings

FE-SEM was utilised to further access HUVEC morphological and spreading behaviour in relation to coating surfaces, and the images are illustrated in Figure 4.6. Cells on untreated control demonstrated a rounded morphology, consistent to earlier observation. Lamellipodia and filopodia protrusions were apparent. On 25 mM EDA, HUVECs seemed to spread but adopted high irregular stretched cell shape, with notable protrusions of large lamellipodia and finer filopodia, It is noted that whole cell body appeared to conform to the surface micro-ridges. On 50-500 mM EDA-cured coatings, cells adopted a highly spread morphology. Cell body spreaded over of the surface micro-ridges on 50-100 mM EDA, while some lamellipodial protrusion seem to be able to protrude across micro-ridges. Cell-cell contact were achieved via lamellipodial or filopodial protrusions. In particular, on 50 mM EDA, cells appeared relatively flat and highly spreaded on the coating surface in comparison to the other EDA coatings.

On PPA cured coatings (50 mM), cells appear non-spread and rounded similar to untreated control, and results are in agreement with other earlier observations.

On MPA cured coatings, at 25 mM MPA, rounded cell morphology with many projections of filopodia appearing to sense the surfaces were apparent. Cell spreading were greatly improved at 100-500 mM MPA, particularly on 500 mM MPA where cells appear more spreaded with noticeably lower degree of filopodial protrusions. In general, cell spreading improved as MPA curing concentration increases.

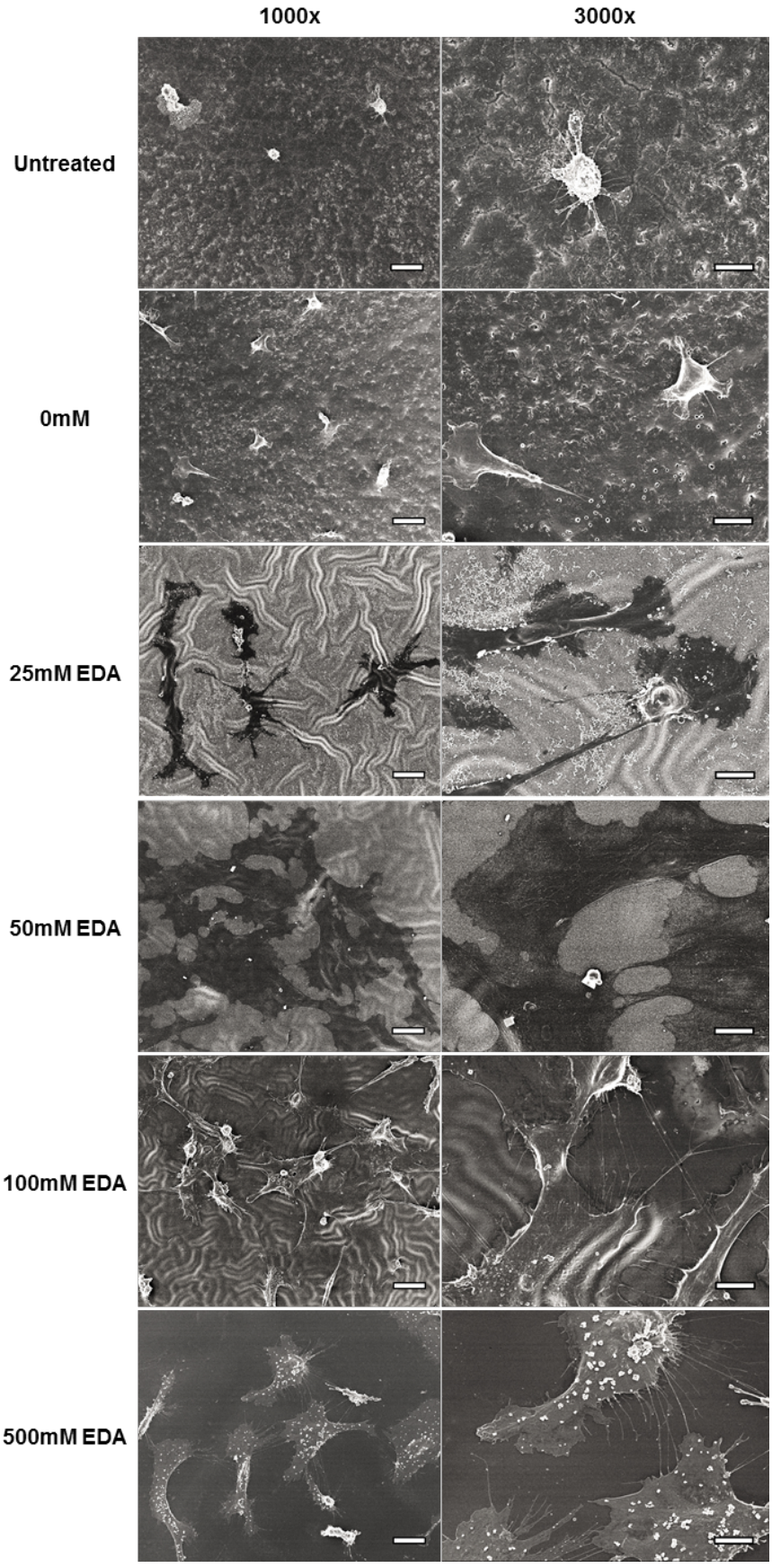

Figure 4.6. (Continued on next page) Representative FE-SEM images illustrating HUVEC on untreated and EDA, PPA and MPA cured coatings at day 1. Magnifications=1000× (scale bar = 25 μm) and 3000× (scale bar = 10 μm).

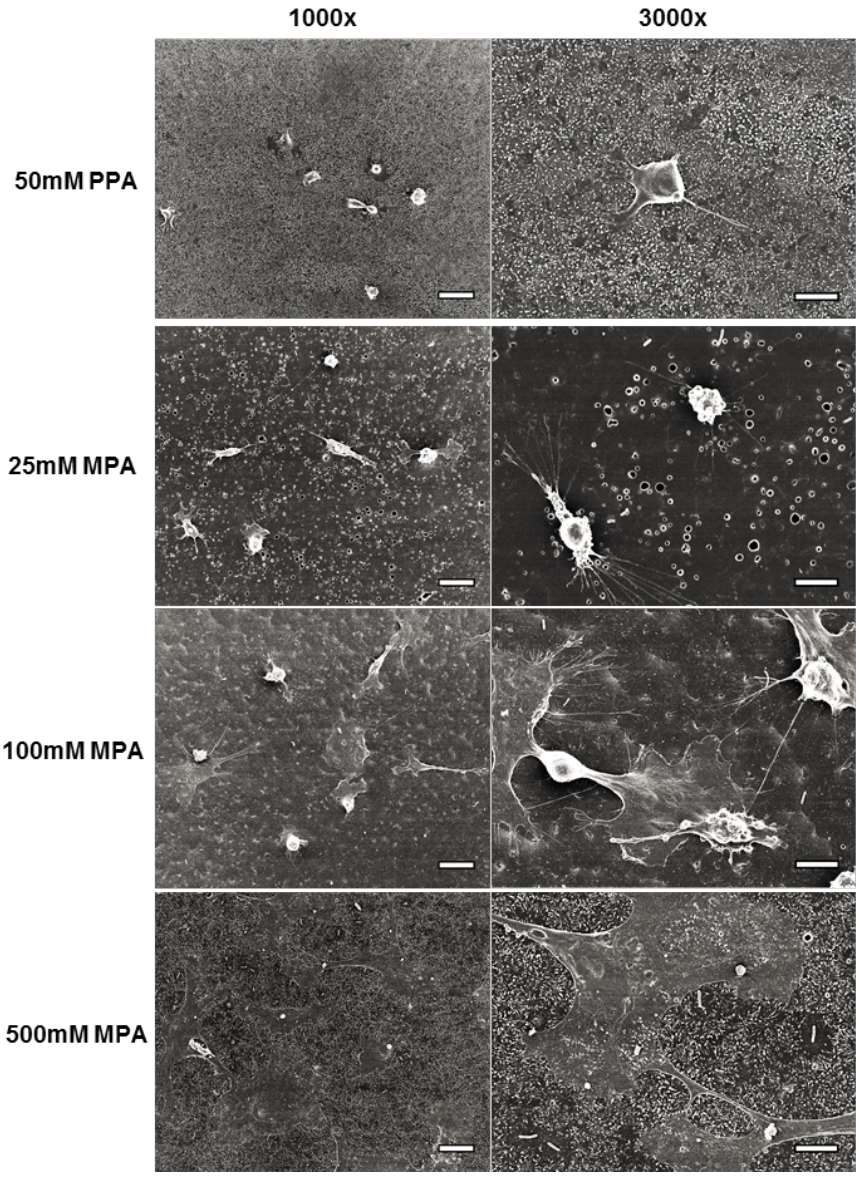

Figure 4.6. (Continued)

4.4 Discussion

4.4.1 Moisture cured coating

Moisture cured coatings (both PCU-PP-AIR and PCU-PP-H_2O) did not support initial HUVEC adhesion and subsequent proliferation. The cell repellent nature of the moisture cure coatings (both PCU-PP-AIR and PCU-PP-H_2O) may be attributed to their relative hydrophobicity, as well as, potentially lack of biomimetic surface functional groups. These may have led to sub-optimal adsorption of cell adhesive proteins such as fibronectin or fibrinogen [192]. Proteins tend to adsorb strongly on hydrophobic surfaces, but could exhibit an unfavourable change in conformation, leading to hindrance of active sites for cell adhesion [259]. The phenomenon may be further exacerbated by the use of low serum growth media conditions (2% FBS) used here, which presents lower composition of cell adhesive serum proteins. Another possible scenario is that albumin, which is abundant in cell culture media, may have adsorbed strongly on to hydrophobic surfaces leading to poor displacement by cell adhesive proteins [260], hence hampering optimal cell adhesion and subsequent fate.

PCU-PP-H_2O may have shown evidence that cell spreading was partially improved. This may be attributed to the slightly increased hydrophilicity of the coating (described in section 2.3.2), which could have contributed to slight improvements in exposed active sites of adsorbed adhesive proteins, although further confirmation is required. Nonetheless, further cell growth was not supported on these coatings. The results obtained with moisture-cured PCU-PP are in agreement with existing PCU studies, where surface modification strategies were widely adopted to enhance cell fate [94,261,262].

4.4.2 Chemical cured coating

Chemical curing of PCU-PP coatings produced a range surface chemistries and topographies, which led to varied HUVEC responses on each coating platform. Along with total DNA content and metabolic activity, cell adhesion was characterised in-depth with F-actin/vinculin staining and FE-SEM imaging.

4.4.2.1 Effect of surface chemistry

The first noticeable effects were in the presentation of favourable surface chemistry on HUVEC fate. PPA-cured coatings with hydrophobic -C≡C chemistry did not support cell adhesion and proliferation. EDA cured coatings with surface $–NH_2$ chemistry displayed enhancement in cell adhesion, and in most cases proliferation and growth. MPA-cured coatings demonstrated a more intuitive trend of improved cell fate with increased click modifications, suggesting a strong correlation between –COOH chemistry and cell fate. Improved cell adhesion was characterised by cell spreading, as well as, the presence of an elongated and mature FA sites. Mature FAs are associated to improved adhesion through mechanotransduction, which in turn regulates cell-substrate adhesion strength and also contributing to cell proliferation and growth [251]. The findings here could be attributed to the surface $-NH_2$ and -COOH, urea or thio-urethane surface chemistry, which could mimic nature's chemistry, such as peptide bonds, hence a preferential interaction with adsorbed proteins to favour specific cell response(s) [94,263]. Numerous studies have incorporated surface functional groups by means such as plasma treatment [94,224,264] or chemical treatment [64,65] to enhance integration of cells or tissues to biomaterials. These findings suggest the importance of surface chemistry in controlling cell fate.

4.4.2.2 Effect of surface nanotopography

Contributions from surface topography appear to be preceded by surface chemistry. The enhancement of HUVEC adhesion and proliferation on both EDA and MPA-cured coatings can be attributed to a synergistic effect of a favourable chemistry ($-NH_2$ or -COOH) and topography. However, in MPA cured coatings, decoupling the contributions between the submicron ridges and surface chemistry is not possible, as both features increases with increasing curing concentration and occur simultaneously.

Results from the EDA-cured coating system allow some extent of elucidation of the interplay between the combinatorial chemistry and nanotopography in influencing cellular responses. No strong correlation between cell fate and the micro-ridges could be observed. Nanotopography has been widely reported to promote preferential endothelialisation [59,255], which is consistent with the optimal cell adhesion with mature FAs, visible cell-cell contact, proliferation and metabolic activity (p>0.05

compared to TCP) on nanofeatured 50-100 mM EDA. In particular, a highly spread cell behaviour was observed on 50 mM EDA coating with nanofeatures (84 nm wide, 15 nm high). In contrast, 25 mM EDA, which presents similar surface chemistry compared to 50 mM EDA but a rougher and more elevated nanotopography (90 nm wide, 35 nm high), elicited non-proliferative and irregular cell morphology. Along with prominent protrusions of lamellipodia, the small dot FAs scattered around the cell periphery may be indicative of more motile cell behaviour [252,265], as migrating cells tend to more readily assemble and disassemble FA sites. The poorer formation of FAs may have contributed to the poor proliferation rate, because sufficient FA formation are associated to improved cell growth [251]. This differential cell response on 25 mM EDA may be attributed to the relatively elevated nanofeatures and higher surface roughness. Dalby *et al.* have shown that endothelial cells displayed better spreading behaviour on shallower 13 nm nanoislands than 95 nm [255]. Potthoff *et al.* also reported that on shallower nanogratings (100-400 nm), HUVECs spread better across the height allowing adaptation of membrane protrusions to the underlying topography [252]. Liliensiek *et al.* illustrated sub-optimal HUVEC growth on nanoscale topography <800nm with depth of 300nm [266]. These results displayed consistency with our findings. It is still unclear that why HUVECs on 25 mM EDA appear to conform more to the micro-ridges, leading to their irregular cell shape. It can be suggested that these are associated to the more elevated dimension of nanofeatures, but the exact interplay warrants further studies.

The mechanism on how nanofeatures influence cell behaviour is still unresolved. One possible explanation is that nanotopography is biomimetic to extracellular matrix proteins which are typically hierarchically structured with presentations of micro- to nanoscale features [267], hence leading to enhanced cell fate. It may also be contributed by a differential protein adsorption behaviour on nanotopographical substrates [268,269]. For instance, it has been reported that nanoscale roughness can increase fibrinogen adsorption over BSA [268]. However, as demonstrated in this study, increasingly elevated nanotopography may induce distortion in cytoskeletal organisation leading to sub-optimal or non-proliferative cell behaviour. Altogether, the cell responses on EDA coatings showed the potential to manipulate EC behaviour by combining nanotopography and surface chemistry, and coatings with shallower

nanotopography (50-100mM EDA) demonstrated optimal cell adhesion, metabolic activity and total DNA content.

4.4.2.3 An interplay between surface chemistry and nanotopography

Overall, the results here provided insights into the interplay between chemistry and topography, which remain a complex area of research [250]. Figure 4.7 presents a working model summarising cellular behaviour in relation to the results reported here. It appears that surface chemistry plays a greater role than topography in influencing HUVEC fate, but surface nanotopography could provide further regulation of the process. It is of great interest in the field of biomaterials to individually decipher these interrelated components of material properties in relation to their biological behaviour [253,270].

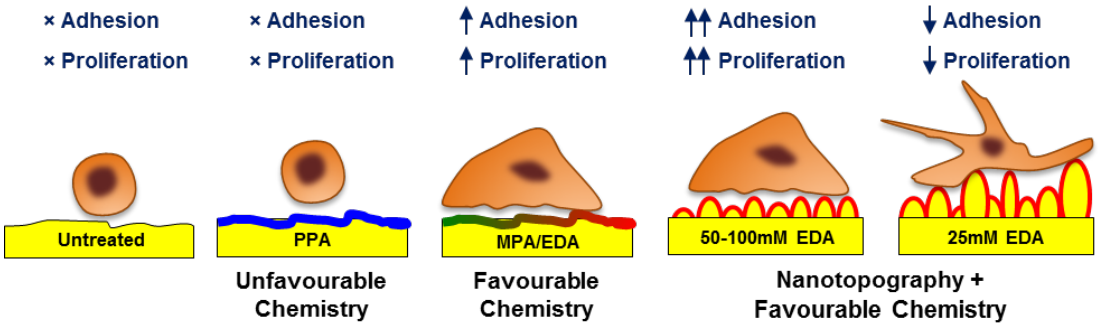

Figure 4.7. Schematic diagram of a working model based on HUVEC response on to chemical cured coatings of varied chemistry and nanotopography. Favourable chemistry includes biomimetic functional groups such as $–NH_2$ and –COOH moieties.

More importantly, the results so far illustrate the potential of the chemical-cured coatings as a biomaterial platform, with optimal cell adhesion, proliferation and metabolic activity up to 7 days *in vitro* demonstrated with selected formulations of the chemical curing systems. This also provides indications that these coatings are non-cytotoxic. Further characterisation of cell migration, function or gene expression on these coatings, and probing the cell responses under biomimetic flow conditions are potential future work to be conducted. Semi-quantitative analysis from the fluorescent images to quantify parameters such as cell area or number of FAs could also be performed using larger sample sizes to better compare cell-material interactions between the coatings. It will also be interesting to investigate the behaviour of different cell types, such as macrophages or SMCs, on these coatings as different cell types are known to respond to varied topographical features differently when compared with one another [253,271].

4.5 Conclusion

Chemical cured PCU-PP coatings show the potential to create tuneable cell responses with respect to surface chemistry and topography. PPA-cured coatings displayed cell repellent surface properties, while MPA and EDA cured coatings greatly enhance cell spreading, adhesion, proliferation and metabolic activity at specific formulations. The versatility and the capability of the chemical curing procedure of PPs to simultaneously alter surface chemistry and topography present tremendous potential not only in development as combinatorial biomaterial platforms, but also as a tool to tailor cell-material interactions at the biointerface. Furthermore, the presentation of surface functional groups could also be further utilised as sites for immobilisation of biomolecules such as peptides, antibodies or growth factors for further biomimicry and regulation of cell behaviour, which will be discussed in the subsequent chapters.

Chapter 5

Biofunctionalisation of Chemical Cured Pre-polymer Coatings to Promote *In Situ* Endothelialisation

5.1 Introduction

Vascular stents are blood-contacting devices that are presently associated to two main complications: (i) thrombosis and (ii) neointimal hyperplasia (NIH) leading to restenosis. A functional endothelium is regarded as the ideal blood-contacting substrate to maintain vascular homeostasis, hence is capable of circumventing the incidence of the complications, and maintaining long-term vessel patency. *In situ* endothelialisation via conjugation of biomolecules that capture endothelial progenitor cells (EPCs) or pro-endothelialisation coatings on to vascular biomaterials represents a promising avenue for development of next generation stents with pro-healing capabilities. However, in the complex *in vivo* environment it can be complicated by the presence of many other cell types and components in the blood, including platelets, smooth muscle cells (SMCs) and leukocytes (e.g. macrophages and monocytes), which may also adhere to biomaterials. In particular, platelet adhesion, aggregation and activation could lead to undesirable thrombotic events. Hence, to selectively promote endothelialisation is one of the many properties that are desirable for vascular stents with *in situ* endothelialisation capability.

Among many biomolecules to promote in situ endothelialisation described in section 1.4, anti-CD34Ab is the most widely studied and translated candidate to augment EPC capture due to expression of CD34 on EPCs, hence serves as an attractive candidate to explore on chemical cured PCU-PP coating platforms. REDV peptides, first reported by Jeffrey Hubbell, are known for their selectivity towards endothelial cells (ECs) over platelets and SMCs [157]. Moreover, peptides offer ease of design and predictable chemistry. Peptides can be synthesised using solid phase peptide

synthesis (SPPS), where peptide sequences and configurations can be custom designed to produce specific biological properties [272]. The pre-defined chemistry of peptides allows more precise control over conjugation chemistry. Therefore, anti-CD34Ab and REDV peptides were selected for immobilisation on to chemical cured coatings.

Conjugation of biomolecules on to biomaterial substrate is one approach to improve stability via covalent chemical bonds, and has the potential to control the biomolecular orientation and/or conformation via defined conjugation chemistry [200]. Bioconjugate reactions require the presence of surface reactive functional groups on the base substrate, such as –COOH, -NH_2, -SH and -C≡C groups.

In this chapter, immobilisation of anti-CD34Ab and REDV peptides on to chemical cured PCU-PP coatings was explored. Firstly, anti-CD34Ab were immobilised on to EDA-cured coatings via a site-directed periodate oxidation (PO) reaction in order to produce covalently linked and oriented antibodies for optimal functionality. EDA cured coatings were selected as a platform due to its nanofeatured surface, as well as, optimal HUVEC adhesion, proliferation and growth. Secondly, cysteine terminated REDV peptides were immobilised on to -C≡C functionalised PPA-cured coatings via thiol-yne click reactions (TYC), which are known to possess higher reaction efficiency. It is hypothesised that the immobilisation of anti-CD34Ab and REDV peptides on to the cured PCU-PP coatings would promote selectivity towards endothelialisation over platelet adhesion and activation. Furthermore, anti-CD34Ab would enhance adhesion and proliferation of EPCs in accordance with a number of recent reports from the literature [149,273].

5.2 Materials and methods

5.2.1 Biofunctionalisation of chemical cured coatings

PCU-PP coatings on SS316L coupons were chemically cured with 50 mM EDA and 50 mM PPA as described in section 3.2.2.

5.2.1.1 Antibody immobilisation on EDA-cured coatings

All reagents described in this section were purchased from Thermofisher Scientific, UK unless stated otherwise. Monoclonal mouse anti-human CD34 antibodies (anti-CD34Ab) (QBEnd-10, #MA1-10202) were immobilised on to 50 mM EDA cured PCU-PP coatings using a site directed PO reaction as described by Yuan *et al*. and Petersen *et al*. [148,197]. The reaction scheme is depicted in Figure 5.1.

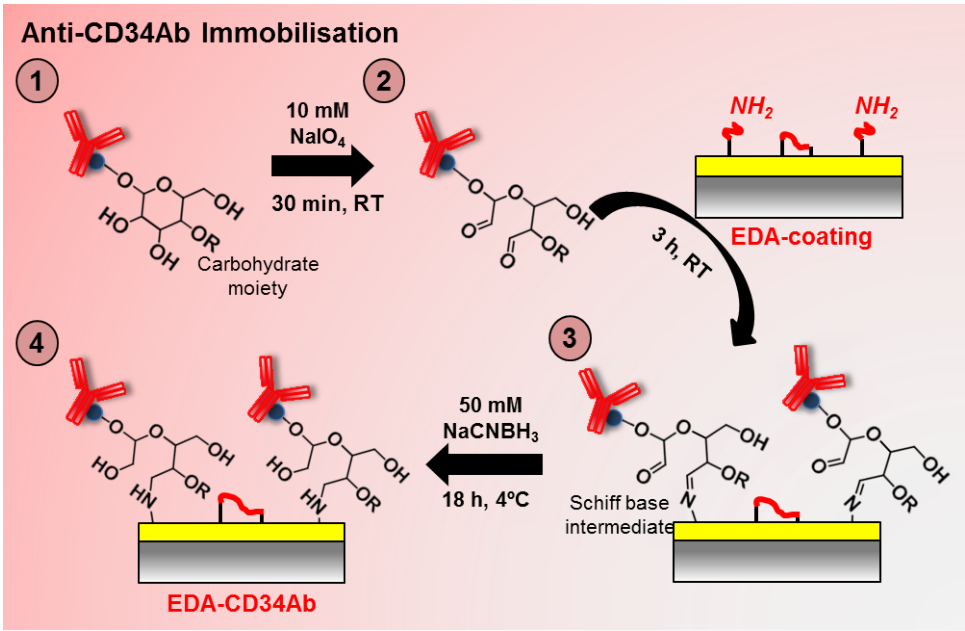

Figure 5.1. Schematic diagram detailing anti-CD34Ab immobilisation on EDA-cured coatings using PO reaction. (1) The carbohydrate moiety located at the Fc region of the antibody were oxidised to (2) aldehyde by sodium periodate ($NaIO_4$). Upon removal of $NaIO_4$ with desalting columns, (3) the aldehyde-functionalised antibodies were incubated on EDA coatings allowing reaction with the surface $–NH_2$ groups, forming a Schiff base intermediate. (4) Incubation with sodium cyanoborohydride ($NaCNBH_3$) reduces the intermediate to form stable amide bonds, leading to oriented antibody configuration.

Firstly, 0.1 mg/mL anti-CD34Ab was incubated with 10 mM sodium periodate ($NaIO_4$) diluted in 0.1 M sodium acetate buffer (SAB). The incubation was performed in the dark at room temperature (RT) for 30 min. The resultant ox-anti-CD34Ab solution was passed through SAB-equilibrated Zeba™ Spin Desalting Columns with a molecular weight (MW) cut-off of 7 kDa in order to remove $NaIO_4$.

The columns were centrifuged with 1500 r.c.f for 2 min to collect the ox-anti-CD34Ab solution. The resultant ox-anti-CD34Ab solution was then diluted with SAB to a determined concentration (0-10 μg/mL) and sterile filtered through a 0.2 μm Corning® Polyether Sulfone (PES) syringe filter (Appleton Woods Ltd, UK). 250 μL of diluted ox-anti-CD34Ab were then incubated on sterilised 50 mM EDA cured PCU-PP coating in 24 well plates under shaking at RT for 3 h. During this process, the aldehyde-functionalised antibodies would react with the surface $–NH_2$ groups via Schiff base reactions to form a Schiff base intermediate. Next, samples were incubated in 300 μL 50 mM sodium cyanoborohydride ($NaCNBH_3$) purchased from Sigma Aldrich (UK) in PBS in and incubated at 4°C overnight (~18 hours). The samples were then rinsed at least 4 times with PBS and stored in PBS in 4°C prior to experimentation.

5.2.1.2 Peptide immobilisation on PPA-cured coatings

Four peptides, presented in Table 5.1, were custom synthesised via solid phase peptide synthesis by Generon Ltd, UK, with the inclusion of a cysteine terminal to provide –SH sites for immobilisation. Peptides were characterised by the manufacturer using liquid chromatography mass spectrometry (LCMS) for verification of MW and purity (Appendix C).

Table 5.1. List of peptides used for immobilisation on PPA cured coatings and their molecular formula, molecular weight and purity.

Peptides	Description	Molecular formula	MW ($gmol^{-1}$)	Purity (%)
CGREDV	Short (6-mer)	$C_{25}H4_3N_9O_{11}S_1$	677.73	98.62
CG_5REDV	Long (10-mer)	$C_{33}H_{55}N_{13}O_{15}S_1$	905.94	98.56
cycREDV (REDV-D-Phe-C)	Cyclic (6-mer)	$C_{32}H_{47}N_9O_{10}S_1$	749.93	90.86
CGREVD	Scrambled (6-mer)	$C_{25}H_43N_9O_{11}S_1$	677.73	92.91

One-letter amino acid codes: C, cysteine; G, glycine; R, arginine; E, glytamic acid; D, aspartic acid; V, valine; D-Phe, D-phenylalanine.

The selected peptides include (i) CGREDV; (ii) CGGGGGREDV (CG_5REDV) with glycine (G) as extended spacer arm; (iii) cyclic REDV-(D-Phe)-C (cycREDV); and (iv) a scrambled sequence CGREVD as negative control. Their structures are depicted in Figure 5.2.

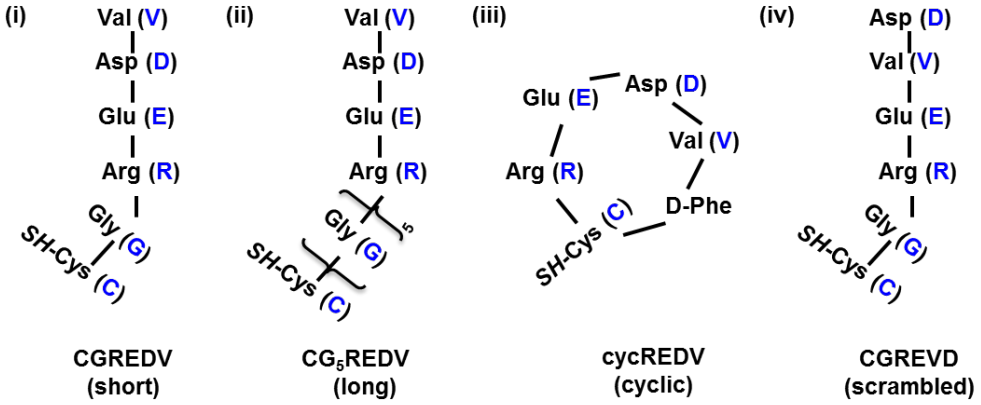

Figure 5.2. Structure of (i) short, (ii) long, (iii) cyclic and (iv) scrambled REDV peptides selected in this study.

The peptides were stored at -20 °C in their lyophilised form. For experimental use, the peptide aliquots were resuspended with PBS to 10 mg/mL (5 mg/mL for cycREDV), stored at 4°C, and used within a one month period. Peptide immobilisation on to 50 mM PPA cured coatings was performed using thiol-yne click reaction (TYC) as depicted in Figure 5.3. As previously shown in section 3.2.4.3, TYC theoretically permits free radical addition of two –SH-terminated peptides to each -C≡C group.

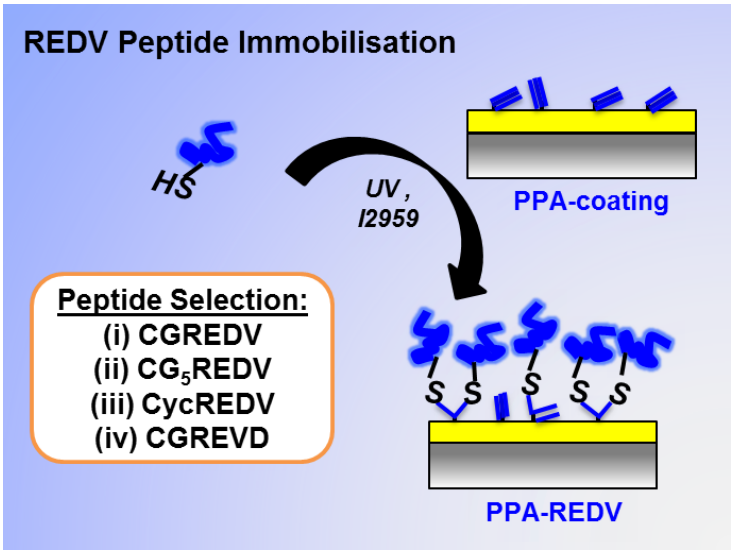

Figure 5.3. Schematic diagram illustrating immobilisation of REDV peptide on to PPA cured coatings using TYC.

The TYC protocol was adapted from Feng *et al.* [235]. As thiols (-SH) tend to oxidise to form disulphide bridges (-S-S-) over time, peptides were first incubated with 0.5 mM tris(2-carboxyethyl)phosphine hydrochloride (TCEP) in PBS for 30 min at RT to allow reduction of –S-S- to –SH. All peptides were diluted to the desired concentration (0, 0.1, 0.5 and 2 mg/mL) in 75:25 (v/v) PBS/ETOH. The

addition of ETOH was to enhance the wettability of the peptide solution on the PPA coatings. Irgacure® 2959 (I2959, Sigma Alrich, UK), a water-soluble photoinitiator was added to the final stock solution at 1 mol% with respect to the each mol of peptide to initiate the TYC reaction.

PPA cured coatings was rinsed with 100% ETOH and placed on a sheet of parafilm. 120 µL peptide solution containing I2959 were spread on to the coatings, followed by UV-irradiation (254 nm, 3.0 mW/cm^2) for 0-450 s. Samples were then rinsed with copious dH_2O and incubated in 70% ETOH for 20 min to minimise risk of infection, followed by rinsing with PBS for 3 times. Peptide immobilised samples were store in sterile PBS at 4 °C, and used for experimentation within a one week period.

5.2.2 Characterisation of antibody and peptide immobilised coatings

5.2.2.1 Direct ELISA to quantify immobilised anti-CD34Ab

Quantification of immobilised anti-CD34Ab on EDA coating was carried out using enzyme-linked immunosorbent assay (ELISA) using goat anti-mouse IgG conjugated to horseradish peroxidase (HRP). Firstly, samples were incubated in 2% BSA in PBS/0.1% Tween20 for 1 h. Samples were then rinsed with PBST and incubated with 1 µg/mL goat anti-mouse IgG-HRP (#A16072, Thermofisher Scientific) in 1% BSA/PBST at RT for 1 h. Subsequently, each sample was rinsed with 1 mL PBST 6 times and transferred to new 24 well plates. TMB substrate reagent (BD Bioscience, UK), was prepared accordingly to the manufacturer's instruction where two reagent components were mixed in 1:1 ratio at RT, resulting in a TMB solution containing hydrogen peroxide (H_2O_2). 200µL TMB solution was added to each sample, whereby TMB reduces H_2O_2 to H_2O under presence of HRP to form *3,3',5,5'*-tetramethylbenzidine diimine which causes the solution to adopt a blue colour, whose intensity can be correlated to the quantity of HRP, and thus the amount of mouse anti-CD34Ab. After 6 min, the reaction was stopped by addition of 200 µL 1M H_2SO_4, which lead to a change in colour from blue to yellow. The respective solutions were then transferred to a 96 well plate, and the absorbance was read at 450 nm using a TECAN Infinite 200 Pro microplate reader.

5.2.2.2 Modified sandwich ELISA to correlate CD34 antigen binding capability

A modified sandwich ELISA was adapted from Petersen *et al*., and was used to measure CD34 antigen binding capability of anti-CD34Ab immobilised coatings [197]. Samples were first incubated in 2% BSA in PBST for 1 h, followed by PBST rinsing. 200µL 2.5 µg/mL CD34 Recombinant Human Protein with inclusion of His-Tag® (#10103H08H50, Thermofisher Scientific, UK) in 1%BSA/PBST was incubated with the samples under orbital shaking for 2 h at RT. Samples were rinsed thrice with PBST. Subsequently, to quantify the amount of CD34-His Tag protein, samples were incubated with 1 µg/mL chicken polyclonal anti-His Tag antibody-HRP (ab3553, Abcam, UK) in 1% BSA/PBST at RT for 1 h. This was followed by 6 rinsing steps with PBST, and transferred into a new 24 well plate. 200µL TMB solution was added to each sample and incubated at RT for 12 min to initiate colour development, which correlates with the amount of HRP and amount of CD34 antigen. This is followed by the addition of 1M H_2SO_4 stop solution. The respective solutions were then transferred to a 96 well plate, and the absorbance was read at 450 nm using a TECAN Infinite 200 Pro microplate reader.

5.2.2.3 Ellman's assay to quantify immobilised peptides

Ellman's reagent, or 5,5'-dithiobis-(2-nitrobenzoic acid) (DTNB), is a colorimetric assay quantifying free –SH groups, which correlates with the amount of –SH-containing peptides. DTNB reacts with free –SH groups leading to cleavage of its –S-S- group to yield *2*-nitro-5-thiobenzoic acid (TNB), which gives rise to a yellow TNB^{2-} anion solution under mild alkaline conditions (pH 7-8). Ellman's reagent was used to estimate the amount of immobilised peptides on PPA cured coatings by quantification of the amount of –SH remaining in the supernatant before and after the reaction. However, -SH groups are prone to oxidation to –S-S-. Furthermore, residual TCEP in the solution, which is essential to ensure free –SH group presentation of the peptides, can also react with DTNB and contribute to colour change. Hence, to take into account these external factors, alkyne-free glass cover slips were used as comparative controls.

0.4 mg/mL DTNB (Sigma Aldrich, UK) was prepared in 0.1 M phosphate buffer (pH 8.0) containing 1 mM ethylenediaminetetraacetic acid (EDTA) (Sigma Alrich, UK). Immediately after UV-irradiation to initiate TYC reactions of peptides described previously, 25 µL reaction supernatant on the PPA-coatings or glass cover slips was

incubated with 75 μL DTNB solution in a clear 96-well plate. The absorbance was read at 412 nm using TECAN Infinite 200 Pro microplate reader. The amount of –SH was calibrated with respect to a standard curve generated with known concentrations of MPA (Appendix B.4), and was used to calculate peptide density. The difference in measurements between PPA coatings and glass cover slips were used to correlate with the amount immobilised peptides, based on the assumption that there was no non-specific binding or side reactions of peptides on the glass cover slips.

5.2.2.4 Time-of-flight secondary ion mass spectroscopy (ToF-SIMS)

ToF-SIMS is a highly surface sensitive technique based on mass spectroscopy for the analysis of chemical composition of materials. Essentially, material surfaces at a depth at the nanoscale (<5 nm) are bombarded under ultra-high vacuum with a pulsed ion beam, causing sputtering of surface atoms or molecule, as well as, ionisation leading to production of secondary ions. Positively or negatively charged secondary ions travel through a flight path to a detector, and arrive at different points of time based on the mass of these ions. Hence, by measuring the time-of-flight (ToF) of these ions, a mass spectrum of the surface ionised particles can be obtained with high resolution and sensitivity. Furthermore, it is possible to produce a surface elemental or molecular map, as well as, depth profiles.

In this study, ToF-SIMS was used for verification and distribution mapping of antibodies or peptides on EDA-CD34Ab and PPA-cycREDV. ToF-SIMS was conducted at School of Pharmacy, University of Nottingham, UK, using a ToF-SIMS IV instrument (ION-TOF GmbH, Germany). A bismuth liquid metal ion gun (Bi^{3+}) running at 25 kV (pulsed target current of ~1.0) was used as primary ion beam. Vacuum dried anti-CD34Ab (1 mg/mL) on a glass cover slip and lyophilised cycREDV was used as a positive sample reference. For each sample, data were acquired over 3 separate regions with an area of 2500 μm^2 (500×500 μm), and 6 scans were captured per area. Data acquisition and analysis was conducted using SurfaceLab 6 software (ION-TOF GmbH), and the spectra were normalised with respect to the total intensity.

5.2.3 Cell culture and maintenance

5.2.3.1 Human umbilical vein endothelial cells (HUVECs)

The culture and maintenance of HUVEC were as described in section 4.2.2.

5.2.3.2 Endothelial colony forming cells (ECFCs)

ECFCs are a subpopulation of EPCs as described in section 1.3.3, and were isolated from peripheral blood of healthy adult donors by Prof Jane Mitchell's group (National Heart and Lung Institute, Imperial College London, UK) in accordance with established protocols (Appendix D) [42,274,275]. Briefly, peripheral blood mononuclear cells (PBMCs) were obtained from the collected blood using density gradient centrifugation within 1 hour of blood collection, and plated on to wells of 6-well plates coated with Type I Rat-tail Collagen (Corning, USA).The coating was performed by incubation of 50 μg/mL Type I rat tail collagen in 0.02 N acetic acid in dH_2O for 45-60 min in a humidified incubator at 37 ºC and 5% CO_2, followed by three 7 mL PBS rinses. PBMCs were cultured in Lonza EGM-2™ basal media (Lonza, USA) supplemented with Lonza EGM-2 SingleQuots™ supplements, which includes human epidermal growth factor, vascular endothelial growth factor (VEGF), R3 insulin-like growth factor, ascorbic acid, hydrocortisone, human fibroblast growth factor-β, heparin and gentamicin-amphotericin-B. The 2% FBS provided in the supplement kit was replaced with 10% (v/v) Hyclone™ FBS (Fisher Scientific, UK). Cells were cultured in humidified incubator at 37 ºC and 5% CO_2. Media changes were performed at 24, 72 and 96 h, and subsequently every 48 h. Colonies of ECFCs emerged typically between 7-14 days, and were expanded.

Two ECFC cell lines from different human donors were received at passage 3. Both cell lines were selected as they possess different levels of CD34 expression, and are designated as CD34+ (lower level) and CD34++ (higher level) ECFCs. Their expression levels of CD34, CD31 and CD45 characterised by flow cytometry (Appendix D) are summarised in Table 5.2. Both cell lines highly express endothelial marker CD31 and barely express haematopoietic marker CD45. Both ECFC cell lines appeared as dense cell monolayer typical of EC cobblestone morphology (Figure 5.4).

Table 5.2. Summary of quantified percentage of positively stained cells for CD34, CD31 and CD45 in both CD34+ and CD34++ ECFC isolates. (Data collected and provided by Ms Isra Marei and Prof Jane Mitchell from Imperial College London, UK).

Marker	CD34+ ECFC (% Positive)	CD34++ ECFC (% Positive)
CD34	55.70	88.92
CD31	95.00	96.51
CD45	6.64	2.46

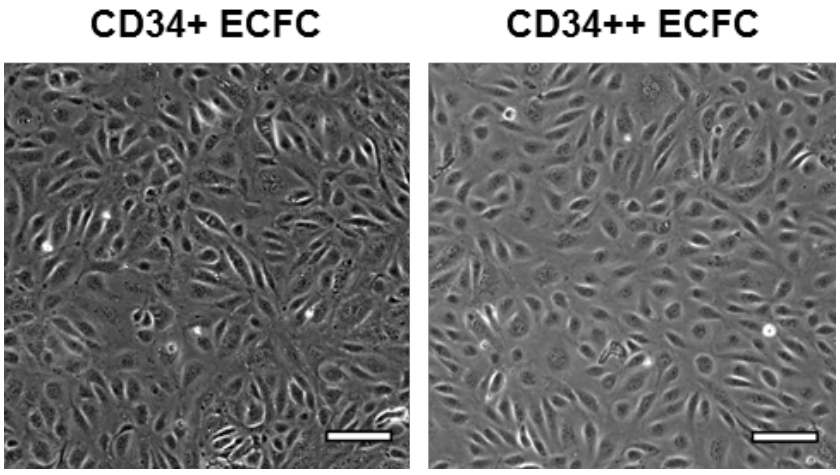

Figure 5.4. Optical images of ECFCs (passage 3) in their typical cobblestone morphology. Scale bar = 100 μm.

The ECFCs were cultured and expanded in 25 or 75 cm^2 culture flasks precoated with Type I rat tail collagen, with 15 mL of the same growth media as described previously (Lonza EGM-2 + SingleQuots™ supplements excluding 2%FBS + 10% Hyclone™ FBS). Growth media was completely replenished every 2 days. ECFCs displayed a higher proliferative rate compared to HUVECs, with the attainment of confluence prompting sub-culturing approximately every 3-4 days. Sub-culturing was performed as described previously for HUVECs (section 4.2.2). Cryopreservation of cells was performed at passage P4-7 using PromoCell Freezing Medium Cryo-SFM (Promocell, Germany). Cell concentration for cryopreservation was at least 1×10^6 cells/mL, and 1 mL of cells in cryovials was promptly transferred to Mr Frosty Freezing Container to be cooled at -1ºC/min overnight. Cryovials were subsequently stored in liquid nitrogen at -196ºC for longer term (>1 mth) storage. Thawing of the cells was performed by immersion of cryovials in 37 ºC water bath followed by quick transfer into collagen precoated flasks containing fresh growth media, and placed in the incubator. Media was changed 18 h later to remove any residual DMSO, which is a component in the Cryo-SFM freezing medium.

5.2.4 Cell seeding and culture

5.2.4.1 HUVEC seeding

The seeding of HUVECs on to samples was the same as described in section 4.2.3. HUVECs of passages between P4-7 were used for experiments, and were maintained up to 28 days with complete change of growth media every other day.

5.2.4.2 ECFC seeding

Seeding of ECFCs on to samples was similar to that of HUVECs, with slight modifications. The experimental culture media for ECFC was Lonza EGM-2 basal media supplemented entirely with EGM-2 SingleQuots^{TM} supplements without the replacement with Hyclone^{TM} FBS, giving rise to 2% (v/v) FBS which was the same used for HUVEC culture. ECFCs were seeded at a density of 1×10^4 cells/cm^2 on to samples in 1 mL ECFC experimental culture media, and were maintained up to 13 days with change of media every 48 h. ECFCs of passages P5-8 were used for experiments. Both ECFC lines (CD34+ and CD34++) were trypsinised and seeded at the same time for each experiment. TCP coated with type I rat-tail collagen was used as positive control (TCP-COL).

5.2.5 *In vitro* characterisation of HUVEC and ECFC fate

Quantitative cell culture experiments were repeated independently at least 3 times (n=3), each with triplicated technical repeats for each condition.

5.2.5.1 Cell metabolic activity using AlamarBlue® assay

Metabolic activities of HUVEC and ECFC on samples were quantified using Alamar Blue® assay as described in section 4.2.4.1.

5.2.5.2 Cell proliferation using total DNA quantification

HUVEC and ECFC proliferation were correlated using total DNA quantification as described in section 4.2.4.2.

5.2.5.3 Fluorescence staining: F-actin, DAPI and vinculin

F-actin, vinculin and nuclear staining to visualise cellular cytoskeletal organisation and focal adhesion (FA) sites were performed with the same protocol as described in section 4.2.5.

5.2.6 Assessment of platelet adhesion and activation

5.2.6.1 Platelet isolation

Platelets were isolated from whole blood (10-15 mL) from healthy consenting adult donors and collected in BD Vacutainer® blood collection tubes containing buffered sodium citrate (Becton Dickinson, UK). Platelet isolation was performed within 1-2 h of blood collection under aseptic conditions. Citrated whole blood was gently transferred into sterile 50 mL polypropylene centrifuge tubes and diluted 1:1 with PBS, and subsequently centrifuged at 200 r.c.f for 20 min without brakes at RT. This resulted in three distinct layers: (i) red blood cells (RBCs) at the bottom layer, (ii) a thin buffy coat layer consisting of PBMCs at the middle and (iii) a platelet rich plasma (PRP) at top layer. The top PRP layer was gently transferred to a clean sterile centrifuge tube with care taken not to interfere with the buffy coat layer to avoid contamination of PBMCs. The collected PRP layer was then subjected to further centrifugation at 100 r.c.f for 15 min without brakes to pellet any contaminating PBMCs or RBCs. The platelet-containing PRP supernatant was then transferred again to a clean sterile centrifuge tube. Platelet concentration was determined after 1:100-1:200 dilution with PBS via triplicate counting using a haemocytometer.

5.2.6.2 Platelet seeding

Sterile samples, including SS316L, untreated PCU-PP coating, EDA, EDA-CD34Ab, PPA and PPA-cycREDV were transferred to 24 well plates. Collagen coated TCP (COL) or SS316L (SS316L-COL) was used as a positive control, and was prepared by incubation of 250 µL 50 µg/mL Type I rat-tail collagen (Corning, USA) in 0.02 N acetic acid in 37 ºC for 1 h. All samples were first incubated in PBS in humidified 37 ºC and 5% CO_2 incubator for 30-60 min. The PRP obtained from section 5.2.6.1 was diluted with PBS to a working concentration of 1×10^6 platelets/mL. Samples were then incubated in 1 mL of the platelet suspension for 1 hour in humidified incubator at 37 ºC and 5% CO_2.

5.2.6.3 Assessment of platelet adhesion and morphology

5.2.6.3.1 Quantification of platelet adhesion

Following 1 h incubation with 1 mL 1×10^6 platelets/mL, the supernatants of each sample was transferred to 2 mL Eppendorf tubes for subsequent counting using a haemocytometer. The amount of platelets adhered was calculated by the difference

between the initial platelet number (1×10^6) and number of platelets remaining in the supernatant. Counting was performed a least 3 times for each single sample, and samples were in triplicates for each experiment. Data were pooled from three sets of independent experiments (n=3) using whole blood from different healthy donors.

5.2.6.3.2 Fluorescent imaging of platelet adhesion

Following 1 h incubation with platelets, samples were immediately fixed with 10% formalin (CellPath, UK) at RT for 30 min for fluorescent imaging. Due to the absence of nucleus in platelets, only F-actin staining was used to visualise platelet adhesion to support quantitative test results. Fixed samples were blocked with 1 w/v% BSA in PBST for 30 min at RT, followed by incubation for 30 min at RT with AlexaFluor-488®-Phalloidin diluted at 1:200 in PBS. Samples were rinsed at least three times with PBS prior to imaging using EVOS Fluorescent Microscope.

5.2.6.3.3 Platelet morphology by FE-SEM to assess platelet activation

Following 1 h incubation with platelets, samples were immediately fixed with 2.5% (v/v) glutaraldehyde grade I (EM grade) diluted in PBS at RT for 15 min for FE-SEM imaging. Glutaraldehyde fixed samples were then dehydrated in increasing concentrations of molecular grade ETOH in dH_2O, followed by air-drying in the fume hood overnight, as described for HUVECs in section 4.2.5.3. Samples were coated with 1 nm platinum using a Cressington Sputter Coater and images were obtained using Zeiss SIGMA FE-SEM at an accelerating voltage of 3-5kV. Platelet morphology on materials serve as an indicator for the degree of platelet activation. Ko and Cooper classified platelet activation into five stages based on platelet morphology [276], as summarised in Table 5.3. This classification was used for analysis of platelet activation from FE-SEM images.

Table 5.3. Ko and Cooper's classification of five stages of platelet morphological change on biomaterials [276]. Stage I represents initial stage of platelet activation while V shows advanced stage of activation**.**

Stage	Shape	Morphological details
I	Round	Round or discoid, no pseudopodia present
II	Dendritic	Early pseudopodial, no flattening evident
III	Spread-dendritic	Intermediate pseudopodial, one or more pseudopodia flattened, hyaloplasm not spread between pseudopodia
IV	Spreading	Late pseudopodial, hyaloplasm spreading
V	Fully-spread	Distinct pseudopodia absent, hyaloplasm well spread.

5.2.7 Statistical analysis

Data were reported as mean ± standard deviation (SD), unless otherwise stated. Statistical analysis was conducted using Prism GraphPad software (version 6.0). ELISA and platelet adhesion data were statistically tested using one-way ANOVA with Tukey's post-hoc tests. Total DNA quantification and metabolic activity data were analysed using two-way ANOVA with Tukey's post-hoc tests. *P* values of $p<0.05$ were considered to be statistically significant.

5.3 Results

5.3.1 Anti-CD34Ab immobilisation on EDA-cured coatings

5.3.1.1 Optimisation of antibody concentration

Anti-CD34Ab was immobilised using site directed PO reactions on to $–NH_2$ functionalised 50 mM EDA cured PCU-PP coatings. The concentration of oxidised anti-CD34Ab for reaction was optimised via serial dilution following sterile filtration, and the quantity of immobilised anti-CD34Ab were determined using a direct ELISA assay as shown in Figure 5.5. It can be seen that the intensity of immobilised anti-CD34Ab increased up until saturation at 2.5 μg/mL, with no distinctive differences in intensity detected above this concentration, indicative of saturation of antibodies on the surface. Hence, subsequent immobilisation of anti-CD34Ab was conducted using 2.5 μg/mL.

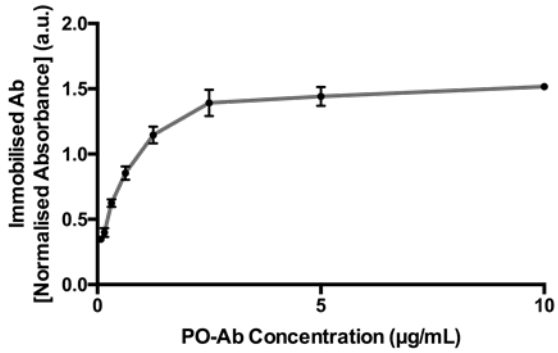

Figure 5.5. Quantification of immobilised anti-CD34Ab on EDA coating following incubation at varying oxidised antibody concentration quantified by direct ELISA (n=3).

5.3.1.2 Functionality of immobilised antibodies

The functionality of immobilised anti-CD34Ab on the coating was evaluated via a modified sandwich-ELISA assay, which quantifies the binding of CD34 antigens after incubation on anti-CD34Ab immobilised EDA coatings (EDA-CD34Ab). The PO conjugation approach was compared to physisorption of antibodies (AD-Ab), whereby antibodies of identical concentration was incubated on EDA coatings without any prior treatment. Figure 5.6A shows that the amount of anti-CD34Ab detected on surfaces of EDA coating were similar using both methods ($p>0.05$). However, the binding capacity of CD34 antigens was much higher for PO-Ab compared with physisorption and EDA controls ($p<0.05$), suggesting that enhanced

antigen binding functionality was achieved by antibody immobilisation via site-directed PO chemistry.

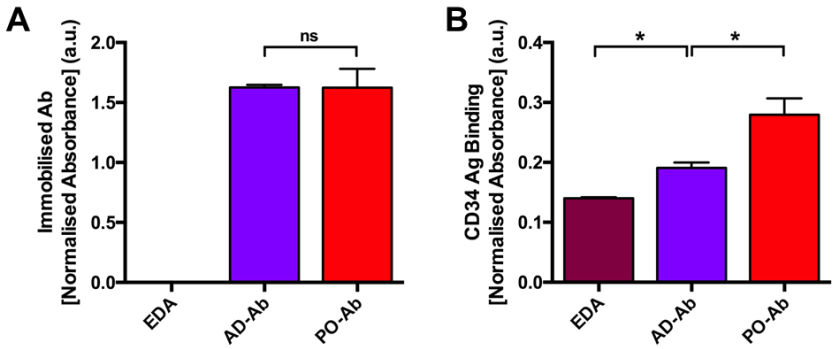

Figure 5.6. (A) Quantification of immobilised anti-CD34Ab and (B) CD34 antigen binding capability on unmodified EDA coatings (EDA), antibodies immobilised via physisorption (AD-Ab) and PO chemistry (PO-Ab) (n=3). One-way ANOVA with Tukey's post-hoc tests were performed to reveal significant differences between different conditions. ns, non significant. *=p<0.05.

5.3.1.3 Distribution of immobilised antibody by ToF-SIMS

The presence and distribution of immobilised anti-CD34Ab was verified by ToF-SIMS mapping as depicted in Figure 5.7.

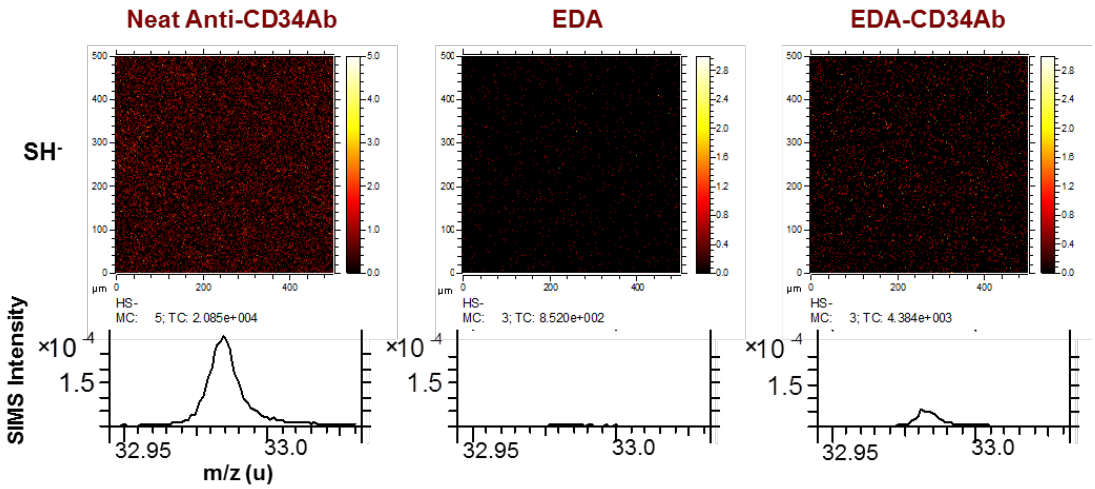

Figure 5.7. ToF-SIMS image map and spectral intensity of SH^- ion markers on EDA and EDA-CD34Ab to illustrate presence and distribution of anti-CD34Ab. Neat vacuum-dried anti-CD34Ab solution on glass cover slip was used as positive reference. Image scale = 500 × 500 µm. (Joint experiment with Mr Jeffrey Leung [277], analysis performed by Dr Long Jiang and Dr David Scurr at University of Nottingham, UK)

ToF-SIMS intensity and image map of anti-CD34Ab positive reference showed a relatively high signal of SH^- ion markers. SH^- could be associated with ionisation of disulphide bridges (-S-S-) within the antibodies. The same signal was barely detected on EDA coatings, but was detected with increased intensity with an even distribution

on surfaces of EDA-CD34Ab. The results support the presence and homogenous distribution of immobilised anti-CD34Ab on EDA-CD34Ab.

5.3.1.4 HUVEC response to anti-CD34Ab immobilised coating

HUVEC fate on EDA and EDA-CD34Ab coatings are depicted in Figure 5.8, which shows their total DNA content and metabolic activity up to day 7. Untreated controls showed minimal levels of DNA content and metabolic activity from day 1 to 7. Both EDA and EDA-CD34Ab coatings revealed similar levels of enhancement in DNA content and metabolic activity, and were comparable to TCP, hence suggestive of optimal cell fate on these coatings. In fact, EDA-CD34Ab demonstrated a significantly higher metabolic activity (p<0.05) compared with TCP at day 7 and a slightly higher total DNA content albeit non-significant (p>0.05).

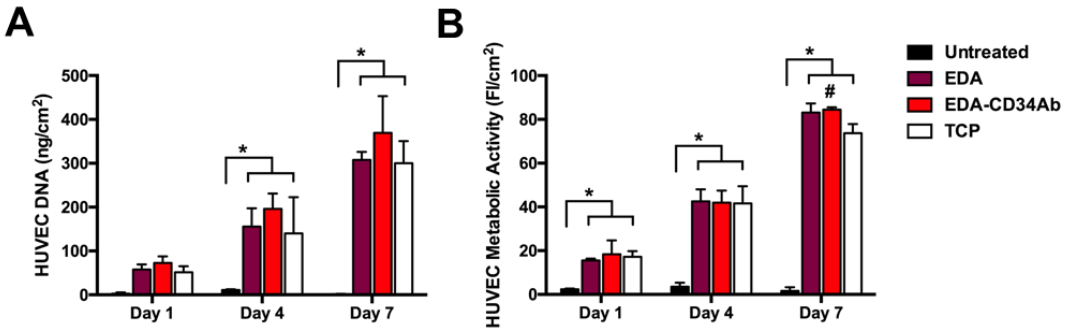

Figure 5.8. (A) Total DNA content and (B) metabolic activity of HUVEC on EDA and EDA-CD34Ab, along with untreated and positive TCP controls on day 1-7 (n=3 independent experiments). Data plotted as mean ± SEM. Two-way ANOVA with Tukey's post-hoc tests were performed to reveal significant differences between conditions at each time point. *=p<0.05. #=p<0.05 compared to TCP.

Fluorescent images of HUVECs are shown in Figure 5.9 and HUVECs presented rounded, non-spread cell morphology on untreated controls. HUVECs appeared to spread optimally on EDA and EDA-CD34Ab comparable to that observed with TCP. At day 7, it can be seen that confluence was achieved on all EDA, EDA-CD34Ab and TCP, but not on untreated controls.

Longer-term sustainability of HUVECs on EDA and EDA-CD34Ab was further evaluated up to 28 days in cell culture. It was apparent that in Figure 5.9 that cells remained densely populated on EDA and EDA-CD34Ab, and retained the level of confluence achieved at day 7 as described previously. No signs of cell sheet detachment were apparent throughout the time course of the experiment.

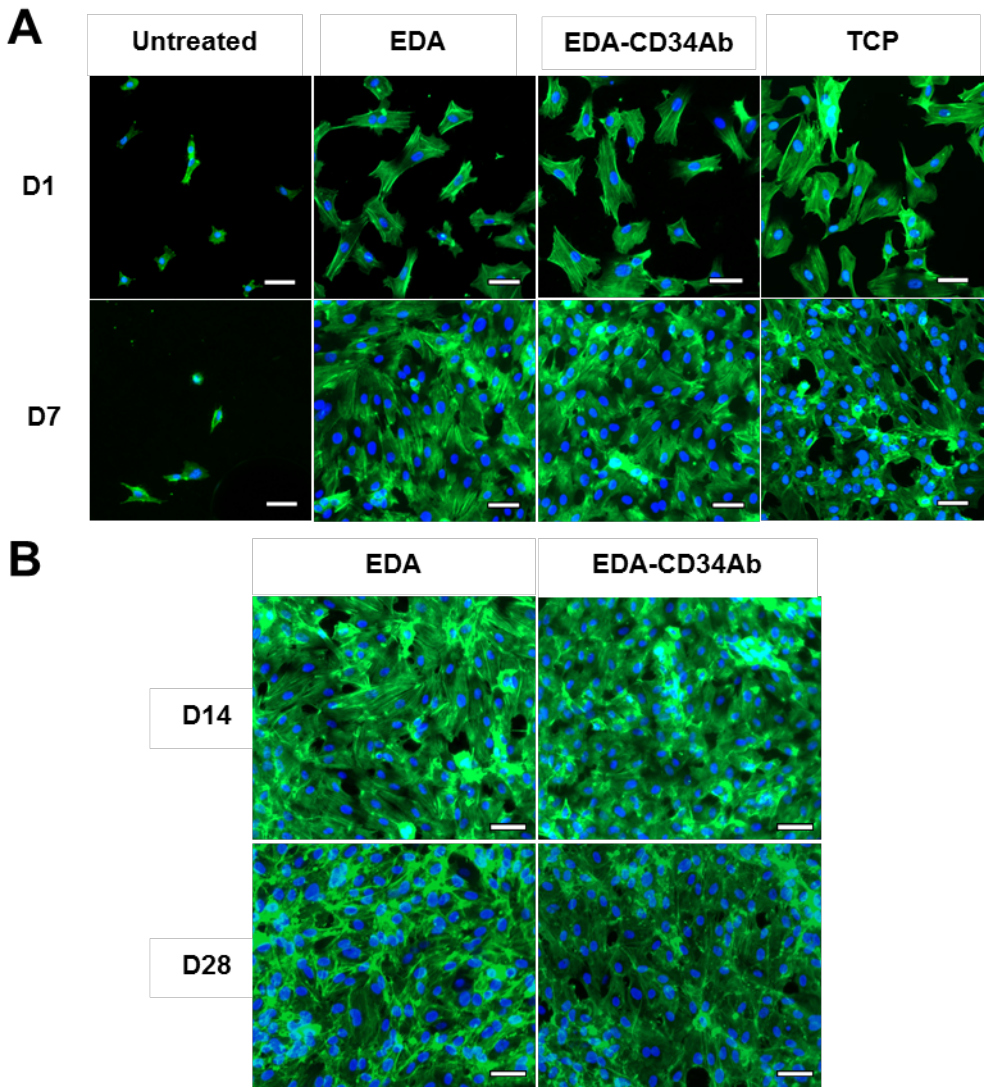

Figure 5.9. Fluorescent images of HUVECs on untreated, EDA, EDA-CD34Ab and TCP on day 1 and 7, as well as, long term culture up to day 28 for EDA and EDA-CD34Ab. Scale bar = 50 µm. Green: F-actin, blue: nuclei.

HUVECs on both EDA and EDA-CD34Ab were further stained with vinculin alongside F-actin and imaged at higher magnification (Figure 5.10. On both samples, HUVECs exhibited defined F-actin filaments along with densely distributed vinculin-containing FA sites throughout the cells. Localised elongated dash-like FA sites were observed at the cell periphery, indicating mature adhesion. There were no observable differences in the level of vinculin detected between both coatings.

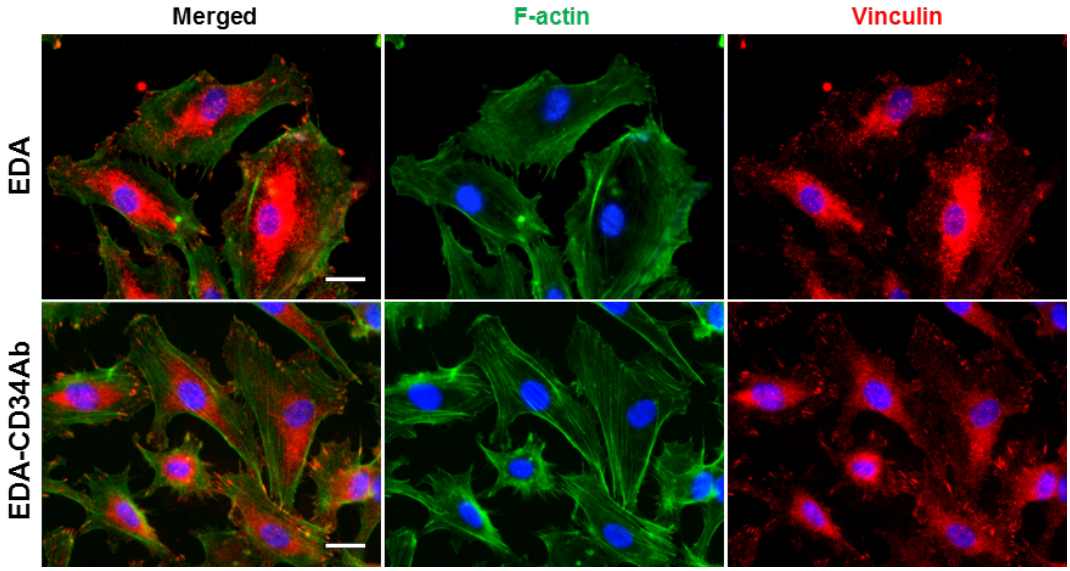

Figure 5.10. Representative images of HUVECs stained for focal adhesion sites and cytoskeletal organisation on day 1 on EDA and EDA-CD34Ab. Scale bar = 20 µm. Green: F-actin, red: vinculin, blue: nuclei.

5.3.1.5 ECFC response to anti-CD34Ab immobilised coating

The effect of anti-CD34Ab immobilisation on ECFC fate was explored using two ECFC lines with varying levels of CD34 expression: CD34+ and CD34++. This also allows investigation of the effect of CD34 expression levels to responsiveness of the immobilised anti-CD34Ab on EDA coatings.

5.3.1.5.1 CD34+ ECFC

Figure 5.11 depicts the total DNA content, metabolic activity and F-actin stained CD34+ ECFC on EDA and EDA-CD34Ab along with untreated and collagen-coated TCP (TCP-COL) positive controls. Consistent with the results already observed with HUVECs (section 5.3.1.4), CD34+ ECFCs displayed very low DNA content and metabolic activity on untreated control throughout all time points indicative of poor cell proliferation and growth. Cells also displayed poorly spread cell morphology associated to poor adhesion at day 1 on these coatings. On EDA and EDA-CD34Ab, CD34+ ECFC showed enhancement in total DNA content and metabolic activity from day 1 to 13 similar to TCP-COL (p>0.05). On these samples, DNA content and metabolic activity levels peaked at day 7, and were sustained up to day 13. However, no detectable differences in cell adhesion and proliferation was detected between EDA and EDA-CD34Ab. Fluorescent images also showed spread cell morphology with clear F-actin stress fibres on day 1, and achievement of a dense confluent cell monolayer at day 7.

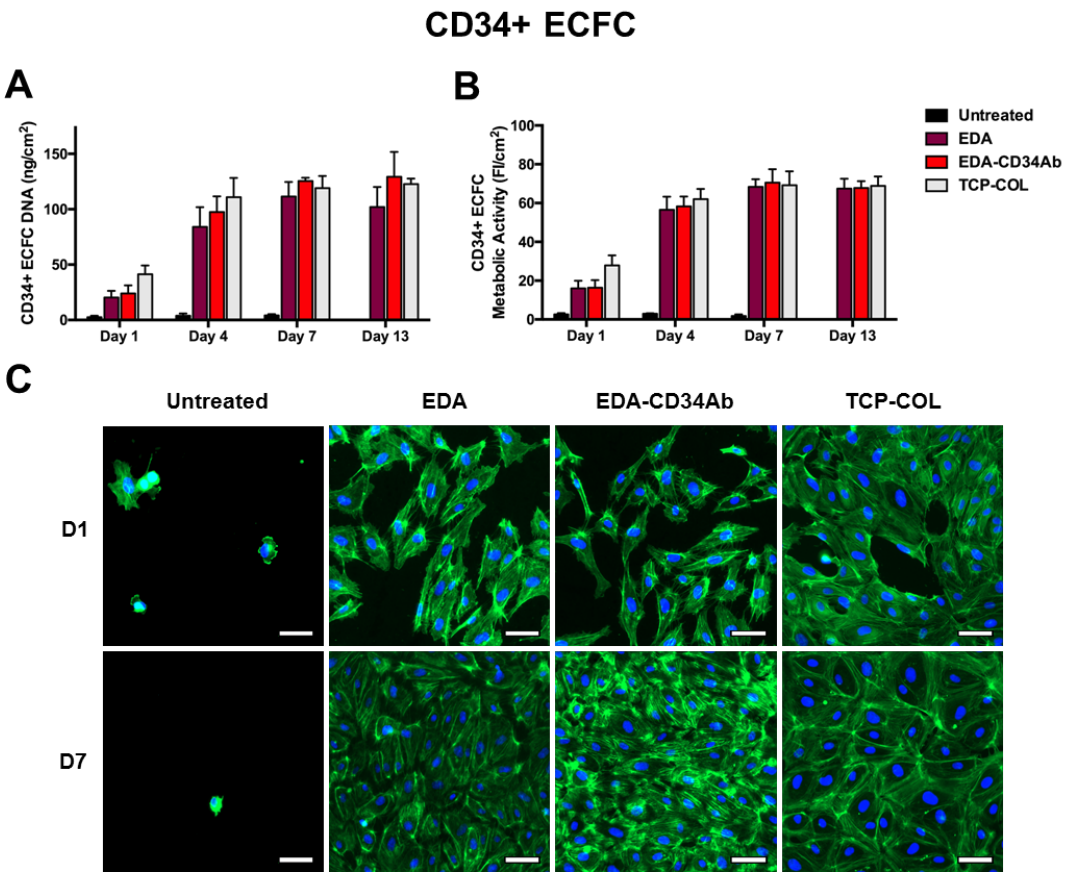

Figure 5.11. (A) Total DNA content (n=3 independent experiments), (B) metabolic activity (n=3 independent experiments) and (C) fluorescent images of CD34+ ECFC on EDA and EDA-CD34Ab, along with untreated and collagen-coated TCP (TCP-COL) positive controls. Data plotted as mean ± SEM.. Scale bar = 50 µm. Green: F-actin, blue: nuclei.

5.3.1.5.2 CD34++ ECFCs

The results for CD34++ ECFC are demonstrated in Figure 5.12. Similarly, cells were barely detected on untreated control as supported by low total DNA content and low metabolic activity on all time points (day 1-13). Cells appeared rounded and non-spread indicative of poor cell adhesion. On EDA and EDA-CD34Ab, the results illustrated the same trend as CD34+ ECFC up to day 7, where total DNA content and metabolic activity were similar to TCP-COL. Nevertheless, CD34++ ECFC on EDA demonstrated a reduction in DNA content on day 13. Whereas, on EDA-CD34Ab, the DNA content was sustained and were higher compared to EDA and TCP-COL (p<0.05). It is noted the metabolic activity levels remained similar throughout. The results here suggest enhanced longer-term survival of CD34++ ECFC on EDA-CD34Ab. This trend was not apparent in the case of CD34+ ECFC (Figure 5.11). Fluorescent images also demonstrate spread cobblestone cell morphology with well-

defined F-actin fibres at day 1, and a confluent, densely packed cell monolayer at day 7 on EDA and EDA-CD34Ab coatings.

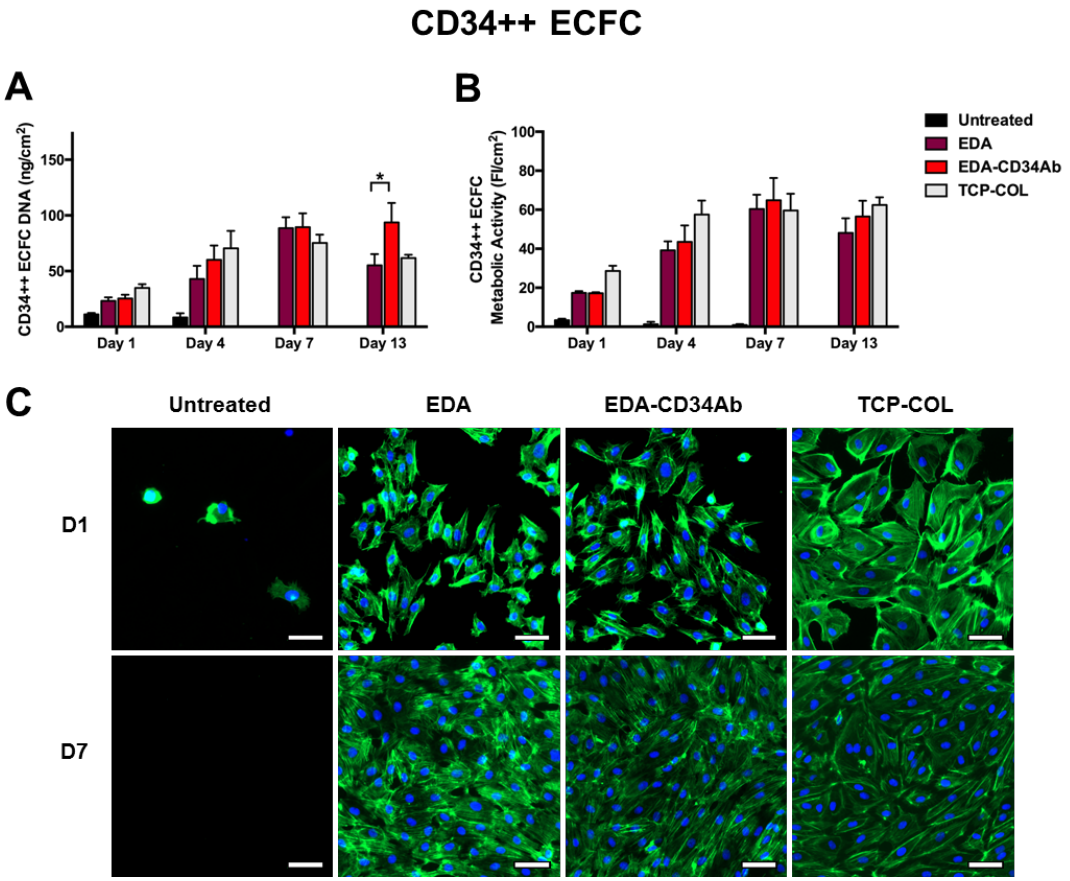

Figure 5.12. (A) Total DNA content (n=3 independent experiments), (B) metabolic activity (n=3 independent experiments) and (C) fluorescent images of CD34++ ECFC on EDA and EDA-CD34Ab, along with untreated and collagen-coated TCP (TCP-COL) positive controls. Data plotted as mean ± SEM. Two-way ANOVA with Tukey's post-hoc tests revealed significant difference in total DNA content between EDA and EDA-CD34Ab at day 13. *=p<0.05. Scale bar = 50 µm. Green: F-actin, blue: nuclei.

5.3.2 REDV peptide immobilisation on PPA-cured coating

5.3.2.1 Optimisation of peptide immobilisation based on HUVEC response

Cysteine-terminated REDV peptides were immobilised on to 50 mM PPA-cured coatings via TYC reaction. The immobilisation procedure requires optimisation on several parameters, including (i) the reaction duration under UV-irradiation and (ii) peptide concentration. As bench-top assays such as Ellman's assay was not sensitive to detect the differences in immobilised peptides, the optimisation was conducted using CGREDV (short) peptides based on cell culture and the response of HUVECs.

5.3.2.1.1 Reaction duration

The reaction duration under UV-irradiation was varied from 0-450s with a fixed peptide concentration of 0.5 mg/mL, and its effect was tested by HUVEC responses at day 1. Figure 5.13 showed that by incubation with CGREDV peptides without UV-irradiation (0s), a low metabolic activity and rounded, non-spread HUVEC morphology was observed. A rise in HUVEC metabolic activity beyond 300 s of UV-irradiation, and a further increase at 450 s were detected. Fluorescent images of HUVECs also showed apparent improved spreading at 300-450 s, which was consistent with metabolic activity data. The results altogether suggest that UV-irradiation is important to conjugate peptides on to the PPA coatings to yield improved cell responses. Hence, UV-irradiation duration of 450 s was kept for subsequent experiments.

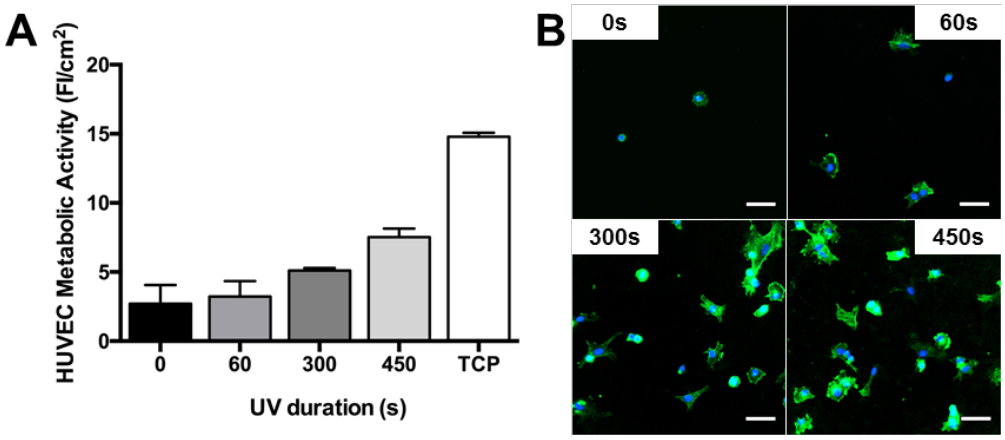

Figure 5.13. (A) HUVEC metabolic activity (n=3), data plotted as mean ± SD; (B) Fluorescent images of HUVECs on PPA-cured coating immobilised with CGREDV peptide at varying UV-irradiation duration on day 1. Scale bar = 50 µm. Green: F-actin, blue: nuclei.

5.3.2.1.2 CGREDV peptide concentration

The concentration of the CGREDV solutions (0-2 mg/mL) for TYC reaction was further investigated on HUVEC behaviour up to day 7, and the results are presented in Figure 5.14. Control sample (0 mg/mL peptide) showed poor cell metabolic activity and spreading behaviour, suggesting that UV-irradiation alone without peptides did not enhance cell fate. It can be seen that under presence of peptides (0.1, 0.5 and 2 mg/mL), HUVEC metabolic activity and spreading behaviour were improved. However, there were no detectable differences in terms of metabolic activity and cell morphology among the concentrations tested. It is also noted that no further increase in metabolic activity and increase in cell density was recorded between day 1 to 7, suggesting that while CGREDV minimally improved cell adhesion and survival, there were no enhancement in subsequent cell proliferation.

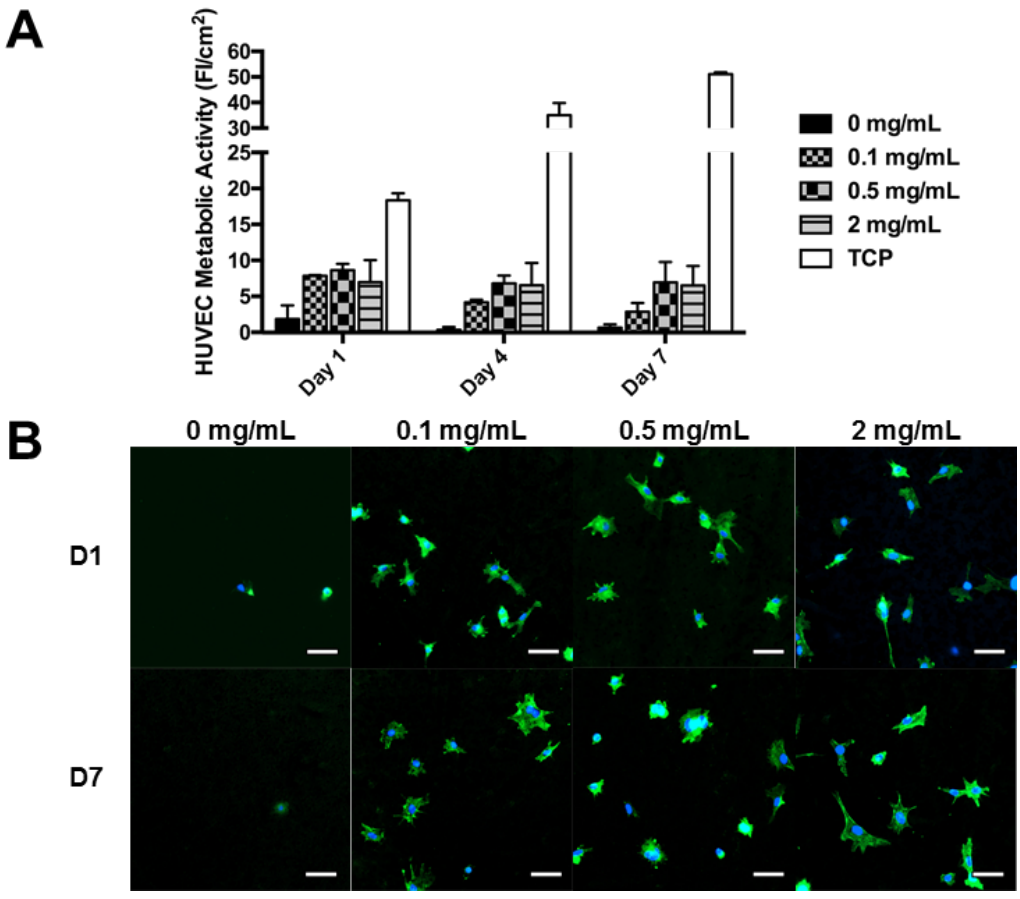

Figure 5.14. (A) HUVEC metabolic activity over 7 days (n=3). Data plotted as mean ± SD. (B) Fluorescent images showing HUVEC morphology on day 1 and 7 on PPA-cured coating immobilised with CGREDV peptides at varying concentrations. Scale bar = 20 µm. Green: F-actin, blue: nuclei.

5.3.2.2 *Immobilisation of peptide of varying spacer arm length and cyclisation*

To further improve the effect of peptide immobilisation on HUVEC fate, peptides with increased spacer arm length (CG_5REDV), and a cyclic peptide (cycREDV) were explored. A peptide with scrambled sequence (CGREVD) as a sham control was also incorporated into the experiments to investigate specificity. Peptides were immobilised under the previously optimised parameters of 450 s UV-irradiation and a concentration of 0.5 mg/mL. A conservative estimate of the amount of peptide immobilised on each coating was measured using the Ellman's assay, and are summarised in Table 5.4. It can be seen that all 4 types of peptides were successfully immobilised on PPA, and that density was similar to each other at ~50 pmol/cm^2.

Table 5.4. Density of immobilised peptides on PPA coatings quantified using Ellman's assay (n=3).

Samples	Description	Peptide density	
		pmol/cm^2	ng/cm^2
PPA-CGREDV	Short	55.5±14.7	37.6±10.0
PPA-CG_5REDV	Long	53.6±11.9	48.6±10.8
PPA-cycREDV	Cyclic	51.4±23.7	38.5±17.8
PPA-CGREVD	Scrambled	56.8±8.9	38.5±6.0

5.3.2.3 *Effect of peptide spacer arm chain length and cyclisation on HUVEC behaviour*

The effect of peptide spacer arm length and cyclisation on HUVEC fate was investigated. Figure 5.15 presents total DNA content and metabolic activity of HUVECs on the modified coatings. The total DNA content and metabolic activity on PPA-CGREDV, PPA-CG_5REDV and PPA-CGREVD from day 1-7 were similar, and were not significantly different from untreated, PPA or PPA-0%peptide controls. A distinctive response was apparent with cycREDV immobilisation, which displayed the greatest enhancement in total DNA and metabolic activity from day 1 to 7. The difference became clearer at day 7, where HUVEC total DNA content and metabolic activity on PPA-cycREDV was significantly higher than all other coatings. However, it is also noted that the total DNA content and metabolic activity on PPA-cycREDV were still approximately three-fold lower when compared with TCP.

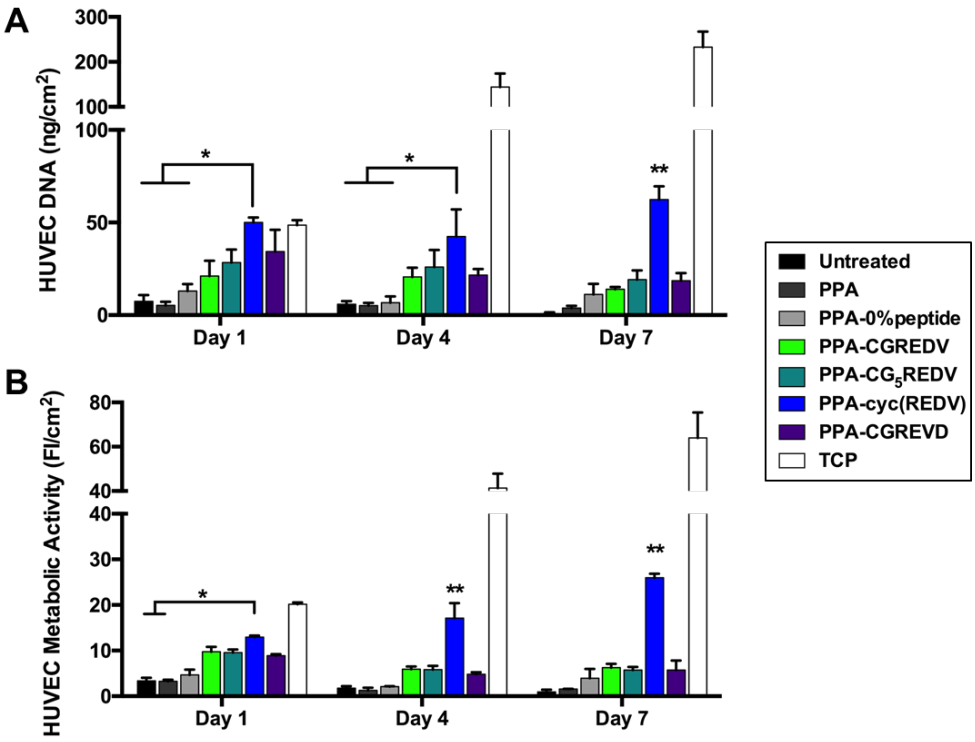

Figure 5.15. (A) Total DNA content and (B) metabolic activity of HUVECs on PPA coatings conjugated with REDV peptides (short, long, cyclic and scrambled) on day 1-7 (n=3 independent experiments). Data plotted as mean ± SEM. Two-way ANOVA with Tukey's post-hoc tests were performed to reveal significant differences between conditions at each time point. *=p<0.05. **=p<0.05 compared with all other sample groups.

Figure 5.16 demonstrates representative fluorescent images of HUVECs on the peptide-immobilised coatings. It can be observed that on PPA-0%peptide controls, HUVECs exhibited a rounded, non-spread morphology and poor cell coverage up until day 7. Immobilisation of all types of peptides, including the scrambled CGREVD, appeared to slightly improve cell spreading behaviour at day 1. However, on PPA-cycREDV, cell spreading appear to be more prominent among all peptides tested, and was sustained up until day 7. The results were in agreement with the total DNA and metabolic activity data described previously. Prolonged HUVEC culture up until 28 days was also conducted on PPA-cycREDV, and fluorescent images of day 14 and 28 showed that HUVEC coverage seem to have greatly increased in comparison to day 7, suggesting that cells were able to continue proliferation until confluence. However, bare patches were still noticeable up to day 28 and had not achieved a fully confluent monolayer.

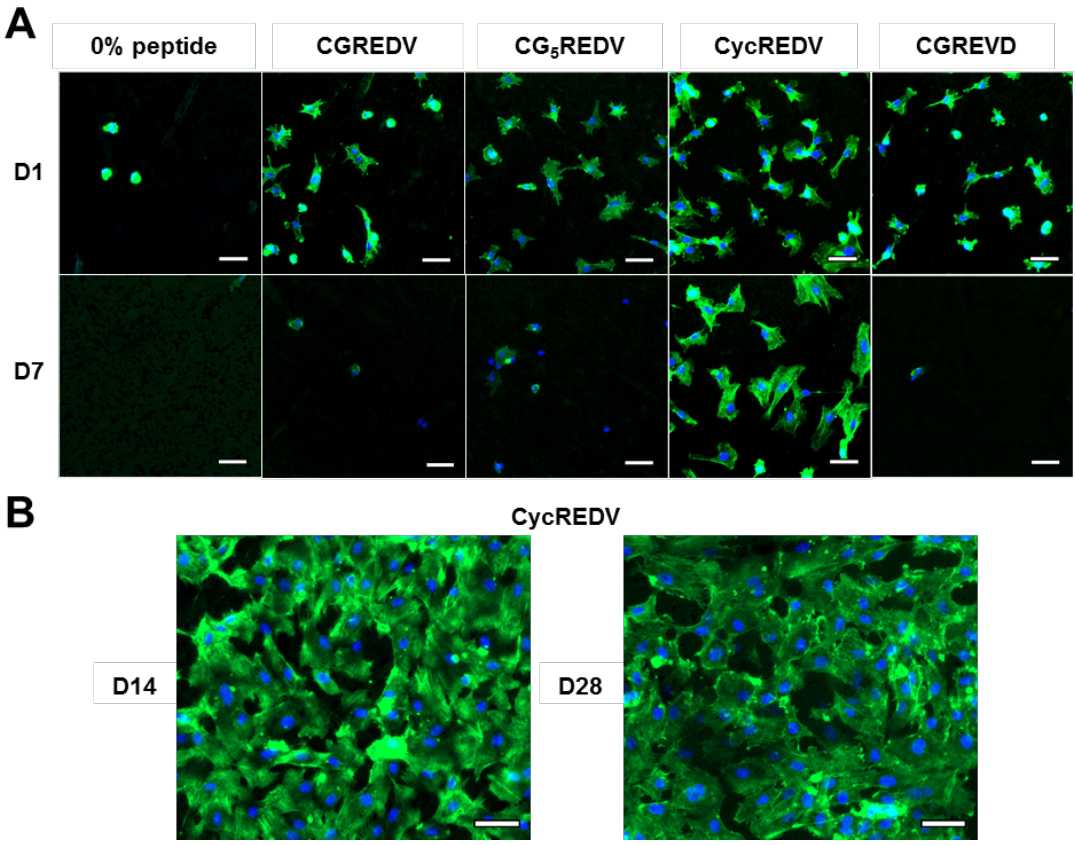

Figure 5.16. Fluorescent images showing HUVEC morphology on PPA immobilised with varying peptide candidates on day 1 and 7, as well as, on PPA-cycREDV up to day 28. Scale bar = 20 µm. Green: F-actin, blue: nuclei.

Vinculin and F-actin stained HUVECs on PPA and PPA-cycREDV were also evaluated at higher magnification as illustrated in Figure 5.17. On PPA coating, cells appear to display a non-spread and highly dense pool of inactive vinculin. On PPA-cycREDV, the cells were increasingly spread and showed distinctive F-actin filaments alongside slightly elongated vinculin-containing FA points at the cell's periphery. This suggests that cycREDV improved FA formation and hence supported cell adhesion leading to improved total DNA content and metabolic activity as reported earlier.

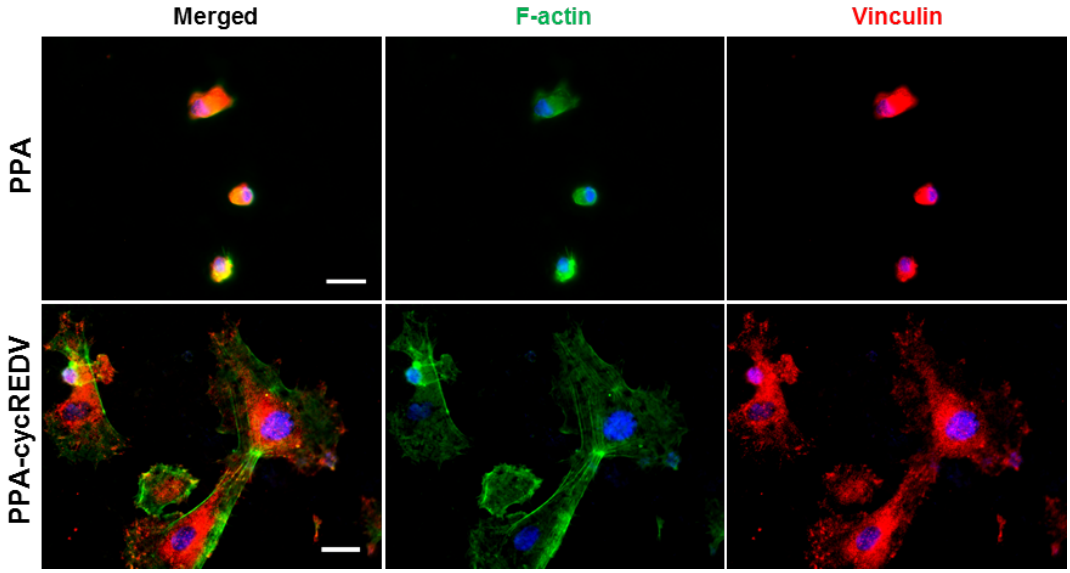

Figure 5.17. Representative fluorescent images of HUVECs stained for focal adhesion complexes and cytoskeletal organisation on day 1 on PPA and PPA-cycREDV. Scale bar = 20 µm. Green: F-actin, red: vinculin, blue: nuclei.

5.3.2.4 Distribution of immobilised peptide by ToF-SIMS

The distribution of cycREDV immobilised on PPA was characterised by ToF-SIMS analysis, and is shown in Figure 5.18.

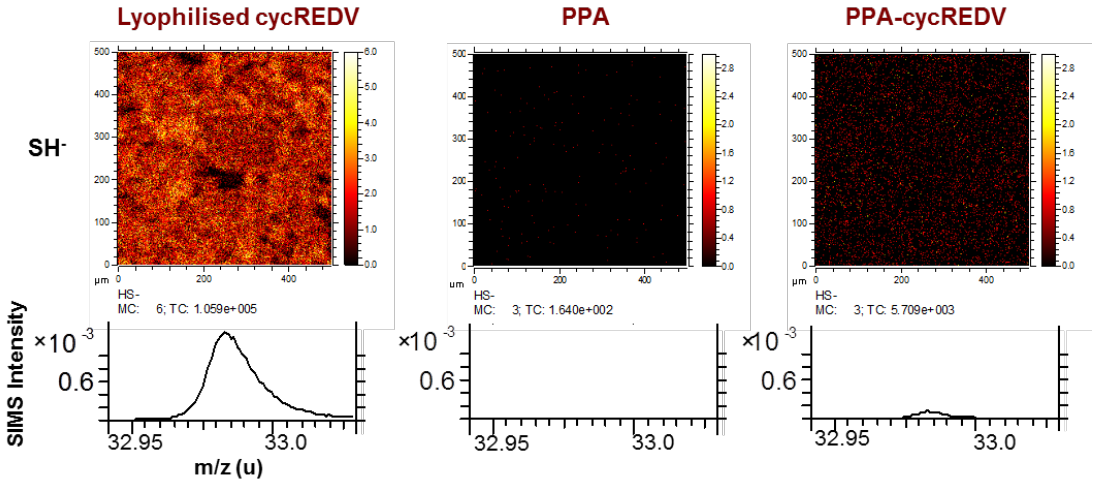

Figure 5.18. ToF-SIMS image maps and spectral intensity of SH^- ion markers on PPA and PPA-cycREDV, illustrating the presence and distribution of cycREDV. Neat lyophilised cycREDV was used as positive reference. Image scale = 500 × 500 µm. (Joint experiment with Mr Jeffrey Leung [277], analysis performed by Dr Long Jiang and Dr David Scurr at University of Nottingham, UK)

Lyophilised cycREDV revealed relatively intense signals of SH^-, which most likely originate from the cysteine residues of the peptides. Hence, SH^- can be a suitable ion marker for mapping of distribution of cycREDV on PPA-cycREDV. No SH^- signal was detected on PPA coating, but PPA-cycREDV revealed increased presence of the

signal. Image mapping of SH^- ions on PPA-cycREDV showed microscopically even distributions, which could indicate a homogeneous immobilisation of cycREDV peptides detected at this scale.

5.3.3 Platelet studies on EDA-CD34Ab and PPA-cycREDV coatings

5.3.3.1 Platelet adhesion

The effect of immobilisation of anti-CD34Ab and cycREDV on platelet adhesion was investigated. Figure 5.19A presents the number of adhered platelets while Figure 5.19B shows representative fluorescent images of platelets to show platelet coverage on each of the coatings.

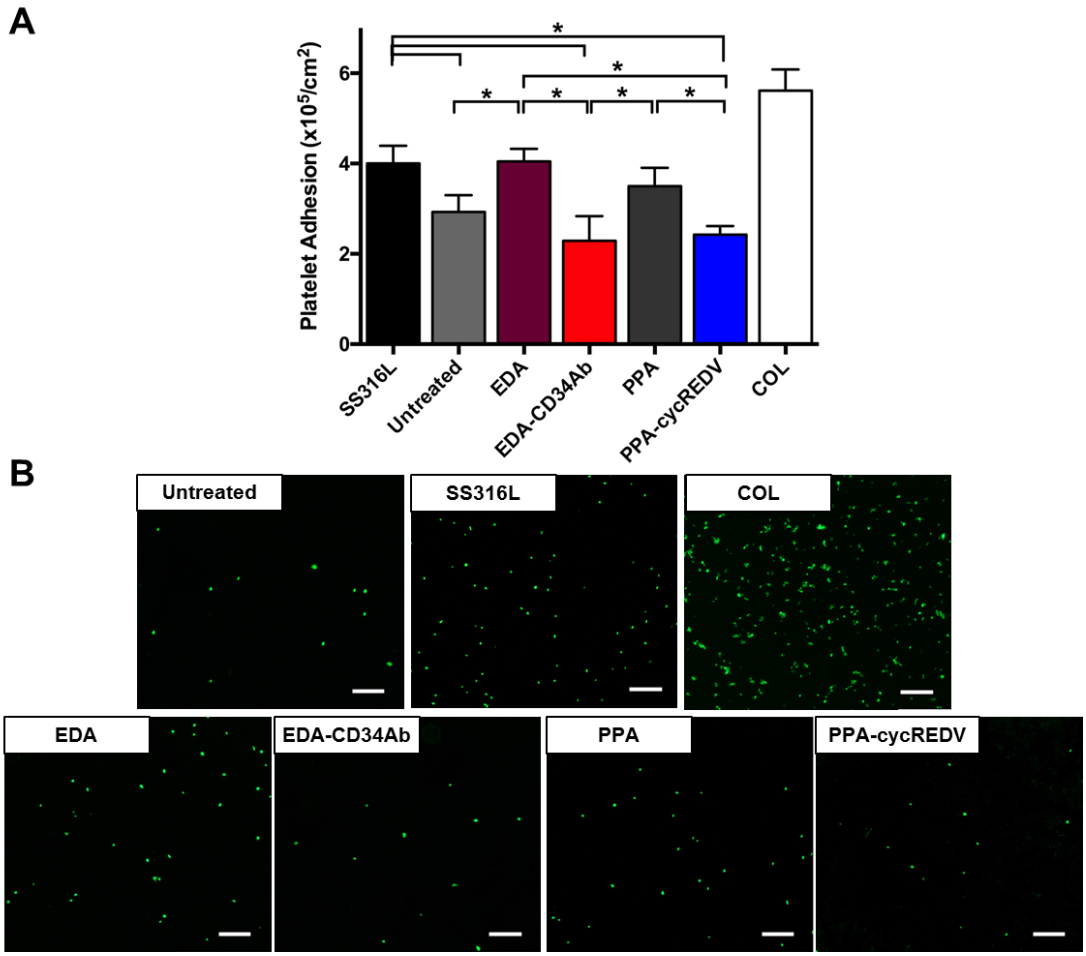

Figure 5.19. (A) Quantification of platelet adhesion (n=3 independent experiments from different platelet donors). One-way ANOVA with Tukey's post-hoc tests were performed to reveal significant differences between different conditions. *=p<0.05. (B) Supportive fluorescent images of platelets on material surfaces. Scale bar = 50 µm. Green: F-actin of platelets.

Platelet adhesion on collagen I coated TCP (COL) was highest with signs of platelet aggregation observed in the fluorescent images. Untreated PCU-PP coatings showed reduced platelet adhesion compared to SS316L controls ($p<0.05$). Nonetheless, EDA curing increased the number of adhered platelet to a level similar to SS316L ($p>0.05$). Interestingly, anti-CD34Ab immobilisation was capable of reducing platelet adhesion ($p<0.05$) by 1.5-2 fold. On the other hand, PPA coating exhibited a platelet adhesion in between that of SS316L and untreated controls. CycREDV immobilisation on to PPA (PPA-cycREDV) also demonstrated a reduction in platelet adhesion ($p<0.05$). Importantly, the fluorescent images, which show platelet coverage on the coatings, appear in agreement with the quantification data of platelet adhesion.

5.3.3.2 Platelet activation based on shape morphology

Platelet morphology obtained by FE-SEM on the coatings are presented in Figure 5.20, and their activation state were determined with reference to Ko and Cooper's classification index (described in section 5.2.6.3.3) [276]. On untreated controls, platelets appeared to be relatively non-spread with some pseudopodia protrusions, indicative of stage II activation. On both SS316L and positive control collagen-coated SS316L (SS316L-COL), fully spread stage V platelet morphology was evident alongside some stage IV spread platelets with prominent pseudopodia, both of which were indicative of highly activated platelets. On EDA coating, platelets displayed a spread-dendritic morphology with protrusions of pseudopodia, some of which were flattened, but with no spreading of hyaloplasm. This is typical of stage III activation. On EDA-CD34Ab, platelet displayed a rounded morphology, and pseudopodia were minimal or non-existent, hence leading to a classification of stage I-II activation. The results suggest that platelet activation was reduced after anti-CD34Ab immobilisation on EDA coatings. As for PPA coatings and PPA-cycREDV, platelets were sparse, low in number and difficult to be located on the surface due to interference from their irregular surface morphology. Platelets that were detected on both coatings appeared non-spread and displayed signs of early pseudopodia development. Hence, both coatings were likely to be of stage II activation based on morphological appearance.

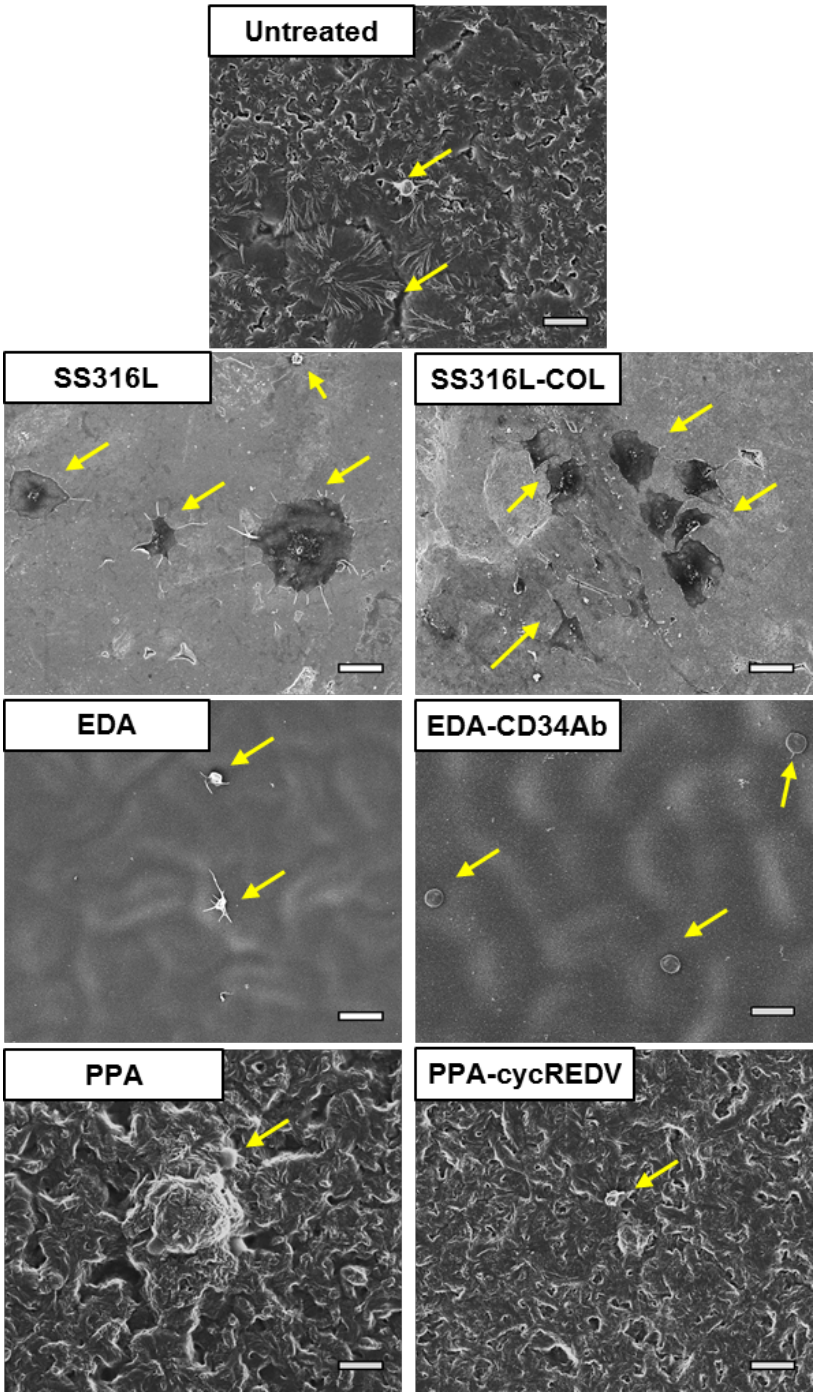

Figure 5.20. Representative FE-SEM images of platelets on sample surfaces for assessment of platelet activation. Yellow arrows as a guide to visualise platelets. Scale bar = 50 µm.

Overall, platelet adhesion and activation results clearly demonstrate that anti-CD34Ab and cycREDV were able to prevent platelet adhesion on the coatings, which can be associated with improved anti-thrombogenicity of the functionalised coatings at the vascular interface.

5.4 Discussion

5.4.1 Selection of conjugation chemistry

5.4.1.1 Antibody immobilisation

Immobilisation of anti-CD34Ab on to EDA-cured coatings was optimised via quantification using direct ELISA, and the reaction concentration (2.5 μg/mL) was selected based on highest amount of detectable anti-CD34Ab on the surface. One limitation of such approach is that it is difficult to determine the actual quantity of immobilised antibodies on surfaces, as it is difficult to accurately produce known quantity of surface-bound antibodies. One possible approach to determine the quantity of immobilised anti-CD34Ab would be using radiolabelling methods.

In this study, it is also demonstrated that immobilisation of anti-CD34Ab using site-directed PO chemistry revealed higher CD34 binding capabilities in comparison to physisorbed antibodies (AD-Ab), suggesting greater exposure of active antigen-binding sites on PO-Ab, and thus higher specificity and reactivity. Physisorption tends to yield a uncontrollable random orientation of antibodies on surfaces, masking some of the antigen-binding sites. The results here are consistent with previous studies [148,197], which have more thoroughly compared PO approach with other non-site-directed approaches such as glutaraldehyde surface activation or EDC/NHS carbodiimide chemistry, both of which involves bioconjugation via the abundant –NH_2 or –COOH functional groups on the antibodies. PO targets the carbohydrate moiety at the Fc region to form aldehyde, hence minimally alters the antigen-binding Fab site. This also allows immobilised antibodies to adopt a ‘tail-on’ conformation, maximising the antigen-binding sites and hence improving their functionality, specificity and reactivity.

Antibody immobilisation using PO is relatively established approach particularly in the field of biosensor technology [200,278], but has not been common in the immobilisation of antibodies on vascular biomaterials. By employing mild oxidation and reduction process to ensure minimal disruption to antibody functions, it is a relatively straightforward methodology with an emphasis on maximisation of specific antibody function.

5.4.1.2 Peptide immobilisation

Radical mediated TYC reaction has recently emerged as a facile and efficient chemical reaction, and has been used for polymer synthesis, protein modification, post-polymerisation modification and surface functionalisation [246]. In this study, TYC reaction conditions for chemical immobilisation of peptides was optimised using CGREDV based on HUVEC fate, owing to lack of sensitivity of bench-top peptide quantification assays. The optimised conditions were extended to four varied peptide structures, i.e. (i) short CGREDV, (ii) long CG_5REDV, (iii) cyclic cycREDV and (iv) scrambled CGREVD, and the density of immobilised peptides estimated using Ellman's assay was found to be similar. The efficiency could be shown by the relatively short reaction duration of 450 s as employed in this study. Indeed, using small molecules such as cysteamine, Feng and co-workers have reported TYC with a reaction duration as fast as 0.5 s in the presence of a photoinitiator, and just 5 s without photoinitiator [235]. The reaction was also employed with a peptide at 15 s of UV-irradiation. Hensarling *et al.* even reported possibility to use 1 h sunlight exposure instead of UV-irradiation [279]. However, other surface modification studies have employed a longer range of UV-irradiation ranging from 20-60 min [244,247,280]. It could also be an avenue to explore longer UV exposure times in this study, although it is noted that longer UV-irradiation duration could lead to degradation to the PCU-PP substrates or immobilised biomolecules.

Another advantage of TYC is that each -C≡C terminal could in principle contribute to immobilisation of two peptide chains, thus largely increasing the overall yield. However, due to potential steric hindrance and limitation of UV penetration to deeper topographies, residual alkyne groups are likely to be present at the coating, which is also reported by Feng and co-workers [235]. This may be better improved by further optimisation of the reaction conditions and apparatus. Furthermore, by employing TYC, which specifically targets the –SH terminals of peptides, it is likely that the orientation of the immobilised peptides remained similar. In terms of practicality, TYC is a facile method that could be employed under ambient conditions. Hence, it serves as promising immobilisation chemistry with potential scaling-up capabilities for medical devices.

5.4.2 Distribution of immobilised biomolecules

Probing the distribution of immobilised biomolecules is vital to ensure homogenous surface modification and cell responses, but has not been commonly reported in many surface modification studies. In this study, ToF-SIMS was utilised to map the distribution of biomolecules on EDA-CD34Ab and PPA-cycREDV coatings,and have successfully demonstrated homogeneous distribution of biomolecules in the microscale, suggesting that the immobilisation procedures using PO and TYC are viable. However, it is also important to probe the nanoscale distribution of the immobilised biomolecules, as nanoscale ligand spacing have been reported to influence cell fate and signal transduction [281,282]. For instance, nanoscale clustering of RGD peptides have been shown to improve HUVEC adhesion and migration compared to a random distribution [283]. Hence, further characterisation of nanoscale distribution may provide further insight into HUVEC behaviour. Nonetheless, the precise characterisation nanoscale biomolecule distribution remains a challenge. The usage of immunogold labelling in tandem with FE-SEM to qualitative visualise such distribution can be a potential solution.

5.4.3 Anti-CD34Ab enhances selectivity towards HUVEC and ECFC

5.4.3.1 HUVECs on EDA-CD34Ab

There were no major detectable differences in HUVEC adhesion, total DNA content and metabolic activity between EDA and EDA-CD34Ab. This is in contrast in other studies, which have reported improved HUVEC densities on anti-CD34Ab immobilised surfaces [148,180,183]. It is likely that HUVEC adhesion and proliferation on EDA-cured coating were already optimal, as indicated by its comparability to TCP. Hence, the potential enhancement provided by anti-CD34Ab may not be detectable. Other reported studies mostly involved base substrates that demonstrated poorer cell fate. It can be postulated that further cell function, protein or gene expression analysis on the EDA-CD34Ab, which have not been explored in this study, might be altered via the presentation of anti-CD34Ab. Nonetheless, the fact that a stable formation of dense endothelial layer on the coatings in prolonged culture up to day 28 is a promising indication of endothelialisation potential and a highlight of this study.

5.4.3.2 ECFCs on EDA-CD34Ab

ECFCs are a highly proliferative subpopulation of the vaguely defined 'EPCs' in the field, which directly leads to endothelial formation (as described in Chapter 1), and were selected for this study to investigate their behaviour on EDA-CD34Ab. Both ECFC lines, CD34+ and CD34++ ECFCs, were able to adhere and proliferate optimally on EDA-CD34Ab up until day 13 in cell culture. Similar to HUVEC, total DNA content and metabolic activities of ECFCs on EDA and EDA-CD34Ab were similar until day 7, but this finding is in contrast to other studies showing enhanced EPC proliferation on anti-CD34Ab immobilised surfaces [149,273]. This may be associated with the optimal ECFC proliferation on EDA, which is comparable to TCP-COL (p>0.05).

The differential trend on day 13 between both CD34+ and CD34++ represents an interesting observation, which has not been reported previously. Total DNA content of CD34++ ECFCs appeared to decline on EDA, but was maintained on EDA-CD34Ab, suggesting enhanced long-term survival with surface presentation of anti-CD34Ab. However, this trend was less apparent for CD34+ ECFCs (p>0.05). It is unclear as to why there is a decrease in cell number at day 13 for CD34++ ECFC but less so in CD34+ ECFC. This may partly be attributed to overconfluence, and both primary cell lines may respond slightly differently to these conditions. The enhanced survivability of CD34++ ECFCs on EDA-CD34Ab may indicate a differential level of cell adhesion or signal transduction response provided by the immobilised anti-CD34Ab. These CD34++ ECFCs possess more CD34 surface markers to anchor to the immobilised anti-CD34Ab, which may in turn promote adhesion and induce a range of intracellular biochemical signals through mechanotransduction to enhance cell fate such as long-term survival. It can be postulated that the increase CD34 expression could lead to increase responsiveness of the ECFCs to the anti-CD34Ab ligands presented on the coating surface. It is likely that certain cell function, signalling mechanism, protein or gene expression may be altered on EDA-CD34Ab coatings, and thus warrants further investigation.

The findings so far suggest that expression levels of CD34 on ECFCs may have an influence on their responses to anti-CD34Ab functionalised surfaces. It is known that EPC/ECFC phenotype and expression profiles vary between individuals [51,284], hence the findings here may suggest individual-specific biological responses to anti-

CD34Ab functionalised medical devices. The interaction between individual specific EPCs and functionalised coatings undoubtedly serve as an exciting avenue for further research, which may foreseeably lead itself to a more personalised approach for vascular devices including vascular stents, grafts or heart valves. Overall, the results so far demonstrated an optimal ECFC fate on EDA-CD34Ab coatings.

5.4.3.3 Platelets on EDA-CD34Ab

EDA curing of PCU-PP led to increased platelet adhesion and activation in comparison to untreated controls. This is attributed to the surface $–NH_2$ and enhanced wettability, which may have improved adsorption of platelet adhesive proteins such as fibrinogen. While this could contribute to improved cell fate, it could also promote platelet adhesion and activation [285,286]. Anti-CD34Ab immobilisation reduced platelet adhesion and activation on EDA-cured coatings. This finding is in agreement with other anti-CD34Ab bioconjugation studies [99,151,287]. Chong *et al*. performed haemocompatibility tests including thromboelastography (TEG) and blood compatibility index assay, which corroborated that anti-CD34Ab conjugation on to PCL improved its haemocompatibility [151]. The enhancement in anti-platelet properties could be attributed to surface passivation of the coatings by anti-CD34Ab, leading to decreased adsorption of other proteins such as fibrinogen, hence decreasing platelet adhesion and activation. The anti-platelet properties described here could connote enhanced anti-thrombogenicity of the coatings, although warrants further verification with other haemocompatibility assays. Such assays can be done using whole plasma, such as measuring partial thromboplastin time (PTT) and activated PTT (APTT) to evaluate blood coagulation cascade, or using whole blood with TEG.

Altogether, the findings of anti-CD34Ab immobilisation illustrated optimal HUVEC and ECFC endothelialisation properties, as well as, reduced platelet adhesion and activation. This suggests that EDA-CD34Ab presented selectively towards EC adhesion over platelets, which is important to enhance *in situ* endothelialisation while minimising incidence of thrombosis.

5.4.4 CycREDV enhances selectively towards HUVEC

5.4.4.1 HUVECs on PPA-cycREDV

In contrast to EDA, PPA coatings did not support HUVEC adhesion and proliferation. Cells on PPA-CGREDV and PPA-CG_5REDV displayed poor adhesion, cell density and metabolic activity, and were not different from PPA-CGREVD. CycREDV immobilisation revealed a notable improvement in cell adhesion, density and metabolic activity from day 1 to 7, indicating improved cell survival. Cells appeared to proliferate and populate the surface fairly well up to day 28, although the coverage and proliferation rate was clearly sub-optimal in comparison to TCP or EDA-CD34Ab.

Most bioconjugation studies utilising linear REDV on polymers have reported enhancement in HUVEC fate [141,160,288], which is in contrast to the findings reported here. However, Noel *et al*. also demonstrated poor HUVEC adhesion or proliferation on REDV-functionalised polyvinylamine-coated PET when compared to RGD and YIGSR peptides at similar density [240]. The reason behind these contrasting findings remains unclear and prompts further investigation. It is plausible that the conformation of peptides might have been affected owing to interactions with hydrophobic PPA-coatings, leading to poor exposure of active sites to cells [259]. The use of cycREDV has not been reported to date for immobilisation on biomaterials. Its superiority in enhancing HUVEC fate may be similar to that of cyclic RGD, which has been known for its improved biostability [289], higher binding affinity [290], as well as, higher activity [291]. Cyclic RGD peptide have been reported to promote better EC adhesion and proliferation than linear RGD [292]. The superiority of cycREDV immobilisation compared to its linear counterparts in this study may be attributed to these favourable characteristics of cyclic RGD. Nevertheless, cell coverage and proliferation even on PPA-cycREDV still appear to be sub-optimal compared to TCP or as seen in the EDA coatings. This may be attributed to insufficient distribution or spacing of REDV ligands, which requires further evaluation. It is also possible that the presence of a single REDV ligand alone on the PPA coating may not be sufficient for optimal enhancement in cell fate.

5.4.4.2 Platelets on PPA-cycREDV

PPA and PPA-cycREDV both demonstrated equally low platelet activation capability. Despite enhancement in HUVEC fate, platelet adhesion was significantly reduced on PPA-cycREDV compared with PPA coating. The results here are likely due to the specificity of REDV peptide, and are in agreement to other studies [160,240,288]. Similar to the case of anti-CD34Ab, this may be attributed to decreased fibrinogen adsorption due to passivation of the surface with chemically immobilised cycREDV. Cyclic RGD peptides have been reported to be able to reduce platelet adhesion and activation further compared to linear RGD, which is attributed to its higher specificity [293]. However, the effect of cycREDV compared to its linear counterparts on platelet adhesion was not investigated in this study, but serve as an interesting future work in vascular biology. Altogether, the findings of cycREDV immobilisation also imply enhanced selectivity towards HUVEC adhesion over platelets.

While ECFCs behaviour has not been evaluated on PPA-cycREDV coatings in this study, it is likely that such cycREDV would result in enhanced ECFC adhesion and survival similar to HUVECs. It has been previously reported that REDV immobilisation supported adhesion and capturing of ECFCs [166]. Considering the enhanced survivability of CD34++ ECFCs on EDA-CD34Ab reported previously, it would be interesting to evaluate long-term cell fate of ECFCs on PPA-cycREDV.

5.4.5 Implications for bioconjugation towards *in situ* endothelialisation

The present study reported in this chapter evaluated two independent PCU-PP platforms with contrasting innate properties: (i) EDA coating with optimal HUVEC adhesion and proliferation, and remained similar after anti-CD34Ab immobilisation; (ii) PPA coating with poor HUVEC adhesion and growth, leading to significant enhancement after cycREDV peptide immobilisation. Both platforms demonstrated anti-platelet properties after bioconjugation. The findings so far may reveal the influence of substrate material properties, particularly surface hydrophilicity, on the enhancement effects of cell fate observed after conjugation with biomolecules, and should be taken into consideration when critically evaluating other studies.

More importantly, this chapter demonstrated the potential of immobilised anti-CD34Ab and cycREDV peptides on chemical cured PCU-PP coatings to enhance

selectivity towards EC adhesion over platelets. This is a major milestone to achieve in the development of substrates that enhance *in situ* endothelialisation. Apart from improved haemocompatibility, which could prevent thrombosis upon implantation, such selectivity promotes specific recruitment of endothelial lineage cells, including ECFCs/EPCs, to form a functional endothelium on the coating surface. This selectively is vital especially due to the low number of ECFCs/EPCs in circulating blood, which may take time to be captured and proliferate to form a functional endothelium despite their high proliferative capability. It is recognised that the *in vivo* environment is complicated by the presence of many competing cells types, most notably SMCs or leukocytes (e.g. monocytes, macrophages). Both of these cell types have been associated to inflammation and formation of NIH, which ultimately lead to ISR [9,294]. Hence, it is also important to determine the responses of such cell types on newly developed coatings. Promisingly, studies have reported the non-selectively of anti-CD34Ab [180] and REDV peptides [140,141,160] towards SMC proliferation. However, the response of immune cells has not been widely explored on biomolecule-immobilised coatings and remains poorly understood. Along with the emerging focus on immunomodulatory biomaterials, it is foreseeable that in the near future this area will be an exciting research area [295]. In addition, to better mimic the *in vivo* environment, further studies evaluating capturing efficiency and subsequent fate of these cells on the coatings should be performed under simulated physiological flow conditions. Furthermore, the development of such platforms may be further complicated by protein adsorption *in vivo*. In this study, a low serum media of 2% FBS was used for cell culture. The interaction of the coatings with serum or plasma proteins in blood remains unexplored. Creating anti-fouling surfaces via strategies such as PEGylation may circumvent the problem [67,296], but the effects of anti-fouling, which typically also prevents cell adhesion, on EC behaviour should be investigated.

The choice of anti-CD34Ab and REDV peptides are not without their limitations. As reviewed in section 1.6.3.1, CD34 is not an entirely specific to EPCs, due to its expression by haematopoietic stem cells (HSCs) and other cell types. Furthermore, clinical results from Genous^{TM} stent, a commercialised anti-CD34Ab functionalised stent, have been associated with higher degree of NIH. As for REDV peptides, its stability and functionality *in vivo* is still poorly explored, although cycREDV may

provide an advent for further development due to its potentially enhanced biostability. A wide range of studies has investigated other types of antibodies, peptides and also aptamers to capture EPCs. However, no systematic comparative studies have been performed to evaluate these candidates. Furthermore, the differences in biomolecule production or synthesis, peptide sequences, immobilisation chemistry, and selection of base substrate materials employed in different studies complicate comparisons. Hence, using similar approaches, varying types of antibodies or peptides could be immobilised on to the developed chemically cured PCU-PP coating platform for future investigations. Moreover, it has been demonstrated in Chapter 3 that EDA and PPA cured coatings can be applied on to stents via ultrasonic atomisation spray coating technique. Hence, by applying the bioconjugation procedures developed in this chapter, anti-CD34Ab or cycREDV functionalised vascular stents based on PCU-PP could be manufactured with relative ease.

5.5 Conclusion

This chapter describes the potential to immobilise anti-CD34Ab and REDV peptides on to EDA and PPA cured PCU-PP coatings that presents surface $–NH_2$ and-C≡C groups. Both bioconjugation approaches promoted selectivity towards EC over platelet adhesion, serving as an important milestone towards the realisation of *in situ* endothelialisation. EDA-CD34Ab supports HUVEC and ECFC adhesion and proliferation, and reduces platelet adhesion and activation. PPA-cycREDV displays enhanced HUVEC adhesion and supports their subsequent proliferation, as well as, reduces platelet adhesion and maintains low platelet activation. Nevertheless, the findings raise important questions particularly related to the complex *in vivo* environment, as well as, the selection of biomolecules to achieve *in situ* endothelialisation. While there is so far no ideal biomolecule for specific capturing EPCs from blood, it may be postulated that combinatorial immobilisation of multiple EPC-capturing and pro-endothelialisation biomolecules may lead to synergistic effects in promoting *in situ* endothelialisation capability for vascular stents, as well as, a range of other cardiovascular devices.

Chapter 6

Multifunctional Chemical Cured Pre-polymer Coatings for Co-immobilisation of Antibody and Peptide

6.1 Introduction

The advent of *in situ* endothelialisation aims to promote long-term patency of blood-contacting devices such as vascular stents by enhancing endothelialisation upon implantation *in vivo*. Upon contact with blood, vascular biomaterials adsorb plasma proteins, which subsequently direct the adhesion and fate of platelets, leukocytes, endothelial cells (ECs), endothelial progenitor cells (EPCs), smooth muscle cells (SMCs) and other cell types. Platelets, which are abundant in blood, are the first components to come into contact with the adsorbed protein layer [297]. Hence, the complexity lies on the requirement to simultaneously regulate multiple cell responses to achieve selectivity towards endothelialisation *in vivo*.

Hitherto, immobilisation of single type of biomolecule or drug on to vascular biomaterials has been widely explored to promote *in situ* endothelialisation (as described in previous chapters). However, immobilisation of a single biomolecule may not be sufficient to orchestrate multiple cell responses *in vivo*. The success of *in situ* endothelialisation does not only rely on EPC capturing, but also optimal responses upon blood contact. These include enhanced adhesion, proliferation and differentiation of EPCs, prevention of SMC overproliferation, anti-thrombogenicity, as well as, a desirable immune response. Therefore, it is postulated that a multicomponent approach involving co-immobilisation of more than one type of biological molecules may be necessary.

Combinatorial approaches using physical and biochemical cues such as biomolecules could be used to modulate different cell signalling pathways leading to synergistic effects on cell selectivity and cell fate [66]. In the context of *in situ*

endothelialisation, this multicomponent approach may lead to enhanced endothelialisation, and reduced complications at the vascular interface, such as thrombosis and in-stent restenosis (ISR). Presently, there have been several studies that had explored such avenues and reported synergistic enhancements in selective endothelialisation, as reviewed in section 1.6.5. Most of these studies involve the use of combinatorial endothelial cell adhesive ligands (e.g. anti-CD34Ab, RGD peptides) with growth factors (e.g. VEGF, bFGF) [185,298,299], anticoagulant (e.g. heparin) [183], as well as, topographical cues [293].

To controllably achieve co-immobilisation of biomolecules, multifunctional surfaces consisting of a variety of functional groups are desirable. The production of multifunctional surfaces typically necessitates multi-step approaches and/or specially designed chemical reactions and synthesis. For example, Spruell *et al*. produced polymers with azide (-N_3) and alkyne (-C≡C) functionality by controlling the extent of thermal crosslinking between -N_3-functionalised and -C≡C-functionalised polymers [300]. Other studies tend to incorporate one or more specific active sites which are prone to reactions with selected molecular precursors within synthesised polymer to incorporate post-polymerisation multifunctionality [301,302]. Yang *et al*. reported another possible approach by immobilising multifunctional gallic acid molecules (containing –COOH and –OH groups) on to –NH_2 functionalised plasma-polymerised allylamine, yielding triple presentation of –NH_2, -COOH and phenol functional groups [133].

Chemical curing procedure, as developed in this Chapter 3, utilises the highly versatile chemistry of poly(carbonate)urethane pre-polymers (PCU-PP) as building blocks to produce coatings with a range of surface functional groups and micro- and nanoscale topographies. It is envisaged that this approach can be utilised as a facile approach to yield and tailor multifunctional coatings. It is hypothesised that by chemical curing in a combination of small molecular precursors such as EDA and PPA, a multifunctional coating of –NH_2 and -C≡C groups with changes in surface topography can be easily achieved. Subsequently, the EDA-PPA multifunctional surfaces can be applied for controlled co-immobilisation of biomolecules. It is postulated that combinatorial immobilisation of cycREDV and anti-CD34Ab may further augment EC behaviour, and was investigated in this chapter.

6.2 Materials and Methods

6.2.1 Combinatorial chemical curing of PCU-PP coating to yield multifunctional chemistry

Combinatorial approaches to chemical curing of PCU-PP coatings was conducted with minor adaptation to the procedure described in section 3.2.2. A combination of EDA and PPA was used as the curing agent in order to tailor coating chemistry with combinatorial $-NH_2$ and -C≡C functional groups. 50 mM PPA and 50 mM EDA were mixed at different proportions to yield EDA-PPA solutions (0, 12.5, 25, 50, 75 and 100% 50 mM PPA in 50 mM EDA). Spin-coated silanised SS316L were immediately cured in these solutions. The procedure and expected surface chemistry are depicted in Figure 6.1.

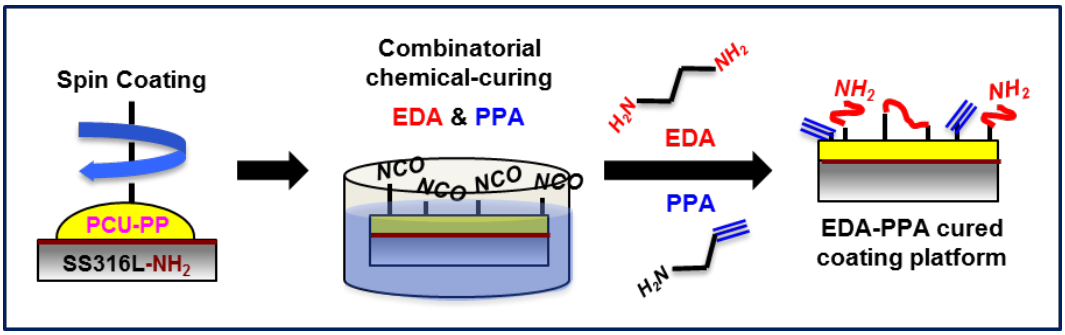

Figure 6.1. Schematic diagram demonstrating combinatorial chemical curing procedures using EDA and PPA curing solutions to yield $-NH_2$ and -C≡C surface chemistry.

6.2.2 Co-immobilisation of anti-CD34Ab and cycREDV on EP coating

CycREDV and anti-CD34Ab were co-immobilised on to a selected formulation of EDA-PPA cured coatings (EP coating). The details of the immobilisation protocols are described in section 5.2.1. EDA-PPA coatings were first immobilised with 0.5 mg/mL TCEP-reduced cycREDV containing Irgacure® 2959 (I2959) via thiol-yne click (TYC) reaction using 450 s of UV-irradiation, yielding EP-cycREDV. Coatings were then incubated in 70% ETOH for 20 min to minimise risk of infection. Subsequently, under sterile conditions, the coatings were further immobilised with 2.5 µg/mL anti-CD34Ab using periodate oxidation (PO) conjugation chemistry, hence yielding EP-cycREDV-CD34Ab. Samples were maintained in sterile conditions, and stored in PBS at 4ºC prior to experiments.

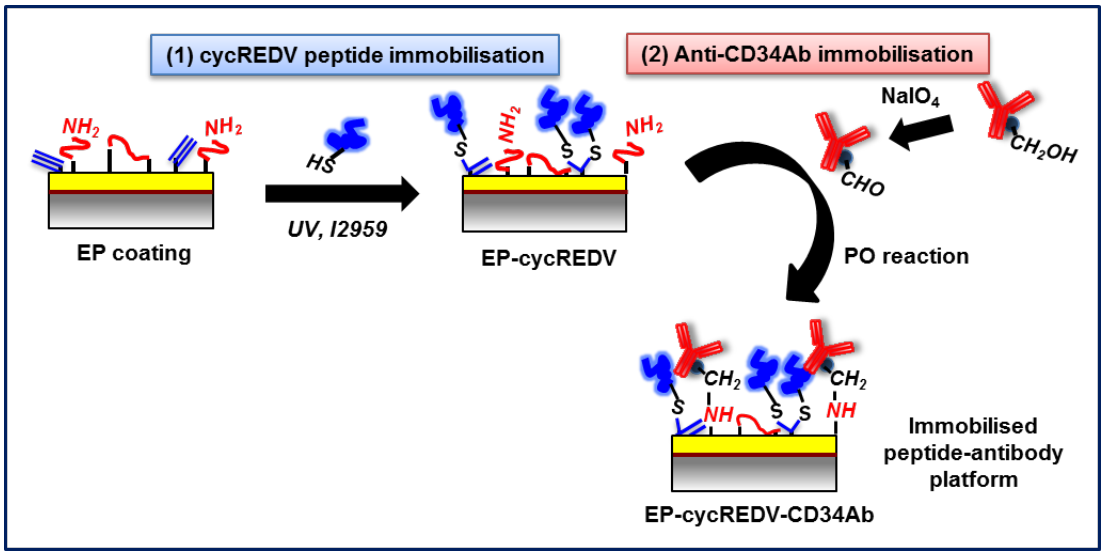

Figure 6.2. Illustration of co-immobilisation of cycREDV and anti-CD34Ab on EDA-PPA multifunctional coatings. EDA-PPA coatings were first immobilised with (1) cycREDV using TYC, and then sterilised, followed by (2) anti-CD34Ab immobilisation using PO chemistry.

6.2.3 Coating characterisation

6.2.3.1 Water contact angle (θ°) measurements

θ° was measured on EDA-PPA coatings cured at varying EDA-PPA concentrations with the same methodology as described in section 2.2.5.1.

6.2.3.2 Colorimetric assay quantifying surface functional groups

Colorimetric assays were employed to measure surface -NH_2, and -C≡C groups of coatings cured in EDA-PPA of varying EDA-PPA compositions. Furthermore, surface -NH_2 groups were quantified after cycREDV immobilisation to determine remaining amount of –NH_2. The procedure for quantification of surface –NH_2 and -C≡C functional groups using Orange II and post MPA-TYC TBO assays were used as described in section 3.2.4.3.

6.2.3.3 Field emission scanning electron microscopy (FE-SEM)

Coatings cured in varying EDA-PPA compositions were imaged with FESEM as described in section 2.2.5.3.

6.2.3.4 Direct ELISA

Direct ELISA was employed to confirm immobilisation of anti-CD34Ab on both EP-CD34Ab and EP-cycREDV-CD34Ab. The protocol is as reported in section 5.2.2.1.

6.2.3.5 ToF-SIMS

ToF-SIMS was conducted as described in section 5.2.2.4 to verify presence and map distributions of immobilised anti-CD34Ab and cycREDV on the coatings.

6.2.4 Cell culture, seeding and *in vitro* assays

HUVECs were used for evaluation of endothelial cell response on cured PP coatings with varying EDA-PPA compositions, as well as, cycREDV and anti-CD34Ab immobilised EP coatings. The details of cell culture, maintenance, as well as, cell seeding are described in sections 4.2.2 and 4.2.3. HUVECs of passages between P4-7 were used throughout this study.

6.2.5 Characterisation of HUVEC response

HUVEC fate was characterised using total DNA quantification and AlamarBlue® metabolic assays. Experiments were repeated independently at least 3 times (n=3), each with triplicated technical repeats per condition. The procedures are as described in section 4.2.4. Qualitative images were obtained by F-actin cytoskeletal and DAPI nuclear staining on formalin fixed cells at day 1 and 7, as described in section 4.2.5.

6.2.6 Statistical analysis

Data were reported as mean ± standard deviation (SD), unless otherwise stated. Statistical analysis was conducted using Prism GraphPad software (version 6.0). HUVEC total DNA quantification and metabolic activity data on coatings co-immobilised with anti-CD34Ab and cycREDV were statistically tested using two-way ANOVA with Tukey's post-hoc test. *P* values of $p<0.05$ were considered to be statistically significant.

6.3 Results

6.3.1 EDA-PPA combinatorial chemical cured coatings

Spin-coated PCU-PP coating on SS316L were chemically cured for 15 min in EDA-PPA solutions of varying proportions of 50 mM EDA and 50 mM PPA in IPA: 0% (100% EDA), 12.5%, 25, 50, 75% and 100% PPA.

6.3.1.1 Water contact angle (θº) measurements

θº measurements of EDA-PPA cured coatings are shown in Figure 6.3. There appears to be a distinctive trend of increasing θº from 68.3º±1.8 at 0% PPA (100% EDA) to 91.5º±0.7 at 100% PPA with increasing %PPA, indicating increased hydrophobicity. This may be attributed to increasing surface -C≡C groups and decreasing $–NH_2$ groups.

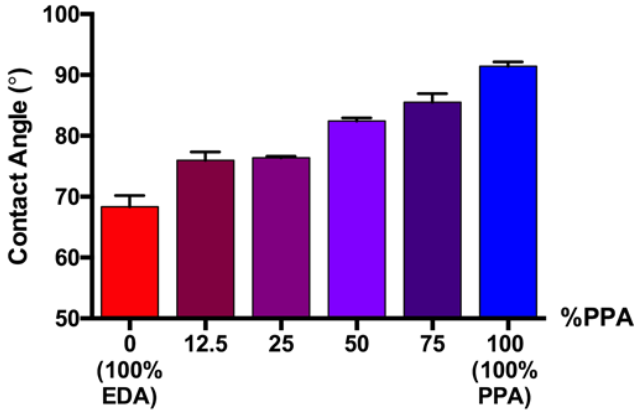

Figure 6.3. Water contact angle (θº) measurements of PCU-PP coatings cured at varying EDA-PPA composition (n=3).

6.3.1.2 Quantification of surface functional groups

Surface $–NH_2$ group densities on the EDA-PPA cured coatings quantified by Orange II assay are depicted in Figure 6.4. Surface $–NH_2$ groups was highest at 100% EDA coating, but declined by approximately two-fold at 12.5% and 25% PPA. Further reduction of $-NH_2$ groups was apparent as %PPA increases to 100%. No significant difference in surface $–NH_2$ group density was detected between 50-100% PPA.

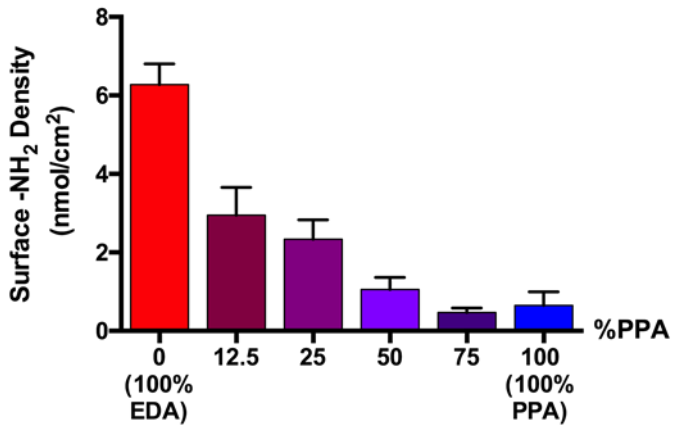

Figure 6.4. Quantification of surface $-NH_2$ group density by Orange II assay on PCU-PP coatings cured at varying EDA-PPA composition (n=4).

Surface -C≡C groups on EDA-PPA cured coatings were quantified by TBO assay after reaction with MPA via TYC. As shown in Figure 6.5, surface –COOH groups were relatively low on unmodified EDA and PPA controls. After TYC reactions with MPA, all samples, including 100% EDA, revealed a significant increase in –COOH group density. No major differences in –COOH group density was observed between the coatings, except for 75% PPA, which showed lower –COOH functionality. Overall, the results did not show specific trend as detected in Orange II and contact angle measurements. It is also unclear as to why 100% EDA revealed similarly enhanced –COOH density after click reactions with MPA.

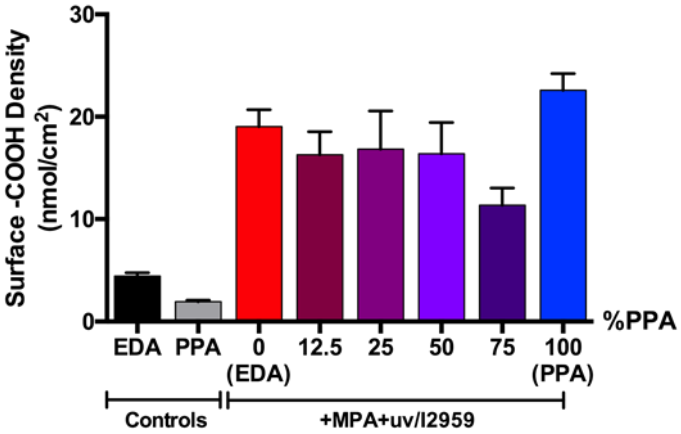

Figure 6.5. Surface –COOH density following TYC reaction with MPA on PCU-PP coatings cured at varying EDA-PPA compositions (n=3).

6.3.1.3 Surface morphology by FE-SEM

Surface morphology of PCU-PP coatings cured at varying EDA-PPA compositions are illustrated in Figure 6.6. 100% EDA control samples yielded surface micro-ridges and nanofeatures as observed previously in section 3.3.4.1. At 12.5% PPA, micro-ridges similar to EDA were apparent but seem less distinctive, which may be attributed to a lower height profile. Beyond this PPA concentration (>25%PPA), coatings appeared to be relatively flat with minimal detectable defects in the microscale. Higher magnification images revealed formation of ~100-200 nm wide nanowhisker-like structures on EDA-PPA curing composition above 25% PPA. On 75% PPA, the distribution of nanowhisker features appeared to be more irregularly alongside appearance of nanofibrous like structure, similar to those observed in 100% PPA control (as shown in section 3.3.4.1).

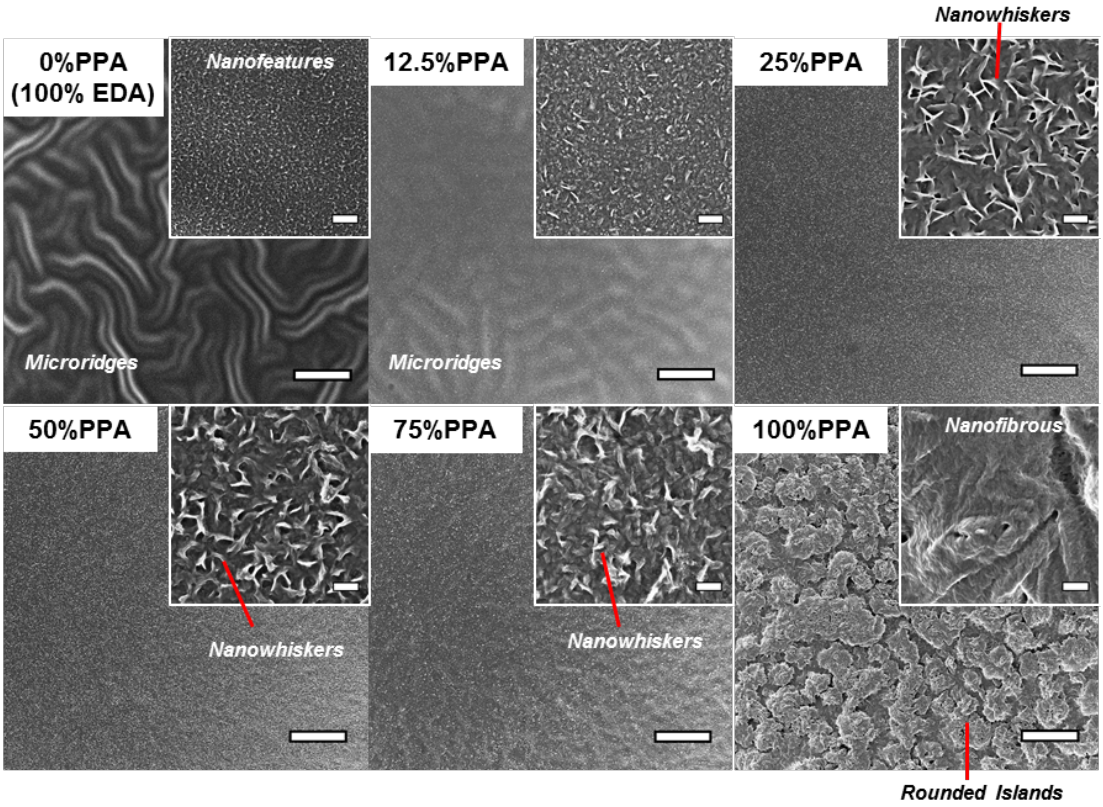

Figure 6.6. Representative FESEM of PCU-PP coatings cured at varying EDA-PPA curing compositions. . Magnification = 1000× (scale bar = 25 μm); Inset magnification = 25000× (scale bar = 1 μm).

6.3.1.4 HUVEC fate

HUVEC responses on PCU-PP coatings cured at varying EDA-PPA compositions were evaluated by total DNA quantification and metabolic activity measurement on day 1-7, shown in Figure 6.7A-B. Both HUVEC total DNA content and metabolic activity revealed a similar reducing trend with increasing %PPA from 0% to 100%. Both measurements were highest on positive control 100% EDA, where cells adhered and proliferated optimally up to day 7, consistent to that reported previously in Chapter 4. 12.5% PPA was consistently slightly lower on both measurements up to day 7, while 25% PPA showed a ~2-fold reduction in total DNA and metabolic activity values up to day 7 compared to 100% EDA, suggestive of sub-optimal HUVEC fate. At 75-100% PPA, total DNA content and metabolic activity were lowest across all time points, and displayed no signs of increase up to day 7, hence suggesting poor HUVEC adhesion and survival.

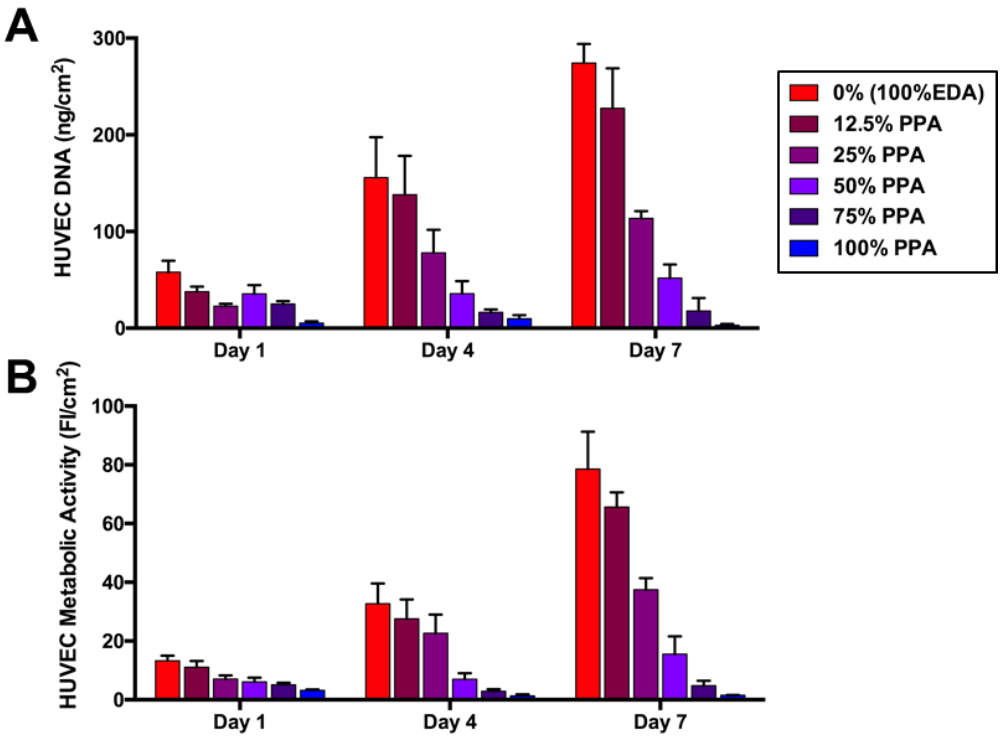

Figure 6.7. (A) Total DNA quantification and (B) metabolic activity of HUVEC on PCU-PP coatings cured at varying EDA-PPA composition on day 1-7 (n=3 independent experiments). Data plotted as mean ± SEM.

Fluorescent micrographs of F-actin stained HUVEC are demonstrated in Figure 6.8. On 100% EDA, cells appeared spread with distinctive F-actin stress fibre indicative of preferential cell adhesion, and were able to proliferate to confluence on day 7. Decreasing %PPA seemingly resulted in more appearance of less spreaded and

rounded cell morphology, as well as, decreased cell proliferation up to day 7. 12.5-25% PPA were able to support spreaded HUVEC morphology on day 1, as well as, formation of confluent HUVEC monolayer on day 7, particularly for 12.5% PPA. At 50% PPA and above, rounded cell morphology on day 1 and poorer cell coverage on day 7 were increasingly apparent, suggestive of poorer cell adhesion and survival.

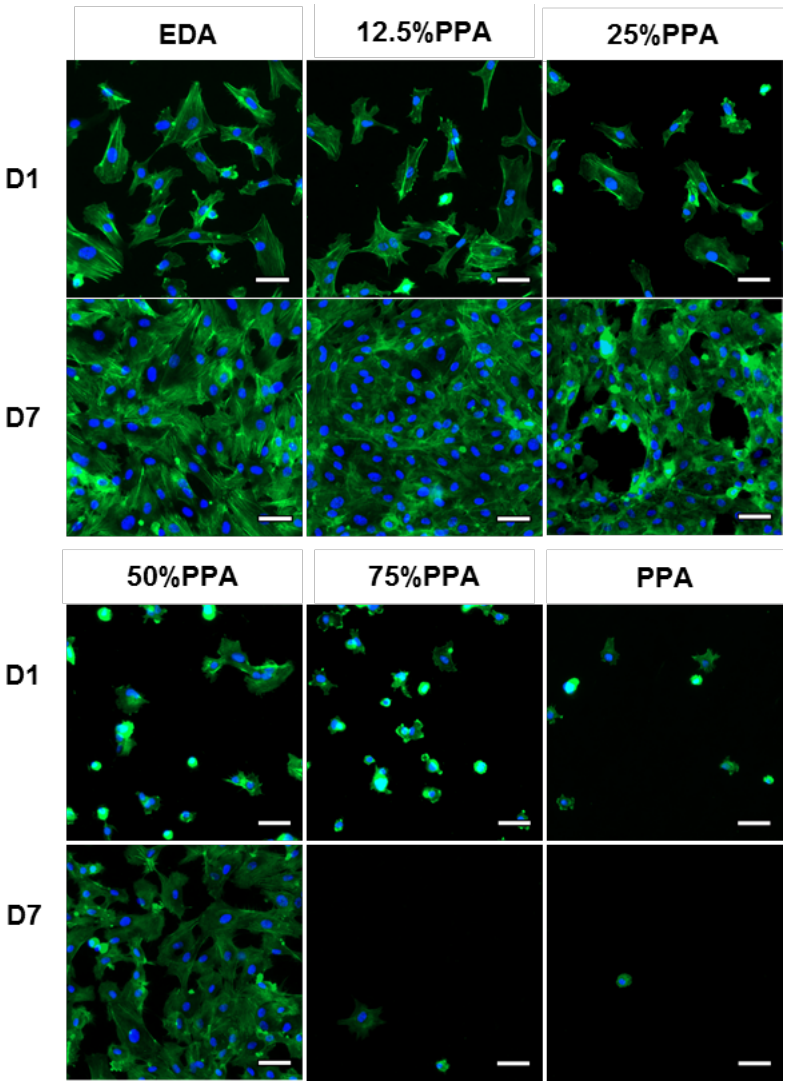

Figure 6.8. Fluorescent images of HUVECs on PCU-PP coatings cured in varying EDA-PPA composition on day 1 and 7, illustrating morphology and coverage. Scale bar = 50 µm. Green: F-actin, blue: nuclei.

The results so far demonstrate the potential to tailor the $–NH_2$ and -C≡C chemistry while altering nanotopography on EDA-PPA multifunctional coatings. These properties subsequently result in a differential cell response, where trends of increasing cell adhesion, density and metabolic activity on coatings with higher $–NH_2$ group density (lower %PPA).

6.3.2 Co-immobilisation of cycREDV and anti-CD34Ab on EDA-PPA coatings

The multifunctional EDA-PPA cured coatings were used for co-immobilisation of cycREDV and anti-CD34Ab. A curing composition of 25%PPA/75%EDA (EP) was selected due to its ~2 fold decrease in surface $–NH_2$ groups, presence of -C≡C groups, and its ability to support HUVEC adhesion and growth. The co-immobilisation procedure was conducted first by cycREDV immobilisation, followed by 70% ETOH disinfection and subsequently anti-CD34Ab immobilisation.

6.3.2.1 Verification of antibody immobilisation after peptide immobilisation

To ensure surface $–NH_2$ groups remained on anti-CD34Ab immobilisation after cycREDV immobilisation, the remaining surface $–NH_2$ group density after cycREDV immobilisation on EP was measured using Orange II assay. Figure 6.9A shows that surface $–NH_2$ groups remained similar following cycREDV immobilisation, suggesting no detectable side reactions between $–NH_2$ and cycREDV had occurred. Furthermore, direct ELISA was used for quantification of immobilised anti-CD34Ab on EP and EP-cycREDV. As depicted in Figure 6.9B, the coatings without anti-CD34Ab did not revealed signals for anti-CD34Ab, while EP-CD34Ab and EP-cycREDV-CD34Ab demonstrated similar levels of immobilised anti-CD34Ab. The results support that the immobilisation procedures had occurred as intended, with no detectable interference between both immobilisation chemistries used in this study.

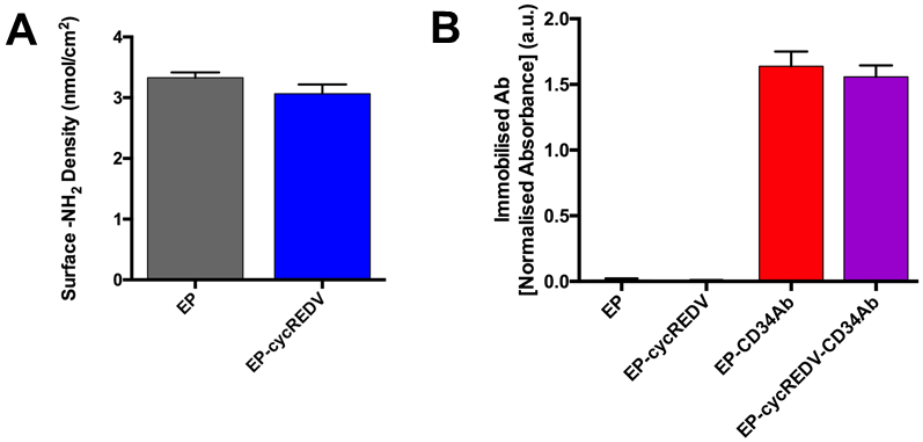

Figure 6.9. (A) Surface $–NH_2$ density on EP coating before and after cycREDV immobilisation; (B) Quantification of immobilised anti-CD34Ab via direct ELISA on EP, EP-cycREDV, EP-CD34Ab and EP-cycREDV-CD34Ab (n=3). (Joint experiment with Mr Jeffrey Leung [277])

6.3.2.2 ToF-SIMS mapping

Figure 6.10 presents ToF-SIMS distribution map and spectra of SH^- ion markers on the biofunctionalised EP coatings.

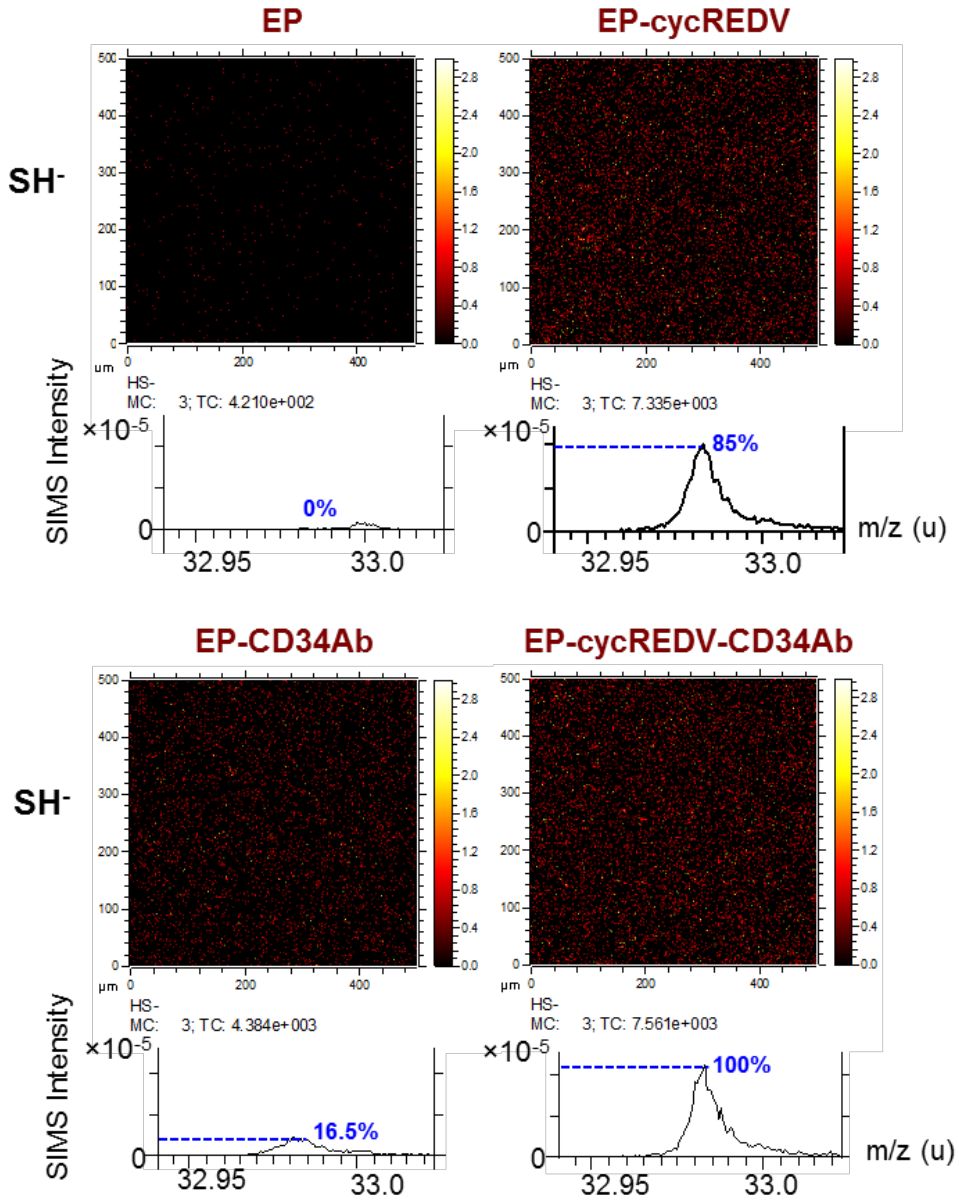

Figure 6.10. ToF-SIMS representative image map and spectral intensity of SH^- ions on EP coating after cycREDV and/or anti-CD34Ab immobilisation. Percentage values stated are with respect to spectral intensity of EP-cycREDV-CD34Ab. Image scale = 500×500 µm. (Joint experiment with Mr Jeffrey Leung [277], analysis performed by Dr Long Jiang and Dr David Scurr at University of Nottingham, UK).

As described previously in section 5.3.1.3, SH^- appeared to be a prominent ion marker for association to both anti-CD34Ab and cycREDV. SH- signals were not present on EP coatings, but increased in EP-cycREDV and EP-CD34Ab, confirming cycREDV and anti-CD34Ab immobilisation. SH^- intensity appeared five-fold higher

and more densely distributed on EP-cycREDV than EP-CD34Ab, although this may be associated to the larger size and lower SH^- density present on anti-CD34Ab compared to cycREDV. SH^- distribution appeared even on both coatings in the microscale, suggesting a homogeneous distribution of immobilised cycREDV and anti-CD34Ab. EP-cycREDV-CD34Ab revealed an enhanced and densely distributed SH^- signal likely to be attributed from combinatorial of cycREDV (~85%) and anti-CD34Ab (~15%).

6.3.2.3 HUVEC responses to biofunctionalised multifunctional EP coating

The potential of combinatorial biomolecules immobilised on multifunctional EP coatings to influence HUVEC behaviour was investigated. Figure 6.11 demonstrates HUVEC total DNA content and metabolic activity on these coatings.

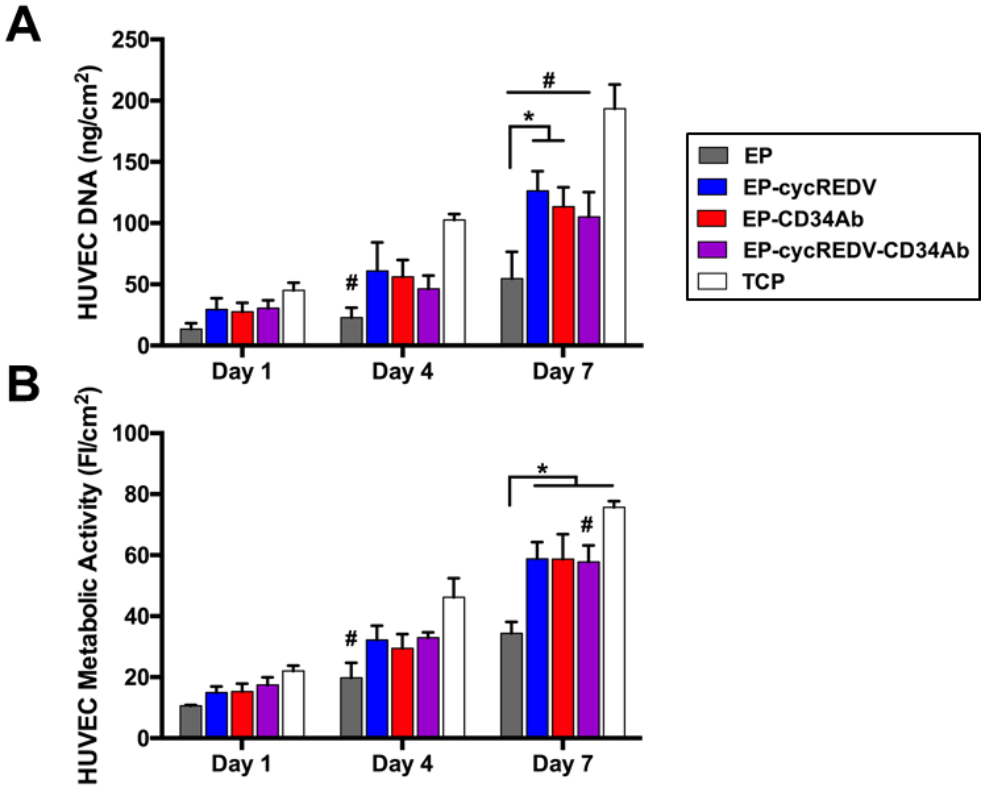

Figure 6.11. (A) Total DNA content and (B) metabolic activity of HUVEC on EP, EP-cycREDV, EP-CD34Ab, EP-cycREDV-CD34Ab and TCP as positive control on day 1-7 (n=3 independent experiments). Data plotted as mean ± SEM. Two-way ANOVA with Tukey's post-hoc tests were performed to reveal significant differences between conditions at each time point. *=p<0.05. #=p<0.05 compared to TCP. (Joint experiment with Mr Jeffrey Leung [277])

It can be seen that total DNA content and metabolic activity on EP coatings demonstrated lower levels compared to other samples up to day 7. Immobilisation of

cycREDV (EP-cycREDV) and anti-CD34Ab (EP-CD34Ab) have led to significant enhancement in total DNA content, as well as, metabolic activity compared with non-functionalised EP coating. Co-immobilisation of both biomolecules (EP-cycREDV-CD34) revealed similar level of DNA content and metabolic activity compared to the single biomolecule immobilisation EP-cycREDV and EP-CD34Ab. Results were still slightly sub-optimal compared to TCP. The findings here suggest that the co-immobilisation strategy employed here on EP coatings did not seem to display a significant synergistic enhancement effect in cell proliferation as originally anticipated.

6.4 Discussion

6.4.1 Combinatorial chemical curing yields multifunctional surfaces

Combinatorial EDA-PPA curing on PCU-PP generated multifunctional coating with $–NH_2$ and -C≡C groups. The hydrophilicity and surface $–NH_2$ density both exhibited a decreasing trend with increasing %PPA. While it was expected that surface -C≡C would increase with increasing %PPA, quantification of -C≡C groups via detection of –COOH after TYC reaction with MPA did not illustrate such a trend. It is surprising that even 100% EDA displayed enhancement in –COOH comparable to the other samples, although such phenomenon was not observed on untreated controls (shown in section 3.3.2.3). The reason for this finding is unclear. It is plausible that the indirect methodology of quantifying –COOH groups after MPA-TYC may have suffered from potential side reactions under the reaction condition employed (with UV-irradiation). The urea or $–NH_2$ group enriched surfaces of 100% EDA could have acted as catalyst locally for protonation of –SH to thiolate anion [303], hence further contributing to the nucleophilic potency in addition to UV-irradiation and I2959. This may eventually lead to attack of other chemical moieties on the coating by MPA molecules, leading to increased –COOH groups, although further investigation is needed.

The appearance of micro-corrugated morphology on 100% EDA, which were attributed to phase separation [80,216,217], gradually diminished with %PPA. Above 25% PPA, coatings became relatively flat at the microscale. It is likely that the addition of PPA had allowed increased chain termination in expense of crosslinking by EDA, leading to decreased molecular weight, although further verification with GPC is needed. Moreover, the combinatorial incorporation of hydrophilic EDA moieties and hydrophobic PPA moieties may have led to a different phase interaction. This may also have contributed to the distinct formation of nanowhisker features.

Overall, despite uncertainties in relation the surface -C≡C density, results from θº, -NH_2 group density and surface morphology showed noticeable trend with contributions from EDA and PPA depending on their compositions. Increasing %PPA leads to increasing convergence of properties to wards 100% PPA.

Nevertheless, further chemical characterisation including FTIR, Raman spectroscopy, XPS, GPC will be needed to better understand the chemistry of these multifunctional coatings. It would also be interesting to map the distribution of $–NH_2$ and -C≡C groups on these surfaces, potentially by ToF-SIMS mapping.

HUVECs appeared to display preferential adhesion and proliferation on 100% EDA, and the responses became poorer at increasing %PPA. The findings clearly demonstrated a trend correlating to the surface θº and $–NH_2$ density. Increasing %PPA decreases the presentation of biomimetic surface $–NH_2$ groups and increases the hydrophobicity, which may have impeded optimal adsorption of cell adhesive proteins on the surface to support initial cell adhesion [192,259,260]. No detectable effects of surface topography was apparent here, although it would be interesting to probe the interaction of cells with the nanowhiskers-like features potentially via SEM. Overall, the findings show the capacity to tailor HUVEC fate by controlling the balance between two distinctive chemistry ($-NH_2$ and -C≡C groups) using combination of small molecular precursors.

It is convincing to report that multifunctional coatings can be generated using facile combinatorial chemical curing of PCU-PP. The potential of such platforms are enormous, as different small molecular precursors can be employed for generation for a wide array of combinatorial surface chemistry and topography. Further studies can explore the mechanical properties (e.g. stiffness) of these coatings and potentially be tailored to mimic native tissues. Such facile, single-step curing approach serves as a promising addition to current approaches to controllably generate multiple surface reactive chemical groups [298,300,301]. The findings altogether further revealed the versatility of the PCU-PP chemical curing procedure.

6.4.2 Co-immobilisation potential of biomolecules on multifunctional coatings

25%PPA/75%EDA cured coating (EP) was selected to demonstrate co-immobilisation of cycREDV and anti-CD34Ab sequentially. Unaltered $–NH_2$ group density after cycREDV immobilisation indicates that TYC reaction did not influence the presentation of surface $–NH_2$ groups. Similar amount of anti-CD34Ab were immobilised on to EP-CD34Ab and EP-cycREDV-CD34Ab, which may also imply that cycREDV did not deter $–NH_2$ sites from anti-CD34Ab conjugation. This may be attributed to the smaller sizes of cycREDV (749.93 $gmol^{-1}$) in comparison to anti-

CD34Ab (~150 $kgmol^{-1}$). Along with homogeneous distribution of anti-CD34Ab and cycREDV detected by ToF-SIMS analysis, the results altogether demonstrate the potential of sequentially co-immobilising biomolecules using different conjugation chemistries. Such approach provides improved control over biomolecular densities and orientation by tuning the EDA/PPA curing formulation and bioconjugate chemistries, respectively.

In this study, the role of cycREDV and anti-CD34Ab immobilisation in enhancing HUVEC adhesion and subsequently proliferation can be recorded. The results further support the discussion in Chapter 5, which suggest that the detectable enhancement effect is dependent on the substrate material. In this case, the sub-optimal HUVEC fate on non-functionalised EP coating permits noticeable improvements contributed from the immobilised biomolecules. Both cycREDV and anti-CD34Ab provided similar effects in enhancing cell density, although further differences may lie on cellular function and signalling pathways. Hitherto, limited studies have directly compared the different biomolecules in influencing cell fate. Anti-CD34Ab and VEGF has more frequently been compared, and results from two separate studies have also shown similar enhancement levels of HUVEC proliferation on anti-CD34Ab and VEGF surfaces, respectively [183,298]. However, EPC adhesion and proliferation were higher on anti-CD34Ab compared to VEGF eluting or coated surfaces. No known studies have compared effects between REDV peptides and anti-CD34Ab immobilisation on cell fate.

In contrary to the original hypothesis, co-immobilisation of cycREDV and anti-CD34Ab did not show further enhancement in cell proliferation compared to its individual counterparts. Castellanos *et al*. also showed no synergistic effects in promotion of HUVEC adhesion and proliferation on combinatorial RGD and REDV functionalised surfaces compared to combinatorial RGD and YIGSR [159]. In contrast, other studies have shown that co-immobilisation of anti-CD34Ab and VEGF, RGD and bFGF, or anti-CD34 and a mussel-adhesive polypeptide (consisting of dihydroxyphenylalanine and L-lysine), was able to display further enhancement in HUVEC proliferation [287,298,299]. In the present study, one possible justification of the non-significant increase in HUVEC density on EP-cycREDV-CD34Ab is that the enhancement effect on proliferation from the cell adhesive ligands cycREDV and anti-CD34Ab may have reached its optimum on EP coating [157,304]. In fact, the

presence of each individual ligand may have been sufficient in promoting cell proliferation and activity. This is different from VEGF which is known for its biochemical effect in angiogenesis and vasculogenesis [110], hence may lead to enhanced synergistic effects on cell behaviour in combination with cell adhesive ligands. Another possibility is that the density of cycREDV and anti-CD34Ab may not have been sufficient to achieve detectable synergistic effects in proliferation. Nonetheless, it is also likely that the co-immobilised biomolecules here may have influenced other aspects of cell behaviour, such as enhanced long-term survival as seen in CD34++ ECFCs on EDA-CD34Ab coatings (section 5.3.1.5), or promoted differentiation. It has been reported that co-immobilisation of RGD peptide and bFGF on polymer film enhanced CD31 and vWF expression [299].

Altogether, it is clear that further work is warranted to assess cell-material interactions on such combinatorial biomolecular platforms. This combinatorial approach to functionalisation may require further optimisation in relation to densities and types of biomolecules [66]. The combinatorial chemical curing composition of 25%EDA/75%PPA used here could be modified to tailor the functional group density and subsequent immobilised biomolecule density. Haemocompatibility, cell selectivity, long-term maintenance, migration, and differentiation should be further evaluated. Optimisation with respect to other cell types including EPCs, platelets, SMCs and leukocytes should be taken into consideration. Importantly, the combinatorial platform developed here presents an opportunity to study and further understand cell-material interactions, leading to development of multiplexed biofunctional surfaces for better modulation of cell behaviour at the tissue-implant interface.

6.5 Conclusion

This chapter reported the potential of using combinatorial chemical curing procedure to generate multifunctional coatings with tailorable surface reactive groups (in this case $–NH_2$ and -C≡C) and micro-/nanotopography. The versatility of PP curing chemistry permits such approach to be applied to generate other types of combinatorial chemistries (e.g. –COOH, $-N_3$, epoxy groups) and topography. Furthermore, the opportunity to co-immobilise biomolecules, in this case cycREDV and anti-CD34Ab, to influence cell response was demonstrated on these multifunctional coating platforms. The proof-of-concept study here highlights the versatility and tuneability of this facile approach to chemical cure pre-polymers, which can lend itself towards multiplexed engineering of biointerfaces for improved control on cell selectivity and fate for vascular stents, as well as, a range of clinically relevant biomaterials.

Chapter 7

Conclusion and Future Prospects

7.1 Conclusion

The development of next generation pro-healing vascular stents with *in situ* endothelialisation capability requires new biomaterials with tuneable surface chemistry and topography, as well as, intricate design of biomolecule immobilisation in order to control biological interactions at the tissue-implant interface. This thesis described the development of novel PCU-PP coatings for vascular stents, which combine these key factors to produce combinatorial coating platforms. PCU-PP could be easily applied on to vascular stents via ultrasonic atomisation spray coating, and was optimised on to SS316L coupons using spin coating as a model to facilitate evaluation of thin film coatings. This approach can be potentially applied on to other cardiovascular biomaterials including metals (e.g. CoCr, PtCr, Nitinol) and polymers (e.g. Dacron^{TM}, ePTFE and PUs).

A chemical curing procedure was successfully developed on PCU-PP coatings using $–NH_2$ or –SH terminated small molecular precursors (e.g. EDA, PPA and MPA) to create new coating platforms with tailorable surface chemistry and topography. Chemical curing with EDA yielded highly crosslinked, hydrophilic coatings with surface $–NH_2$ functional groups, as well as, surface micro-ridges (~7-10 μm wide) and nanofeatures (~90 nm wide). In contrast, PPA cured coatings revealed lower molecular weight (MW), higher hydrophobicity with surface -C≡C groups alongside irregular surface morphology with the appearance of some micro-islands (~15 μm wide) and nanofibrous structures (<120 nm wide). MPA curing resulted in intermediate MW, hydrophilic coatings with surface –COOH functional groups, as well as, formation of sub-micron ridges (~0.5 μm wide). The formation of such unique combinatorial chemical and topographical properties are likely a result of differential phase separation behaviour between the different PU segments after chemical curing. Further investigations will be needed to elucidate the curing

mechanisms using techniques such as differential scanning calorimetry (DSC) or nuclear magnetic resonance (NMR), as well as, mechanical properties of the coatings using nanoindentation. The chemical curing procedure offers a bottom-up material functionalisation approach that possesses advantages including single-step generation of combinatorial surface chemistry and topography, tailorability of final properties, high formulation versatility, as well as, ease of scalability. Importantly, such approach can be applied with ease on to complex geometries, such as curved surfaces and struts on vascular stents. Hence, such approach can serve as an addition to current physicochemical surface modification strategies, such as plasma treatment or chemical etching.

The potential of the chemical cured coatings as vascular biomaterials to promote endothelialisation was tested *in vitro* using HUVECs. HUVEC adhesion was poor on untreated (moisture-cured) and PPA coatings, but overall showed great enhancement in cell fate on most EDA and MPA coatings. The data suggest that surface chemistry played a dominant role in influencing HUVEC fate compared to micro-/nanotopography, and this is consistent to other surface modification approaches, which yield biomimetic and hydrophilic surface functional groups (e.g. $–NH_2$, -COOH) that enhance cell fate. Microscale topographies on EDA cured coatings did not show significant effect in HUVEC fate in this study. Importantly, nanotopography played a role in determining HUVEC fate. While some degree of nanotopography (nanofeatures of ~35 nm high) appeared to enhance HUVEC spreading, adhesion and proliferation, rougher nanotopography with nanofeatures (~35 nm high) on EDA coating was found to impede optimal cell adhesion leading to lower cell proliferation. Similar findings have also been previously reported, where higher nanoscale roughness have shown sub-optimal HUVEC adhesion and proliferation [252,255,266]. Such cellular response to nanotopography can be attributed to the similar nanoscale lengthscale of cell-adhesive proteins (~10 nm) [305], as well as, the biomimicry of nanoscale topography to native tissues. Altogether, the potential of the chemical-cured coatings with combinatorial chemistry and topography to be used in applications where cell fate needs to be controlled can be demonstrated. Such coatings can also serve as a tool to study the interplay between surface chemistry and topography on cell fate.

The next part of the thesis successfully demonstrated immobilisation of anti-CD34Ab and REDV peptides on to selected EDA (50 mM) and PPA (50 mM) coatings, respectively, to promote *in situ* endothelialisation. Anti-CD34Ab, which binds to CD34 epitopes expressed on endothelial progenitor cells (EPCs) in circulating peripheral blood, were immobilised on to EDA coatings using site-directed periodate oxidation (PO) chemistry. EDA-CD34Ab showed increased binding capability of CD34 antigen, optimal adhesion and proliferation of HUVEC and ECFC, as well as, reduced platelet adhesion, aggregation and activation. Cysteine terminated REDV peptides, which are ligands selective to endothelial cells (ECs), were immobilised on to PPA coatings using the efficient thiol-yne click reaction (TYC). CycREDV was the most effective peptide in enhancing HUVEC adhesion and survival when compared to linear short and long peptide chains (CGREDV and CG_5REDV). PPA-cycREDV also reduced platelet adhesion. The selectivity of both anti-CD34Ab and cycREDV immobilised coatings towards HUVEC adhesion over platelets was consistent with other studies immobilising similar biomolecules [99,141,151,160,287,288]. These findings illustrate the possibility to selectively enhance HUVEC fate on chemical cured coatings by immobilisation of endothelial-specific biomolecules. Such selectivity is vital to promote endothelialisation and vascular healing *in vivo*, which could prevent thrombosis, inflammation and restenosis and enhance long-term patency of vascular stents. Furthermore, several new findings were demonstrated for the first time in this thesis. These include the long-term survivability of CD34++ ECFCs on EDA-CD34Ab, which can serve as basis for future studies on longer-term cell fate on antibody-immobilised surfaces. In addition, the superiority of cycREDV in enhancing HUVEC adhesion and proliferation compared to its linear counterparts on hydrophobic PPA coatings was also demonstrated, and can be attributed to improved biostability, activity and binding affinity of cyclic peptides [292]. The poor enhancement in HUVEC fate with the linear peptides could also be attributed to interactions with the hydrophobic coatings, which may highlight the importance of considering the innate surface properties of the base substrate material such as wettability. Overall, it is demonstrated that immobilisation of biomolecules on to the chemical cured coatings can increase control of the biological events, which is in this study enhanced selectivity in EC adhesion over platelets at the vascular interface.

Finally, the potential of the chemical curing reaction was expanded using mixtures of small molecular precursors (e.g. EDA and PPA) of varying ratios. This combinatorial curing approach enabled the generation of multifunctional coatings with a variety of functional groups (e.g. $–NH_2$ and -C≡C functionality), and the ability to tailor the hydrophilicity using functional group density and topography. The results revealed the great versatility of the chemical-curing platforms, which can be applied using other combinations of precursors (e.g. MPA and EDA) to generate new coating platforms. Next, a combination of EDA and PPA precursors was used to formulate a multifunctional platform to co-immobilise cycREDV and anti-CD34Ab, although the co-immobilised platform did not lead to further improvements in HUVEC proliferation compared to the immobilisation of single biomolecules alone. This finding is in contrary to several reported studies that have included combinations of adhesive molecules (e.g. anti-CD34Ab, RGD peptide) and growth factors, which have shown enhanced HUVEC adhesion and proliferation [287,298,299]. However, such enhancement might be due to the different biochemical pathways activated by the different selection of biomolecules compared to this study. It is also plausible that the formulation of biomolecular densities used in this study may require further optimisation to achieve synergistic effects in HUVEC fate, and this can be achieved by varying the formulation of small molecular precursors during the chemical curing procedure. Overall, the results show the potential and tuneability of the combinatorial chemical curing platforms, which are useful for further optimisation of surface chemistry or topography, and conjugation of multiple biomolecules to control biological response at the vascular interface.

In conclusion, a facile, scalable, and highly versatile PCU-PP chemical curing procedure has been developed as a vascular stent coating platform. Immobilisation of anti-CD34Ab and cycREDV ligands on to the coatings successfully promoted selective EC adhesion over platelets, as well as, supported subsequent EC proliferation. These properties constitute a major milestone for attainment of *in situ* endothelialisation to promote vascular healing. In comparison to the commercialised anti-CD34Ab-immobilised stents, Genous™ and Combo™ stents, the coating platform developed in this thesis presents combinatorial topography, chemistry and biomolecules to better control fates of different cell types, which include the promotion of endothelialisation from EPCs to mature ECs. Furthermore, the

chemical reactions utilised were carefully selected in relation to efficiency and functionality. In particular, the PO and TYC chemistries both promote site directed immobilisation of the anti-CD34Ab and cycREDV peptides on to the coatings to improve control of their orientations and hence maximising their functionality. While there is still no specific markers for EPCs identified, it is envisaged that co-immobilisation of multiple biomolecules to provide a pro-endothelialisation microenvironment could better control biological responses at the vascular interface for improved EPC capturing, proliferation and differentiation. Further work on this combinatorial coating platform could involve investigation of different type of biomolecules to enhance *in situ* endothelialisation. *In situ* endothelialisation remains a complex process, and much research will be needed for to understand the level of interaction between material interfaces and vascular biology of varying cell types *in vivo*. Nevertheless, it presents a promising and practical strategy for off-the-shelf bioactive pro-healing platforms for vascular stents, which can circumvent the complications of excessive thrombosis, inflammation and restenosis. The chemical curing and biomolecular immobilisation procedures developed in this thesis could serve as a tool to produce new biomaterial platforms for investigations and optimisations for pro-healing blood-contacting devices with *in situ* endothelialisation capability. Such platforms can pave the way towards new generation of biomaterials not only for vascular applications, but also in other areas of regenerative medicine and tissue engineering, where cell behaviour needs to be controlled.

7.2 Recommendations and future work

There are several directions in which the work in this thesis can be further advanced, as listed in the following:

7.2.1 Development as a vascular stent coating

The biofunctionalised coatings developed in this thesis can be developed towards clinical applications. Before evaluation in *in vivo* animal models such as rabbits, several important aspects should be evaluated. Firstly, the long-term biostability and mechanical integrity of the coatings on stents should be evaluated. This can be performed with accelerated aging studies, as well as, evaluation of the acute coating durability on stents following multiple cycles of expansion and folding. In addition, the long-term stability and bioactivity of the immobilised biomolecules upon storage and implantation *in vivo* should be studied. It is also imperative to evaluate further on the EPC capturing capability and subsequent cell fate on the coatings with a physiological pulsatile flow circuit in comparison to static conditions. It is recommended that the responses of other vascular cell types, including SMCs and leukocytes (e.g. monocytes, macrophages), should be further studied on the coatings.

The biocompatibility and haemocompatibility of the coatings should be evaluated in accordance to relevant standards such as the ISO10993, along with viable sterilisation, storage and packaging strategies, which are compliant to the ISO25539 international standard. Importantly, the bioactivity of the immobilised biomolecules needs to be characterised following such procedures. As a reference, Genous^{TM} stents have evolved from a wet, hand-crimped device sterilised by 15-25 kGy gamma irradiation to dry, pre-mounted sterilised by <15 kGy gamma irradiation in order to improve bioactivity of the immobilised anti-CD34Ab [306]. It is anticipated that peptides may better withstand harsher environments (e.g. gamma irradiation) than antibodies.

7.2.2 Expansion of chemical curing procedure to other pre-polymer systems

Apart from the synthetic biostable PCU-based soft segment pre-polymer (PP) used in this study, the chemical curing procedure can be applied to other types of PU-PP systems. For instance, a bioresorbable polymer building block, such as PCL or

poly(glycerol sebacate) represents a promising new avenue to extend the application of such curing procedure to applications where controlled degradation is desirable. Furthermore, new small molecular precursors could be explored, with possibility of incorporating $–NH_2$ or –SH terminated amino acid precursors such as L-lysine derivatives to incorporate biological signatures within the coatings [76]. Essentially, the flexibility of urethane chemistry permits the possibility to generate a large range of new materials with varying properties.

7.2.3 Improving control of biological responses at the coating interface

Cells respond to surface chemistry, topography, mechanical stiffness and biological cues (e.g. biomolecules) on materials. The combinatorial surface chemistry and topography produced by the chemical cured coatings can be used as a toolkit to study cell-material interactions, as seen in Chapter 4. Information on the substrate stiffness of the coatings can be collected by nanoindentation techniques. Different types of biomolecules, such as those reviewed in section 1.6, can be immobilised at various combinations to evaluate their efficacies and mechanisms to promote *in situ* endothelialisation. The combinatorial chemical cured coatings could serve as a useful platform for systematic investigation by controllably immobilise different types and densities of biomolecules. The avenue of drug or growth factors (e.g. heparin, sirolimus, VEGF or bFGF) could also be incorporated by bioconjugation or controlled elution to improve control of biological response at the vascular interface to enhance *in situ* endothelialisation.

To effectively evaluate the effect of such wide range of factors in controlling biological response (e.g. cell adhesion, proliferation, growth and differentiation), it is proposed that such studies could be performed using high-throughput microarray screening technology, where a large range of chemical curing and biomolecular formulations can be screened to monitor cell behaviour, including adhesion, proliferation and differentiation. Furthermore, different cell types could also be efficiently evaluated. Such high-throughput characterisation will not only assist in the optimisation of material formulation to achieve desired cell response, but may also lead to obtaining larger trends in relation to cell-material interactions, hence improving understanding of cell-material interactions.

In addition, it is important to ensure presentation of active sites of immobilised biomolecules *in vivo*. The impact of protein adsorption from blood to the presentation of immobilised biomolecules have to be evaluated, and can likely be circumvented by anti-fouling strategies such as PEGylation. Furthermore, the superiority of cycREDV over its linear counterparts in enhancing HUVEC fate could be elucidated. It may be associated to the influence of the hydrophobic PPA base coating surface chemistry on conformation of the immobilised peptides, leading to poorer presentation of active sites to cells in the case of linear peptides. As a first step, it is suggested that these peptides could be immobilised on to other -C≡C functionalised coatings (e.g. combinatorial EDA-PPA coatings) of different wettability via the same TYC chemistry to evaluate if similar HUVEC responses were obtainable. Subsequent efforts could focus on detection and quantification of the active sites of these peptides upon immobilisation. Improved understanding of biomolecule-substrate interactions at the nanobiointerface could be important in ensuring optimal bioconjugation in the field of biomaterials.

7.2.4 Other applications

The application of the chemical cured coatings and the subsequent bioconjugation chemistry are not only restricted to vascular applications. They could also be applied to other medical devices requiring control on cell behaviour, such as tissue engineering scaffolds or devices to promote tissue repair, replacement and regeneration, and molecular toolkits to understand cell biology.

Appendix A
Characterisation of PCU-PP

PCU-PP solution synthesised as described in section 1.2.1 was characterised with ATR-FTIR, GPC and quantification of NCO content.

Methods:

ATR-FTIR: ATR-FTIR of freshly synthesised PCU-PP was conducted as described in section 2.2.5.2.

GPC: PCU-PP after 1 month storage in -20 ºC was characterised by GPC as described in section 3.2.4.6.

Quantification of NCO content: NCO content of PCU-PP stored in -20 ºC over 0-5 months were quantified via a standardly used back-titration procedure, in accordance to ASTM D 2572-97 [210]. 5 g 28 wt% PCU-PP were transferred to oven-dried conical flask and diluted with 25 mL of anhydrous DMAc. 25 mL 0.1 N *n*-butylamine was then added and allowed to magnetic stir for 15 min. 12 drops of bromophenol blue solution were added, and titration was performed with 0.1 N HCl until a yellow end point (n=3). Blank control was performed without PCU-PP. The following equation is used for calculation of the NCO content:

$$\%NCO = \frac{(V_{HCl,blank} - V_{HCl,sample})(N_{HCl})(0.042)}{W_{sample}} \times 100$$

where $V_{HCl,blank}$: volume of HCl for titration of blank (mL); $V_{HCl,sample}$: volume of HCl for titration of sample (mL); N_{HCl}: normality of HCl (0.1 N); 0.042: milliequivalent weight of NCO group; W_{sample}: mass of sample (g).

Results:

The characterisation data of PCU-PP are shown in Figure A.1.

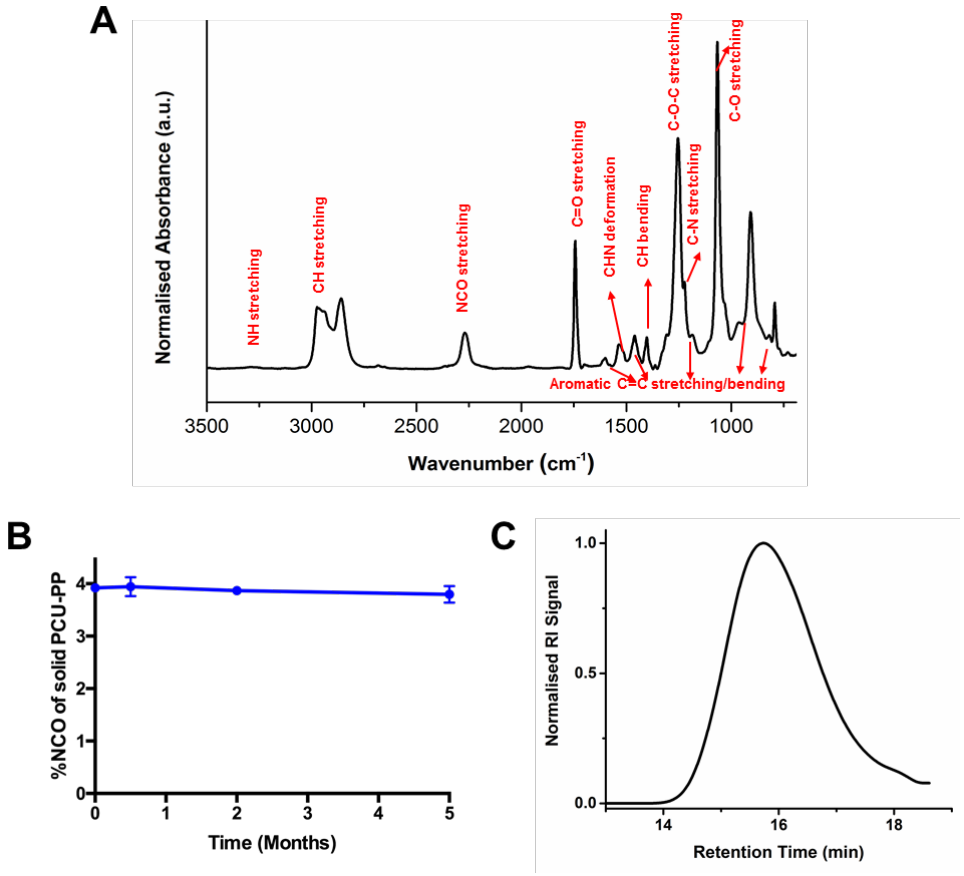

Figure A.1. (A) ATR-FTIR spectrum; (B) Quantification of NCO content over 5 months and (C) GPC data on synthesised PCU-PP solution (28 wt%).

ATR-FTIR spectrum of synthesised 28 wt% PCU-PP revealed notable –NCO peaks (2265 cm^{-1}), as well as chemical peaks including urethane, carbonate, alkyl and aromatic rings, hence verifying expected structure of PCU-PP. These includes urethane N-H asymmetric stretching (3317 cm^{-1}), alkyl C-H stretching (2939 and 2868 cm^{-1}), carbonyl C=O stretching (1730 cm^{-1}), aromatic stretching (1590, 1465 and 790 cm^{-1}), carbonate C-O-C stretching (1246 cm^{-1}), urethane C-N stretching (1223 cm^{-1}) and C-O stretching (1066 cm^{-1}). The presence of urethane bond indicates successful reaction between NCO and OH. Quantification of NCO content of the synthesised PCU-PP yields 3.92±0.06 wt% NCO of solid PP, which is consistent to theoretically calculated value at 4 wt%. No significant decrease in NCO content was detected through storage in -20ºC up to 5 months. GPC revealed a single-peak Gaussian distribution of MW. $M_{n,GPC}$ based on PMMA standards (DMF eluent) was 8297, and polydispersity index (PDI) was 1.87. The theorectical M_n should be 2501, although this can be attributed to the different sample-column interaction, and crosslinking between chains could have happened during sample preparation.

Appendix B

Assay standard curves

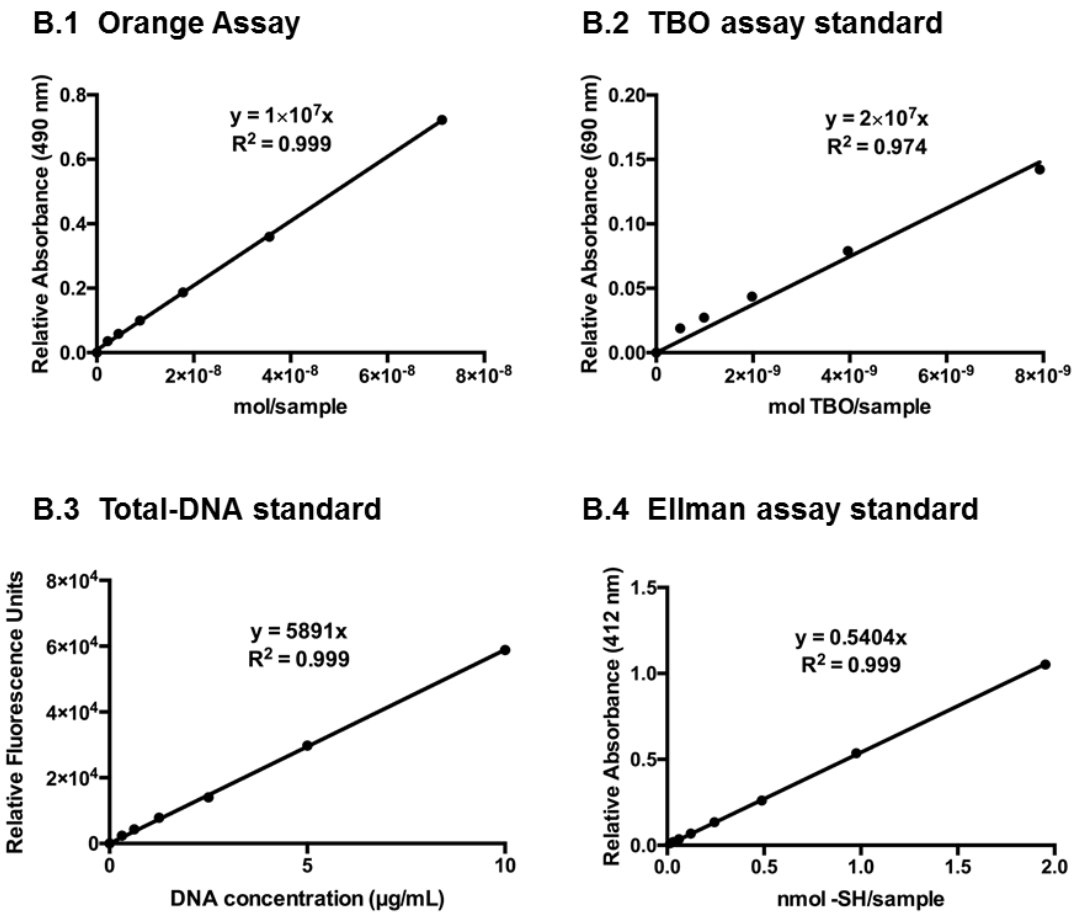

Figure A.2. Standard curves for (B.1) Orange assay, (B.2) TBO assay, (B.3) Total DNA assay using calf thymus DNA, (B.4) Ellman assay using 3-mercaptopropionic acid**.**

Appendix C

Peptide characterisation data

Characterisation of the peptides (i) CGREDV, (ii) CG_5REDV, (iii) cycREDV and (iv) CGREVD were carried out the by manufacturer (Generon Ltd, UK).

(i) CGREDV, short

Generon
the protein company

CERTIFICATE OF ANALYSIS:
Custom Peptide Synthesis

CoA#: P160705-TL521894

Product Name	CUST-GEN-PEP-21062016-01			
Synthesis ID:	521894		**Operator**	SJF
Amount:	**Requested**	1 * 100 mg	**Delivered**	1 * 101.0 mg
Peptide Sequence:	CGREDV			
Molecular Formula:	$C_{25}H_{43}N_9O_{11}S_1$			
Notes				
	Quality Control Test			
TESTS	**SPECIFICATIONS**		**RESULTS**	
Appearance:	White or off white solid powder		Consistent	
Purity(LC):	>90%		98.62 %	
Molecular Weight(MS):	677.73		Consistent	
Amino Acid Analysis:	N/A		N/A	
Solubility:	N/A		N/A	
UV/VIS Absorbance:	N/A		N/A	
Water Contents:	<1.0%		N/A	
Prolonged Storage:	Keep cool and dry			
Test Date:	08/07/2016			
Final QC	☒ **Passed** ☐ **Failed** ☐ **Hold** ☐ **Other:**			
Signature	**By**	**SG**	**Date:**	25/07/2016

Generon Ltd, 12 Rawcliffe House, Howarth Road, Maidenhead, Berkshire, SL6 1AP
Telephone:+44 (0)1753 866 511 Fax:+44 (0)1753 208 899

Structure:GEN-CUST-PEP-21062016-01 CV-6
Number: 0200046
Lot No:P160705-TL521894
Column: 4.6mm*250mm,Inertsil ODS-SP
Solvent A: 0.1%Trifluoroacetic in 100% Acetonirile
Solvent B: 0.1%Trifluoroacetic in 100% Water
Gradient:

	A	B
0.01min	8%	92%
25.00min	33%	67%
25.01min	100%	0%
30.00min	Stop	

Flow rate:1.0ml/min
Wavelength:220nm
Volume:10μl

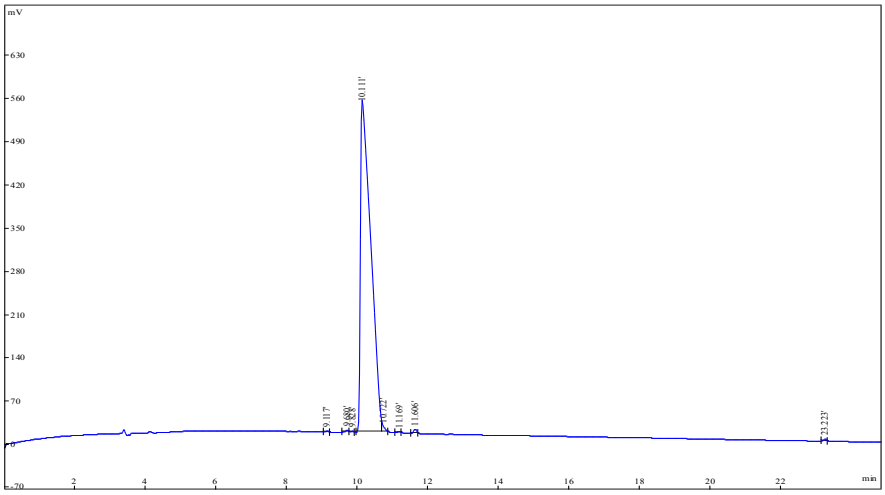

Rank	Time	Conc.	Area	Height
1	9.117	0.07802	8578	1639
2	9.680	0.1406	15462	2619
3	9.828	0.08108	8914	1568
4	10.111	98.62	10843541	539514
5	10.722	0.4625	50848	7823
6	11.169	0.1023	11252	1864
7	11.606	0.3596	39542	6663
8	23.223	0.1546	16994	3163
Total		100	10995131	564853

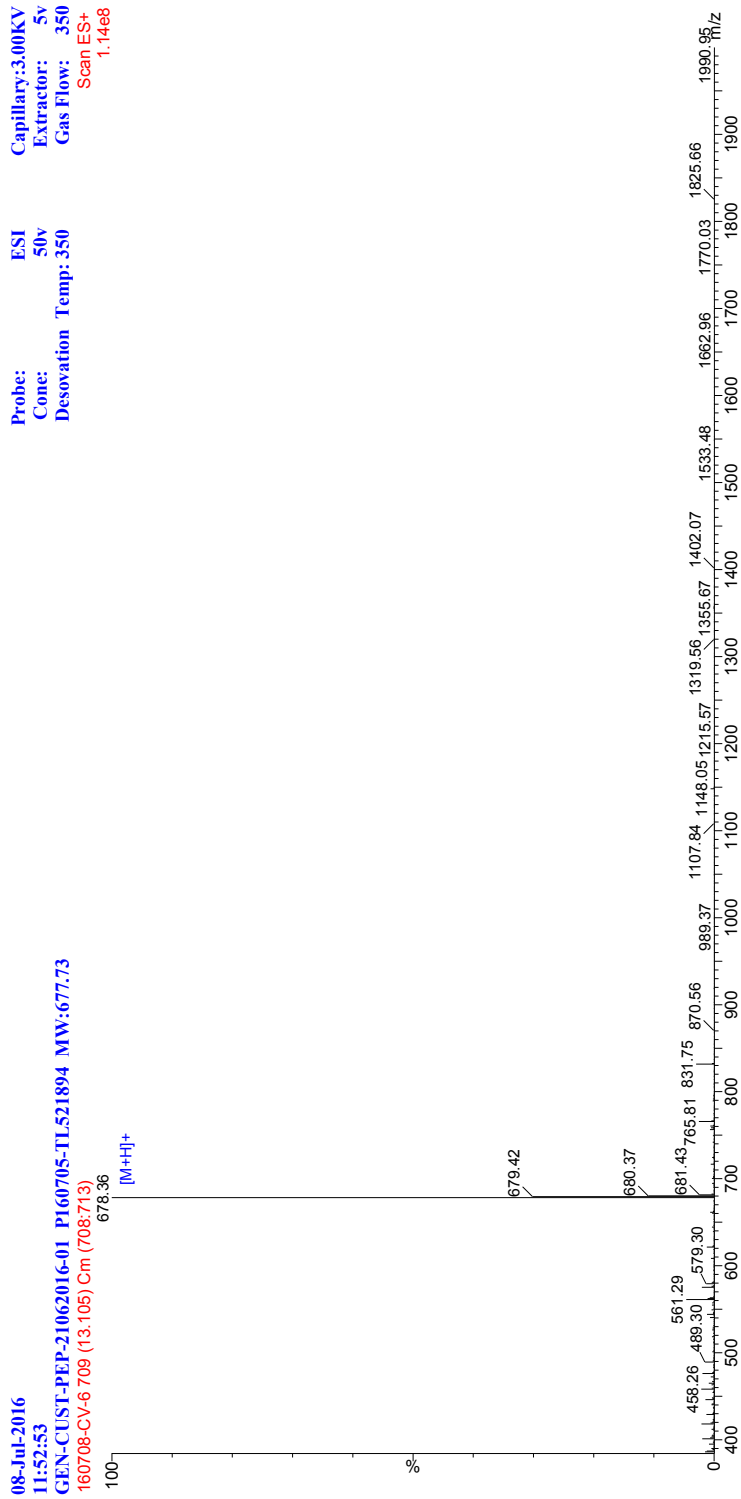

Generon Ltd, 12 Rawcliffe House, Howarth Road, Maidenhead, Berkshire, SL6 1AP
Telephone:+44 (0)1753 866 511 Fax:+44 (0)1753 208 899

(ii) CG_5REDV, long

Generon
the protein company

CERTIFICATE OF ANALYSIS:
Custom Peptide Synthesis

CoA#: P160705-TL521895

Product Name	CUST-GEN-PEP-21062016-02			
Synthesis ID:	521895		**Operator**	SJF
Amount:	**Requested**	1 * 100 mg	**Delivered**	1 * 102.0 mg
Peptide Sequence:	CGGGGGREDV			
Molecular Formula:	$C_{33}H_{55}N_{13}O_{15}S_1$			
Notes				
	Quality Control Test			
TESTS	**SPECIFICATIONS**		**RESULTS**	
Appearance:	White or off white solid powder		Consistent	
Purity(LC):	>90%		98.56 %	
Molecular Weight(MS):	905.94		Consistent	
Amino Acid Analysis:	N/A		N/A	
Solubility:	N/A		N/A	
UV/VIS Absorbance:	N/A		N/A	
Water Contents:	<1.0%		N/A	
Prolonged Storage:	Keep cool and dry			
Test Date:	08/07/2016			
Final QC	☒ **Passed** ☐ **Failed** ☐ **Hold** ☐ **Other:**			
Signature	**By**	**SG**	**Date:**	25/07/2016

Generon Ltd, 12 Rawcliffe House, Howarth Road, Maidenhead, Berkshire, SL6 1AP
Telephone:+44 (0)1753 866 511 Fax:+44 (0)1753 208 899

Structure:GEN-CUST-PEP-21062016-02 CV-10
Number: 0200046
Lot No:P160705-TL521895
Column: 4.6mm*250mm,Inertsil ODS-SP
Solvent A: 0.1%Trifluoroacetic in 100% Acetonirile
Solvent B: 0.1%Trifluoroacetic in 100% Water
Gradient:

	A	B
0.01min	7%	93%
25.00min	32%	68%
25.01min	100%	0%
30.00min	Stop	

Flow rate:1.0ml/min
Wavelength:220nm
Volume:10μl

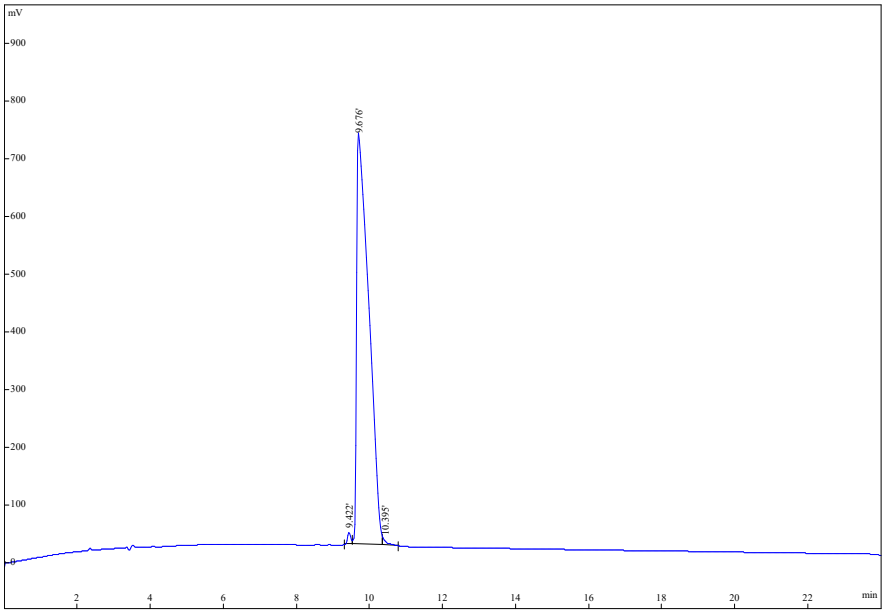

Rank	Time	Conc.	Area	Height
1	9.422	0.8837	148032	22104
2	9.676	98.56	16511184	715610
3	10.395	0.5493	92019	9207
Total		100	16751235	746921

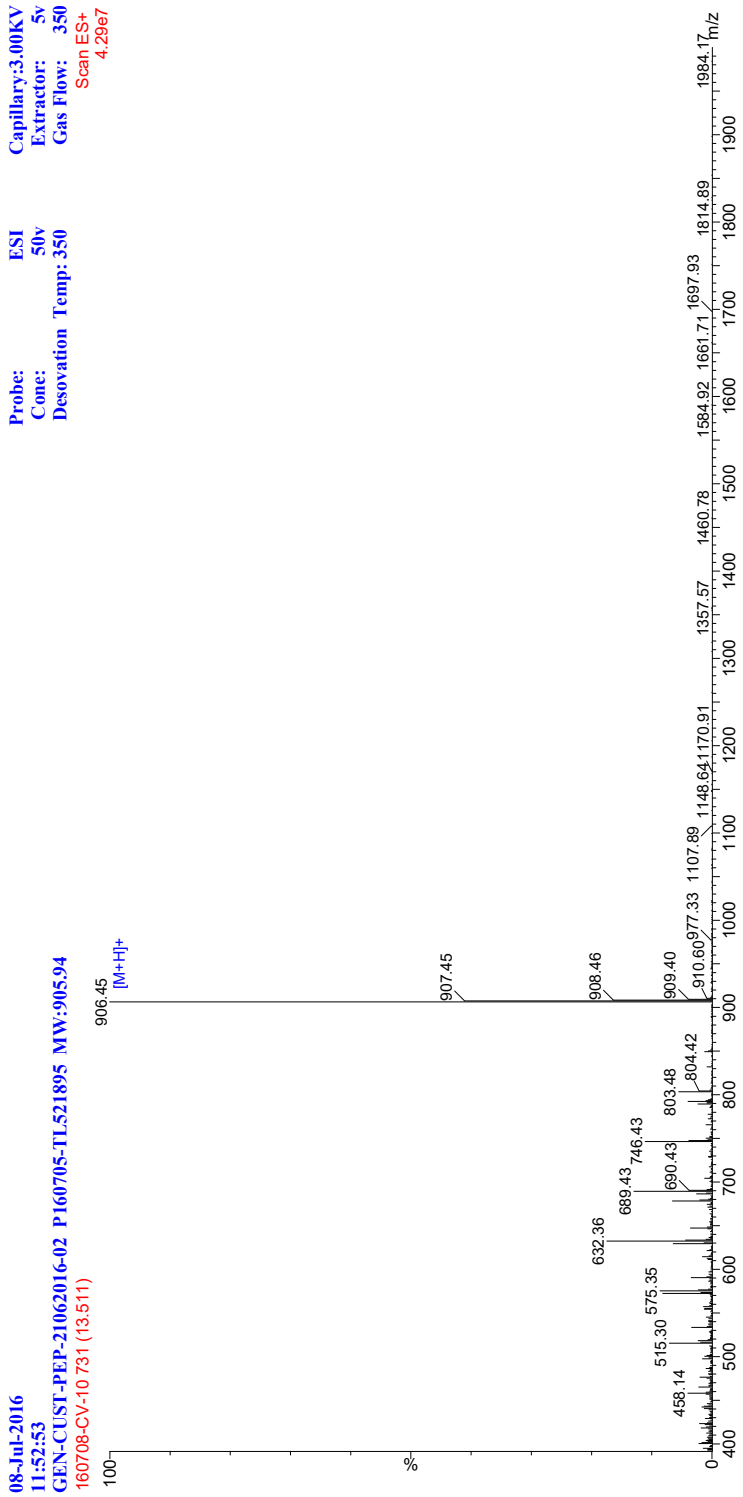

Generon Ltd, 12 Rawcliffe House, Howarth Road, Maidenhead, Berkshire, SL6 1AP
Telephone:+44 (0)1753 866 511 Fax:+44 (0)1753 208 899

(iii) cycREDV, cyclic

Generon
the protein company

CERTIFICATE OF ANALYSIS:
Custom Peptide Synthesis

CoA#: P160705-WJ521898

Product Name	CUST-GEN-PEP-21062016-04			
Synthesis ID:	521898		**Operator**	SJF
Amount:	**Requested**	1 * 100 mg	**Delivered**	1 * 100.4 mg
Peptide Sequence:	REDV-(d-Phe)-C			
Molecular Formula:	$C_{32}H_{47}N_9O_{10}S_1$			
Notes	Cyclic Backbone, d-Phenylalanine enantiomer.			
	Quality Control Test			
TESTS	**SPECIFICATIONS**		**RESULTS**	
Appearance:	White or off white solid powder		Consistent	
Purity(LC):	>90%		90.86 %	
Molecular Weight(MS):	749.93		Consistent	
Amino Acid Analysis:	N/A		N/A	
Solubility:	N/A		N/A	
UV/VIS Absorbance:	N/A		N/A	
Water Contents:	<1.0%		N/A	
Prolonged Storage:	Keep cool and dry			
Test Date:	18/07/2016			
Final QC	☒ **Passed** ☐ **Failed** ☐ **Hold** ☐ **Other:**			
Signature	**By**	**SG**	**Date:**	25/07/2016

Generon Ltd, 12 Rawcliffe House, Howarth Road, Maidenhead, Berkshire, SL6 1AP
Telephone:+44 (0)1753 866 511 Fax:+44 (0)1753 208 899

Structure:GEN-CUST-PEP-21062016-04 RC-6

Number: 0200046

Lot No:P160705-WJ521898

Column: 4.6mm*250mm,Inertsil ODS-SP

Solvent A: 0.1%Trifluoroacetic in 100% Acetonirile

Solvent B: 0.1%Trifluoroacetic in 100% Water

Gradient:	A	B
0.01min	20%	80%
25.00min	45%	55%
25.01min	100%	0%
30.00min	Stop	

Flow rate:1.0ml/min

Wavelength:220nm

Volume:10μl

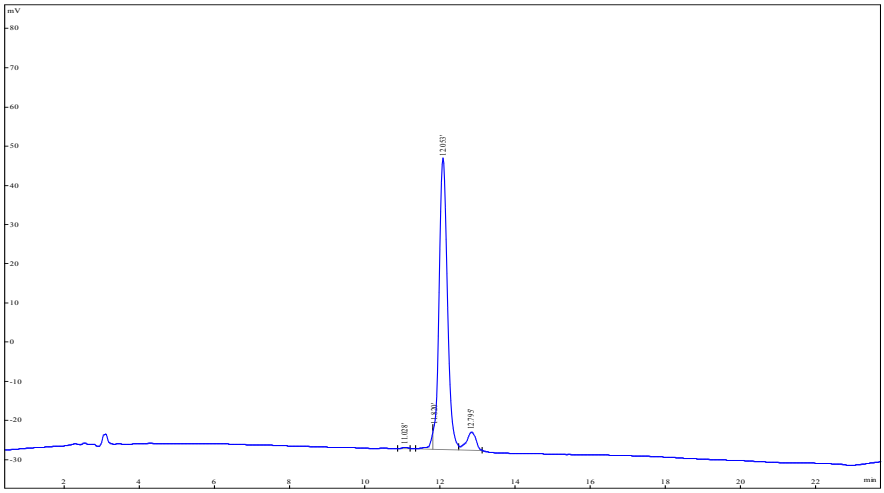

Rank	Time	Conc.	Area	Height
1	11.028	0.2853	3576	338
2	11.820	2.2797	28578	6152
3	12.053	90.8691	1139104	74636
4	12.795	6.5659	82308	4638
Total		100	1253566	85764

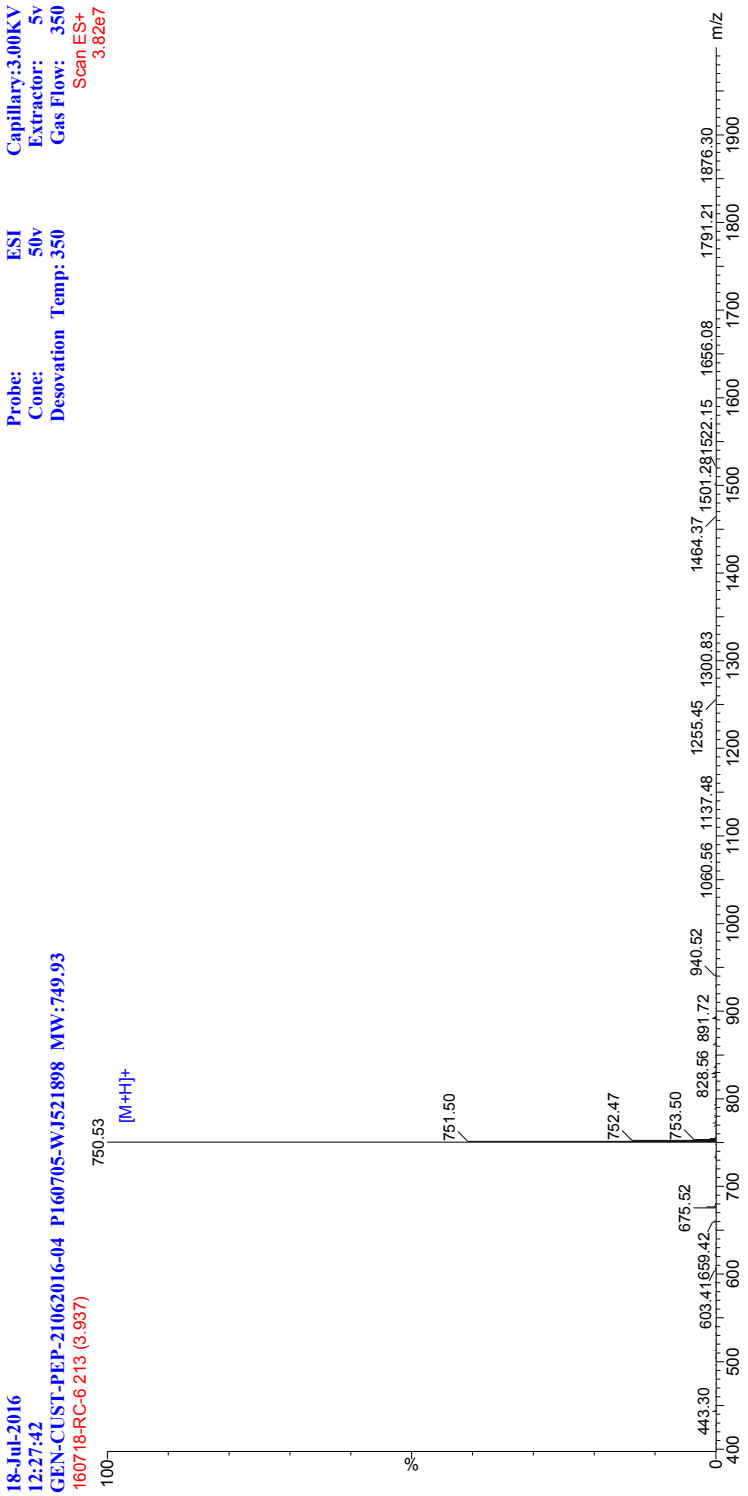
18-Jul-2016
12:27:42
GEN-CUST-PEP-21062016-04 P160705-WJ521898 MW:749.93
160718-RC-6 213 (3.937)
Probe: ESI
Cone: 50v
Desovation Temp: 350
Capillary:3.00KV
Extractor: 5v
Gas Flow: 350
Scan ES+
3.82e7
100
%
0
[M+H]+
750.53
751.50
752.47
753.50
828.56
891.72
940.52
1060.56
1137.48
1255.45
1300.83
1464.37
1501.28
1522.15
1656.08
1791.21
1876.30
675.52
659.42
603.41
443.30
400
500
600
700
800
900
1000
1100
1200
1300
1400
1500
1600
1700
1800
1900
m/z

(iv) CGREVD, scrambled

Generon
the protein company

CERTIFICATE OF ANALYSIS:
Custom Peptide Synthesis

CoA#: P160705-TL521896

Product Name	CUST-GEN-PEP-21062016-03			
Synthesis ID:	521896		**Operator**	SJF
Amount:	**Requested**	1 * 100 mg	**Delivered**	1 * 102.0 mg
Peptide Sequence:	CGREVD			
Molecular Formula:	$C_{25}H_{43}N_9O_{11}S_1$			
Notes				
	Quality Control Test			
TESTS	**SPECIFICATIONS**		**RESULTS**	
Appearance:	White or off white solid powder		Consistent	
Purity(LC):	>90%		92.91 %	
Molecular Weight(MS):	677.73		Consistent	
Amino Acid Analysis:	N/A		N/A	
Solubility:	N/A		N/A	
UV/VIS Absorbance:	N/A		N/A	
Water Contents:	<1.0%		N/A	
Prolonged Storage:	Keep cool and dry			
Test Date:	08/07/2016			
Final QC	☒ **Passed** ☐ **Failed** ☐ **Hold** ☐ **Other:**			
Signature	**By**	**SG**	**Date:**	25/07/2016

Generon Ltd, 12 Rawcliffe House, Howarth Road, Maidenhead, Berkshire, SL6 1AP
Telephone:+44 (0)1753 866 511 Fax:+44 (0)1753 208 899

Structure:GEN-CUST-PEP-21062016-03 CD-6

Number: 0200046

Lot No:P160705-TL521896

Column: 4.6mm*250mm,Inertsil ODS-SP

Solvent A: 0.1%Trifluoroacetic in 100% Acetonirile

Solvent B: 0.1%Trifluoroacetic in 100% Water

Gradient:	A	B
0.01min	5%	95%
25.00min	30%	70%
25.01min	100%	0%
30.00min	Stop	

Flow rate:1.0ml/min

Wavelength:220nm

Volume:10μl

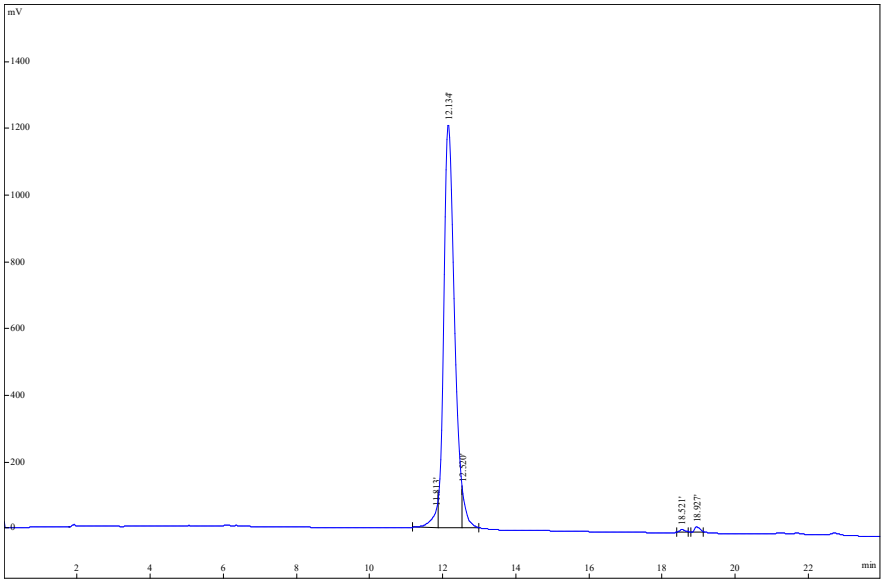

Rank	Time	Conc.	Area	Height
1	11.813	3.129	810272	58753
2	12.134	92.91	24060578	1214872
3	12.520	3.103	803610	115019
4	18.521	0.2774	71844	7005
5	18.927	0.5876	152167	15146
Total		100	25898471	1410795

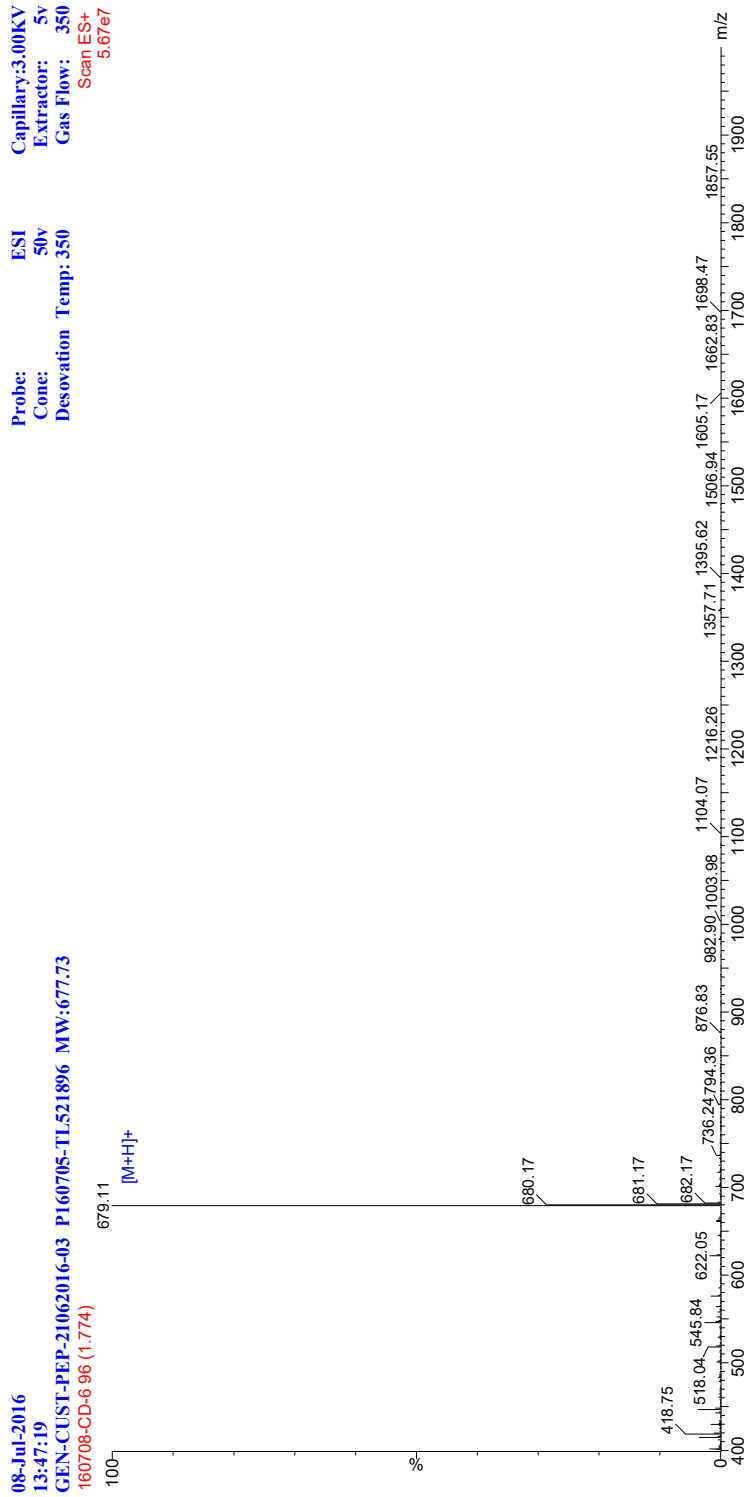
08-Jul-2016
13:47:19
GEN-CUST-PEP-210620160-03 P160705-TL521896 MW:677.73
160708-CD-6 96 (1.774)
Probe: ESI
Cone: 50v
Desovation Temp: 350
Capillary:3.00KV
Extractor: 5v
Gas Flow: 350
Scan ES+
5.67e7
100
%
0
679.11
[M+H]+
680.17
681.17
682.17
736.24
794.36
876.83
982.90
1003.98
1104.07
1216.26
1357.71
1395.62
1506.94
1605.17
1662.83
1698.47
1857.55
418.75
518.04
545.84
622.05
400
500
600
700
800
900
1000
1100
1200
1300
1400
1500
1600
1700
1800
1900
m/z

Appendix D

Characterisation of ECFCs

Two ECFC isolates from two different donors (CD34+ ECFCs and CD34++ ECFCs) were provided by Prof Jane Mitchell and Ms Isra Marei (Imperial College London, UK). Figure A.3 briefly outlines the isolation procedure. Figure A.4 shows the flow cytometry data of the ECFCs.

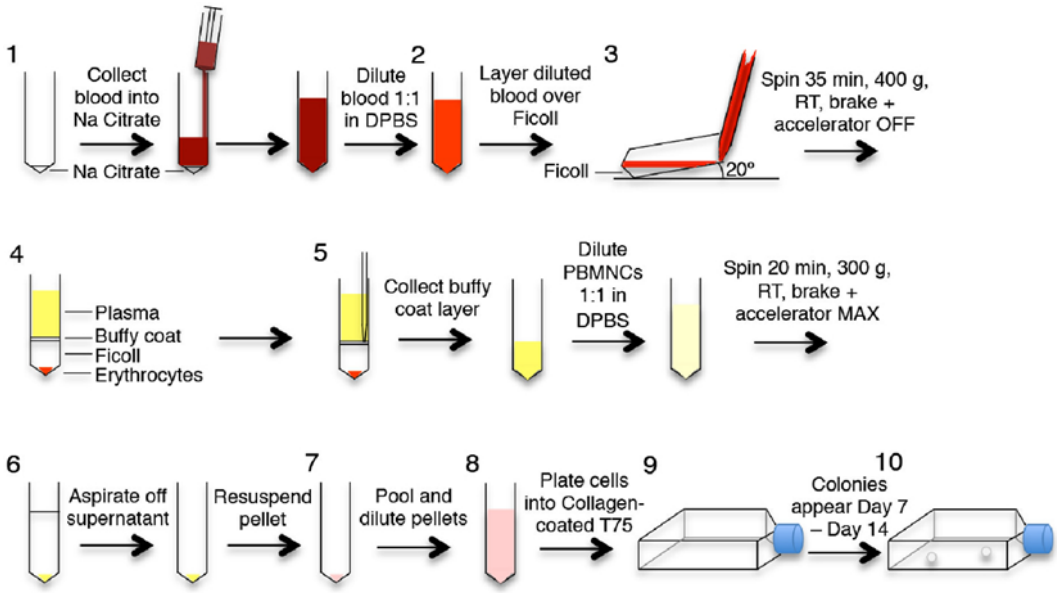

Figure A.3. Schematic diagram outlining the steps for ECFC isolation from peripheral blood. Figure reproduced from [275].

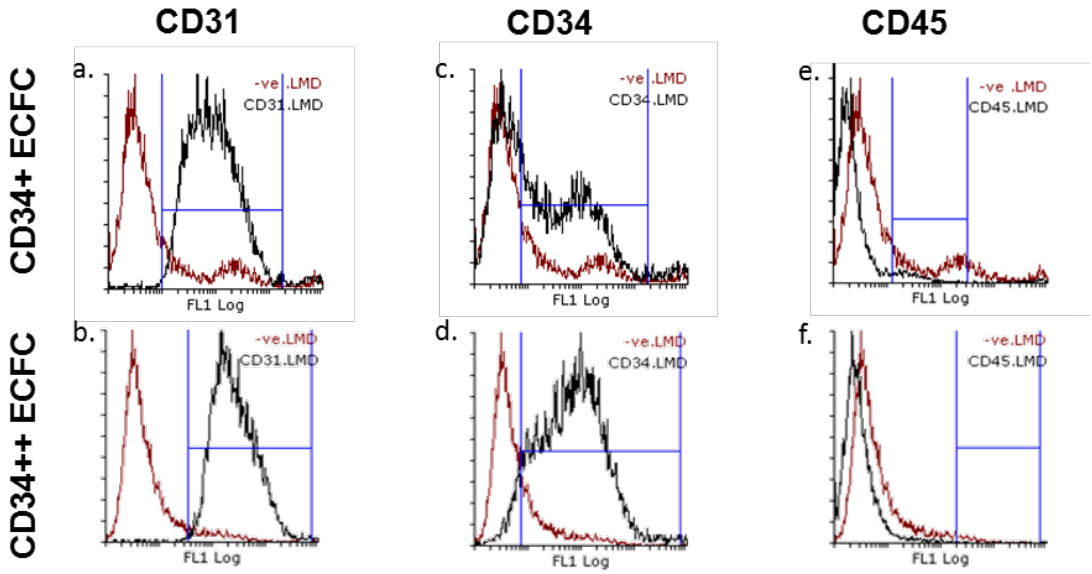

Figure A.4. Characterisation of isolated ECFCs from two different donors by flow cytometry: CD34+ and CD34++ ECFCs. Histograms showed the expression of (a-b) CD31, (c-d) CD34 and (e-f) CD45 by each isolate. Isotype negative control is represented in red, and positively stained cells in black. (a-b) Both isolates highly expressed the endothelial cell marker CD31. (c-d) In terms of the expression of the progenitor marker CD34, CD34+ ECFCs showed two populations, half of which expressed this antigen (55.7%), while CD34++ ECFCs showed a high expression of this marker (89%). (e-f) To further confirm the identity of the isolated cells, the expression of the hematopoietic marker CD45 was measured. Both isolates were negative for this marker. (Experiment performed by Ms Isra Marei).

Bibliography

[1] World Health Organization (WHO). Cardiovascular Diseases (CVDs) 2013;2014.

[2] Weber C, Noels H. Atherosclerosis: current pathogenesis and therapeutic options. Nat Med 2011;17:1410–22.

[3] Grüntzig AR, Senning Å, Siegenthaler WE. Nonoperative Dilatation of Coronary-Artery Stenosis. N Engl J Med 1979;301:61–8.

[4] Palmaz JC, Sibbitt RR, Reuter SR, Tio FO, Rice WJ. Expandable intraluminal graft: a preliminary study. Work in progress. Radiology 1985;156:73–7.

[5] Sigwart U, Puel J, Mirkovitch V, Joffre F, Kappenberger L. Intravascular Stents to Prevent Occlusion and Re-Stenosis after Transluminal Angioplasty. N Engl J Med 1987;316:701–6.

[6] Simard T, Hibbert B, Ramirez FD, Froeschl M, Chen Y-X, O'Brien ER. The Evolution of Coronary Stents: A Brief Review. Can J Cardiol 2014;30:35–45.

[7] Fischman DL, Leon MB, Baim DS, Schatz RA, Savage MP, Penn I, et al. A Randomized Comparison of Coronary-Stent Placement and Balloon Angioplasty in the Treatment of Coronary Artery Disease. N Engl J Med 1994;331:496–501.

[8] Serruys PW, de Jaegere P, Kiemeneij F, Macaya C, Rutsch W, Heyndrickx G, et al. A Comparison of Balloon-Expandable-Stent Implantation with Balloon Angioplasty in Patients with Coronary Artery Disease. N Engl J Med 1994;331:489–95.

[9] Chaabane C, Otsuka F, Virmani R, Bochaton-Piallat M-L. Biological responses in stented arteries. Cardiovasc Res 2013;99:353–63.

[10] Flores-Ríos X, Marzoa-Rivas R, Abugattás-de Torres JP, Piñón-Esteban P, Aldama-López G, Salgado-Fernández J, et al. Late thrombosis of paclitaxel-eluting stents: Long-term incidence, clinical consequences, and risk factors in a cohort of 604 patients. Am Heart J 2008;155:648–53.

[11] Joner M, Finn A V., Farb A, Mont EK, Kolodgie FD, Ladich E, et al. Pathology of Drug-Eluting Stents in Humans. Delayed Healing and Late Thrombotic Risk. J Am Coll Cardiol 2006;48:193–202.

[12] Witzenbichler B. Dual antiplatelet therapy after drug-eluting stent implantation: is it time to slacken the reins? J Am Coll Cardiol 2012;60:1349–51.

[13] Rizas KD, Mehilli J. Stent polymers: Do they make a difference? Circ Cardiovasc Interv 2016;9:1–14.

[14] Otsuka F, Vorpahl M, Nakano M, Foerst J, Newell JB, Sakakura K, et al. Pathology of second-generation everolimus-eluting stents versus first-generation sirolimus-and paclitaxel-eluting stents in humans. Circulation 2014;129:211–23.

[15] Joner M, Nakazawa G, Finn A V, Quee SC, Coleman L, Acampado E, et al. Endothelial cell recovery between comparator polymer-based drug-eluting stents. J Am Coll Cardiol 2008;52:333–42.

[16] Garg S, Bourantas C, Serruys PW. New concepts in the design of drug-eluting coronary stents. Nat Rev Cardiol 2013;10:248–60.

[17] von Birgelen C, Kok MM, van der Heijden LC, Danse PW, Schotborgh CE, Scholte M, et al. Very thin strut biodegradable polymer everolimus-eluting and sirolimus-eluting stents versus durable polymer zotarolimus-eluting stents in allcomers with coronary artery disease (BIO-RESORT): a three-arm, randomised, non-inferiority trial. Lancet 2016;388:2607–17.

[18] Indolfi C, De Rosa S, Colombo A. Bioresorbable vascular scaffolds — basic concepts and clinical outcome. Nat Rev Cardiol 2016;13:719–29.

[19] Serruys PW, Chevalier B, Sotomi Y, Cequier A, Carrié D, Piek JJ, et al. Comparison

of an everolimus-eluting bioresorbable scaffold with an everolimus-eluting metallic stent for the treatment of coronary artery stenosis (ABSORB II): a 3 year, randomised, controlled, single-blind, multicentre clinical trial. Lancet 2016;388:2479–91.

[20] Bowen PK, Shearier ER, Zhao S, Guillory RJ, Zhao F, Goldman J, et al. Biodegradable Metals for Cardiovascular Stents: From Clinical Concerns to Recent Zn-Alloys. Adv Healthc Mater 2016;5:1121–40.

[21] Peuster M, Wohlsein P, Brügmann M, Ehlerding M, Seidler K, Fink C, et al. A novel approach to temporary stenting: degradable cardiovascular stents produced from corrodible metal-results 6-18 months after implantation into New Zealand white rabbits. Heart 2001;86:563–9.

[22] Peuster M, Hesse C, Schloo T, Fink C, Beerbaum P, von Schnakenburg C. Long-term biocompatibility of a corrodible peripheral iron stent in the porcine descending aorta. Biomaterials 2006;27:4955–62.

[23] Heublein B, Rohde R, Kaese V, Niemeyer M, Hartung W, Haverich A. Biocorrosion of magnesium alloys: a new principle in cardiovascular implant technology? Heart 2003;89:651–6.

[24] Rapetto C, Leoncini M. Magmaris: a new generation metallic sirolimus-eluting fully bioresorbable scaffold: present status and future perspectives. J Thorac Dis 2017;9:S903–13.

[25] Bowen PK, Drelich J, Goldman J. Zinc exhibits ideal physiological corrosion behavior for bioabsorbable stents. Adv Mater 2013;25:2577–82.

[26] Satzl S, Henn C, Christoph P, Kurz P, Stampfl U, Stampfl S, et al. The efficacy of nanoscale poly[bis(trifluoroethoxy) phosphazene] (PTFEP) coatings in reducing thrombogenicity and late in-stent stenosis in a porcine coronary artery model. Invest Radiol 2007;42:303–11.

[27] Cutlip DE, Garratt KN, Novack V, Barakat M, Meraj P, Maillard L, et al. 9-Month Clinical and Angiographic Outcomes of the COBRA Polyzene-F NanoCoated Coronary Stent System. JACC Cardiovasc Interv 2017;10:160–7.

[28] Otsuka F, Finn A V, Yazdani SK, Nakano M, Kolodgie FD, Virmani R. The importance of the endothelium in atherothrombosis and coronary stenting. Nat Rev Cardiol 2012;9:439–53.

[29] Schwartz BG, Economides C, Mayeda GS, Burstein S, Kloner RA. The endothelial cell in health and disease: its function, dysfunction, measurement and therapy. Int J Impot Res 2009;22:77–90.

[30] Lerman A, Zeiher AM. Endothelial function: cardiac events. Circulation 2005;111:363–8.

[31] Patel SD, Waltham M, Wadoodi a, Burnand KG, Smith a. The role of endothelial cells and their progenitors in intimal hyperplasia. Ther Adv Cardiovasc Dis 2010;4:129–41.

[32] Hahn C, Schwartz MA. Mechanotransduction in vascular physiology and atherogenesis. Nat Rev Mol Cell Biol 2009;10:53–62.

[33] Avci-Adali M, Ziemer G, Wendel HP. Induction of EPC homing on biofunctionalized vascular grafts for rapid in vivo self-endothelialization — A review of current strategies. Biotechnol Adv 2010;28:119–29.

[34] Asahara T, Murohara T, Sullivan A, Silver M, van der Zee R, Li T, et al. Isolation of Putative Progenitor Endothelial Cells for Angiogenesis. Science (80-) 1997;275:964–6.

[35] Hristov M, Weber C. Endothelial progenitor cells in vascular repair and remodeling. Pharmacol Res 2008;58:148–51.

[36] Asahara T, Kawamoto A, Masuda H. Concise review: Circulating endothelial progenitor cells for vascular medicine. Stem Cells 2011;29:1650–5.

[37] Yoder MC. Human endothelial progenitor cells. Cold Spring Harb Perspect Med 2012;2:a006692.

[38] Hirschi KK, Ingram D a, Yoder MC. Assessing identity, phenotype, and fate of endothelial progenitor cells. Arterioscler Thromb Vasc Biol 2008;28:1584–95.

[39] Medina RJ, Barber CL, Sabatier F, Dignat-George F, Melero-Martin JM, Khosrotehrani K, et al. Endothelial Progenitors: A Consensus Statement on Nomenclature. Stem Cells Transl Med 2017;6:1316–20.

[40] Prater DN, Case J, Ingram D a, Yoder MC. Working hypothesis to redefine endothelial progenitor cells. Leukemia 2007;21:1141–9.

[41] Ingram D a, Mead LE, Tanaka H, Meade V, Fenoglio A, Mortell K, et al. Identification of a novel hierarchy of endothelial progenitor cells using human peripheral and umbilical cord blood. Blood 2004;104:2752–60.

[42] Reed DM, Paschalaki KE, Starke RD, Mohamed NA, Sharp G, Fox B, et al. An autologous endothelial cell: Peripheral blood mononuclear cell assay that detects cytokine storm responses to biologics. FASEB J 2015;29:2595–602.

[43] Lin Y, Weisdorf DJ, Solovey A, Hebbel RP. Origins of circulating endothelial cells and endothelial outgrowth from blood. J Clin Invest 2000;105:71–7.

[44] Ingram DA, Mead LE, Moore DB, Woodard W, Fenoglio A, Yoder MC. Vessel wall-derived endothelial cells rapidly proliferate because they contain a complete hierarchy of endothelial progenitor cells. Blood 2005;105:2783–6.

[45] Miglionico M, Patti G, D'Ambrosio A, Di Sciascio G. Percutaneous coronary intervention utilizing a new endothelial progenitor cells antibody-coated stent: A prospective single-center registry in high-risk patients. Catheter Cardiovasc Interv 2008;71:600–4.

[46] Klomp M, Beijk M a M, Damman P, Woudstra P, Koch KT, Tijssen JGP, et al. Three-year clinical follow-up of an unselected patient population treated with the genous endothelial progenitor cell capturing stent. J Interv Cardiol 2011;24:442–9.

[47] Silber S, Damman P, Klomp M, Beijk M, Grisold M, Ribeiro E, et al. Clinical results after coronary stenting with the Genous™ Bio-engineered R stent™: 12-month outcomes of the e-HEALING (Healthy Endothelial Accelerated Lining Inhibits Neointimal Growth) worldwide registry. EuroIntervention 2011;6:819–25.

[48] Sethi R, Lee C-H. Endothelial Progenitor Cell Capture Stent: Safety and Effectiveness. J Interv Cardiol 2012;25:493–500.

[49] Klomp M, Beijk M a, Varma C, Koolen JJ, Teiger E, Richardt G, et al. 1-Year Outcome of TRIAS HR (TRI-Stent Adjudication Study–High Risk of Restenosis). JACC Cardiovasc Interv 2011;4:896–904.

[50] Beijk MAM, Klomp M, van Geloven N, Koch KT, Henriques JPS, Baan J, et al. Two-year follow-up of the genous™ endothelial progenitor cell capturing stent versus the taxus liberté stent in patients with De Novo coronary artery lesions with a high-risk of restenosis. Catheter Cardiovasc Interv 2011;78:189–95.

[51] PEARSON JD. Endothelial progenitor cells - hype or hope? J Thromb Haemost 2009;7:255–62.

[52] Haude M, Lee SWL, Worthley SG, Silber S, Verheye S, Erbs S, et al. The REMEDEE Trial. JACC Cardiovasc Interv 2013;6:334–43.

[53] Woudstra P, Kalkman DN, den Heijer P, Menown IBA, Erglis A, Suryapranata H, et al. 1-Year Results of the REMEDEE Registry. JACC Cardiovasc Interv 2016;9:1127–34.

[54] Nakazawa G, Granada JF, Alviar CL, Tellez A, Kaluza GL, Guilhermier MY, et al. Anti-CD34 antibodies immobilized on the surface of sirolimus-eluting stents enhance stent endothelialization. JACC Cardiovasc Interv 2010;3:68–75.

[55] Rossi ML, Zavalloni D, Gasparini GL, Mango R, Belli G, Presbitero P. The first report of late stent thrombosis leading to acute myocardial infarction in patient

receiving the new endothelial progenitor cell capture stent. Int J Cardiol 2010;141:e20–2.

[56] Bangalore S, Toklu B, Amoroso N, Fusaro M, Kumar S, Hannan EL, et al. Bare metal stents, durable polymer drug eluting stents, and biodegradable polymer drug eluting stents for coronary artery disease: mixed treatment comparison meta-analysis. BMJ 2013;347:f6625–f6625.

[57] Williams DF. On the nature of biomaterials. Biomaterials 2009;30:5897–909.

[58] Tay CY, Irvine SA, Boey FYC, Tan LP, Venkatraman S. Micro-/nano-engineered cellular responses for soft tissue engineering and biomedical applications. Small 2011;7:1361–78.

[59] Lee PP, Cerchiari A, Desai TA. Nitinol-Based Nanotubular Coatings for the Modulation of Human Vascular Cell Function. Nano Lett 2014;14:5021–8.

[60] Dalby MJ, Berry CC, Riehle MO, Sutherland DS, Agheli H, Curtis ASG. Attempted endocytosis of nano-environment produced by colloidal lithography by human fibroblasts. Exp Cell Res 2004;295:387–94.

[61] Nazneen F, Herzog G, Arrigan DWM, Caplice N, Benvenuto P, Galvin P, et al. Surface chemical and physical modification in stent technology for the treatment of coronary artery disease. J Biomed Mater Res B Appl Biomater 2012;100:1989–2014.

[62] Wise SG, Waterhouse A, Kondyurin A, Bilek MM, Weiss AS. Plasma-based biofunctionalization of vascular implants. Nanomedicine (Lond) 2012;7:1907–16.

[63] Noel S, Liberelle B, Robitaille L, De Crescenzo G. Quantification of primary amine groups available for subsequent biofunctionalization of polymer surfaces. Bioconjug Chem 2011;22:1690–9.

[64] Zhu Y, Gao C, He T, Shen J. Endothelium regeneration on luminal surface of polyurethane vascular scaffold modified with diamine and covalently grafted with gelatin. Biomaterials 2004;25:423–30.

[65] Serrano MC, Portolés MT, Vallet-Regí M, Izquierdo I, Galletti L, Comas JV, et al. Vascular endothelial and smooth muscle cell culture on NaOH-treated poly(epsilon-caprolactone) films: a preliminary study for vascular graft development. Macromol Biosci 2005;5:415–23.

[66] Mager MD, LaPointe V, Stevens MM. Exploring and exploiting chemistry at the cell surface. Nat Chem 2011;3:582–9.

[67] Khan M, Yang J, Shi C, Lv J, Feng Y, Zhang W. Surface tailoring for selective endothelialization and platelet inhibition via a combination of SI-ATRP and click chemistry using Cys-Ala-Gly-peptide. Acta Biomater 2015;20:69–81.

[68] Xiong GM, Yuan S, Tan CK, Wang JK, Liu Y, Yang Tan TT, et al. Endothelial cell thrombogenicity is reduced by ATRP-mediated grafting of gelatin onto PCL surfaces. J Mater Chem B 2014;2:485.

[69] Farhatnia Y, Tan A, Motiwala A, Cousins BG, Seifalian AM. Evolution of covered stents in the contemporary era: clinical application, materials and manufacturing strategies using nanotechnology. Biotechnol Adv 2013;31:524–42.

[70] Delebecq E, Pascault J, Boutevin B, Ganachaud F. On the Versatility of Urethane/Urea Bonds: Reversibility, Blocked Isocyanate, and Non-isocyanate Polyurethane. Chem Rev 2013;113:80–118.

[71] Engels H-W, Pirkl H-G, Albers R, Albach RW, Krause J, Hoffmann A, et al. Polyurethanes: Versatile Materials and Sustainable Problem Solvers for Today's Challenges. Angew Chemie Int Ed 2013;52:9422–41.

[72] Cooper SL, Guan J, editors. Advances in Polyurethane Biomaterials. Woodhead Publishing; 2016.

[73] Bayer O, Siefken W, Rinke H, Orthner L, Schild H. Verfahren zur Herstellung von Polyurethanen bzw. Polyharnstoffen. DRP 728981, 1937.

[74] Król P. Synthesis methods, chemical structures and phase structures of linear

polyurethanes. Properties and applications of linear polyurethanes in polyurethane elastomers, copolymers and ionomers. Prog Mater Sci 2007;52:915–1015.

[75] Kannan RY, Salacinski HJ, Odlyha M, Butler PE, Seifalian AM. The degradative resistance of polyhedral oligomeric silsesquioxane nanocore integrated polyurethanes: an in vitro study. Biomaterials 2006;27:1971–9.

[76] Marcos-Fernández A, Abraham GA, Valentín JL, Román JS. Synthesis and characterization of biodegradable non-toxic poly(ester-urethane-urea)s based on poly(ε-caprolactone) and amino acid derivatives. Polymer (Guildf) 2006;47:785–98.

[77] Guan J, Sacks MS, Beckman EJ, Wagner WR. Biodegradable poly(ether ester urethane)urea elastomers based on poly(ether ester) triblock copolymers and putrescine: Synthesis, characterization and cytocompatibility. Biomaterials 2004;25:85–96.

[78] Nguyen L-TT, Truong TT, Nguyen HT, Le L, Nguyen VQ, Van Le T, et al. Healable shape memory (thio)urethane thermosets. Polym Chem 2015;6:3143–54.

[79] Cooper SL, Tobolsky A V. Properties of linear elastomeric polyurethanes. J Appl Polym Sci 1966;10:1837–44.

[80] Santerre JP, Woodhouse K, Laroche G, Labow RS. Understanding the biodegradation of polyurethanes: From classical implants to tissue engineering materials. Biomaterials 2005;26:7457–70.

[81] Stankus JJ, Guan J, Fujimoto K, Wagner WR. Microintegrating smooth muscle cells into a biodegradable, elastomeric fiber matrix. Biomaterials 2006;27:735–44.

[82] Schubert MA, Wiggins MJ, Anderson JM, Hiltner A. Role of oxygen in biodegradation of poly(etherurethane urea) elastomers. J Biomed Mater Res 1997;34:519–30.

[83] Zhao Q, Agger MP, Fitzpatrick M, Anderson JM, Hiltner A, Stokes K, et al. Cellular interactions with biomaterials:In vivo cracking of pre-stressed pellethane 2363-80A. J Biomed Mater Res 1990;24:621–37.

[84] Faré S, Petrini P, Motta A, Cigada A, Tanzi MC. Synergistic effects of oxidative environments and mechanical stress on in vitro stability of polyetherurethanes and polycarbonateurethanes. J Biomed Mater Res 1999;45:62–74.

[85] Khan I, Smith N, Jones E, Finch DS, Cameron RE. Analysis and evaluation of a biomedical polycarbonate urethane tested in an in vitro study and an ovine arthroplasty model. Part I: Materials selection and evaluation. Biomaterials 2005;26:621–31.

[86] Wang F, Li Z, Lannutti JL, Wagner WR, Guan J. Synthesis, characterization and surface modification of low moduli poly(ether carbonate urethane)ureas for soft tissue engineering. Acta Biomater 2009;5:2901–12.

[87] Hong Y, Guan J, Fujimoto KL, Hashizume R, Pelinescu AL, Wagner WR. Tailoring the degradation kinetics of poly(ester carbonate urethane)urea thermoplastic elastomers for tissue engineering scaffolds. Biomaterials 2010;31:4249–58.

[88] Ye S, Hong Y, Sakaguchi H, Shankarraman V, Luketich SK, D'Amore A, et al. Nonthrombogenic, Biodegradable Elastomeric Polyurethanes with Variable Sulfobetaine Content. ACS Appl Mater Interfaces 2014;6:22796–806.

[89] Pereira MJN, Ouyang B, Sundback CA, Lang N, Friehs I, Mureli S, et al. A highly tunable biocompatible and multifunctional biodegradable elastomer. Adv Mater 2013;25:1209–15.

[90] Xu C, Huang Y, Wu J, Tang L, Hong Y. Triggerable Degradation of Polyurethanes for Tissue Engineering Applications. ACS Appl Mater Interfaces 2015;7:20377–88.

[91] Ahmed M, Hamilton G, Seifalian AM. The performance of a small-calibre graft for vascular reconstructions in a senescent sheep model. Biomaterials 2014;35:9033–40.

[92] Farhatnia Y, Pang JH, Darbyshire A, Dee R, Tan A, Seifalian AM. Next generation covered stents made from nanocomposite materials: A complete assessment of

uniformity, integrity and biomechanical properties. Nanomedicine Nanotechnology, Biol Med 2016;12:1–12.

[93] Qiu X, Lee BL-P, Ning X, Murthy N, Dong N, Li S. End-point immobilization of heparin on plasma-treated surface of electrospun polycarbonate-urethane vascular graft. Acta Biomater 2017;51:138–47.

[94] Griffin MF, Palgrave RG, Seifalian AM, Butler PE, Kalaskar DM. Enhancing tissue integration and angiogenesis of a novel nanocomposite polymer using plasma surface polymerisation, an in vitro and in vivo study. Biomater Sci 2016;4:145–58.

[95] Bax D V, Kondyurin A, Waterhouse A, McKenzie DR, Weiss AS, Bilek MMM. Surface plasma modification and tropoelastin coating of a polyurethane co-polymer for enhanced cell attachment and reduced thrombogenicity. Biomaterials 2014;35:6797–809.

[96] You I, Kang SM, Byun Y, Lee H. Enhancement of blood compatibility of poly(urethane) substrates by mussel-inspired adhesive heparin coating. Bioconjug Chem 2011;22:1264–9.

[97] Ding YH, Floren M, Tan W. Mussel-inspired polydopamine for bio-surface functionalization. Biosurface and Biotribology 2016;2:121–36.

[98] Hung H-S, Yang Y-C, Lin Y-C, Lin S-Z, Kao W-C, Hsieh H-H, et al. Regulation of human endothelial progenitor cell maturation by polyurethane nanocomposites. Biomaterials 2014;35:6810–21.

[99] Tan A, Goh D, Farhatnia Y, G N, Lim J, Teoh S-H, et al. An anti-CD34 antibody-functionalized clinical-grade POSS-PCU nanocomposite polymer for cardiovascular stent coating applications: a preliminary assessment of endothelial progenitor cell capture and hemocompatibility. PLoS One 2013;8:e77112.

[100] Lu Y, Shen L, Gong F, Cui J, Rao J, Chen J, et al. Polycarbonate urethane films modified by heparin to enhance hemocompatibility and endothelialization. Polym Int 2012;61:1433–8.

[101] Chattopadhyay DK, Prasad PSR, Sreedhar B, Raju KVSN. The phase mixing of moisture cured polyurethane-urea during cure. Prog Org Coatings 2005;54:296–304.

[102] Kläusler O, Clauß S, Lübke L, Trachsel J, Niemz P. Influence of moisture on stress–strain behaviour of adhesives used for structural bonding of wood. Int J Adhes Adhes 2013;44:57–65.

[103] Sheikh N, Mirzadeh H, Katbab a a, Salehian P, Daliri M, Amanpour S. Isocyanate-terminated urethane prepolymer as bioadhesive material: evaluation of bioadhesion and biocompatibility, in vitro and in vivo assays. J Biomater Sci Polym Ed 2001;12:707–19.

[104] Sheikh N, Katbab a. a., Mirzadeh H. Isocyanate-terminated urethane prepolymer as bioadhesive base material: Synthesis and characterization. Int J Adhes Adhes 2000;20:299–304.

[105] Nagai N, Nakayama Y, Nishi S, Munekata M. Development of novel covered stents using salmon collagen. J Artif Organs 2009;12:61–6.

[106] De Visscher G, Mesure L, Meuris B, Ivanova A, Flameng W. Improved endothelialization and reduced thrombosis by coating a synthetic vascular graft with fibronectin and stem cell homing factor SDF-1α. Acta Biomater 2012;8:1330–8.

[107] Shindo S, Motohashi S, Katsu M, Kaga S, Inoue H, Matsumoto M. Coated prostheses are associated with prolonged inflammation in aortic surgery: a cost analysis. Artif Organs 2008;32:183–7.

[108] Zheng W, Wang Z, Song L, Zhao Q, Zhang J, Li D, et al. Endothelialization and patency of RGD-functionalized vascular grafts in a rabbit carotid artery model. Biomaterials 2012;33:2880–91.

[109] Eichmann A, Simons M. VEGF signaling inside vascular endothelial cells and beyond. Curr Opin Cell Biol 2012;24:188–93.

[110] Ferrara N, Gerber H-P, LeCouter J. The biology of VEGF and its receptors. Nat Med 2003;9:669–76.

[111] Hristov M. Endothelial Progenitor Cells: Mobilization, Differentiation, and Homing. Arterioscler Thromb Vasc Biol 2003;23:1185–9.

[112] Shin YM, Lee Y Bin, Kim SJ, Kang JK, Park J-C, Jang W, et al. Mussel-inspired immobilization of vascular endothelial growth factor (VEGF) for enhanced endothelialization of vascular grafts. Biomacromolecules 2012;13:2020–8.

[113] Xu H, Nguyen KT, Brilakis ES, Yang J, Fuh E, Banerjee S. Enhanced endothelialization of a new stent polymer through surface enhancement and incorporation of growth factor-delivering microparticles. J. Cardiovasc. Transl. Res., vol. 5, 2012, p. 519–27.

[114] von Degenfeld G, Banfi A, Springer ML, Wagner R a, Jacobi J, Ozawa CR, et al. Microenvironmental VEGF distribution is critical for stable and functional vessel growth in ischemia. FASEB J 2006;20:2657–9.

[115] Paul A, Elias CB, Shum-Tim D, Prakash S. Bioactive baculovirus nanohybrids for stent based rapid vascular re-endothelialization. Sci Rep 2013;3:2366.

[116] Miyazu K, Kawahara D, Ohtake H, Watanabe G, Matsuda T. Luminal surface design of electrospun small-diameter graft aiming at in situ capture of endothelial progenitor cell. J Biomed Mater Res B Appl Biomater 2010;94:53–63.

[117] Suzuki Y, Yamamoto K, Ando J, Matsumoto K, Matsuda T. Arterial shear stress augments the differentiation of endothelial progenitor cells adhered to VEGF-bound surfaces. Biochem Biophys Res Commun 2012;423:91–7.

[118] Matsuda T, Kuwana M, Aomizu T, Yamagishi M, Ohtake H, Watanabe G. Surface design for in situ capture of endothelial progenitor cells: VEGF-bound surface architecture and behaviors of cultured mononuclear cells. J Biomed Mater Res B Appl Biomater 2013;101:50–60.

[119] Kawahara D, Matsuda T. Hydrodynamic shear-stress-dependent retention of endothelial and endothelial progenitor cells adhered to vascular endothelial growth factor-fixed surfaces. J Biomed Mater Res B Appl Biomater 2012;100:1218–28.

[120] Takabatake S, Hayashi K, Nakanishi C, Hao H, Sakata K, Kawashiri M-A, et al. Vascular endothelial growth factor-bound stents: application of in situ capture technology of circulating endothelial progenitor cells in porcine coronary model. J Interv Cardiol 2014;27:63–72.

[121] Goel HL, Mercurio AM. VEGF targets the tumour cell. Nat Rev Cancer 2013;13:871–82.

[122] Zeng W, Wen C, Wu Y, Li L, Zhou Z, Mi J, et al. The use of BDNF to enhance the patency rate of small-diameter tissue-engineered blood vessels through stem cell homing mechanisms. Biomaterials 2012;33:473–84.

[123] Zeng W, Yuan W, Li L, Mi J, Xu S, Wen C, et al. The promotion of endothelial progenitor cells recruitment by nerve growth factors in tissue-engineered blood vessels. Biomaterials 2010;31:1636–45.

[124] de Mel A, Murad F, Seifalian AM. Nitric oxide: a guardian for vascular grafts? Chem Rev 2011;111:5742–67.

[125] Andukuri A, Sohn Y, Anakwenze CP, Lim D, Brott BC, Yoon Y, et al. Enhanced human endothelial progenitor cell adhesion and differentiation by a bioinspired multifunctional nanomatrix. Tissue Eng Part C Methods 2013;19:375–85.

[126] de Mel A, Naghavi N, Cousins BG, Clatworthy I, Hamilton G, Darbyshire A, et al. Nitric oxide-eluting nanocomposite for cardiovascular implants. J Mater Sci Mater Med 2013;25:917–29.

[127] Kushwaha M, Anderson JM, Bosworth C a, Andukuri A, Minor WP, Lancaster JR, et al. A nitric oxide releasing, self assembled peptide amphiphile matrix that mimics native endothelium for coating implantable cardiovascular devices. Biomaterials

2010;31:1502–8.

[128] Naghavi N, de Mel A, Alavijeh OS, Cousins BG, Seifalian AM. Nitric oxide donors for cardiovascular implant applications. Small 2013;9:22–35.

[129] Taite LJ, Yang P, Jun H, West JL. Nitric oxide-releasing polyurethane-PEG copolymer containing the YIGSR peptide promotes endothelialization with decreased platelet adhesion. J Biomed Mater Res B Appl Biomater 2008;84:108–16.

[130] Yang Z, Tu Q, Wang J, Huang N. The role of heparin binding surfaces in the direction of endothelial and smooth muscle cell fate and re-endothelialization. Biomaterials 2012;33:6615–25.

[131] Wang S, Mo XM, Jiang BJ, Gao CJ, Wang HS, Zhuang YG, et al. Fabrication of small-diameter vascular scaffolds by heparin-bonded P(LLA-CL) composite nanofibers to improve graft patency. Int J Nanomedicine 2013;8:2131–9.

[132] Daenens K, Schepers S, Fourneau I, Houthoofd S, Nevelsteen A. Heparin-bonded ePTFE grafts compared with vein grafts in femoropopliteal and femorocrural bypasses: 1- and 2-year results. J Vasc Surg 2009;49:1210–6.

[133] Yang Z, Xiong K, Qi P, Yang Y, Tu Q, Wang J, et al. Gallic Acid Tailoring Surface Functionalities of Plasma-Polymerized Allylamine-Coated 316L SS to Selectively Direct Vascular Endothelial and Smooth Muscle Cell Fate for Enhanced Endothelialization. ACS Appl Mater Interfaces 2014;6:2647–56.

[134] He Y, Wang J, Yan W, Huang N. Gallic acid and gallic acid-loaded coating involved in selective regulation of platelet, endothelial and smooth muscle cell fate. RSC Adv 2014;4:212–21.

[135] Plouffe BD, Kniazeva T, Mayer JE, Murthy SK, Sales VL. Development of microfluidics as endothelial progenitor cell capture technology for cardiovascular tissue engineering and diagnostic medicine. FASEB J 2009;23:3309–14.

[136] Markway BD, McCarty OJT, Marzec UM, Courtman DW, Hanson SR, Hinds MT. Capture of flowing endothelial cells using surface-immobilized anti-kinase insert domain receptor antibody. Tissue Eng Part C Methods 2008;14:97–105.

[137] Lim W-H, Seo W-W, Choe W, Kang C-K, Park J, Cho H-J, et al. Stent coated with antibody against vascular endothelial-cadherin captures endothelial progenitor cells, accelerates re-endothelialization, and reduces neointimal formation. Arterioscler Thromb Vasc Biol 2011;31:2798–805.

[138] Lee JM, Choe W, Kim B-K, Seo W-W, Lim W-H, Kang C-K, et al. Comparison of endothelialization and neointimal formation with stents coated with antibodies against CD34 and vascular endothelial-cadherin. Biomaterials 2012;33:8917–27.

[139] Sedaghat A, Sinning J-M, Paul K, Kirfel G, Nickenig G, Werner N. First in vitro and in vivo results of an anti-human CD133-antibody coated coronary stent in the porcine model. Clin Res Cardiol 2013;102:413–25.

[140] Wei Y, Ji Y, Xiao L-L, Lin Q, Xu J, Ren K, et al. Surface engineering of cardiovascular stent with endothelial cell selectivity for in vivo re-endothelialisation. Biomaterials 2013;34:2588–99.

[141] Ceylan H, Tekinay AB, Guler MO. Selective adhesion and growth of vascular endothelial cells on bioactive peptide nanofiber functionalized stainless steel surface. Biomaterials 2011;32:8797–805.

[142] Lei Y, Rémy M, Labrugère C, Durrieu M-C. Peptide immobilization on polyethylene terephthalate surfaces to study specific endothelial cell adhesion, spreading and migration. J Mater Sci Mater Med 2012;23:2761–72.

[143] Li Q, Wang Z, Zhang S, Zheng W, Zhao Q, Zhang J, et al. Functionalization of the surface of electrospun poly(epsilon-caprolactone) mats using zwitterionic poly(carboxybetaine methacrylate) and cell-specific peptide for endothelial progenitor cells capture. Mater Sci Eng C Mater Biol Appl 2013;33:1646–53.

[144] Ji Q, Zhang S, Zhang J, Wang Z, Wang J, Cui Y, et al. Dual functionalization of

poly(ε-caprolactone) film surface through supramolecular assembly with the aim of promoting in situ endothelial progenitor cell attachment on vascular grafts. Biomacromolecules 2013;14:4099–107.

[145] Larsen CC, Kligman F, Tang C, Kottke-Marchant K, Marchant RE. A biomimetic peptide fluorosurfactant polymer for endothelialization of ePTFE with limited platelet adhesion. Biomaterials 2007;28:3537–48.

[146] Hoffmann J, Paul A, Harwardt M, Groll J, Reeswinkel T, Klee D, et al. Immobilized DNA aptamers used as potent attractors for porcine endothelial precursor cells. J Biomed Mater Res A 2008;84:614–21.

[147] Strahm Y, Flueckiger A, Billinger M, Meier P, Mettler D, Weisser S, et al. Endothelial-cell-binding aptamer for coating of intracoronary stents. J Invasive Cardiol 2010;22:481–7.

[148] Yuan Y, Yin M, Qian J, Liu C. Site-directed immobilization of antibodies onto blood contacting grafts for enhanced endothelial cell adhesion and proliferation. Soft Matter 2011;7:7207.

[149] Chong MSK, Chan J, Choolani M, Lee CN, Teoh SH. Development of cell-selective films for layered co-culturing of vascular progenitor cells. Biomaterials 2009;30:2241–51.

[150] Lin R-Z, Hatch A, Antontsev VG, Murthy SK, Melero-Martin JM. Microfluidic Capture of Endothelial Colony-Forming Cells from Human Adult Peripheral Blood: Phenotypic and Functional Validation In Vivo. Tissue Eng Part C Methods 2014;21:1–11.

[151] Chong MSK, Teoh S, Teo EY, Zhang Z, Lee CN, Koh S, et al. Beyond cell capture: antibody conjugation improves hemocompatibility for vascular tissue engineering applications. Tissue Eng Part A 2010;16:2485–95.

[152] Lewandowska K, Kaplan D, Husel W. CD34 expression on platelets. Platelets 2003;14:83–7.

[153] Yeh ETH, Zhang S, Wu HD, Körbling M, Willerson JT, Estrov Z. Transdifferentiation of human peripheral blood CD34+-enriched cell population into cardiomyocytes, endothelial cells, and smooth muscle cells in vivo. Circulation 2003;108:2070–3.

[154] Rotmans JI, Heyligers JMM, Verhagen HJM, Velema E, Nagtegaal MM, de Kleijn DP V, et al. In vivo cell seeding with anti-CD34 antibodies successfully accelerates endothelialization but stimulates intimal hyperplasia in porcine arteriovenous expanded polytetrafluoroethylene grafts. Circulation 2005;112:12–8.

[155] Peichev M, Naiyer AJ, Pereira D, Zhu Z, Lane WJ, Williams M, et al. Expression of VEGFR-2 and AC133 by circulating human CD34(+) cells identifies a population of functional endothelial precursors. Blood 2000;95:952–8.

[156] Dineen SP, Lynn KD, Holloway SE, Miller AF, Sullivan JP, Shames DS, et al. Vascular endothelial growth factor receptor 2 mediates macrophage infiltration into orthotopic pancreatic tumors in mice. Cancer Res 2008;68:4340–6.

[157] Hubbell JA, Massia SP, Desai NP, Drumheller PD. Endothelial Cell-Selective Materials for Tissue Engineering in the Vascular Graft Via a New Receptor. Nat Biotechnol 1991;9:568–72.

[158] Yu S, Gao Y, Mei X, Ren T, Liang S, Mao Z, et al. Preparation of an Arg-Glu-Asp-Val Peptide Density Gradient on Hyaluronic Acid-Coated Poly(ε-caprolactone) Film and Its Influence on the Selective Adhesion and Directional Migration of Endothelial Cells. ACS Appl Mater Interfaces 2016;8:29280–8.

[159] Castellanos MI, Zenses AS, Grau A, Rodríguez-Cabello JC, Gil FJ, Manero JM, et al. Biofunctionalization of REDV elastin-like recombinamers improves endothelialization on CoCr alloy surfaces for cardiovascular applications. Colloids Surfaces B Biointerfaces 2015;127:22–32.

[160] Yang J, Khan M, Zhang L, Ren X, Guo J, Feng Y, et al. Antimicrobial surfaces grafted random copolymers with REDV peptide beneficial for endothelialization. J Mater Chem B 2015;3:7682–97.

[161] Plouffe BD, Njoka DN, Harris J, Liao J, Horick NK, Radisic M, et al. Peptide-mediated selective adhesion of smooth muscle and endothelial cells in microfluidic shear flow. Langmuir 2007;23:5050–5.

[162] Jun H-W, West JL. Modification of polyurethaneurea with PEG and YIGSR peptide to enhance endothelialization without platelet adhesion. J Biomed Mater Res 2005;72B:131–9.

[163] Andukuri A, Minor WP, Kushwaha M, Anderson JM, Jun HW. Effect of endothelium mimicking self-assembled nanomatrices on cell adhesion and spreading of human endothelial cells and smooth muscle cells. Nanomedicine Nanotechnology, Biol Med 2010;6:289–97.

[164] Ren T, Yu S, Mao Z, Moya SE, Han L, Gao C. Complementary Density Gradient of Poly(hydroxyethyl methacrylate) and YIGSR Selectively Guides Migration of Endotheliocytes. Biomacromolecules 2014;15:2256–64.

[165] Fittkau M., Zilla P, Bezuidenhout D, Lutolf M., Human P, Hubbell J., et al. The selective modulation of endothelial cell mobility on RGD peptide containing surfaces by YIGSR peptides. Biomaterials 2005;26:167–74.

[166] Seeto WJ, Tian Y, Lipke E a. Peptide-grafted poly(ethylene glycol) hydrogels support dynamic adhesion of endothelial progenitor cells. Acta Biomater 2013;9:8279–89.

[167] Bazan J, Całkosiński I, Gamian A. Phage display--a powerful technique for immunotherapy: 1. Introduction and potential of therapeutic applications. Hum Vaccin Immunother 2012;8:1817–28.

[168] Veleva AN, Cooper SL, Patterson C. Selection and initial characterization of novel peptide ligands that bind specifically to human blood outgrowth endothelial cells. Biotechnol Bioeng 2007;98:306–12.

[169] Veleva AN, Heath DE, Cooper SL, Patterson C. Selective endothelial cell attachment to peptide-modified terpolymers. Biomaterials 2008;29:3656–61.

[170] Chen H, Li X, Zhao Y, Li J, Chen J, Yang P, et al. Construction of a multifunctional coating consisting of phospholipids and endothelial progenitor cell-specific peptides on titanium substrates. Appl Surf Sci 2015;347:169–77.

[171] Dudash L a, Kligman FL, Bastijanic JM, Kottke-Marchant K, Marchant RE. Cross-reactivity of cell-selective CRRETAWAC peptide with human and porcine endothelial cells. J Biomed Mater Res A 2013:1–7.

[172] Ohuchi S. Cell-SELEX Technology. Biores Open Access 2012;1:265–72.

[173] Qi P, Yan W, Yang Y, Li Y, Fan Y, Chen J, et al. Immobilization of DNA aptamers via plasma polymerized allylamine film to construct an endothelial progenitor cell-capture surface. Colloids Surfaces B Biointerfaces 2015;126:70–9.

[174] Avci-Adali M, Steinle H, Michel T, Schlensak C, Wendel HP. Potential capacity of aptamers to trigger immune activation in human blood. PLoS One 2013;8:e68810.

[175] Pislaru S V., Harbuzariu A, Agarwal G, Witt T, Gulati R, Sandhu NP, et al. Magnetic forces enable rapid endothelialization of synthetic vascular grafts. Circulation 2006;114:314–9.

[176] Kyrtatos PG, Lehtolainen P, Junemann-Ramirez M, Garcia-Prieto A, Price AN, Martin JF, et al. Magnetic Tagging Increases Delivery of Circulating Progenitors in Vascular Injury. JACC Cardiovasc Interv 2009;2:794–802.

[177] Astanina K, Simon Y, Cavelius C, Petry S, Kraegeloh A, Kiemer AK. Superparamagnetic iron oxide nanoparticles impair endothelial integrity and inhibit nitric oxide production. Acta Biomater 2014;10:4896–911.

[178] Uttayarat P, Perets A, Li M, Pimton P, Stachelek SJ, Alferiev I, et al.

Micropatterning of three-dimensional electrospun polyurethane vascular grafts. Acta Biomater 2010;6:4229–37.

[179] Csaderova L, Martines E, Seunarine K, Gadegaard N, Wilkinson CDW, Riehle MO. A biodegradable and biocompatible regular nanopattern for large-scale selective cell growth. Small 2010;6:2755–61.

[180] Lin Q, Ding X, Qiu F, Song X, Fu G, Ji J. In situ endothelialization of intravascular stents coated with an anti-CD34 antibody functionalized heparin-collagen multilayer. Biomaterials 2010;31:4017–25.

[181] Camci-Unal G, Nichol JW, Bae H, Tekin H, Bischoff J, Khademhosseini A. Hydrogel surfaces to promote attachment and spreading of endothelial progenitor cells. J Tissue Eng Regen Med 2013;7:337–47.

[182] Lu S, Zhang P, Sun X, Gong F, Yang S, Shen L, et al. Synthetic ePTFE grafts coated with an anti-CD133 antibody-functionalized heparin/collagen multilayer with rapid in vivo endothelialization properties. ACS Appl Mater Interfaces 2013;5:7360–9.

[183] Melchiorri AJ, Hibino N, Yi T, Lee YU, Sugiura T, Tara S, et al. Contrasting Biofunctionalization Strategies for the Enhanced Endothelialization of Biodegradable Vascular Grafts. Biomacromolecules 2015;16:437–46.

[184] Yang Z, Yang Y, Yan W, Tu Q, Wang J, Huang N. SupportingInfo:Construction of polyfunctional coatings assisted by gallic acid to facilitate Co-immobilization of diverse biomolecules. ACS Appl Mater Interfaces 2013;5:10495–501.

[185] Liu S, Liu T, Chen J, Maitz M, Chen C, Huang N. Influence of a layer-by-layer-assembled multilayer of anti-CD34 antibody, vascular endothelial growth factor, and heparin on the endothelialization and anticoagulation of titanium surface. J Biomed Mater Res A 2013;101:1144–57.

[186] Chen Z, Li Q, Chen J, Luo R, Maitz MF, Huang N. Immobilization of serum albumin and peptide aptamer for EPC on polydopamine coated titanium surface for enhanced in-situ self-endothelialization. Mater Sci Eng C 2016;60:219–29.

[187] Minelli C, Lowe SB, Stevens MM. Engineering nanocomposite materials for cancer therapy. Small 2010;6:2336–57.

[188] Venturelli E, Fabbro C, Chaloin O, Ménard-Moyon C, Smulski CR, Da Ros T, et al. Antibody covalent immobilization on carbon nanotubes and assessment of antigen binding. Small 2011;7:2179–87.

[189] Ueda H, Dong J. From fluorescence polarization to Quenchbody: Recent progress in fluorescent reagentless biosensors based on antibody and other binding proteins. Biochim Biophys Acta 2014.

[190] Pernagallo S, Tura O, Wu M, Samuel K, Diaz-Mochon JJ, Hansen A, et al. Novel biopolymers to enhance endothelialisation of intra-vascular devices. Adv Healthc Mater 2012;1:646–56.

[191] Goddard JM, Hotchkiss JH. Tailored functionalization of low-density polyethylene surfaces. J Appl Polym Sci 2008;108:2940–9.

[192] Rabe M, Verdes D, Seeger S. Understanding protein adsorption phenomena at solid surfaces. Adv Colloid Interface Sci 2011;162:87–106.

[193] Tajima N, Takai M, Ishihara K. Significance of antibody orientation unraveled: well-oriented antibodies recorded high binding affinity. Anal Chem 2011;83:1969–76.

[194] Kosobrodova E, Jones RT, Kondyurin A, Chrzanowski W, Pigram PJ, Mckenzie DR, et al. Orientation and conformation of anti-CD34 antibody immobilised on untreated and plasma treated polycarbonate. Acta Biomater 2015;19:128–37.

[195] Whittle JD, Bullett N a., Short RD, Ian Douglas CW, Hollander AP, Davies J. Adsorption of vitronectin, collagen and immunoglobulin-G to plasma polymer surfaces by enzyme linked immunosorbent assay (ELISA). J Mater Chem 2002;12:2726–32.

[196] Schramm W, Paek S-H, Voss G. Strategies for the Immobilization of Antibodies.

Immunomethods 1993;3:93–103.

[197] Petersen S, Strohbach A, Busch R, Felix SB, Schmitz K-P, Sternberg K. Site-selective immobilization of anti-CD34 antibodies to poly(l-lactide) for endovascular implant surfaces. J Biomed Mater Res B Appl Biomater 2014;102:345–55.

[198] de Mel A, Jell G, Stevens MM, Seifalian AM. Biofunctionalization of biomaterials for accelerated in situ endothelialization: a review. Biomacromolecules 2008;9:2969–79.

[199] Sharma H, Mutharasan R. Half Antibody Fragments Improve Biosensor Sensitivity without Loss of Selectivity. Anal Chem 2013;85:2472–7.

[200] Trilling AK, Beekwilder J, Zuilhof H. Antibody orientation on biosensor surfaces: a minireview. Analyst 2013;138:1619–27.

[201] Li Y, Wei S, Wu J, Jasensky J, Xi C, Li H, et al. Effects of peptide immobilization sites on the structure and activity of surface tethered antimicrobial peptides. J Phys Chem C 2015;119:7146–55.

[202] Hersel U, Dahmen C, Kessler H. RGD modified polymers: Biomaterials for stimulated cell adhesion and beyond. Biomaterials 2003;24:4385–415.

[203] Thapa P, Espiritu MJ, Cabalteja C, Bingham J-P. The emergence of cyclic peptides: the potential of bioengineered peptide drugs. Int J Pept Res Ther 2014;20:545–51.

[204] Maeda T, Titani K, Sekiguchi K. Cell-adhesive activity and receptor-binding specificity of the laminin-derived YIGSR sequence grafted onto Staphylococcal protein A. J Biochem 1994;115:182–9.

[205] Kurihara H, Nagamune T. Cell adhesion ability of artificial extracellular matrix proteins containing a long repetitive Arg-Gly-Asp sequence. J Biosci Bioeng 2005;100:82–7.

[206] Lee JW, Park YJ, Lee SJ, Lee SK, Lee KY. The effect of spacer arm length of an adhesion ligand coupled to an alginate gel on the control of fibroblast phenotype. Biomaterials 2010;31:5545–51.

[207] Bonzani IC, Adhikari R, Houshyar S, Mayadunne R, Gunatillake P, Stevens MM. Synthesis of two-component injectable polyurethanes for bone tissue engineering. Biomaterials 2007;28:423–33.

[208] Haghayegh M, Mirabedini SM, Yeganeh H. Microcapsules containing multi-functional reactive isocyanate-terminated polyurethane prepolymer as a healing agent. Part 1: synthesis and optimization of reaction conditions. J Mater Sci 2016;51:3056–68.

[209] McDermott M, Chatterjee S, Hu X, Ash-Shakoor A, Avery R, Belyaeva A, et al. Application of Quality by Design (QbD) Approach to Ultrasonic Atomization Spray Coating of Drug-Eluting Stents. AAPS PharmSciTech 2015;16:811–23.

[210] ASTM D2572-97. Standard Test Method for Isocyanate Groups in Urethane Materials or Prepolymers 2010.

[211] Rajan R, Pandit AB. Correlations to predict droplet size in ultrasonic atomisation. Ultrasonics 2001;39:235–55.

[212] Ma Z, Mao Z, Gao C. Surface modification and property analysis of biomedical polymers used for tissue engineering. Colloids Surf B Biointerfaces 2007;60:137–57.

[213] Lawrence CJ, Zhou W. Spin coating of non-Newtonian fluids. J Nonnewton Fluid Mech 1991;39:137–87.

[214] Sahu N, Parija B, Panigrahi S. Fundamental understanding and modeling of spin coating process: A review. Indian J Phys 2009;83:493–502.

[215] Agnihotri A, Garrett JT, Runt J, Siedlecki CA. Atomic force microscopy visualization of poly(urethane urea) microphase rearrangements under aqueous environment. J Biomater Sci Polym Ed 2006;17:227–38.

[216] Garrett JT, Runt J, Lin JS. Microphase Separation of Segmented Poly(urethane urea) Block Copolymers. Macromolecules 2000;33:6353–9.

[217] Wu Z, Wang H, Tian X, Cui P, Ding X, Ye X. The effects of polydimethylsiloxane on transparent and hydrophobic waterborne polyurethane coatings containing polydimethylsiloxane. Phys Chem Chem Phys 2014;16:6787.

[218] Wisse E, Govaert LE, Meijer HEH, Meijer EW. Unusual tuning of mechanical properties of thermoplastic elastomers using molecular fillers. Macromolecules 2006;39:7425–32.

[219] Yu Y-J, Hearon K, Wilson TS, Maitland DJ. The effect of moisture absorption on the physical properties of polyurethane shape memory polymer foams. Smart Mater Struct 2011;20:85010.

[220] Ni H, Yap CK, Jin Y. Effect of curing moisture on the indentation force deflection of flexible polyurethane foam. J Appl Polym Sci 2007;104:1679–82.

[221] Lepene BS, Long TE, Meyer A, Kranbuehl DE. Moisture-Curing Kinetics of Isocyanate Prepolymer Adhesives. J Adhes 2002;78:297–312.

[222] Huang Y, Venkatraman SS, Boey FYC, Lahti EM, Umashankar PR, Mohanty M, et al. In vitro and in vivo performance of a dual drug-eluting stent (DDES). Biomaterials 2010;31:4382–91.

[223] Bakhshi R, Darbyshire A, Evans JE, You Z, Lu J, Seifalian AM. Polymeric coating of surface modified nitinol stent with POSS-nanocomposite polymer. Colloids Surfaces B Biointerfaces 2011;86:93–105.

[224] Kamath S, Bhattacharyya D, Padukudru C, Timmons RB, Tang L. Surface chemistry influences implant-mediated host tissue responses. J Biomed Mater Res - Part A 2008;86:617–26.

[225] Chen Z, Bachhuka A, Han S, Wei F, Lu S, Visalakshan RM, et al. Tuning Chemistry and Topography of Nanoengineered Surfaces to Manipulate Immune Response for Bone Regeneration Applications. ACS Nano 2017;11:4494–506.

[226] Bachhuka A, Hayball JD, Smith LE, Vasilev K. The Interplay between Surface Nanotopography and Chemistry Modulates Collagen i and III Deposition by Human Dermal Fibroblasts. ACS Appl Mater Interfaces 2017;9:5874–84.

[227] Hensarling RM, Rahane SB, LeBlanc AP, Sparks BJ, White EM, Locklin J, et al. Thiol–isocyanate "click" reactions: rapid development of functional polymeric surfaces. Polym Chem 2011;2:88–90.

[228] Beamson G, Briggs D. High resolution XPS of organic polymers: the scienta ESCA300 database. Chichester (England): Wiley; 1992.

[229] Ding H, Wei J-S, Xiong H-M. Nitrogen and sulfur co-doped carbon dots with strong blue luminescence. Nanoscale 2014;6:13817–23.

[230] Dong Y, Pang H, Yang H Bin, Guo C, Shao J, Chi Y, et al. Carbon-Based Dots Co-doped with Nitrogen and Sulfur for High Quantum Yield and Excitation-Independent Emission. Angew Chemie Int Ed 2013;52:7800–4.

[231] Graf N, Yegen E, Gross T, Lippitz A, Weigel W, Krakert S, et al. XPS and NEXAFS studies of aliphatic and aromatic amine species on functionalized surfaces. Surf Sci 2009;603:2849–60.

[232] Khung YL, Ngalim SH, Scaccabarozi A, Narducci D. Thermal and UV Hydrosilylation of Alcohol-Based Bifunctional Alkynes on Si (111) surfaces: How surface radicals influence surface bond formation. Sci Rep 2015;5:11299.

[233] Lin-Vien D, Colthup NB, Fateley WG, Grasselli JG. The Handbook of Infrared and Raman Characteristic Frequencies of Organic Molecules. San Diego: Academic Press; 1991.

[234] Janik H, Pałys B, Petrovic ZS. Multiphase-Separated Polyurethanes Studied by Micro-Raman Spectroscopy. Macromol Rapid Commun 2003;24:265–8.

[235] Feng W, Li L, Ueda E, Li J, Heißler S, Welle A, et al. Surface Patterning via Thiol-Yne Click Chemistry: An Extremely Fast and Versatile Approach to Superhydrophilic-Superhydrophobic Micropatterns. Adv Mater Interfaces

2014;1:1400269.

[236] Silverstein JS, Casey BJ, Natoli ME, Dair BJ, Kofinas P. Rapid Modular Synthesis and Processing of Thiol–Ene Functionalized Styrene–Butadiene Block Copolymers. Macromolecules 2012;45:3161–7.

[237] Ramiasa-MacGregor M, Mierczynska A, Sedev R, Vasilev K. Tuning and predicting the wetting of nanoengineered material surface. Nanoscale 2016;8:4635–42.

[238] Ruckenstein E, Sun F. Anomalous sorption and pervaporation of aqueous organic mixtures by poly(vinyl acetal) membranes. J Memb Sci 1994;95:207–19.

[239] Huang S-L, Ou C-F, Lai J-Y. Polyurethane membrane prepared via a dry/wet phase inversion method for protein adsorption. J Appl Polym Sci 1999;74:1334–40.

[240] Noel S, Hachem A, Merhi Y, De Crescenzo G. Development of a Polyester Coating Combining Antithrombogenic and Cell Adhesive Properties: Influence of Sequence and Surface Density of Adhesion Peptides. Biomacromolecules 2015;16:1682–94.

[241] Keen I, Broota P, Rintoul L, Fredericks P, Trau M, Grøndahl L. Introducing amine functionalities on a poly(3-hydroxybutyrate-co-3-hydroxyvalerate) surface: comparing the use of ammonia plasma treatment and ethylenediamine aminolysis. Biomacromolecules 2006;7:427–34.

[242] Wisse E, Spiering AJH, van Leeuwen ENM, Renken RAE, Dankers PYW, Brouwer LA, et al. Molecular Recognition in Poly(ε-caprolactone)-Based Thermoplastic Elastomers. Biomacromolecules 2006;7:3385–95.

[243] Soto-Cantu E, Lokitz BS, Hinestrosa JP, Deodhar C, Messman JM, Ankner JF, et al. Versatility of alkyne-modified poly(glycidyl methacrylate) layers for click reactions. Langmuir 2011;27:5986–96.

[244] Hu X, Tan H, Wang X, Chen P. Surface functionalization of hydrogel by thiol-yne click chemistry for drug delivery. Colloids Surfaces A Physicochem Eng Asp 2016;489:297–304.

[245] Mehrban N, Abelardo E, Wasmuth A, Hudson KL, Mullen LM, Thomson AR, et al. Assessing Cellular Response to Functionalized α-Helical Peptide Hydrogels. Adv Healthc Mater 2014;3:1387–91.

[246] Lowe AB. Thiol-yne "click"/coupling chemistry and recent applications in polymer and materials synthesis and modification. Polym (United Kingdom) 2014;55:5517–49.

[247] Bhairamadgi NS, Gangarapu S, Caipa Campos MA, Paulusse JMJ, Van Rijn CJM, Zuilhof H. Efficient functionalization of oxide-free silicon(111) surfaces: Thiol-yne versus thiol-ene click chemistry. Langmuir 2013;29:4535–42.

[248] Hacking A, Khademhosseini A. Cells and Surfaces in vitro. In: Ratner BD, Hoffman AS, Schoen FJ, Lemons JE, editors. Biomater. Sci. An Introd. to Mater. Med., Elsevier; 2013, p. 408–26.

[249] Dhowre HS, Rajput S, Russell NA, Zelzer M. Responsive cell–material interfaces. Nanomedicine 2015;10:849–71.

[250] Wong JY, Leach JB, Brown XQ. Balance of chemistry, topography, and mechanics at the cell-biomaterial interface: Issues and challenges for assessing the role of substrate mechanics on cell response. Surf Sci 2004;570:119–33.

[251] Geiger B, Spatz JP, Bershadsky AD. Environmental sensing through focal adhesions. Nat Rev Mol Cell Biol 2009;10:21–33.

[252] Potthoff E, Franco D, D'Alessandro V, Starck C, Falk V, Zambelli T, et al. Toward a rational design of surface textures promoting endothelialization. Nano Lett 2014;14:1069–79.

[253] Miller DC, Thapa A, Haberstroh KM, Webster TJ. Endothelial and vascular smooth muscle cell function on poly(lactic-co-glycolic acid) with nano-structured surface features. Biomaterials 2004;25:53–61.

[254] De S, Sharma R, Trigwell S, Laska B, Ali N, Mazumder MK, et al. Plasma treatment

of polyurethane coating for improving endothelial cell growth and adhesion. J Biomater Sci Polym Ed 2005;16:973–89.

[255] Dalby MJ, Riehle MO, Johnstone H, Affrossman S, Curtis ASG. In vitro reaction of endothelial cells to polymer demixed nanotopography. Biomaterials 2002;23:2945–54.

[256] Geiger B, Tokuyasu KT, Dutton a H, Singer SJ. Vinculin, an intracellular protein localized at specialized sites where microfilament bundles terminate at cell membranes. Proc Natl Acad Sci 1980;77:4127–31.

[257] Bakolitsa C, Cohen DM, Bankston LA, Bobkov AA, Cadwell GW, Jennings L, et al. Structural basis for vinculin activation at sites of cell adhesion. Nature 2004;430:583–6.

[258] Humphries JD, Wang P, Streuli C, Geiger B, Humphries MJ, Ballestrem C. Vinculin controls focal adhesion formation by direct interactions with talin and actin. J Cell Biol 2007;179:1043–57.

[259] Roach P, Farrar D, Perry CC. Interpretation of Protein Adsorption: Surface-Induced Conformational Changes. J Am Chem Soc 2005;127:8168–73.

[260] Arima Y, Iwata H. Effect of wettability and surface functional groups on protein adsorption and cell adhesion using well-defined mixed self-assembled monolayers. Biomaterials 2007;28:3074–82.

[261] Khan M, Yang J, Shi C, Feng Y, Zhang W, Gibney K, et al. Surface Modification of Polycarbonate Urethane with Zwitterionic Polynorbornene via Thiol-ene Click-Reaction to Facilitate Cell Growth and Proliferation. Macromol Mater Eng 2015;300:802–9.

[262] Khan M, Yang J, Shi C, Feng Y, Zhang W, Gibney K, et al. Manipulation of polycarbonate urethane bulk properties via incorporated zwitterionic polynorbornene for tissue engineering applications. RSC Adv 2015;5:11284–92.

[263] Lee JH, Jung HW, Kang I-K, Lee HB. Cell behaviour on polymer surfaces with different functional groups. Biomaterials 1994;15:705–11.

[264] Navaneetha Pandiyaraj K, Selvarajan V, Rhee YH, Kim HW, Pavese M. Effect of DC glow discharge plasma treatment on PET/TiO(2) thin film surfaces for enhancement of bioactivity. Colloids Surf B Biointerfaces 2010;79:53–60.

[265] Brammer KS, Oh S, Gallagher JO, Jin S. Enhanced cellular mobility guided by TiO2 nanotube surfaces. Nano Lett 2008;8:786–93.

[266] Liliensiek SJ, Wood JA, Yong J, Auerbach R, Nealey PF, Murphy CJ. Modulation of human vascular endothelial cell behaviors by nanotopographic cues. Biomaterials 2010;31:5418–26.

[267] Kim D-H, Provenzano PP, Smith CL, Levchenko A. Matrix nanotopography as a regulator of cell function. J Cell Biol 2012;197:351–60.

[268] Rechendorff K, Hovgaard MB, Foss M, Zhdanov VP, Besenbacher F. Enhancement of Protein Adsorption Induced by Surface Roughness. Langmuir 2006;22:10885–8.

[269] Ngandu Mpoyi E, Cantini M, Reynolds PM, Gadegaard N, Dalby MJ, Salmerón-Sánchez M. Protein Adsorption as a Key Mediator in the Nanotopographical Control of Cell Behavior. ACS Nano 2016;10:6638–47.

[270] Danoux C, Sun L, Koçer G, Birgani ZT, Barata D, Barralet J, et al. Development of Highly Functional Biomaterials by Decoupling and Recombining Material Properties. Adv Mater 2016;28:1803–8.

[271] Koepsel JT, Loveland SG, Schwartz MP, Zorn S, Belair DG, Le NN, et al. A chemically-defined screening platform reveals behavioral similarities between primary human mesenchymal stem cells and endothelial cells. Integr Biol 2012;4:1508.

[272] Bellis SL. Advantages of RGD peptides for directing cell association with biomaterials. Biomaterials 2011;32:4205–10.

[273] Li Q-L, Huang N, Chen C, Chen J-L, Xiong K-Q, Chen J-Y, et al. Oriented immobilization of anti-CD34 antibody on titanium surface for self-endothelialization induction. J Biomed Mater Res A 2010;94:1283–93.

[274] Martin-Ramirez J, Hofman M, van den Biggelaar M, Hebbel RP, Voorberg J. Establishment of outgrowth endothelial cells from peripheral blood. Nat Protoc 2012;7:1709–15.

[275] Ormiston ML, Toshner MR, Kiskin FN, Huang CJZ, Groves E, Morrell NW, et al. Generation and Culture of Blood Outgrowth Endothelial Cells from Human Peripheral Blood. J Vis Exp 2015:e53384.

[276] Ko TM, Lin JC, Cooper SL. Surface characterization and platelet adhesion studies of plasma-sulphonated polyethylene. Biomaterials 1993;14:657–64.

[277] Leung J. Development of Novel Pro-healing Composite Coating for Next Generation Coronary Artery Stents (MSc thesis). University College London (UCL), 2017.

[278] Makaraviciute A, Ramanaviciene A. Site-directed antibody immobilization techniques for immunosensors. Biosens Bioelectron 2013;50:460–71.

[279] Hensarling RM, Doughty VA, Chan JW, Patton DL. "Clicking" Polymer Brushes with Thiol-yne Chemistry: Indoors and Out. J Am Chem Soc 2009;131:14673–5.

[280] Sun Z, Han C, Song M, Wen L, Tian D, Li H, et al. Fabrication of Cysteine-Responsive Biomimetic Single Nanochannels by a Thiol-yne Reaction Strategy and Their Application for Sensing in Urine Samples. Adv Mater 2014;26:455–60.

[281] Le Saux G, Magenau A, Gunaratnam K, Kilian K a, Böcking T, Gooding JJ, et al. Spacing of integrin ligands influences signal transduction in endothelial cells. Biophys J 2011;101:764–73.

[282] Shahal T, Geiger B, Dunlop IE, Spatz JP. Regulation of integrin adhesions by varying the density of substrate-bound epidermal growth factor. Biointerphases 2012;7:23.

[283] Karimi F, McKenzie TG, O'Connor AJ, Qiao GG, Heath DE. Nano-scale clustering of integrin-binding ligands regulates endothelial cell adhesion, migration, and endothelialization rate: novel materials for small diameter vascular graft applications. J Mater Chem B 2017;5:5942–53.

[284] Eggermann J, Kliche S, Jarmy G, Hoffmann K, Mayr-Beyrle U, Debatin KM, et al. Endothelial progenitor cell culture and differentiation in vitro: a methodological comparison using human umbilical cord blood. Cardiovasc Res 2003;58:478–86.

[285] Mikhailidis DP, Barradas M a, Maris A, Jeremy JY, Dandona P. Fibrinogen mediated activation of platelet aggregation and thromboxane A2 release: pathological implications in vascular disease. J Clin Pathol 1985;38:1166–71.

[286] Zhang L, Casey B, Galanakis DK, Marmorat C, Skoog S, Vorvolakos K, et al. The influence of surface chemistry on adsorbed fibrinogen conformation, orientation, fiber formation and platelet adhesion. Acta Biomater 2017;54:164–74.

[287] Yin M, Yuan Y, Liu C, Wang J. Combinatorial coating of adhesive polypeptide and anti-CD34 antibody for improved endothelial cell adhesion and proliferation. J Mater Sci Mater Med 2009;20:1513–23.

[288] Butruk-Raszeja BA, Dresler MS, Kuźmińska A, Ciach T. Endothelialization of polyurethanes: Surface silanization and immobilization of REDV peptide. Colloids Surfaces B Biointerfaces 2016;144:335–43.

[289] Bogdanowich-Knipp SJ, Chakrabarti S, Siahaan TJ, Williams TD, Dillman RK. Solution stability of linear vs. cyclic RGD peptides. J Pept Res 1999;53:530–41.

[290] Xiao Y, Truskey GA. Effect of receptor-ligand affinity on the strength of endothelial cell adhesion. Biophys J 1996;71:2869–84.

[291] Dechantsreiter MA, Planker E, Mathä B, Lohof E, Hölzemann G, Jonczyk A, et al. N -Methylated Cyclic RGD Peptides as Highly Active and Selective α V β 3 Integrin Antagonists. J Med Chem 1999;42:3033–40.

[292] Kämmerer P, Heller M, Brieger J, Klein M, Al-Nawas B, Gabriel M. Immobilisation of linear and cyclic RGD-peptides on titanium surfaces and their impact on endothelial cell adhesion and proliferation. Eur Cells Mater 2011;21:364–72.

[293] Cutiongco MFA, Anderson DEJ, Hinds MT, Yim EKF. In vitro and ex vivo hemocompatibility of off-the-shelf modified poly(vinyl alcohol) vascular grafts. Acta Biomater 2015;25:97–108.

[294] Kornowski R, Hong MK, Tio FO, Bramwell O, Wu H, Leon MB. In-stent restenosis: contributions of inflammatory responses and arterial injury to neointimal hyperplasia. J Am Coll Cardiol 1998;31:224–30.

[295] Vishwakarma A, Bhise NS, Evangelista MB, Rouwkema J, Dokmeci MR, Ghaemmaghami AM, et al. Engineering Immunomodulatory Biomaterials To Tune the Inflammatory Response. Trends Biotechnol 2016;34:470–82.

[296] Chen J, Cao J, Wang J, Maitz MF, Guo L, Zhao Y, et al. Biofunctionalization of titanium with PEG and anti-CD34 for hemocompatibility and stimulated endothelialization. J Colloid Interface Sci 2012;368:636–47.

[297] de Mel A, Cousins BG, Seifalian AM. Surface modification of biomaterials: a quest for blood compatibility. Int J Biomater 2012;2012:707863.

[298] Yang Z, Yang Y, Yan W, Tu Q, Wang J, Huang N. Construction of Polyfunctional Coatings Assisted by Gallic Acid to Facilitate Co-Immobilization of Diverse Biomolecules. ACS Appl Mater Interfaces 2013;5:10495–501.

[299] Lee Y Bin, Shin YM, Lee J-H, Jun I, Kang JK, Park J-C, et al. Polydopamine-mediated immobilization of multiple bioactive molecules for the development of functional vascular graft materials. Biomaterials 2012;33:8343–52.

[300] Spruell JM, Wolffs M, Leibfarth FA, Stahl BC, Heo J, Connal LA, et al. Reactive, Multifunctional Polymer Films through Thermal Cross-linking of Orthogonal Click Groups. J Am Chem Soc 2011;133:16698–706.

[301] Kubo T, Figg CA, Swartz JL, Brooks WLA, Sumerlin BS. Multifunctional Homopolymers: Postpolymerization Modification via Sequential Nucleophilic Aromatic Substitution. Macromolecules 2016;49:2077–84.

[302] Brooks K, Yatvin J, McNitt CD, Reese RA, Jung C, Popik V V., et al. Multifunctional Surface Manipulation Using Orthogonal Click Chemistry. Langmuir 2016;32:6600–5.

[303] Hoyle CE, Lowe AB, Bowman CN. Thiol-click chemistry: a multifaceted toolbox for small molecule and polymer synthesis. Chem Soc Rev 2010;39:1355–87.

[304] Hu MC, Chien SL. The cytoplasmic domain of stem cell antigen CD34 is essential for cytoadhesion signaling but not sufficient for proliferation signaling. Blood 1998;91:1152–62.

[305] Koteliansky VE, Glukhova MA, Benjamin M V., Smirnov VN, Filimonov V V., Zalite OM, et al. A Study of the Structure of Fibronectin. Eur J Biochem 1981;119:619–24.

[306] Aoki J, Serruys PW, van Beusekom H, Ong ATL, McFadden EP, Sianos G, et al. Endothelial progenitor cell capture by stents coated with antibody against CD34: the HEALING-FIM (Healthy Endothelial Accelerated Lining Inhibits Neointimal Growth-First In Man) Registry. J Am Coll Cardiol 2005;45:1574–9.

Publications and Presentations

Pang, J. H., Farhatnia, Y., Godarzi, F., Tan, A., Rajadas, J., Cousins, B. G. and Seifalian, A. M. (2015), In situ endothelialization: bioengineering considerations to translation. *Small*, 11: 6248–6264.

Pang, J. H., Darbyshire, A., Tsui, J., Cousins, B. G. (2017), Biofunctionalization of chemical-cured urethane pre-polymer with endothelial cell selectivity for cardiovascular implants. European Society for Biomaterials (ESB) Annual Conference, Athens, Greece.

Pang, J. H., Darbyshire, A., Tsui, J., Cousins, B. G. (2017), Biofunctionalization of chemically-cured urethane pre-polymer coatings for next generation pro-healing cardiovascular implants. European Chapter Meeting of the Tissue Engineering and Regenerative Medicine International Society (TERMIS-EU), Davos, Switzerland.

Pang, J. H., Darbyshire, A., Zhao, J., Tsui, J., Cousins, B. G. (2017), Development of pro-healing vascular stent incorporating antibody stem cell capture technology. European Society for Vascular Society (ESVS) Spring Meeting, Leiden, The Netherlands.

Pang, J. H., Darbyshire, A., Tsui, J., Cousins, B. G. (2017), Chemical functionalization of urethane pre-polymer to enhance endothelial cell fate. Future Investigators of Regenerative Medicine (FIRM) Symposium, Girona, Spain.

Pang, J. H., Farhatnia, Y., Darbyshire, A., Zhao, J., Tsui, J., Cousins, B. G. (2016), Development of pre-polymer coatings with pro-endothelialisation potential for cardiovascular devices. European Society for Vascular Society (ESVS) Spring Meeting, London, UK.